UNIVERSITY OF LEEDS

DOCTORAL THESIS

---

# Descent and Near-Surface Evolution of Atmospheric Downdraughts

---

Sam WILLIAMS

*Supervisors:*

Professor Alan BLYTH

Dr Stephen GRIFFITHS

Dr John MARSHAM

*A thesis submitted in fulfilment of the requirements*

*for the degree of Doctor of Philosophy*

*in the*

EPSRC Centre for Doctoral Training in Fluid Dynamics

School of Computing

# Declaration of Authorship

I, Sam WILLIAMS, declare that this thesis titled, "Descent and Near-Surface Evolution of Atmospheric Downdraughts" and the work presented in it are my own. I confirm that:

- This work was done wholly or mainly while in candidature for a research degree at this University.
- Where any part of this thesis has previously been submitted for a degree or any other qualification at this University or any other institution, this has been clearly stated.
- Where I have consulted the published work of others, this is always clearly attributed.
- Where I have quoted from the work of others, the source is always given. With the exception of such quotations, this thesis is entirely my own work.
- I have acknowledged all main sources of help.
- Where the thesis is based on work done by myself jointly with others, I have made clear exactly what was done by others and what I have contributed myself.

Signed:

_____

Date:

_____

*"On the vast windy plain, there was plenty of nothing to be looked at."*

Larry McMurtry - The Last Kind Words Saloon

UNIVERSITY OF LEEDS

# *Abstract*

Faculty of Engineering

School of Computing

Doctor of Philosophy

**Descent and Near-Surface Evolution of Atmospheric Downdraughts**

by Sam WILLIAMS

Evaporation and drag from precipitation in convective clouds induce regions of negative buoyancy and momentum, generating downward motion known as downdraughts. The impact and near-surface evolution of strong downdraughts creates hazardous gust fronts that are often responsible for the peak surface winds associated with convective storms. A combination of theory, laboratory experiments and numerical simulations are used to analyse the descent and near-surface evolution of idealised downdraughts. Downdraughts are represented as releases of negatively buoyant fluid in i) saline releases in laboratory experiments and ii) cold bubbles in large eddy simulations using the Met Office and NERC Collaboration model. Both methodologies reproduce the salient features of atmospheric downdraughts. Existing theory from Rooney (2015) is compared to both methodologies of downdraught model, finding good agreement subject to changes in empirical constants. Scalings from Lundgren, Yao, and Mansour (1992) are used to compare the experimental results with the numerical simulations and demonstrate the radial propagation of idealised downdraughts can be related to their initial properties at source. Similarity solutions from Rooney (2015) are extended to include expressions for the kinetic energy and potential energy. Previous field experiments and observations have indicated that downdraughts from elevated convection can impact stable boundary layers and generate gravity currents, waves and bores. Numerical simulations are used to examine the novel scenario of a downdraught impacting a stable boundary layer. The vertical descent and radial propagation of the downdraught, and resulting disturbance of the stable boundary are mapped out for this flow regime. Entrainment and mixing of ambient air above the SBL is suggested as an explanation for atmospheric observations of downdraughts, where the cold downdraught actually results in a warm surface signal. The initial buoyancy of the downdraught relative to stable boundary layer is shown to determine whether the regime is i) current drive or ii) wave dominated. An assessment of the resulting wave dynamics is made and compared to the relevant internal gravity wave theory. The results of this study demonstrate how the properties of the resulting outflow (gravity current, bore or wave) can be related to the initial conditions of an elevated source of negative buoyancy or momentum.

# *Acknowledgements*

I am eternally indebted to my three supervisors, Alan Blyth, Stephen Griffiths and John Marsham whose insight, guidance and support made this PhD possible. Each has left their distinct mark on the thesis, elevating the work beyond what solely, I could ever have achieved. Stephen ensured a rigour to the theoretical work throughout the thesis, and I have relied heavily on his deep understanding of fluid dynamics. John brought the perspective and expertise of an atmospheric scientist, relating the motions of salt water in a tank to his observations of atmospheric phenomenon across the globe. Finally, my thanks go to Alan for your mentoring and friendship - you are the architect of this whole adventure.

I am grateful to the EPSRC Centre for Doctoral Training in Fluid Dynamics, the education you have provided is not limited to this PhD but will remain with me always. In particular, thank you Claire Savy and Peter Jimack. Similarly, thank you to Ben Shipway, Adrian Hill and Gabriel Rooney at the UK Met Office for your unwavering patience in the onslaught of my naive questions, and hosting me on my visits.

Thank you Cath, Ric, and Chris for your implacable support. Marianne, kiitos.

# Contents

# List of Figures

# List of Tables

# List of Symbols

| | | |
|---|---|---|
| $\phi_0$ | Indicates $\phi$ is a constant or conserved property | - |
| $\varphi_i$ | Indicates variable $\varphi$ at impingement. | - |
| $\alpha$ | Entrainment constant | - |
| $A_*$ | Threshold parameter | - |
| $b$ | Plume or thermal width | m |
| $b_0$ | Characteristic width | m |
| $B$ | Total buoyancy | $m^4\ s^{-2}$ |
| $\beta$ | Dimensionless constant | - |
| $c$ | Ultrasound velocity | $m\ s^{-1}$ |
| $c_{ds}$ | Coefficient of surface drag | - |
| $c_{ds}$ | Coefficient of friction drag | - |
| $c_*$ | Curve fitting constant | - |
| $C_1, C_2, C_3$ | Dimensionless constants | - |
| $C_4, C_5$ | Dimensionless constants | - |
| $CFL$ | Courant, Friedri hs and Levy number | - |
| $CVEL$ | largest advective Courant number | - |
| $CVIS$ | worst viscous stability parater | - |
| $\hat{e}$ | Fractional entrainment per distance travelled | $m^{-1}$ |
| $f, f_1, f_2$ | Dimensionless functions | - |
| $f_D$ | Doppler shift in the ultrasound frequency | - |
| $f_o$ | Ultrasound frequency | - |
| $F$ | Buoyancy flux | $m^4\ s^{-3}$ |
| $Fr_c$ | Froude number of gravity current | - |
| $Fr_T$ | Froude number of thermal | - |
| $\hat{g}$ | Cooling function | $K\ s^{-1}$ |
| $g$ | Gravitational acceleration | $m\ s^{-2}$ |
| $g'$ | Reduced gravity | $m\ s^{-2}$ |
| $\gamma$ | Gravity current parameter | - |
| $\gamma_*$ | Empirically determined constant | - |
| $h$ | Height of gravity current | m |
| $H$ | Initial height | m |
| $I$ | A camera image | - |
| $I_b$ | Base camera image | - |
| $k$ | Non-dimensional constant | - |
| $k_r$ | Non-dimensional constant | - |
| $k_*$ | Curve fitting constant | - |
| $k_u$ | Dimensionless constant | - |
| $k_w$ | Wave number | - |
| $\kappa$ | Cooling ratio | - |
| $KE$ | Kinetic energy | $kg\ m^{-1}\ s^{-2}$ |
| $\lambda$ | Dimensionless constant | - |
| $\hat{\lambda}$ | Length scale | - |

| | | |
|---|---|---|
| $L$ | Length scale | m |
| $m$ | Thermal shape factor | - |
| $n, n_1$ | Dimensionless constant | - |
| $n_*$ | Curve fitting constant | - |
| $N$ | Brunt–Vaisala frequency | $s^{-1}$ |
| $N_{x,y,z}$ | Number of $x, y, z$ grid points | - |
| $\pi$ | The constant Pi | - |
| $\phi$ | Dimensionless radius | - |
| $\hat{\phi}$ | Cooling ratio | - |
| $p$ | Pressure | Pa |
| $\Omega$ | Threshold parameter | - |
| $\Omega_*$ | Earth's angular velocity | - |
| $PE$ | Potential energy | kg $m^{-1}$ $s^{-2}$ |
| $\rho$ | Density | kg $m^{-3}$ |
| $q$ | Volume flux | $m^3$ $s^{-1}$ |
| $\hat{q}$ | Other scalar variables | - |
| $Q$ | Volumetric flow rate of source | $m^3$ $s^{-1}$ |
| $\hat{Q}$ | Cooling function | K $s^{-1}$ |
| $r$ | Radial coordinate | m |
| $r_f$ | Radial position of gravity current front | m |
| $R$ | Cylinder radius | m |
| $R_0$ | Characteristic length | m |
| $Re$ | Reynolds number | - |
| $\dot{r_f}$ | Speed of gravity current front | m $s^{-1}$ |
| $\theta$ | Potential temperature | K |
| $S$ | Empirically determined constant | - |
| $t$ | Time | s |
| $\tau$ | Dimensionless time | - |
| $TE$ | Total energy | kg $m^{-1}$ $s^{-2}$ |
| $u$ | $x$ component of velocity | m $s^{-1}$ |
| $u_r$ | Radial velocity | m $s^{-1}$ |
| $v$ | $y$ component of velocity | m $s^{-1}$ |
| $V$ | Volume | $m^3$ |
| $V_c$ | Volume of cylinder | $m^3$ |
| $w$ | $z$ component of velocity | m $s^{-1}$ |
| $\omega_{i3}$ | Kroneker delta function | - |
| $z_v$ | Virtual origin | m |
| $\zeta$ | Similarity variable | - |
| $\zeta_*$ | Vertical displacement | m |

*For Ric*

# Chapter 1

# Introduction

Downdraughts form part of the life-cycle of atmospheric moist convection. Throughout the day, solar radiation heats the ground, which in turn heats the air directly above it. This warmer air becomes less dense than its surroundings and consequentially the parcel of warm air rises upwards. As the warm air rises, it begins to cool and the water vapour within condenses forming clouds. If the cooling continues, precipitation (rain, hail, graupel) forms. The associated loading and evaporation of the falling precipitation induces downdraughts. This convective process of ascending warm air, formation of precipitation and resulting downdraught is integral to thunderstorms. Figure 1.1 is a schematic representation of the structure of a thunderstorm. The top image shows an isolated thunderstorm travelling from left to right. Warm air at the front edge of the thunderstorm rises, forming a cumulonimbus cloud. Whilst in the centre and rear of the thunderstorm, cold air descends as a downdraught.

The impact and near-surface evolution of strong downdraughts creates hazardous gust fronts that are often responsible for the peak surface winds associated with thunderstorms. These downdraughts and their associated outflows occur across a range of scales; from intense local events defined by Fujita (1985) as 'downbursts' (or when the radial outflow is less than 4 km, the subcategory 'microburst'), to cold pools between 10 to 100 km in diameter. In arid, dusty regions these cold pools can trigger dust storms known as 'haboobs'. The bottom image in Figure 1.1 shows a schematic of an isolated microburst. The particularly strong downdraught has impacted the ground and is spreading radially, with the leading edge of outflow

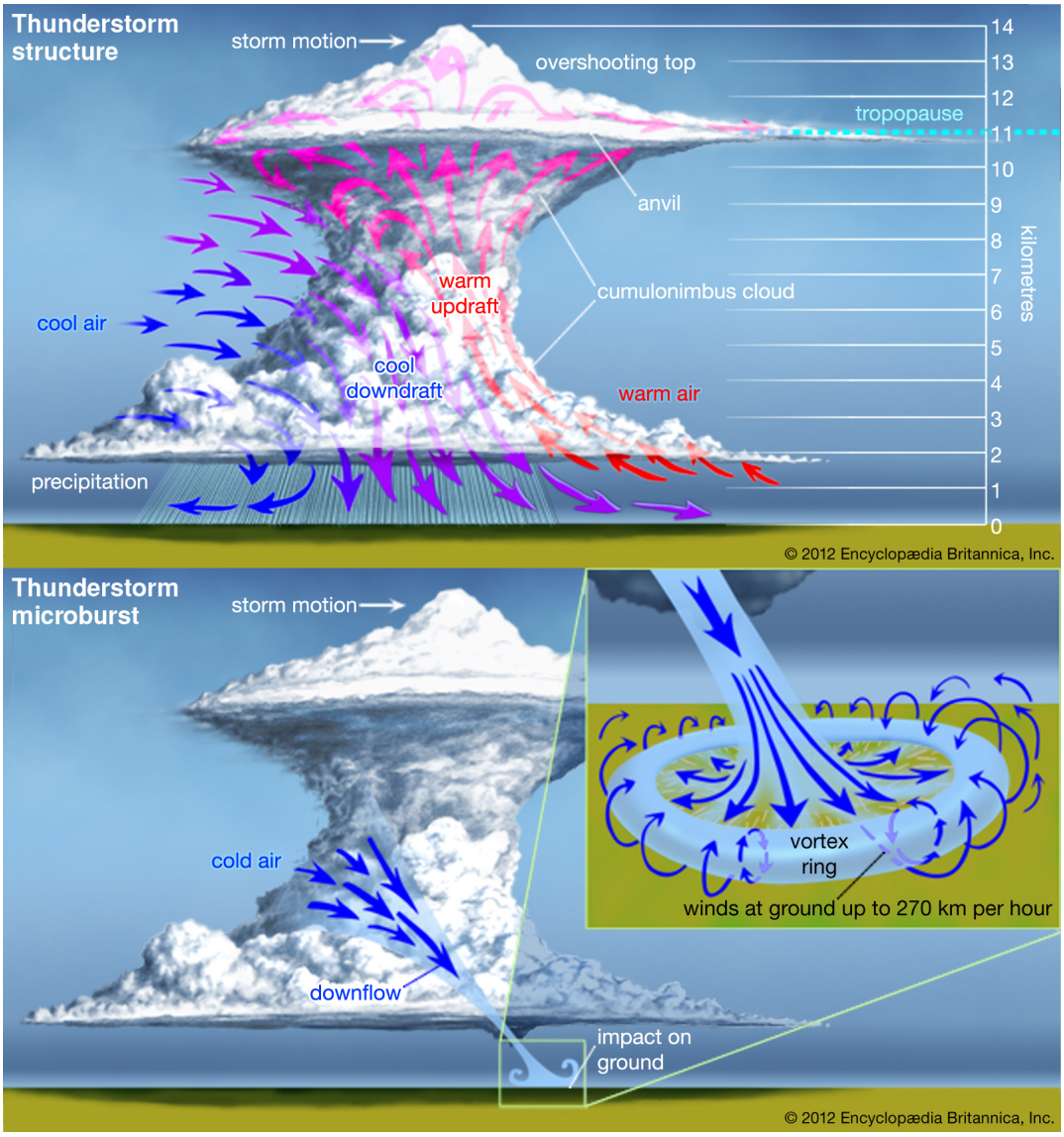


FIGURE 1.1: Schematic of a thunderstorm structure (top) and a thunderstorm microburst (bottom) reproduced from Britannica (2012), available at `https://www.britannica.com/science/microburst`.

forming a vortex ring that contains high wind speeds and shear.

The consequences of the extreme wind events created by downdraughts can be devastating. The initial field campaigns into downbursts (Northern Illinois Meteorological Research on Downbursts (NIMROD) 1978 and the Joint Airport Weather Studies (JAWS) Project 1982) were triggered in response to a series of fatal aviation disasters in the mid-West US (Fujita, 1985; Fujita, 1986). More recently, concerns have been raised over the unusual loading from the high wind shears in downdraughts on engineering structures (Wood et al., 2001; Mason, Letchford, and James, 2005; Chay, Albermani, and Wilson, 2006; Sengupta and Sarkar, 2008) such as high-rise buildings (Zhang, Sarkar, and Hu, 2013), oil rigs and wind farms (Huy Nguyen and Manuel, 2013; Zhang, Sarkar, and Hu, 2014; Lu et al., 2019).

From a meteorological perspective, downdraughts are an important part of the convective cycle; transferring momentum and energy to the surface, uplifting and transporting dust, and potentially triggering low-level jets, subsequent convection and the breakdown of nocturnal stable boundary layers (Parker, 2008; Marsham et al., 2011; Marsham et al., 2013; Heinold et al., 2013). Furthermore, global atmospheric numerical models, which do not explicitly resolve convection, require downdraughts to be parameterized. Typical parametrizations of downdraughts use an inverted entraining plume model where the magnitude of the downdraught mass flux has to be determined (Gregory, 1997). These parametrizations usually do not account for i) differences in downdraught radius and therefore may under-represent the intensity of downbursts or ii) complex interactions with stable boundary layers, which could lead to misrepresentations of wave-turbulence interactions, surface winds, dust uplift and the triggering of convection (Sun et al., 2015).

Downbursts have several stages of development. Firstly, evaporation or precipitation in convective clouds induce downward momentum and negative buoyancy, forming a downdraught. As the downdraught descends, shear instabilities can form a vortex ring at the leading edge (Morton, Taylor, and Turner, 1956). Upon impact with the surface, this vortex ring 'billows' up and propagates out radially, forming

FIGURE 1.2: Stills from a wet microburst occurring January 2015 around 80km North-East of Roma, Texas, USA. Credit: Peter Thompson. Available at: `https://higginsstormchasing.com/tag/microburst/`

the head of the gust front (Fujita, 1985) . Single intense downdraughts may form individual microbursts or a series of downdraughts might sustain the outflow for great distances (Hjelmfelt, 1988). Figure 1.2 shows the descent and impact of an isolated wet (precipitation at the surface) microburst in Texas. An example of the head of a microburst gust front is shown in Figure 1.3, where uplifted dust highlights the circulation within the leading vortex ring.

Numerous experimental and numerical studies have attempted to model the various stages of downdraught development. Despite the complex microphysics that both generate and sustain downbursts, most previous studies choose to model the downburst as: i) a velocity driven impinging jet or ii) a buoyancy-driven, plume or thermal. In either case, the microphysics are represented as a momentum or cooling source. Despite being a major simplification of reality, multiple studies have shown how simple idealised models can accurately represent the bulk features actual atmospheric events (Fujita, 1985; Hjelmfelt, 1988; Mason, Letchford, and James, 2005; Chay, Albermani, and Wilson, 2006; Anabor et al., 2011; Rooney, 2015). The advantage of neglecting the microphysics allows the creation of 'simple' theoretical parameterizations to determine downburst behaviour. These 'simple' parameterizations can then ultimately be incorporated into numerical weather prediction models - something that would be difficult and computational expensive if the parameterization scheme relied on a microphysics solver. Additionally, study of a simplified

version of reality allows easier identification of the fundamental parameters or properties that govern the entire dynamical system.

Impinging jet studies compare well with certain aspects of atmospheric observations, typically three stages of simulated downburst are identified: the vertical downdraught, an impact stage with the ground and a horizontal outflow stage. Various useful empirical relations are proposed for downdraught structure such as the vertical profile of the horizontal outflow (Hjelmfelt, 1988; Wood et al., 2001; Mason, Letchford, and James, 2005; Chay, Albermani, and Wilson, 2006; Sengupta and Sarkar, 2008; Anabor et al., 2011; Zhang, Sarkar, and Hu, 2014). However, the motivation of these studies was primarily focused on combating the hazardous windshear associated with downbursts for the civil and aeronautical industry, therefore these studies do not rigorously investigate the fundamental fluid dynamics of an atmospheric downburst. Furthermore, several salient features of the downdraught are not reproduced in steady impinging jet experiments such as the leading vortex ring and the tendency of the horizontal outflow to 'pulse' (Hjelmfelt, 1988; Holmes and Oliver, 2000). Vermeire, Orf, and Savory (2011) compared impinging jet models to buoyancy-driven cooling sources and noted that impinging jet forcing parameters cannot accurately capture the buoyancy-driven features present in actual storms. In reality, downdraughts are both partially momentum and buoyancy-driven.

Instead of using impinging jets, it is possible to simulate the buoyancy effects of downdraughts in the atmosphere by a release of an excess density fluid into neutral surroundings (such as saline solution into a water tank, or release of a cold bubble) (Scorer, 1957; Turner, 1962; Turner, 1969; Turner, 1979; Lundgren, Yao, and Mansour, 1992). The density difference between the two liquids $\Delta\rho$, relative to the ambient density $\rho_0$ is assumed to be equivalent to the temperature differences $\Delta\theta$ in the atmosphere with the ambient temperature $\Delta\theta$:

$$\frac{\Delta\rho}{\rho_0} \approx \frac{\Delta\theta}{\theta_0}. \tag{1.1}$$

FIGURE 1.3: Dust uplifted in a microburst outflow highlights the structure of the gust front head. Picture taken 15th July 1982 as part of the JAWS field campaign. Reproduced from Fujita (1985). For scale, the electricity pylons are approximately 40m high.

A density difference between a given volume or source of fluid and that fluid's environment can generate motion known as buoyancy-driven flow. The gravitational acceleration of the source fluid is either reduced or increased relative to the fluid's environment,

$$g' = g\frac{(\rho_0 - \rho)}{\rho_1} \tag{1.2}$$

where $g'$ is the reduced gravity, $\rho_0$ is the density of the ambient fluid, $\rho$ is the density of the buoyant fluid and $\rho_1$ is a reference density. A volume of fluid $V$ with this reduced gravity has integrated (or total) buoyancy

$$B = g'V. \tag{1.3}$$

Throughout the rest of the these, $B$ referred to simply as buoyancy.

Vertical transport of buoyant fluid in the atmosphere is common, examples include volcano plumes, chimney smoke plumes, hydrothermal vents, and ocean and atmospheric convective thermals. Conceptually, there are two idealised models that capture the extremes of buoyancy release: (i) thermal - an instantaneous release of a parcel of buoyant fluid with time-evolving characteristics, (ii) plume - a steady state

continuous release of buoyancy flux (Morton, Taylor, and Turner, 1956). Equally, the propagation of buoyant fluid over a horizontal surface is well known in many areas of science as the gravity current (Simpson, 1999). Examples include avalanches, pyroclastic flow, mud slides, turbidity currents and haboobs. However, how theory for the vertical motion of buoyant fluid is related to the radial outflow of the resulting gravity current after impingement on a horizontal surface is an ongoing topic of research. Rooney and Linden (2012) and Rooney (2015) use similarity solutions to relate bulk input properties of plumes or thermals with gravity current theory to predict the characteristics of the radial outflow. Determining this relationship between initial conditions and horizontal outflow is the key underpinning theme throughout this study. How can the properties of the resulting gravity current, gust front or gravity wave be related to the initial conditions of some elevated source of negative buoyancy or momentum? In order to answer this principal research question, this study combines theory, laboratory experiments and numerical simulations in order to understand the descent and near-surface evolution of idealised downdraughts.

The structure of the thesis is as follows. Chapter 2 provides the reader with the derivation of the relevant background theory. The classical work from Morton, Taylor, and Turner (1956) for the descent (or as originally intended, ascent) of a thermal is described along with solutions for axisymmetric gravity currents, derived from the shallow water equations following Grundy and Rottman (1985). The similarity solutions from Rooney (2015) that combine the vertical descent of thermal with the radial propagation using conservation of buoyancy is then outlined. The scalings used by Lundgren, Yao, and Mansour (1992) to compare laboratory saline releases to atmospheric downbursts are discussed. Finally, an alternative energy based equation set from Romps and Jeevanjee (2016) is presented.

Chapter 3 presents analysis of data collected from laboratory experiments on the descent and spread of negatively buoyant fluid. Saline releases into fresh water are designed to represent idealised atmospheric downbursts. The focus of the chapter is on the rate of vertical descent and horizontal propagation, and the near-surface evolution of the downburst. The rate of vertical descent and entrainment is compared to

the classical solutions described in Turner (1962). The formation time of the vortex ring (as proposed by Shusser and Gharib (2000)), is identified as an important mechanism for determining the rate of vertical descent. Similarity solutions from Rooney (2015) for the radial propagation of outflow are evaluated against experimental data. Modifications to certain empirical constants (following Hallworth et al. (1996)) are shown to improve the estimation of radial propagation. Modified scalings developed by Lundgren, Yao, and Mansour (1992) are used to non-dimensionalise the experimental results and compare with the numerical work of Rooney (2015). In addition, the properties of the resulting gust front are analysed. The vertical profile of the horizontal velocity is compared with an empirical profile developed by previous experimental and numerical studies (Wood et al., 2001; Sengupta and Sarkar, 2008), and is found to fit well. A simple relation to determine the maximum horizontal velocity of experimental outflow is developed, depending only on the radial propagation and initial properties of saline release.

Chapter 4 presents the methodology used to set-up Large Eddy Simulations (LES), designed to investigate the descent and near-surface evolution of idealised downdraughts in the new Met Office and NERC Collaboration (MONC) model. The downdraught is represented by an instantaneous release of a cold bubble, which is allowed to fall freely, impact the surface and spread radially. MONC has not previously been extensively tested for this idealised experimental set-up, and therefore it is not clear what resolution and settings can be used. Chapter 4 performs a sensitivity study in order to determine an appropriate model set-up for further investigation into the descent and near-surface evolution of atmospheric downdraughts. This set-up is then used for Chapters 5 and 6.

Chapter 5 compares the results of MONC cold bubble simulations with the adapted similarity solutions from Rooney (2015), and experimental data from the laboratory experiments in Chapter 3. The modifications to the expression for radial spread from Rooney (2015), proposed in Chapter 5, are in good agreement with the numerical simulations. The similarity solutions are then extended to include expressions for the kinetic energy and potential energy, which are supported by the numerics.

Extension of the theory from Rooney (2015) to include the energetics, allows for comparison with an alternative energy balanced equation for a collapsing cylinder proposed by Romps and Jeevanjee (2016). Several modifications are made to Romps and Jeevanjee (2016) to make their theory applicable for an impacting bubble. Both theories estimate the radial propagation well, although the buoyancy based expressions from Rooney (2015) achieve a slightly better correlation to the numerical bubble runs.

Chapter 6 examines descent and near-surface evolution of atmospheric downdraughts impacting a stable boundary layer (SBL). The SBL was created by imposing a constant potential temperature gradient from the surface to a height of 1000 m throughout the modelled domain. These experiments were novel, with little previous work available on this subject, therefore the initial part of the chapter provides a visualisation of the flow to understand how cold bubbles interact with SBLs. In addition, several quantitative methods are then applied. Analysis of the vorticity provided estimation of the vertical descent and horizontal spread of the bubble fluid. In the vertical, horizontal vorticity reached depths in the SBL proportional to the initial buoyancy of bubble. In the radial, the horizontal vorticity of bubbles spread at two different rates when scaled by buoyancy. Comparison with analogous laboratory experiments from Maxworthy et al. (2002), showed that this study's numerical runs emulated the two behaviours of i) surface current driven and ii) wave-dominated regimes observed in Manasseh, Ching, and Fernando (1998) and Maxworthy et al. (2002), depending on the relative density difference between the initial bubble (or lock gate release) and the SBL. Using wave speeds derived from Hovmöller plots of horizontal velocity, a qualitative assessment of the resulting wave dynamics is made and compared to the relevant internal gravity wave theory. Examination of the volume flux of different bins of the potential temperature across the whole domain provided insight into magnitudes and time scales of SBL mixing. It was found that stronger downbursts can significantly alter the vertical structure of the SBL, weakening the vertical potential temperature gradient, for sustained time periods.

Chapter 7 summarises and concludes the entire thesis and discusses future work,

and implications for atmospheric science and the wind industry.

# Chapter 2

# Buoyancy Driven Flows: Theoretical Background

This chapter reproduces the background theory that is integral to the rest of the thesis. Discussion of the merits, weaknesses, applicability, and validation is saved for the subsequent analysis chapters. However, hopefully this chapter proves useful for the reader to reacquaint themselves with the derivation and fundamental assumptions that go into the theoretical analysis of downdraught descent and radial spread. The classical similarity solutions for buoyant plume and thermal motion from Morton, Taylor, and Turner (1956) are provided, followed by the expressions for a propagating axisymmetric gravity current based on the shallow water approximations Grundy and Rottman (1985). These two separate theories are matched by Rooney (2015) through conservation of buoyancy. An alternative energy based equation set for spread of fluid from a collapsing cylinder is also provided (Romps and Jeevanjee, 2016).

## 2.1 Thermals, Plumes and Gravity Currents: Theoretical Background

A density difference between a given volume or source of fluid and that fluid's environment can generate motion known as buoyancy driven flow. The gravitational acceleration of the source fluid is either reduced or increased relative to the fluid's environment,

$$g' = g\frac{\rho_0 - \rho}{\rho_1} \tag{2.1}$$

where $g'$ is the reduced gravity, $\rho_0$ is the density of the ambient fluid, $\rho$ is the density of the buoyant fluid and $\rho_1$ is a reference density. For a point source of buoyant fluid surrounded by an infinite ambient fluid, the behaviour of this buoyant flow is dependent on the density (or equivalent temperature) difference and the length of time that buoyancy is supplied. Since this study is motivated by atmospheric downdraughts, the density (or temperature) of the buoyant fluid is taken as greater than (or less than) the ambient throughout, and consequently the net motion of fluid and relative buoyancy is downward and negative. However, the dynamics are equivalent for an upward, positively buoyant case (such as warm air rising). When variations are small, differences in temperature and density are assumed to be analagous. This assumption is used later in the thesis to compare the density difference in saline experiments in water, to the temperature difference in numerical simulations of atmospheric downdraughts. The second important assumption is the Boussinesq approximation, which assumes density differences are small except in terms which are multiplied by acceleration due to gravity $g$ (Turner, 1979).

It is convenient to first analyse the two extreme cases of buoyancy release: (i) continuous, steady release resulting in a flow known as a 'plume'; and (ii) a transient, instantaneous release resulting in discreet volume of fluid known as a 'thermal'. The behaviour of plumes and thermals is addressed by Morton, Taylor and Turner (1956, henceforth referred to as (MTT)), and has been an area of much research (see Hunt and Bremer (2011) for an overview of the development of classical plume theory). MTT showed that by considering the conservation equations for volume, momentum and density deficiency that the horizontal radius, velocity and reduced gravity of thermals or plumes can be determined exactly for certain idealised cases. MTT's treatment is reproduced in Section 2.1.1 for an incompressible, unstratified plume and thermal case. There are a number of underlying assumptions in this work:

1. The rate of entrainment at the edge of the plume/thermal is proportional to a characteristic velocity at that height.

2. Profiles of mean vertical velocity and mean buoyancy force in the horizontal are of a similar form at all heights.

3. The Boussinesq approximation is valid, i.e. local variations in density are small in comparison to the reference density.

4. A 'top hat profile' is assumed, i.e. the momentum and mass fluxes are represented by a step function that is 0 outside the buoyant fluid and a mean value, gained by integrating across the buoyant fluid at a given height, inside the buoyant fluid.

5. The plume or thermal is modelled as axisymmetric in the vertical coordinate.

### 2.1.1 Buoyant Plumes

Plumes are present in diverse settings over a wide range of scales. Plumes are found across the natural environment; in erupting volcanoes, atmospheric convection, subsea geysers and in man-made; chimneys, smoke stacks, and jets and fountains (Morton, Taylor, and Turner, 1956; Turner, 1969; Drysdale, 2011; Hunt and Bremer, 2011). In all of these settings, plumes form due to a density (or temperature) difference between a source and an ambient fluid and the buoyancy force leads to the bulk vertical movement of fluid. Much of our understanding of classical plume theory is based on Morton, Taylor, and Turner (1956) who build on work from Schmidt (1941), Batchelor (1954), and Taylor (1946) use conservation equations for volume, momentum and density deficiency to describe a plume's width, mean velocity and density deficiency.

Fluid is released with steady buoyancy flux $F$ from a point source into an ambient incompressible fluid of uniform density. For a cylindrical polar co-ordinate system $(z, r)$, with the $z$-axis in the vertical and the source at the origin, $w = w(z, r)$ is the vertical velocity, $\rho = \rho(z, r)$ and $\rho_0 = \rho_0(z)$ are the fluid densities inside and outside of the plume respectively and $b = b(z)$ is the horizontal radius of the plume. Following MTT's analysis, the conservation equations for volume, momentum and

density deficiency are:

$$\frac{\mathrm{d}}{\mathrm{d}z}(\pi b^2 w) = 2\pi b\alpha w, \qquad \text{(volume)} \tag{2.2}$$

$$\frac{\mathrm{d}}{\mathrm{d}z}(\pi b^2 w^2 \rho) = \pi b^2 g(\rho_0 - \rho), \qquad \text{(momentum)} \tag{2.3}$$

$$\frac{\mathrm{d}}{\mathrm{d}z}(\pi b^2 w(\rho_1 - \rho)) = 2\pi b\alpha w(\rho_0 - \rho), \qquad \text{(density)} \tag{2.4}$$

where $\alpha$ is the rate of entrainment (determined experimentally). Equation (2.2) can be substituted into (2.4), and assuming the density variations are small with respect to the reference density $\rho_1$, the density $\rho$ in (2.3) can be taken as $\rho_1$. This rearrangement gives:

$$\frac{\mathrm{d}}{\mathrm{d}z}(b^2 w) = 2b\alpha w, \qquad \text{(volume)} \tag{2.5a}$$

$$\frac{\mathrm{d}}{\mathrm{d}z}(b^2 w^2) = b^2 g\frac{\rho_0 - \rho}{\rho_1}, \qquad \text{(momentum)} \tag{2.5b}$$

$$\frac{\mathrm{d}}{\mathrm{d}z}\left(b^2 w g\frac{\rho_1 - \rho}{\rho_1}\right) = b^2 w\frac{g}{\rho_1}\frac{\mathrm{d}\rho_0}{\mathrm{d}z}. \qquad \text{(density deficiency)} \tag{2.5c}$$

For the case of an ambient fluid of uniform density, $\rho_0 = \rho_1$. Taking boundary conditions as zero radius and momentum flux at the source, and assuming a constant rate of buoyancy supply allows (2.5c) to be integrated. $\frac{\mathrm{d}\rho_0}{\mathrm{d}z} = 0$, therefore

$$b^2 w g\frac{\rho_1 - \rho}{\rho_1} = F, \tag{2.6}$$

where $F$ is the constant buoyancy flux. By rearrangement and eliminating the density difference from (2.5b), the exact solutions for plume radius, vertical velocity and reduced gravity can be found as:

$$b = \frac{6\alpha}{5}z \tag{2.7a}$$

$$w = \frac{5}{6\alpha\pi^{1/3}}\left(\frac{9}{10}\alpha F\right)^{1/3} z^{-1/3} \tag{2.7b}$$

$$g' = \frac{5F}{6\alpha\pi^{2/3}}\left(\frac{9}{10}\alpha F\right)^{-1/3} z^{-5/3} \tag{2.7c}$$

The formulation of the plume conservation equations from Morton, Taylor, and Turner (1956) relies on the concept of entrainment. Entrainment is the physical process where ambient fluid is mixed into the plume. Morton, Taylor, and Turner (1956) suggest a simple parameterization of this complex process where a constant of entrainment $\alpha$ is proportional to the width and vertical distance travelled of the plume. This assumption of entrainment works remarkably well and been observed in many laboratory experiments and numerical simulations for 'pure' plumes - plumes that achieve a local equilibrium with height (Morton, 1959; Morton and Middleton, 1973; Hunt and Kaye, 2005). However, more recent work questions this assumption of constant entrainment for non-pure plumes, those are ones that are either 'lazy' or 'forced'. A plume can be characterised as pure or non-pure depending if the Richardson number $Ri$ varies with height (Morton, 1959; Hunt and Kaye, 2005; Ciriello and Hunt, 2020).

In the classical plume solutions from Morton, Taylor, and Turner (1956), the plume originates from an unrealistic point source at origin. In reality, most plumes originate from an area source. Fortunately, significant subsequent work has been devoted to exploring plumes generated from area sources. Plumes from a non-idealised source tend to the behaviour of an idealised plume in the far field. This tendency allows the introduction of a virtual origin to account for the finite area source. For pure, lazy and certain forced plumes from an area with constant $\alpha$, the virtual origin can be obtained from Hunt and Kaye (2001). For all plumes with an area source with variable $\alpha$, the virtual origin can be obtained form Ciriello and Hunt (2020).

### 2.1.2 Thermals

A thermal is an isolated parcel of fluid whose motions are governed by buoyancy forces. Thermals play an important role within the atmosphere by providing the mechanism for convection Scorer (1957), forming cumulus clouds Blyth, Lasher-Trapp, and Cooper (2005) and forming downdraughts Emanuel (1981). The motion of isolated parcels of buoyant fluid was the focus of early laboratory saline experiments which showed these vertical motions could be simply represented through similarity solutions (Scorer, 1956; Scorer, 1957; Woodward, 1959). In particular

Scorer (1956) demonstrated that the width of a thermal release can be directly related to the distance the thermal has travelled by

$$r = \alpha z \tag{2.8}$$

and

$$w = S(gBr)^{1/2} \tag{2.9}$$

where $S$ is a constant. The work of Scorer (1957) formed the basis for a substantive body literature on thermals; their generation, propagation, associated motions and scalings (Turner, 1979; Lundgren, Yao, and Mansour, 1992; Bryan and Fritsch, 2002; Rooney, 2015). Similarly to a plume, $\alpha$ is a constant of entrainment found to be between 0.2 and 0.4 (Scorer, 1956; Turner, 1979; Lecoanet and Jeevanjee, 2019). The assumption of constant entrainment was recently examined in direct numerical simulation by Lecoanet and Jeevanjee (2019) and was observed to be consistent with the classical theory.

There are two important distinctions between the plume and thermal models. Firstly, contrary to the plume model which was dependent on a steady source of buoyancy, the thermal is initiated by an instantaneous release of given volume of buoyant fluid. This released volume of fluid then develops both with distance from the source and crucially, also with time. Secondly, the thermal is released into a uniform environment and therefore due to conservation of heat, and all of the buoyant fluid is released at time $t = 0$, therefore the total buoyancy $B$ is a consequentially a conserved property since. A similar treatment as shown for the plume (Section 2.1.1, see Turner (1969)) using the equations of conservation for a thermal,

$$\frac{\mathrm{d}}{\mathrm{d}z}(\pi b^2 w) = 2b\alpha w \qquad \text{(volume)} \tag{2.10a}$$

$$\frac{\mathrm{d}}{\mathrm{d}z}(b^2 w^2) = b^2 g \frac{\rho_0 - \rho}{\rho_1} \qquad \text{(momentum)} \tag{2.10b}$$

$$\frac{\mathrm{d}}{\mathrm{d}z}\left(b^2 w g \frac{\rho_1 - \rho}{\rho_1}\right) = b^2 w \frac{g}{\rho_1}\frac{\mathrm{d}\rho_0}{\mathrm{d}z} \qquad \text{(density deficiency)} \tag{2.10c}$$

and dimensional arguments allows the horizontal radius, velocity and reduced gravity to be written as:

$$b = \alpha z \tag{2.11a}$$

$$w = B^{1/2} z^{-1} f_1 \frac{b}{b_0} \tag{2.11b}$$

$$g' = B z^{-3} f_2 \frac{b}{b_0} \tag{2.11c}$$

where $f_1$ and $f_2$ are dimensionless unknown functions.

The effect of aspect ratio on thermal development is a topic of study. Bond and Johari (2005) conducts a series of saline solution experiments to examine the effects of the initial geometry on the development of buoyant thermals in the near field. Bond and Johari (2005) find that flow development can be divided into two phases; an initial acceleration phase and a subsequent phase where the flow decelerates and displays thermal-like characteristics. In the first phase, the leading edge of the flow accelerates and the length and time scales are dependent on the initial geometry. In the second phase, the flow attains a constant circulation and the appropriate length and time scales are the cube root of the initial volume and a buoyant time scale. Kruger et al. (2017) conducts a simialr experiment to Bond and Johari (2005) but with the introduction of a horizontal surface. Kruger et al. (2017) suggests that since the aspect ratio of downdraughts is more similar to that of a thermal, that downdraught descent often deviates from traditions plume models based on Turner (1962). Kruger et al. (2017) performs experiments using finite releases of dense fluid from a cylinder of varying lengths, demonstrating that the descent has two regimes, i) an initial phase and then ii) a self similar thermal. Tarshish, Jeevanjee, and Lecoanet (2018) goes further, using direct numerical simulations of thermals at Reynolds number $\mathrm{Re} = 6300$ to show that for an ellipsoidal thermal, the buoyant acceleration is a simple analytical function of the ellipsoid's aspect ratio. For the case of a uniform spherical thermal, the thermal accelerates at $2B/3$. This constant acceleration is in keeping with Turner (1979) who shows that thermals achieve constant circulations (and therefore acceleration) since the downwards acceleration is matched by the rate of entrainment of thermal.

Thermals are sensitive to their method of generation. For thermals generated using a steady piston, Shusser and Gharib (2000) shows that vortex rings develop over a characteristic time $t_F$ which is related to the scaled time $t_0$ by

$$t_F = 4.73 t_0. \tag{2.12}$$

Bond and Johari (2005) offers an alternative formation with a time scale dependent on the cube root of initial volume and a buoyant time scale to delineate the flow into two phases: i) an initial acceleration and ii) a subsequent deceleration where the flow becomes thermal-like.

Thermals have been studied in both experimental (Scorer, 1956; Scorer, 1957; Woodward, 1959; Lundgren, Yao, and Mansour, 1992) and numerical settings (Bryan and Fritsch, 2002; Rooney, 2015; Lecoanet and Jeevanjee, 2019).

### 2.1.3 Starting Plume

So far the two extremes of buoyancy release have been discussed, (i) a plume case, with constant buoyancy flux in a steady environment or (ii) a thermal case, with an instantaneous release of buoyancy. Conceptually, these are the two most obvious cases to begin to build a theoretical model around and have the advantage of providing relatively simple relations to describe the motion of buoyant fluid. However, these two theories portray a rather binary view of buoyant transport; the plume models neglect any development with time and the thermal theories neglect the possibility that the buoyancy source is sustained over a longer time span. In reality, atmospheric processes encompass a wide range of different flow regimes, which have behaviour similar to both plumes and thermals at different stages of their development. Turner (1962) addressed this problem by introducing the concept of a 'starting plume'. The 'starting plume' model combines plume and thermal theory to describe the different stages of flow development. The initial leading edge or 'cap' is modelled as a developing thermal while the supporting column or 'stem' of fluid is modelled using plume relations.

### 2.1.4 Gravity Currents

Gravity currents are horizontal flows driven by density differences in the presence of a gravitational field. The release of negatively buoyant fluid on to a horizontal surface will create a gravity current driven primarily by gravitational and inertial forces (in all but the smallest scales or if viscosity is large). If this buoyant fluid is released into a lighter fluid of much greater depth than the resulting gravity current, then the motion of the gravity current can be modelled by the shallow-water equations, assuming:

- The two fluids are considered incompressible.
- Any mixing between the two fluids is ignored.
- The current's length is much greater than its thickness.
- The Boussinesq approximation is valid.

Grundy and Rottman (1985) use these assumptions to write the shallow-water equations as

$$\frac{\partial h}{\partial t} + u\frac{\partial h}{\partial r} + h\frac{\partial u}{\partial r} + \frac{uh}{r} = 0, \tag{2.13}$$

$$\frac{\partial u}{\partial t} + u\frac{\partial u}{\partial r} + g'\frac{\partial h}{\partial r} = 0, \tag{2.14}$$

where $h(r,t)$ is the height of the gravity current, $u(r,t)$ is the depth-averaged horizontal fluid speed and $g'$ is the reduced gravity. In the context of atmospheric downdraughts, we will consider the axisymmetric case where $r$ is the radial coordinate and $t$ is time after flow initiation. Grundy and Rottman (1985) then impose the following boundary conditions:

$$\lim_{x\to 0}[2\pi ruh] = \frac{\mathrm{d}}{\mathrm{d}t}(q_\gamma t^\gamma), \tag{2.15}$$

$$u(r_f,t) = \dot{r_f}(t), \tag{2.16}$$

$$\beta^2 g' h(r_f,t) = \{\dot{r_f}(t)\}^2, \tag{2.17}$$

where $r_f(t)$ and $\dot{r_f}(t)$ are the position and speed of the gravity current front, and $\beta$ is an empirically determined constant ($\approx 1$ for small $\Delta\rho/\rho_0$). $q$ is the volumetric flux.

The parameters $\gamma(\gamma \geq 0)$ and $q_\gamma(q_\gamma > 0)$ along with (2.15) give the volume $V$ of the gravity current as a function of time. If (2.13) is integrated with respect to $r$ over $[0, r_f(t)]$ using boundary condition (2.16), Grundy and Rottman (1985) show

$$\frac{\mathrm{d}V}{\mathrm{d}t} \equiv \frac{\mathrm{d}}{\mathrm{d}t}\int_0^{r_f(t)} 2\pi r h(r,t)\mathrm{d}x = \lim_{x\to 0}[2\pi r u h]. \tag{2.18}$$

Therefore, using (2.15) gives

$$V(t) = q_\gamma t^\gamma. \tag{2.19}$$

Dimensional analysis is then used on (2.13)-(2.17) to show that the similarity solution has the form

$$g' h(r,t) = (g' q_\gamma)^{1/2} t^{-2(1-\delta)} H(\zeta), \tag{2.20a}$$

$$u(r,t) = (g' q_\gamma)^{1/4} t^{-(1-\delta)} U(\zeta), \tag{2.20b}$$

$$r_f(t) = (g' q_\gamma)^{1/4} t^\delta \zeta_f, \tag{2.20c}$$

$$\zeta = (g' q_\gamma)^{-1/4} r t^{-\delta}, \tag{2.20d}$$

where $\zeta$ is the similarity variable, $H$ and $U$ are dimensionless functions and

$$\delta = \frac{2+\gamma}{4} \tag{2.21}$$

for an axisymmetric case.

It is clear from (2.20) that the form of these equations is heavily dependent on the value of $\gamma$. The variable $\gamma$ is determined by the nature of the volume source condition. The two most obvious cases are for either (i) a constant volume source $(\gamma = 0)$, e.g. an initial fixed volume of dense fluid is released from a lock gate or (ii) constant flux source $(\gamma = 1)$, e.g. an continuous supply of dense fluid.

It is convenient to write (2.20a) and (2.20b) in terms of $r$ since it is often desirable to know the conditions of the gravity current a given distance from the source. From (2.20c),

$$t \propto \left(\frac{r_f}{(g' q_\gamma)^{1/4}}\right)^{1/\delta} \tag{2.22}$$

Substituting into (2.20a) and (2.20b) gives

$$g'h(r,t) \propto (g'q_\gamma)^{2/(2+\gamma)} r^{2(\gamma-2)/(\gamma+2)}, \tag{2.23a}$$

$$u(r,t) \propto (g'q_\gamma)^{1/(2+\gamma)} r^{(\gamma-2)/(\gamma+2)}. \tag{2.23b}$$

Therefore, for an initial volume source ($\gamma = 0$) of constant buoyancy ($B = q_\gamma t^\gamma$),

$$r \propto B^{1/4} t^{1/2}, \tag{2.24a}$$

$$u \propto B^{1/2} r^{-1}, \tag{2.24b}$$

$$g'h \propto B r^{-2}. \tag{2.24c}$$

For a constant buoyancy flux ($\gamma = 1$), where there is a constant supply of buoyant fluid $F = q_\gamma t^\gamma$

$$r \propto F^{1/4} t^{3/4}, \tag{2.25a}$$

$$u \propto F^{1/3} r^{-1/3}, \tag{2.25b}$$

$$g'h \propto F^{2/3} r^{-2/3}. \tag{2.25c}$$

(2.25a-2.25b) are derived following Grundy and Rottman (1985), which is in turn built on the work of Chen and JC (1977) and Britter (1979) who independently obtain the same scalings by i) balancing the buoyancy force and the inertial force and ii) solving the shallow water equations respectively.

The relationship between $r$ and $t$ for gravity current with constant buoyancy flux has been the subject of several studies. The previous literature tends to consider (2.25a) as

$$r = C_F F^{1/4} t^{3/4} \tag{2.26}$$

where $C_F$ is a dimensionless constant. An exception being Slim and Huppert (2011) who suggest that $C_F$ is in fact a function of the entrainment rate. A summary of the previous studies and their formulations of $C_F$ is provided in Table 2.1.

TABLE 2.1: Previous studies into radial propagation of constant buoyancy flux gravity current.

| Study | $C_F$ | Experimental Set-up |
|---|---|---|
| Britter (1979) | 0.85 | Lock gate releases of saline solutions from $10^o$ shaped tank |
| Chen (1980) | 0.6, 1.0 | Various lock gate releases of saline solutions |
| Linden and Simpson (1994) | 0.7 | Saline release from an elevated point source |
| Kaye and Hunt (2007) | 0.85 | Saline release from an elevated fixed area source |
| Rooney and Linden (2012) | 0.66 | Plumes generated from heat sources impinging upon a ceiling |
| Slim and Huppert (2011) | 1.2 to 0.9 | Numerical model |

## 2.2 Similarity Solutions

The behaviour of plumes and thermals has so far been described in an infinite medium far from any boundaries. The introduction of a horizontal plane perpendicular to the buoyant fluid (in the discussed case; the ground, but equivalently the boundary could be the ceiling in a positively buoyant case) adds another layer of complexity to the problem. Basic continuity dictates that upon contact with the horizontal plane, the buoyant fluid will diverge radially. The two solutions for either plume or thermal and gravity current can be combined to give a similarity solution describing the entire system. The initial conditions of the gravity current are matched with the conditions of the plume or thermal at vertical distance $H$, the height from source to horizontal plane. The underlying assumption is that (i) the buoyancy flux $F$ remains constant for the plume case and (ii) in a uniform environment, the total buoyancy $B$ is conserved for the thermal case.

### 2.2.1 Plume-Gravity Current

A schematic of an impinging steady plume, impacting the ground and then spreading radially as a gravity current is shown in Figure 2.1. For a steady axisymmetric gravity current originating from a constant buoyancy flux $F$, Britter (1979) (see Section 2.1.4) solves the governing shallow-water equations to show that the radial

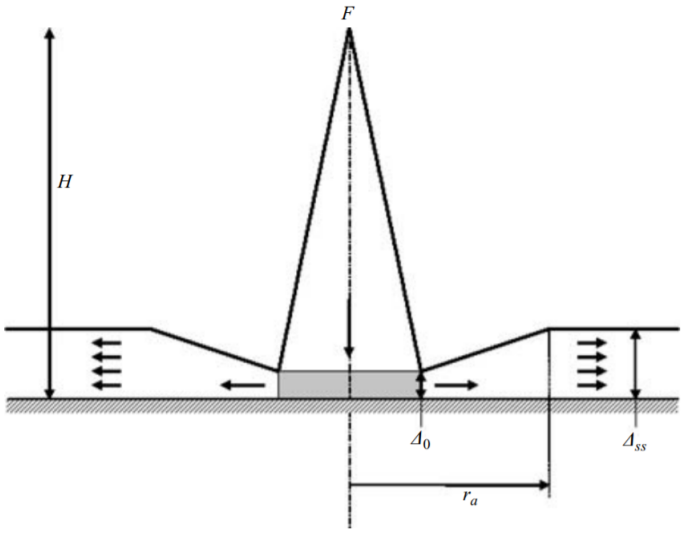


FIGURE 2.1: Schematic of impinging plume reproduced from Kaye and Hunt (2007). Steady negatively buoyant flux $F$, from a point source at height $H$ from the surface, creates a plume. $\Delta_0$ is the depth at the point of plume impingement. $r_a$ is the radius at which the gravity current achieves its steady state depth $\Delta_{ss}$

velocity, steady volume flux and current depth can be written as:

$$u_r = d_1 F^{\frac{1}{3}} r^{-\frac{1}{3}} \tag{2.27a}$$

$$q = 2\pi r u_r h \tag{2.27b}$$

$$h = \frac{q}{2\pi d_1} F r_c^{-\frac{1}{3}} r^{-\frac{2}{3}}, \tag{2.27c}$$

where $u_r$, $q$, $F$ and $h$ are the radial velocity, volume flux, buoyancy flux and height of the gravity current. $d_1$ is a dimensionless constant dependent on the Froude number.

By assuming the fully developed flow (i.e. the plume in the far field) has a constant depth, as observed by Britter (1979), and the horizontal velocity $u$ is independent of depth, Kaye and Hunt (2007) use dimensional analysis to develop scalings for the volume flux, momentum flux and velocity of the current as

$$u_r = C_1 F^{\frac{1}{3}} r^{-\frac{1}{3}} \tag{2.28a}$$

$$Q = C_2 h F^{1/3} r^{2/3} \tag{2.28b}$$

$$M = C_3 h F^{2/3} r^{1/3}, \tag{2.28c}$$

where $C_1, C_2$, and $C_3$ are dimensionless constants estimated at 0.59, 3.7 and 2.2 respectively. Using the expressions for a plume from Morton, Taylor, and Turner (1956) and matching the width, volumetric flux and momentum flux of plume at impingement with source conditions of gravity as

$$r_0 = b_p = 0.15H \tag{2.29a}$$

$$Q_0 = Q_p = 0.16F^{1/3}H^{5/3} \tag{2.29b}$$

$$M_0 = \gamma_* M_p = 0.35\gamma_* F^{2/3}H^{4/3}, \tag{2.29c}$$

where the subscript 0 and $p$ denotes source conditions of gravity current and the plume respectively. $\gamma_*$ is an empirically determined constant.

Dimensionless time and length are introduced as

$$\tau = \frac{t}{H^{4/3}F^{-1/3}} \tag{2.30}$$

and

$$\phi = \frac{r}{H}. \tag{2.31}$$

Which from the integration of (2.28a) yields (2.26), which in turn implies

$$\phi \sim \tau^{3/4}. \tag{2.32}$$

for the far-field pure gravity current. In the adjustment region around plume impact, Kaye and Hunt (2007) propose

$$\tau = 0.69\left(\frac{\gamma_*}{\mathrm{d}h/\mathrm{d}r}\right)^{1/4}\tau^{1/2}. \tag{2.33}$$

Kaye and Hunt (2007) test (2.32) and (2.32) in laboratory experiments, where a header tank supplied a constant buoyancy flux of saline solution at different elevated heights above a table. Kaye and Hunt (2007) (see Figure 10.) found using these scalings collapsed their experimental results on a single lines, validating their scaling arguments. The two lines from (2.32) and (2.32) represent the adjustment-phase and far

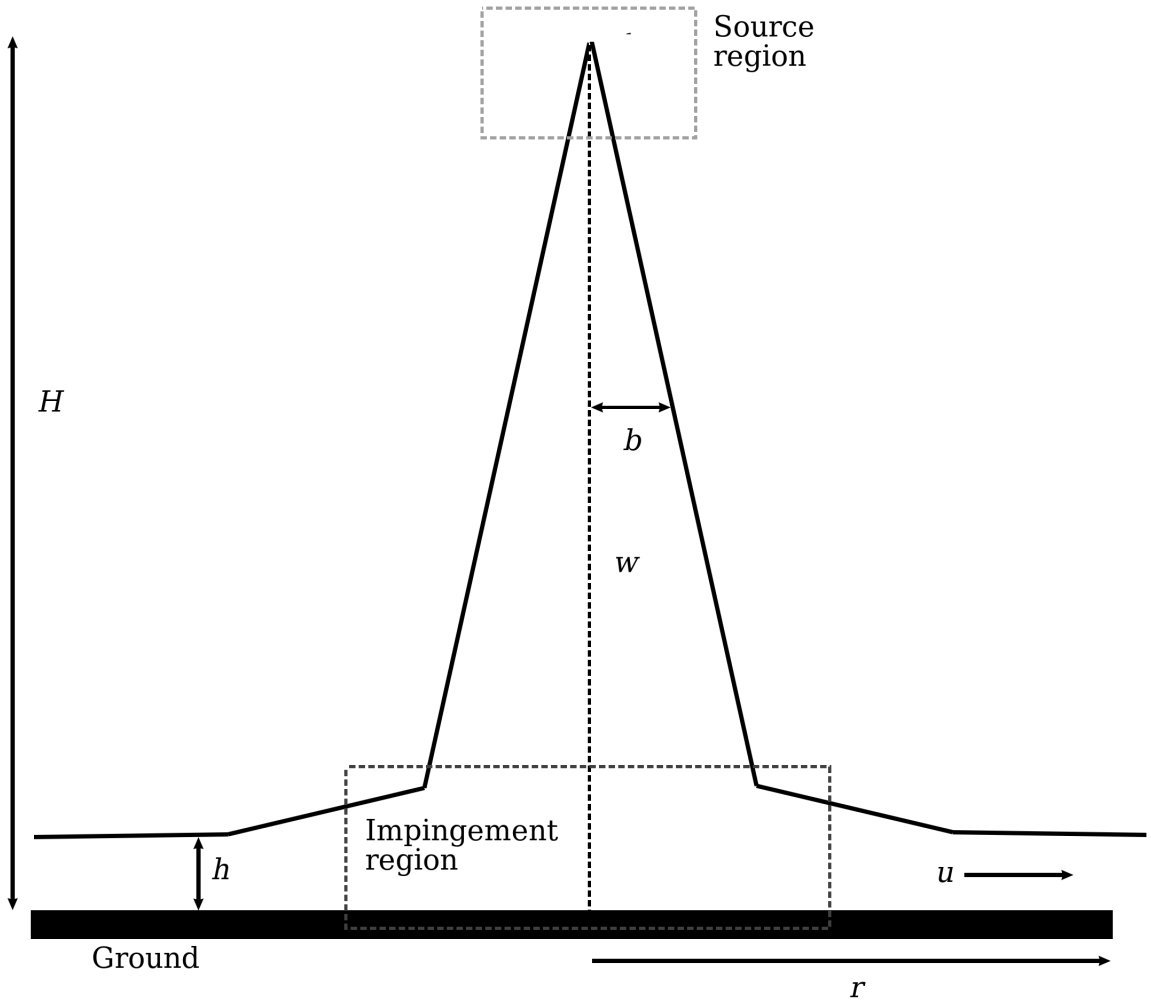


FIGURE 2.2: Schematic of impinging plume. Steady negatively buoyant flux $F$, from a point source at height $H$ from the surface, creates a plume with width $b$ and vertical velocity $w$. The plume impinges on a surface and spreads radially with height $h$ and horizontal velocity $u$.

field well. The transition from adjustment zone to far field appears to occur around $\phi = 0.66$. The laboratory experiments implied $\gamma_* = 0.7$.

A similar analysis is later conducted by Rooney and Linden (2012). Britter (1979) observed that a characteristic of radial gravity currents is that entrainment is confined to the head of the gravity current. Rooney and Linden (2012) use this negligible entrainment in the body of the gravity current to assume $q$ is constant and hence the height of the gravity current depends entirely on the radial distance from source.

Following Rooney and Linden (2012), (2.27) can be matched with (2.7) to give a

similarity solution for plume impingement on a horizontal plane. The buoyancy flux of the plume is assumed to equal the buoyancy flux of the current, $F_p = F_c$ and volume fluxes are matched:

$$q_p = q_c \tag{2.34a}$$

$$= \pi b^2 w \tag{2.34b}$$

$$= \pi^{2/3} \frac{6\alpha}{5} \left(\frac{9\alpha}{10}\right)^{1/3} F^{1/3} H^{5/3}. \tag{2.34c}$$

Re-writing (2.27) with the results of (2.34) gives:

$$u_r = c_1 F^{\frac{1}{3}} r^{-\frac{1}{3}} \tag{2.35a}$$

$$\frac{h}{H} = \frac{3\alpha}{5c_1\pi^{1/3}} \left(\frac{9\alpha}{10}\right)^{1/3} \left(\frac{r}{H}\right)^{2/3} \tag{2.35b}$$

$$g' = \frac{5}{6\alpha\pi^{2/3}} \left(\frac{9\alpha}{10}\right)^{-1/3} F^{2/3} H^{-5/3}. \tag{2.35c}$$

Two slightly contrasting schematics for the transition from vertical to horizontal are presented in Figure 2.1 and 2.2. In Figure 2.1, in the region of impingement, the height of fluid is shown as less than in the far field. Whilst for Figure 2.2, a more continuous transition is shown. This difference may be down to the difference in application. Kaye and Hunt (2007) examine saline releases impinging upon a surface whilst Rooney and Linden (2012) consider smoke impinging on a ceiling. It would be interesting to see if the difference in transition is down to the vertical coordinate or is a sensitivity to the momentum flux supplied to plume.

### 2.2.2 Thermal-Gravity Current

A schematic of a thermal, that falls and then impacts the ground to spread radially as a gravity current is shown in Figure 2.3. Rooney (2015) shows that the thermal relations (2.11) can be re-written as

$$b = \alpha z \tag{2.36a}$$

$$w = Fr_T m^{-1/2} \alpha^{-1} B^{\frac{1}{2}} z^{-1} \tag{2.36b}$$

$$g' = (m^{-1}\alpha^{-3}) B z^{-3} \tag{2.36c}$$

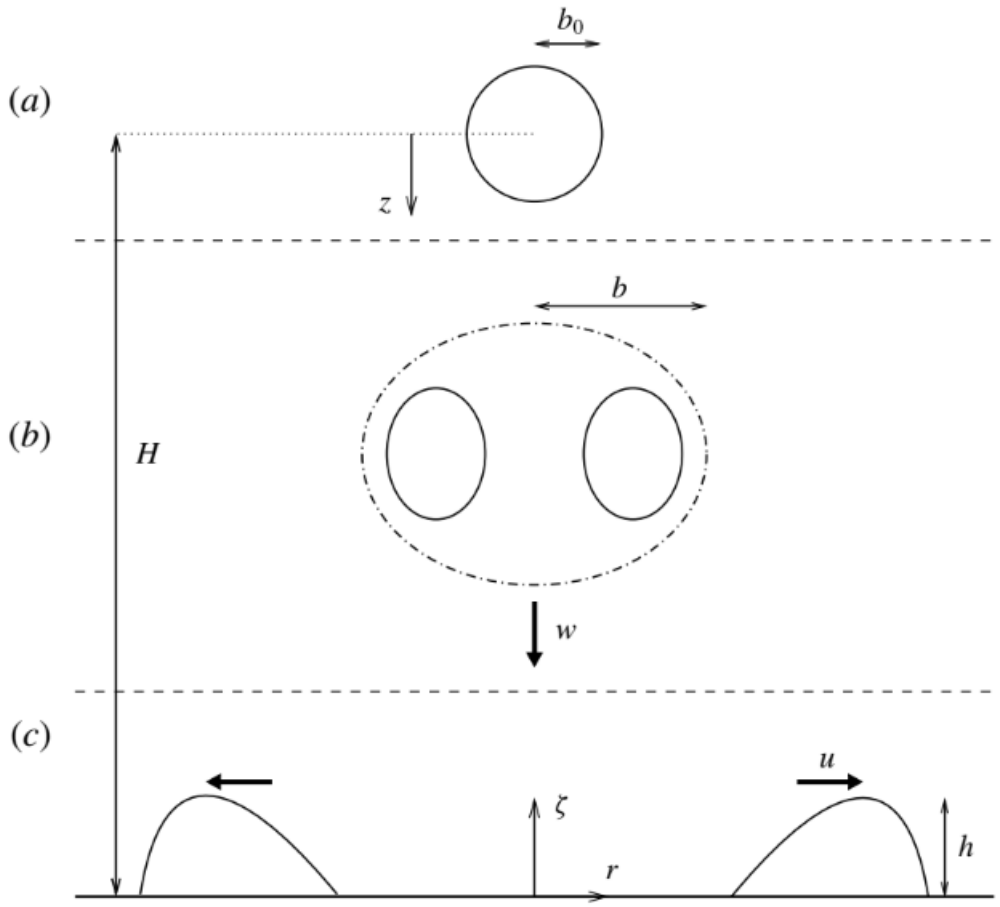


FIGURE 2.3: Schematic of thermal, at three stages of development. (a) the initial sphere of negatively buoyant fluid, with buoyancy $B$, initial width $b_0$, centred at height H. (b) the falling thermal with radius $b$ and vertical velocity $w$. (c) the spreading gravity current with height $h$ and horizontal velocity $u$. Figure taken from Rooney (2015).

by introducing the concept of a 'thermal shape' factor $m = V/b^3$ and the Froude number for the thermal $Fr_T = w/(g'b)^{1/2}$. Note that (2.36) has a non-physical origin at $z = 0$, this is avoided by defining a virtual origin $z_v = \alpha^{-1}b_0$. Hence (2.36a) can be written as

$$b = b_0 + \alpha z. \tag{2.37}$$

Also observe that integration of (2.36b) gives a relation between time and displacement for the falling thermal

$$z + z_v \propto B^{1/4}t^{1/2} \tag{2.38}$$

Rooney (2015) then matches these thermal expressions to initial volume gravity current relations (2.25). These gravity current relations can be re-written using the volume relation

$$\frac{V}{V_i} = f\left(\frac{r}{R_0}\right) \tag{2.39}$$

where $R_0 \sim V_i^{1/3}$ is the radial scale of an equivalent quasi-spherical volume of fluid (see Rooney, 2015 and Hallworth et al., 1996). Combining (2.39) with (2.25) gives

$$u = Fr_T \lambda^{1/2} B^{1/2} r^{-1} \tag{2.40a}$$

$$g' = B\left[V_i f\left(\frac{r}{R_0}\right)\right]^{-1} \tag{2.40b}$$

$$h = \lambda r^{-2} V_i f\left(\frac{r}{R_0}\right) \tag{2.40c}$$

by assuming that the total buoyancy $B$ is conserved. $f$ is an unknown function of the dimensionless radius and $\lambda$ is a constant (suggested as $\pi^{-1}$ by Hallworth et al. (1996) and 1 by Rooney (2015)).

The initial conditions of the gravity current expressions (2.40), specifically the buoyancy and initial volume are taken as those of thermal at impact. The validity of this approach is discussed further in Rooney (2015). It now becomes convenient to determine the radius of thermal at impingement, from (2.37)

$$b_i = \alpha H + b_0 \tag{2.41}$$

Combining with the 'thermal shape' factor $m$, the volume at impingement is then

$$V_i = m b_i^3 = m\alpha^3 H^3 \left(1 + \frac{b_0}{\alpha H}\right)^3 \tag{2.42}$$

Substituting this expression for $V_i$ into (2.40) gives

$$u = Fr_c \lambda^{1/2} B^{1/2} r^{-1} \tag{2.43a}$$

$$g' = m^{-1}\alpha^{-3} B H^{-3} \left(1 + \frac{b_0}{\alpha H}\right)^{-3} f^{-1} \tag{2.43b}$$

$$\frac{h}{H} = \lambda m \alpha^3 \left(1 + \frac{b_0}{\alpha H}\right)^3 \left(\frac{r}{H}\right)^{-2} f. \tag{2.43c}$$

To obtain the radial and temporal propagations, substitute $u = \frac{\mathrm{d}r}{\mathrm{d}t}$ and integrate to give

$$r^2 - R_0^2 = 2Fr_c\lambda^{1/2}B^{1/2}(t - t_i). \tag{2.44}$$

$t_i$ is the time of impact, found by similarly assuming $w = \mathrm{d}z/\mathrm{d}t$ and integrating (2.36b) as

$$t_i = \frac{m^{1/2}\alpha}{2Fr_T}B^{-1/2}H^2\left(1 + \frac{b_0}{\alpha H}\right)^2. \tag{2.45}$$

Rooney (2015) validates these similarity solutions against large-eddy simulations using the Met Office Large Eddy Model (LEM).

Kruger et al. (2017) conducts laboratory saline releases of cylinders with different aspect ratios and tracks their descent and spread. The resulting axisymmetric gravity current varies depending on which regime the descent impacts the ground in. A theoretical model is proposed for this initial phase and compared to the experimental data.

## 2.3 Energy Relations

Downdraughts are not modelled exclusively as buoyancy driven flow. Romps and Jeevanjee (2016) uses potential and kinetic energy balances to provide expressions for the rate of propagation of a cold pool, analogous to the outflow of a downdraught. The cylindrical cold pool has radius $R$, height $H$ and density perturbation $\rho'$. The volume of the cold pool is then

$$V = \pi HR^2 \tag{2.46}$$

As the cold pool collapses, the change of radius is $U = \mathrm{d}R/\mathrm{d}t$ and the radial velocity $u_r$ and vertical velocity are,

$$u_r = \frac{U}{R}r \tag{2.47}$$

and

$$w = -\frac{2U}{R}z. \tag{2.48}$$

The kinetic energy of the cold pool is therefore,

$$\begin{aligned} KE &= \rho \int_0^R dr(2\pi r) \int_0^H dz \frac{1}{2}(u_r^2 + w^2) \\ &= \rho V \left[ \frac{1}{4} + \frac{2}{3} \left( \frac{H}{R} \right)^2 \right]^2 . \end{aligned} \tag{2.49}$$

The gravitational potential energy is

$$PE = \frac{g\rho' VH}{2}. \tag{2.50}$$

Entrainment is defined differently to the buoyancy based relations with

$$\frac{d}{dt}V = \hat{\epsilon} U V \tag{2.51}$$

where $\hat{\epsilon}$ is the fractional entrainment per distance travelled by the cold pool, with units $m^{-1}$. The total energy of the cold pool TE, is the sum of the cold pools PE and KE, with the energy equation

$$\frac{d}{dt}TE = \frac{d}{dt}(KE + PE) = \text{sinks}. \tag{2.52}$$

Romps and Jeevanjee (2016) identifies the sinks of energy as

- Entrainment
- Surface drag
- Form drag, caused by pressure forces between the cold pool and the environment
- Other pressure forces
- Surface enthalpy fluxes

These sinks of energy are combined in (2.52) to provide a governing equation set.

$$\begin{aligned} \frac{d}{dt}U = \left[ \frac{V}{2} + \frac{4\pi H^3}{3} \right]^{-1} \Bigg( &- \left[ \frac{1}{4}\hat{\epsilon} V + 2\pi H^3 (\hat{\epsilon} - 2/R) \right] U^2 + (2/R - \hat{\epsilon}) \frac{\alpha \rho' VH}{2\rho} \\ &- \hat{\epsilon} \left[ \frac{1}{4} V + \frac{2\pi}{3} H^3 \right] U^2 - \frac{2}{5} \pi c_{ds} R^2 U^2 - \pi c_{df} RHU^2 \Bigg) \end{aligned} \tag{2.53}$$

where $c_{ds}$ and $c_{fs}$ are coefficients of surface and form drag. $\alpha$ is an empirical constant. The remaining governing equations are:

$$\frac{d}{dt}R = U \tag{2.54}$$

$$\frac{d}{dt}V = \hat{\epsilon}UV \tag{2.55}$$

$$\frac{d}{dt}\rho' = -\left(\hat{\epsilon} + \frac{2}{3}c_{ds}(1-\rho'_s/\rho')\frac{1}{H}\right)U\rho' \tag{2.56}$$

$$H = V/(\pi R^2). \tag{2.57}$$

These equations whilst thorough, are somewhat complicated and unwieldy. Romps and Jeevanjee (2016) therefore go on to simplify the governing equation set, primarily by i) ignoring higher order $H^3$ terms that become small and ii) instead of solving the complex interactions in the initial collapse of cylinder, the cylinder is prescribed with an initial $U_0$, where

$$\sqrt{\frac{2\alpha g\rho'_0 H_0}{\rho}} \tag{2.58}$$

Assuming that $U = U_0$ at $t = 0$ gives

$$d\log(U) = -\hat{\epsilon}dR \tag{2.59}$$

which when integrated, gives an analytical expression for $U$ as a function of $R$, where

$$U = U_0 \exp\{(-\hat{\epsilon}(R - R_0))\}. \tag{2.60}$$

This simple expression for $U$ allows a simplified theory for a cylindrical cold pool to be described entirely by:

$$R(t) = R_0 + \frac{1}{\hat{\epsilon}}\log(1 + t\hat{\epsilon}U_0) \tag{2.61}$$

$$H(R) = H_0\left(\frac{R_0}{R}\right)^2 \exp\left[\hat{\epsilon}(R - R_0)\right] \tag{2.62}$$

$$\rho'(R) = (\exp\left[-\hat{\epsilon}(R - R_0)\right]) \cdot \left(\rho'_0 + \frac{2}{9}c_{ds}\rho'_s\frac{1}{E_0^2 H_0}(R^3 - R_0^3)\right) \tag{2.63}$$

Romps and Jeevanjee (2016) then verify (2.61) and (2.63) against large eddy simulations.

The work from Romps and Jeevanjee (2016) has a different application to Rooney (2015) but the nature of the problem is fundamentally the same: negatively buoyant fluid is initially elevated and then spreads radially. However, the form of the two equation sets is quite different. Rooney (2015) suggests power law relations for radial propagation, whilst Romps and Jeevanjee (2016) suggests logarithmic relations. This inconsistency between equation sets is examined further in Chapter 5.

# Chapter 3

# Laboratory experiments on the descent and spread of negatively buoyant fluid

## 3.1 Introduction

Numerous experimental studies have attempted to model the various stages of downdraught development. These studies can be predominately divided into two categories, those that model the downburst as: i) an impinging jet or ii) a buoyancy-driven, plume or thermal. Fujita (1985) first made the analogy between laboratory impinging jets and downbursts from observations of downbursts during extensive field campaigns conducted in the Mid-West United States[1], prompting a slew of experimental and numerical studies (Hjelmfelt, 1988; Wood et al., 2001; Mason, Letchford, and James, 2005; Chay, Albermani, and Wilson, 2006; Sengupta and Sarkar, 2008; Anabor et al., 2011; Zhang, Sarkar, and Hu, 2014) that attempted to model the atmospheric downburst using steady jets of air impinging upon a surface. These impinging jet studies compare well with certain aspects of atmospheric observations, typically three stages of simulated downburst are identified: the vertical downdraught, an impact stage and a horizontal outflow stage. The transition between the vertical and horizontal stage occurs over 2-3 jet radii. Various useful empirical

[1]Northern Illinois Meteorological Research on Downbursts (NIMROD) 1978 and the Joint Airport Weather Studies (JAWS) Project 1982

relations are proposed for phenomenon such as the vertical structure of the horizontal outflow,

$$\frac{u}{u_m} = C_4 \left(\frac{z}{n_1}\right)_1^n \left[1 - \text{erf}\left(C_5 \frac{z}{b}\right)\right], \tag{3.1}$$

where $u$ is the horizontal velocity, $u_m$ is the maximum horizontal velocity, $h_{u2}$ is the elevation at which $u = u_m/2$. $C_4, C_5$ and $n_1$ are constants found in Wood et al. (2001) and Sengupta and Sarkar (2008) and erf() is an error function.

However, the motivation of these studies was primarily focused on combating the hazardous windshear associated with downbursts for the civil and aeronautical industry, therefore these studies do not rigorously investigate the fundamental fluid dynamics of an atmospheric downburst. Furthermore, several salient features of the downdraught are not reproduced in steady impinging jet experiments such as the leading vortex ring and the tendency of the horizontal outflow to 'pulse' (Hjelmfelt, 1988; Holmes and Oliver, 2000). Vermeire, Orf, and Savory (2011) compared impinging jet models to buoyancy-driven cooling sources and noted that impinging jet forcing parameters cannot accurately capture the buoyancy-driven features present in actual storms. In reality, downdraughts are both partially momentum and buoyancy-driven. However, there has been no previous study which considers both elements of downdraught development. This study utilises a hybrid source which simulates a downburst generated from both momentum and negative buoyancy.

Vertical transport of buoyant fluid in the atmosphere is well studied. Conceptually, there are two idealised models that capture the extremes of buoyancy release: (i) thermal - an instantaneous release of a parcel of buoyant fluid with time-evolving characteristics, (ii) plume - a steady state continuous release of buoyancy flux (Morton, Taylor, and Turner, 1956). Equally, the propagation of buoyant fluid over a horizontal surface is well known in many areas of science as the gravity current. However, only recently has theory for the vertical motion of buoyant fluid been related to the radial outflow of the resulting gravity current after impingement on a

horizontal surface. Rooney and Linden (2012) and Rooney (2015) use similarity solutions to relate bulk input properties of plumes or thermals with gravity current theory to predict the characteristics of the radial outflow.This study tests the validity of these similarity solutions through experimentally simulated atmospheric downbursts. The focus is on the propagation speed and near-surface evolution of the downburst; arguably the most interesting meteorological parameters because of their potential role on subsequent convection and uptake of aerosols. Rooney (2015) defines a spherical parcel of air in to have initial buoyancy.

Simulating an atmospheric downburst experimentally is not a trivial undertaking, reconciling the scaling between a phenomenon in the range of several kilometres with a laboratory experiment, that by necessity is limited to a couple of metres, presents an interesting problem. Many of the previous engineering studies have conducted experiments in air, however there are significant limitations with this approach when attempting to create a buoyancy-driven flow. The scaling between experiments in air and the atmosphere create insurmountable practical difficulties in the laboratory; the buoyancy differences in the atmosphere cannot be reproduced with the length scales in the laboratory. Instead of experiments in air, it is possible to simulate the buoyancy effects in the atmosphere by a release of an excess density liquid into neutral surroundings (such as saline solution into a water tank) (Scorer, 1957; Turner, 1962; Turner, 1969; Turner, 1979; Lundgren, Yao, and Mansour, 1992). The density difference between the two liquids $\Delta\rho$, relative to the ambient density $\rho_0$ is assumed to be equivalent to the temperature differences $\Delta\theta$ in the atmosphere with the ambient temperature $\Delta\theta$.

$$\frac{\Delta\rho}{\rho_0} \approx \frac{\Delta\theta}{\theta_0}$$

These experiments in water have the combined advantage of a more controllable environment that is easier to measure but more fundamentally, a rigorous scaling can be adopted to more realistically investigate downbursts in an experimental setting.

Much of the previous experimental work into buoyancy effects in thermals, plumes

and by proxy, downbursts, was conducted in the 20th century where limitations in numerical modelling meant that laboratory experiments were one of the few ways to prove idealised atmospheric theory Hunt and Bremer (2011). The advent of sophisticated and readily available CFD meant that research methods changed and density driven tank experiments into downbursts have been neglected. This study aims to utilise the advances in experimental equipment to examine aspects of idealised downbursts hitherto difficult or impossible to measure. Specifically, highspeed cameras capable of recording 30 - 150 frames per second to study the evolution and propagation of experiment. The digitised recordings can then be automatically analysed by tracking scripts. Furthermore, acoustic doppler velocity instrumentation allows an insight into the structure and circulation of the resulting radial gravity currents after impact.

By conducting different density saline experiments in the Sorby Environmental Laboratory at the University of Leeds, this study attempts to utilise developments in laboratory techniques and measurement equipment to either examine new areas of downburst behaviour or provide a new perspective on previous studies. This chapter should be of interest to i) atmospheric scientists wanting to understand how fundamental properties of negatively buoyant fluid result can be related to the subsequent spread and descent and ii) civil or aerospace engineers who want to understand the structure and maxima of the hazardous wind shear that downburst events can generate.

Specifically, this chapter has three aims:

1. Analyse the results of laboratory saline releases of momentum driven negatively buoyant fluid, designed to simulate atmospheric downbursts.

2. By studying the vertical and horizontal rates of downburst propagation, establish if it is possible to determine the properties of the resulting horizontal outflow from the properties of an experimental set-up at the source. This study will test the similarity solution proposed by Rooney (2015) which combines the

descent of an negatively buoyant thermal with the horizontal spread of a gravity current.

3. The properties of the resulting gust front will be examined to determine the structure of the gravity current, the vertical profile of the horizontal wind and the associated wind maxima.

### 3.1.1 Origin of Experimental Data

The experiments detailed in this chapter were conducted in the Sorby Environmental Fluids Laboratory at the University of Leeds over the Spring of 2014, by the student prior to the PhD, as part of a combined MSc project. In many ways this chapter has been a direct continuation of that MSc project. It therefore becomes necessary to delineate between work conducted as part of the MSc and work conducted as part of this chapter. All of the raw experimental data were collected during the MSc. However, a combination of time limitations and focusing on numerical work using the Met Office LEM, meant that the majority of the experimental data were neglected. In fact, Williams (2015) did not analyse any of the experimental data during the MSc and apart from a description of the experimental set-up, Williams (2015) does not contain any mention of the experiments. Kreczak (2015) was able to provide some post-processing and preliminary analysis from some of the velocity measurements and GoPro footage, however again due to the pressures of time this analysis was limited in scope. Where work from Kreczak (2015) has been used it has been appropriately cited, whilst all other handling of experimental data; both post-processing and subsequent analysis and comparison with theory has been conducted as part of the PhD and is described in Section 3.3.

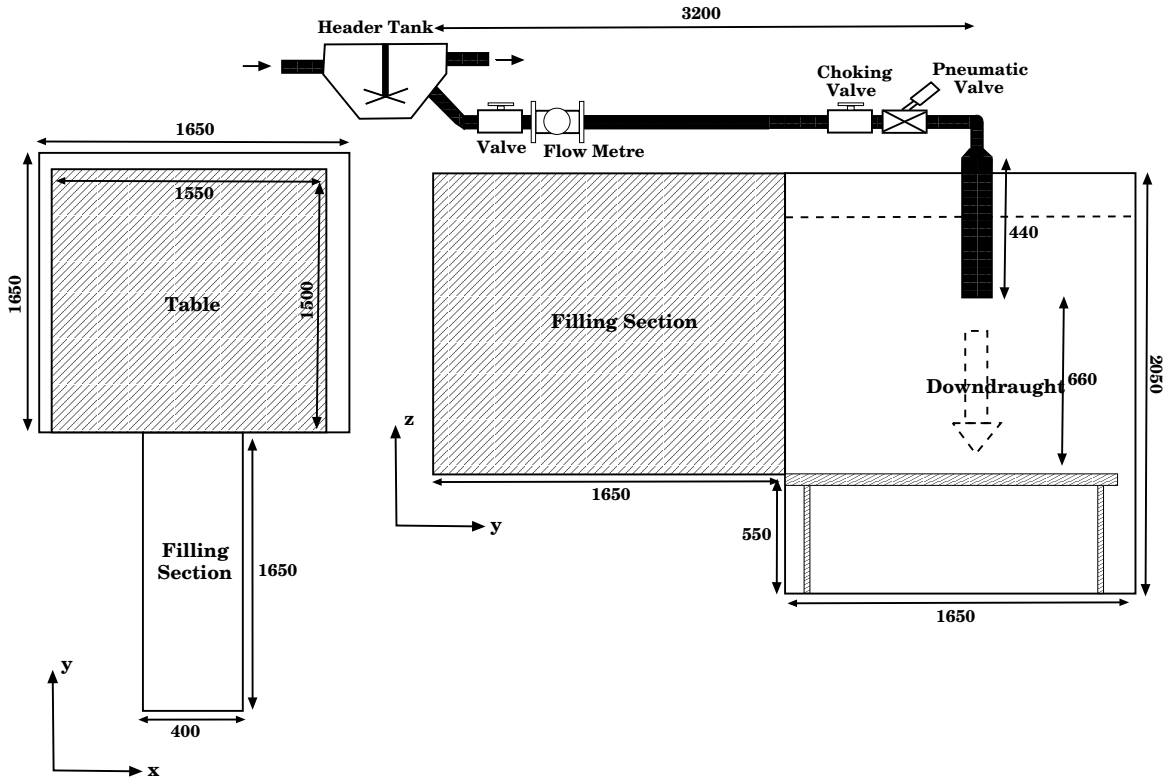


FIGURE 3.1: Schematic of the experimental facility, all dimensions given in mm. Fig. 3.1(a) shows a birds eye view of the tank, Fig. 3.1(b) shows a side profile of the experimental facility.

## 3.2 Experimental Design

### 3.2.1 Laboratory Set-up

Experiments were conducted in a T-shaped tank (T-tank) in the Sorby Environmental Laboratory at the University of Leeds (Fig. 3.1). The T-tank comprises of two distinct sections: (i) a filling section and (ii) a $1.65 \times 1.65 \times 2.05$ m$^3$ rectangular glass-sided test section. In this test section, there is a $1.50 \times 1.55$ m$^2$ table secured 0.55 m above the floor of the tank. 0.66 m above the table a cylindrical pipe with 0.110 m inner diameter was fixed so the circular cross-section of the pipe is perpendicular to the surface of the table. This cylindrical pipe was connected to a header tank via a horizontal pipe attached with a ball valve, flow metre, choking valve and a pneumatic valve.

For a typical experimental run the T-tank would be filled with mains water to a level 0.80 m above the outlet of the pipe (giving a total water level of roughly 0.74 m

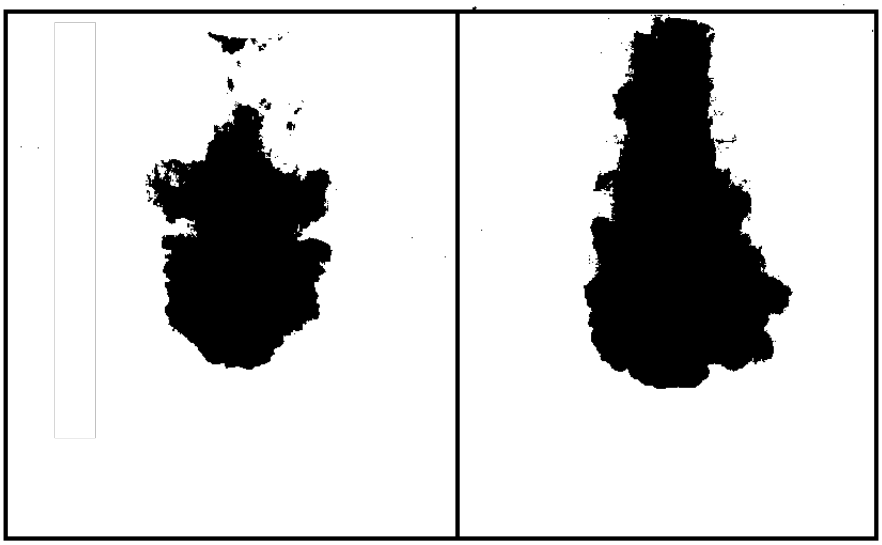

FIGURE 3.2: Two snapshots from a 2% saline experiment taken at approximately $t = 4.2$s after release, buoyant fluid is shown in black. Left shows F2s2p_01. Right shows a F5s2p_01.

above the tank table). This ensured that surface effects on the flow were negligible. The header tank was then filled with saline solution of 1% or 2% excess density. The header tank was continually supplied from a larger mixing tank to ensure a constant head throughout the experiments. The pneumatic valve was then opened for $\sim 30$ secs, and saline released to purge air from the pipe. Purging was repeated until the amount of air bubbles ejected from the pipe was insignificant. The header tank valve was then closed, the tank drained and refilled with fresh water. The header tank valve could then be opened, the button operated pneumatic valve was set to the desired opening time (usually 2 or 5 seconds). The pneumatic valve was a unique feature of the experimental design, allowing accurate releases of different volumes of fluid.

The released volume of fluid passed through a choking valve and two turbulence damping meshes, designed to prevent momentum injection and to ensure a buoyancy-driven flow. High speed cameras, Acoustic Doppler Velocity Profilers (ADVPs) and Ultra Sonic Velocity Profilers (UDVPs) were used to measure the flow velocities at different points. Density was calculated from siphoning at different locations along the base of the table. After each release, the tank was drained to below the level of table and then refilled to ensure similar conditions for each run.

**Dynamic similarity**

The purpose of these laboratory experiments is not to study the motion of saline solution within a water tank for its own sake. These experiments are designed to further understanding of actual atmospheric downbursts. The experiments therefore need to achieve dynamically similarity between the behaviour of saline releases in the laboratory to that of atmospheric downbursts. The simplest criteria is to adopt length scales that are representative of atmospheric events. These experiments were designed following Fujita (1985) and Hjelmfelt (1988) who observed that in the vertical, downbursts have an aspect ratio of between $R : 2H$ and $R : 6H$ where $R$ is the radius of downburst and $H$ is its height of origin above the ground. The experimental set-up has an aspect ration of $R_p : 6H$, where $R_p$ is the radius of outlet pipe and $H$ is the height of pipe outlet above the surface. This selection of aspect ratio is at the upper extreme of those suggested in the literature (the intention was to vary release height but time constraints limited these additional experiments). This higher aspect ratio is means the experiments are more dynamically similar to isolated microbursts that occur in the mid-West United States where air flowing over the Rocky Mountains creates exceptionally stable conditions (as seen in the JAWS field campaign (Fujita, 1985)). The influence of aspect ratio on downdraught descent is further investigated in Bond and Johari (2005), Kruger et al. (2017), and Tarshish, Jeevanjee, and Lecoanet (2018).

The Reynolds number Re is a ratio of the inertial and viscous forces in a flow,

$$\mathrm{Re} = \frac{uL}{\nu} \tag{3.2}$$

where $u$ is a velocity, $L$ is a length scale, and $\nu$ is the kinematic viscosity. Ensuring the Reynolds number Re is sufficiently large i.e. where inertial forces dominate the viscous forces and the flow is turbulent, for both experiment and atmospheric event helps determine dynamic similarity. In this case, the length scale can be taken as the diameter of outlet pipe $L = 0.11$ m, the characteristic velocity is 0.2 $\mathrm{ms}^{-}1$(shown later in Figure 3.13 and the kinematic viscosity of water at 20 degrees is $1 \times 10^{-6}$ $\mathrm{m}^2\mathrm{s}^{-1}$, which yields Re=22000. Whilst this value of Re is far less than for

an atmospheric downdraught (typically in the millions, $L = 1000$ m, $u = 30$ ms$^{-1}$, $\nu = 1.5 \times 10^{-6}$ m$^2$s$^{-1}$), it is comfortably in the turbulent flow regime (Re $> 2000$), meeting the criteria of dynamic similarity.

### 3.2.2 Measurement Techniques

Most of the measurements were designed to examine the flow characteristics of the radial propagation both around and after impact with the table, equivalent to the propagating gust front or cold pool from an atmospheric downburst. Two main techniques were used to measure the experimental runs: (i) in situ velocity measurements, Acoustic Doppler Velocity Profilers (ADVPs) and Ultrasonic Doppler Velocity Profilers (UDVPs) were placed inside the tank to measure three dimensional velocities; (ii) flow visualisation, highspeed cameras outside and above the tank could be used to track the front of the radial propagation. The experimental runs are listed in Table 3.1 and are coded according to the measurement technique (Velocity Measurement - VM or Film - F), the time of release (2s, 3s or 5s) and the relative density (1p or 2p).

#### Highspeed Camera

A highspeed camera recording at 120 frames per second, was placed outside of the T-tank looking in at an $(x, z)$ cross section of the experiment. The camera was used to track the vertical descent of the fluid release. The buoyant fluid was dyed a light purple to stand out from the background. The raw footage was split into individual frames and subsequently converted into greyscale. A background image $I_b$ was taken as the first frame of the footage before any fluid was released, this background image should capture the unperturbed environment. The propagation of buoyant fluid was then tracked by subtracting the background image from each of the individual frames to find the total changes in pixel colour. A threshold condition was applied to each individual pixel,

$$(I - I_b) > \alpha I_b \tag{3.3}$$

TABLE 3.1: Experimental Runs. The experiment names relate to the set-up of that experiment. VM is 'velocity measurement', F is high-speed film, Xs is seconds of experimental releases (2, 3 or 5 s), Yp is percentage saline solution (1% or 2%), _0Z is the repetition number.

| Experiment Number | Release Time (s) | % Relative Density | Measurement Equipment | Measurement Location |
|---|---|---|---|---|
| VM2s1p_01 | 2 | 1 | ADVP, UDVP | 1 |
| VM2s1p_02 | 2 | 1 | ADVP, UDVP | 1 |
| VM2s1p_03 | 2 | 1 | ADVP, UDVP | 2 |
| VM2s1p_04 | 2 | 1 | ADVP, UDVP | 2 |
| VM2s1p_05 | 2 | 1 | ADVP, UDVP | 3 |
| VM2s1p_06 | 2 | 1 | ADVP, UDVP | 3 |
| VM2s1p_07 | 2 | 1 | ADVP, UDVP | 3 |
| VM2s1p_08 | 2 | 1 | ADVP, UDVP | 3 |
| VM2s2p_01 | 2 | 2 | ADVP, UDVP | 1 |
| VM2s2p_02 | 2 | 2 | ADVP, UDVP | 1 |
| VM2s2p_03 | 2 | 2 | ADVP, UDVP | 1 |
| VM2s2p_04 | 2 | 2 | ADVP, UDVP | 2 |
| VM2s2p_05 | 2 | 2 | ADVP, UDVP | 2 |
| VM2s2p_06 | 2 | 2 | ADVP, UDVP | 2 |
| VM2s2p_07 | 2 | 2 | ADVP, UDVP | 2 |
| VM2s2p_08 | 2 | 2 | ADVP, UDVP | 3 |
| VM2s2p_09 | 2 | 2 | ADVP, UDVP | 3 |
| VM2s2p_10 | 2 | 2 | ADVP, UDVP | 3 |
| VM5s1p_01 | 5 | 1 | ADVP, UDVP | 1 |
| VM5s1p_02 | 5 | 1 | ADVP, UDVP | 2 |
| VM5s1p_03 | 5 | 1 | ADVP, UDVP | 3 |
| VM5s2p_01 | 5 | 2 | ADVP, UDVP | 1 |
| VM5s2p_02 | 5 | 2 | ADVP, UDVP | 2 |
| VM5s2p_03 | 5 | 2 | ADVP, UDVP | 3 |
| F2s1p_01 | 2 | 1 | Highspeed | F05 |
| F5s2p_01 | 5 | 2 | Highspeed, GoPro | F06 |
| F2s2p_01 | 2 | 2 | Highspeed, GoPro | F07 |
| F3s2p_01 | 2 | 2 | Highspeed, GoPro | F08 |
| F5s2p_02 | 5 | 2 | GoPro | F09 |
| F5s2p_03 | 5 | 2 | GoPro | F10 |
| F2s2p_03 | 2 | 2 | GoPro | F11 |
| F2s2p_04 | 2 | 2 | GoPro | F12 |

where $I$ is a given image/frame and $\alpha$ is some constant threshold taken as 0.01-0.02. Changes to pixel colour greater than this threshold were attributed to the propagation of fluid and the pixel was set to black, while changes less than this threshold were attributed to flickering in the lighting and the pixel set to white. This pixel threshold then gave black and white images of the fluid propagation where buoyant fluid was black and the rest of the image was white. The centre line of outflow pipe was estimated from the background image and vertical propagation measured along this line. The centre line was divided into a number of 'checkpoints' and the buoyant flow was considered to have reached this checkpoint if every touching pixel (including diagonals) was coloured black.

**GoPro Camera**

A GoPro camera recording at 30 frames per second was mounted above the tank to give a birds eye view of the tank table. The GoPro was used to track the radial outflow of the buoyant fluid after impact with the table. The post processing of footage was similar to the highspeed camera footage except for several additional complications. Firstly, the GoPro has an 'ultra wide' field of view which causes distortion around the edges. In an unprocessed image a pixel width in the centre of the image is equivalent to a much smaller length than a pixel width at the edges of the image. An image transform script developed by Rob Thomas[2] was used to remove the distortion in the image. The second problem was removing the table's grid lines from the image. To help measure the radial propagation of buoyant fluid, a $100 \times 100$ mm$^2$ square grid was drawn onto the surface of the experiment table using black marker. This meant when the image was converted to a black and white image (using the same procedure as for the highspeed camera), both the radial propagation and the grid lines were left on the image, making it difficult to automatically track the front. Two inbuilt Matlab functions were used to remove the grid lines: `imdilate` dilates square structures in the image, the function was applied twice at different levels of intensity; `imerode` removes speckles. While both these techniques removed a small proportion around the edge of the radial propagation, the equivalent loss in accuracy of radial propagation was only of the order of 3-5 mm which was deemed

[2]School of Earth and Environment, University of Leeds

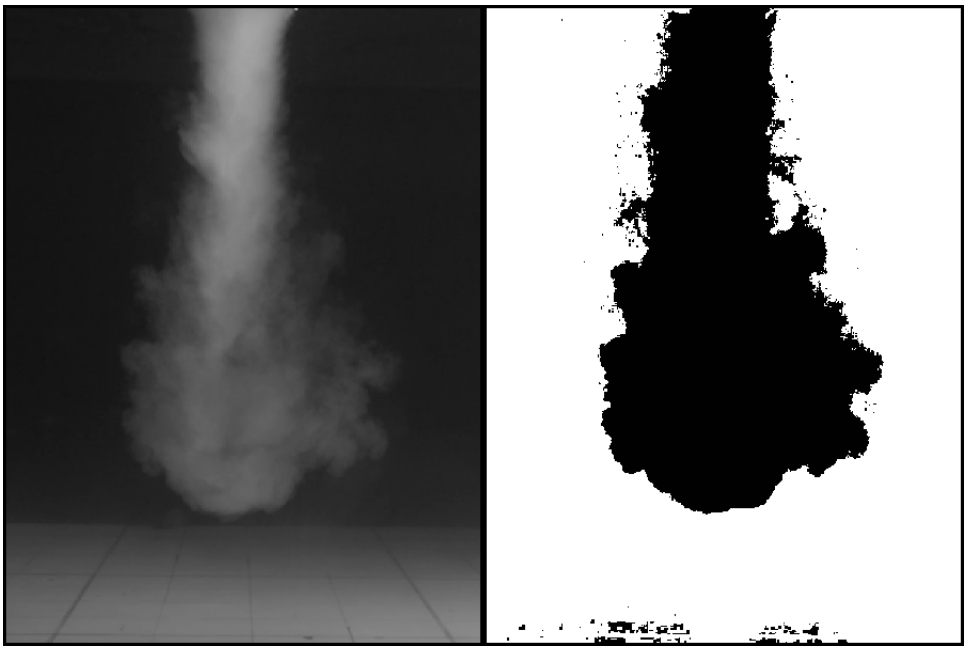

FIGURE 3.3: Snapshots from F5s2p_01. The left image is a raw still from the highspeed camera. The right image is the raw image with a threshold pixel change applied.

acceptable because of the vastly decreased post-processing time required. For certain experimental runs, the resulting radial propagation was sufficiently dilute that the pixel change between the buoyant fluid and colour of the table became very small. In these cases it became impossible to automatically track the front. Instead, the black and white images were manually examined. 15 points around the edge of the outflow were taken and averaged over to provide an estimate of radial propagation. More details of this procedure and the thresholds used are detailed in Kreczak (2015).

### Velocity Measurements

Velocity measurements were taken using either Ultrasonic Doppler Velocity Profilers (UDVPs) or Acoustic Doppler Velocity Profilers (ADVPs). Both measurements techniques are intrusive, requiring the instruments to be physically situated either in or close to the flow. However, since measurements taken either in advance of or above experimental releases, it is unlikely that the presence of the instrumentation had a significant impact on the results. Furthermore, measurements were conducted in line with the corners of the tank to minimise any potential effects of reflection off the tank walls.

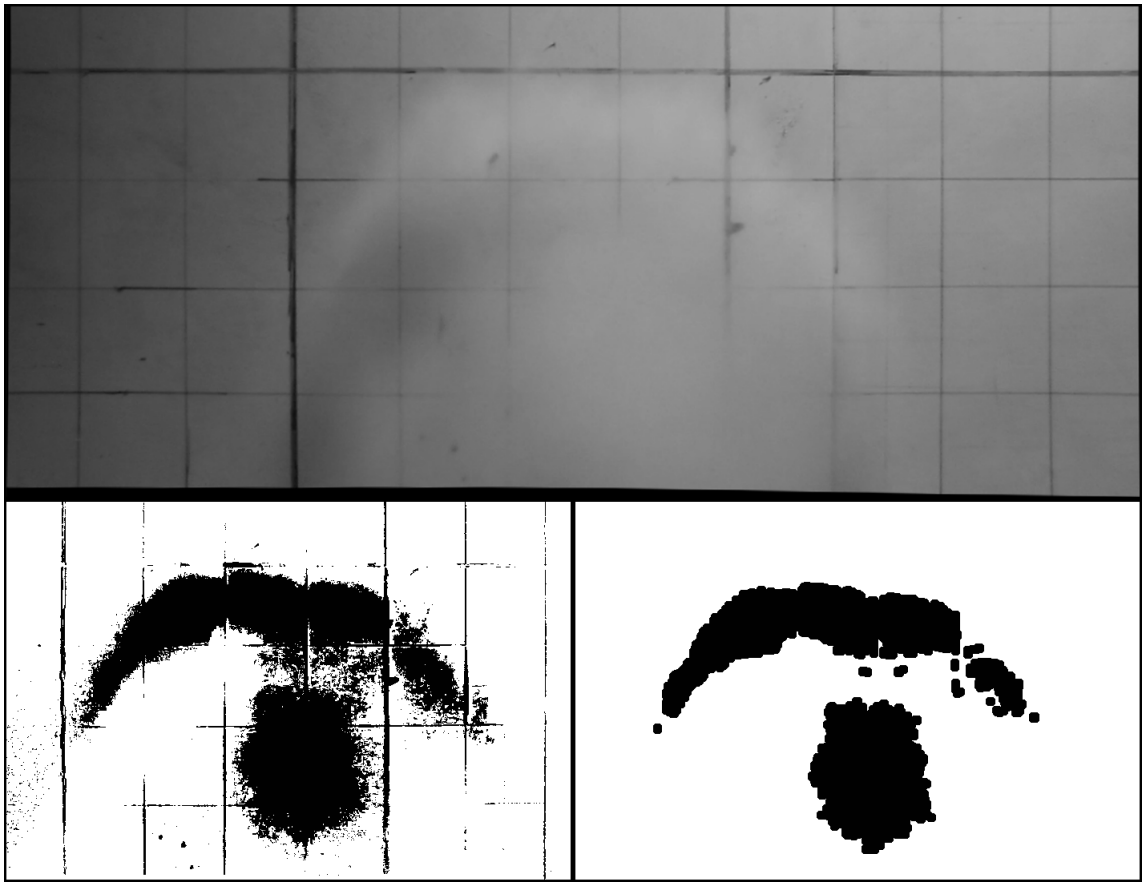

FIGURE 3.4: Snapshots of F5s2p_01 saline release. The top image is a raw still from the GoPro mounted over the tank. The bottom left image is the raw image with a threshold pixel change applied. The bottom right image is after dilating and eroding functions are used to remove the grid lines and speckling, this final image was used to estimate radial propagation.

**UDVP**

Ultrasonic Doppler Velocity Profilers were comprised of a stack of transducers. A single transducer measures the flow velocity by emitting an ultrasound pulse along its axis of orientation. The transducer receives the echo of that ultrasound pulse from reflections from suspended seeding particles within the flow. Velocity $U$ is then calculated from the Doppler shift in the ultrasound frequency $f_D$,

$$U = cf_D/2f_o, \tag{3.4}$$

where $c$ is the ultrasound velocity in the fluid and $f_o$ is the ultrasound frequency.[3] Each transducer can measure the velocity at up to 128 spaced points (or bins) along the axis of orientation. To minimise the noise interference the stack of transducers cannot fire simultaneously, instead they cycle through successively. For example for a stack of 8 transducers, the first transducer would emit an ultrasonic pulse, receive the echo, after a short interval the second transducer would then fire and so on. Typically for a stack of 8-12 transducers a cycle takes 0.5 s. Data are therefore arranged so that for $t_n$, there is instantaneous velocity data at $z_n$ for $z = [z_1, z_2, ..., z_{128}]$ where $t_n$ is the time that transducer $n$ fires and $x$ is spacing of the transducers. Therefore at given $x_n$, there is velocity data for $t_{n0}, (t_{n0} + t_i), (t_{n0} + 2t_i), ....$ where $t_i$ is the time to complete one cycle.

The UDVPs were used to both categorise the outflow conditions and measure the velocities in the radial outflow. A stack of 9 vertically aligned, equally spaced transducers centred below the outlet of the pipe were used to measure the vertical outflow velocities, while an 'L' shaped stack arrangement of 8 horizontally aligned and 5-8 vertically aligned was used to capture both the horizontal and vertical velocities in the radial outflow, see Figure 3.5.

[3] A useful summary on the Principles of UDVPs can be found at http://www.see.leeds.ac.uk/see-research/igs/seddies/best/principles.htm

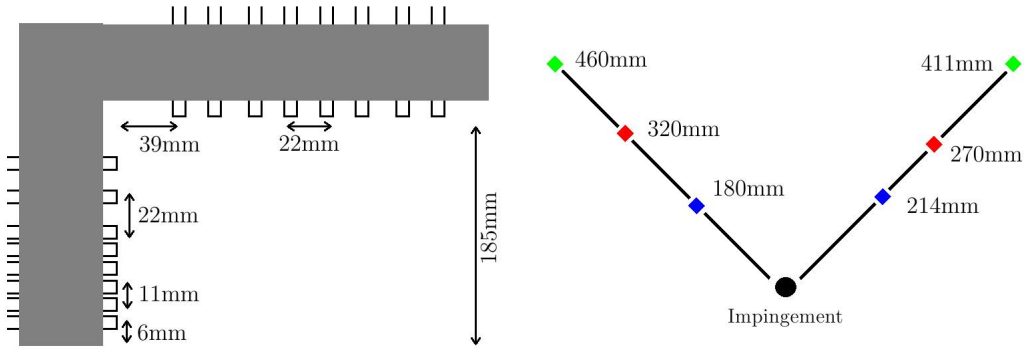


FIGURE 3.5: Layout of the UDVP stack and location of UDVPs and ADVPs. Left: The UDVP 'L' shape arrangement of transducers. Right: The measurement locations of UDVP (left) and ADVP (right), distances from approximate location of impingement. Figure taken with permission from Kreczak (2015).

### ADVP

The Acoustic Doppler Velocity Profiler is an intrusive velocity measurement instrument that can be used to measure instantaneous 3D velocities. The ADVP works on the same principle of Doppler shift from transmitted sound waves reflected off small seeding particles as the UDVP. However, instead of a single transducer, the head of the ADVP has 4 probes that are aligned in $x, y, z_1, z_2$ directions, allowing for instantaneous ($u_x$, $u_y$, $u_z$) velocity measurement. The ADVP can be operated at a higher frequency than the UDVP, allowing for better temporal resolution. However, the ADVP only measures in a single profile of spaced bins, so data is only collected along one line. The high temporal resolution allowed analysis of the structure of the head of the radial outflow. However, since the measurement range of the ADVP is 64 mm and the head of the radial outflow was of the order 100 mm, two ADVPs were used to cover the entire height of the head structure. The lower ADVP measured between 2 - 66 mm from the floor of the tank table, while the higher ADVP measured between 72 - 136 mm. The measurement locations are shown in Figure 3.5.

## 3.2.3 Experimental Uncertainty

All experiments are unfortunately fallible. Uncertainties and errors arise in the methodologies, instrumentation and techniques used - this study was no exception. Williams (2015) and Kreczak (2015) discuss the underlying systematic and random

TABLE 3.2: Properties of velocity measurement instruments

| UDVP | | ADVP | |
|---|---|---|---|
| **Parameter** | **Value** | **Parameter** | **Value** |
| Number of bins | 128 | Number of bins | 20 |
| Velocity range | 0.342 $ms^{-1}$ | Velocity range | 0.70 $ms^{-1}$ |
| Profiles per transducer | 60 | Profiles per transducer | 6000-9000 |
| Cycle time | 0.46-0.75 s | Cycle time | N/A |
| Sampling frequency | 4 Hz | Sampling frequency | 100 Hz |
| Speed of sound | 1480 $ms^{-1}$ | Speed of sound | 1455 $ms^{-1}$ |

errors in the original analysis of results. In this section, the main sources of error and their respective implication on the measurements are discussed.

During the laboratory experiments and analysis, the following sources of error were introduced:

- Concentration of the saline solution. Saline solution was introduced to the header tank by pouring 25kg bags of salt directly from the packet. These packets were not weighed prior to experiment and may have contained impurities or water. The concentration of saline solution was checked from random sample. Kreczak (2015) found the density deficiency varied by +/- 2%. Given experiments compared density deficiency by a factor of 2, it is unlikely this was a major source of error.

- Measurement of valve opening time. The valve opening was operated by a hand pressed switched, whilst the time of opening was read by human eye. This was a significant source of error. Variations in opening times were in the range of (+/- 0.1s), which would result in different volumetric releases and therefore total buoyancy.

- Estimation of point of impingement. Radial propagation is normalised throughout the analysis by radius of impingement. This radius was identified from camera stills of GoPro footage. The GoPro was not directly mounted above the pipe outlet so therefore gives a skewed perspective which in turn may have introduced a systematic error in the estimation of radial propagation.

- Post-processing of camera footage. Both the highspeed camera and GoPro footage was analysed by post-processing scripts. These scripts included alogrithms

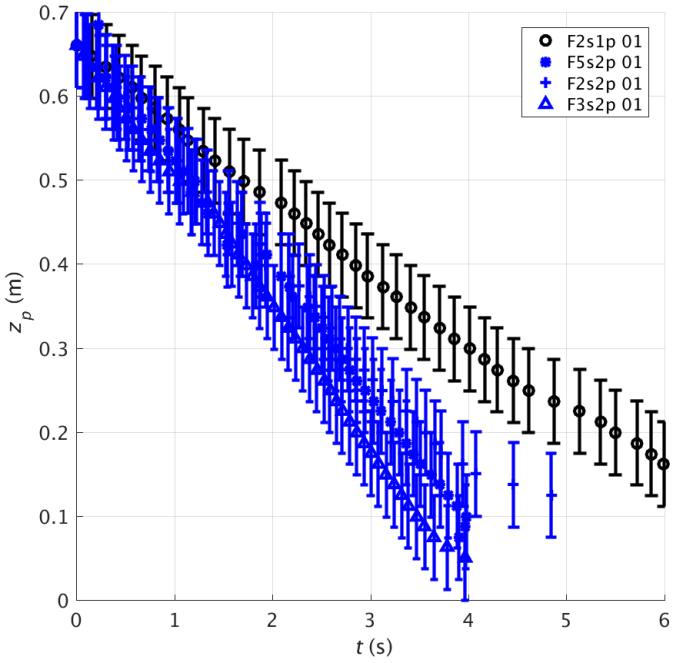


FIGURE 3.6: Vertical propagation minus estimated radius of impingement plotted against time. Errors bars show +/- 0.5 cm.

to flatten the image and remove the 'fish eye' effect of the lens. Changes in pixels of camera stills relative to a background image were then used to estimate vertical and radial propagation. The choice of threshold values in these post-processing scripts introduced a systematic error, estimated at +/- 0.5 cm.

Figures 3.6 and 3.7 provide an indication of how errors in the measurement and post-processing could influence the results.

## 3.3 Results

### 3.3.1 Non-Dimensional Numbers

In an effort to both compare this study's experimental results to previous experimental and numerical studies and examine the results in an atmospheric context, it becomes desirable to non-dimensionalise the results. Previous studies are divided in their approach to non-dimensionalisation, the majority of the engineering literature uses either radius of outlet (either experimental outlet pipe, or velocity outlet in numerical studies) or half the height of maximum velocity as the length scale. The velocity scale is then either the outlet velocity or the horizontal velocity at half

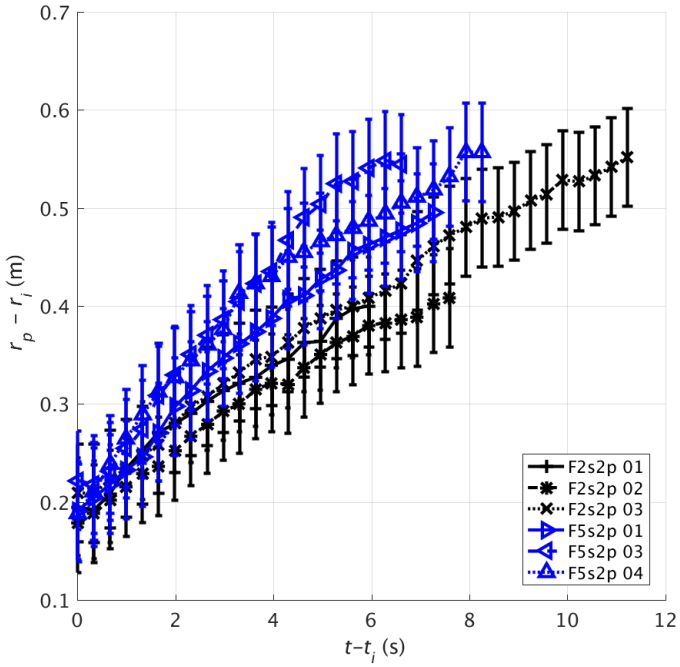


FIGURE 3.7: Radial propagation minus estimated radius of impingement plotted against time. Errors bars show +/- 0.5 cm.

the height of maximum velocity (Hjelmfelt, 1988; Wood et al., 2001; Mason, Letchford, and James, 2005; Sengupta and Sarkar, 2008; Anabor et al., 2011). Whilst these are practical and easily measurable scales, it would be more desirable to develop a non-dimensional system based on the properties of the downdraught phenomenon rather than the specifics of the experimental or numerical set-up.

Lundgren, Yao, and Mansour (1992) introduce a simple scaling based on the equivalent spherical radius $R_0$ of downburst parcel or fluid released, and a characteristic time $t_0$ dependent on $R_0$ and the initial reduced gravity $g'_0$,

$$t_0 = \left(\frac{R_0}{g'_0}\right)^{1/2}. \tag{3.5}$$

Rooney (2015) adopts the scaling of Lundgren for the descent and spread of negatively buoyant thermals, where $R_0$ is taken as the 'equivalent spherical radius of thermal', $R_0 \sim V^{1/3}$ where $V$ is the volume of parcel or thermal. Rooney (2015) defines the initial buoyancy of thermal as $B_0 = g'_0 V$ which allows $t_0$ to be expressed

as

$$t_0 = \left(\frac{R_0}{g'}\right)^{1/2} \sim \frac{R_0^2}{B_0^{1/2}} \,. \tag{3.6}$$

In this study a typical experimental release was more similar to that of a cylindrical shaped release instead of a spherical release. This leads to a slight modification of the length scale, where the characteristic length $R_0$ is taken as the radius of pipe outlet or initial downdraught width. The subsequent time scale remains the same as $t_0 \sim (R_0/g_0')^{1/2}$, and the velocity scale is simply $u_0 = R_0/t_0$. Throughout the results section these scales will be used to non-dimensionalise the results.

### 3.3.2 Flow visualisation

The experiments captured the main elements of downburst behaviour in the laboratory. The two release times were chosen to resemble the two extremes of buoyant fluid transport - an instantaneous thermal and quasi-steady plume. Figure 3.8 shows stills from 2 and 5 s 2% saline experiments (F2s2p_01 and F5s2p_01). In the early stages of development ($0 < t < 2$), both saline releases appear similar. Both releases develop a leading vortex ring over a similar time span (see Fig. 3.9 or the experimental video in supplementary material?). At $t = 2$ s, the valve is shut off for F2s2p_01 and the supply of buoyant fluid is cut off. F2s2p_01 then continues to descend as a single parcel of fluid, detached from the nozzle of the outlet but not yet in contact with the surface of the table. The cutting off of F2s2p_01 cause a small tail to form in the wake of the descending fluid. Continued buoyancy supply in F5s2p_01 led to a continuous plume from outlet pipe to surface until the valve closed after the leading edge had propagated approximately $2R_0$ from the point of impact. Snapshots from the two release rates highlight the conceptual difference of instantaneous parcel versus continuous source (Fig. 3.8).

Highspeed camera footage indicated that the leading vortex ring forms over a similar time scale for all experimental runs (see Figure 3.8). Upon impact with the surface, the vortex ring 'billows' up, with the depth of gravity $h$ rapidly increasing as the ring traverses 2-3 table squares (10 - 15 cm) before achieving an approximately constant depth. It should be noted that while Mason, Letchford, and James (2005)

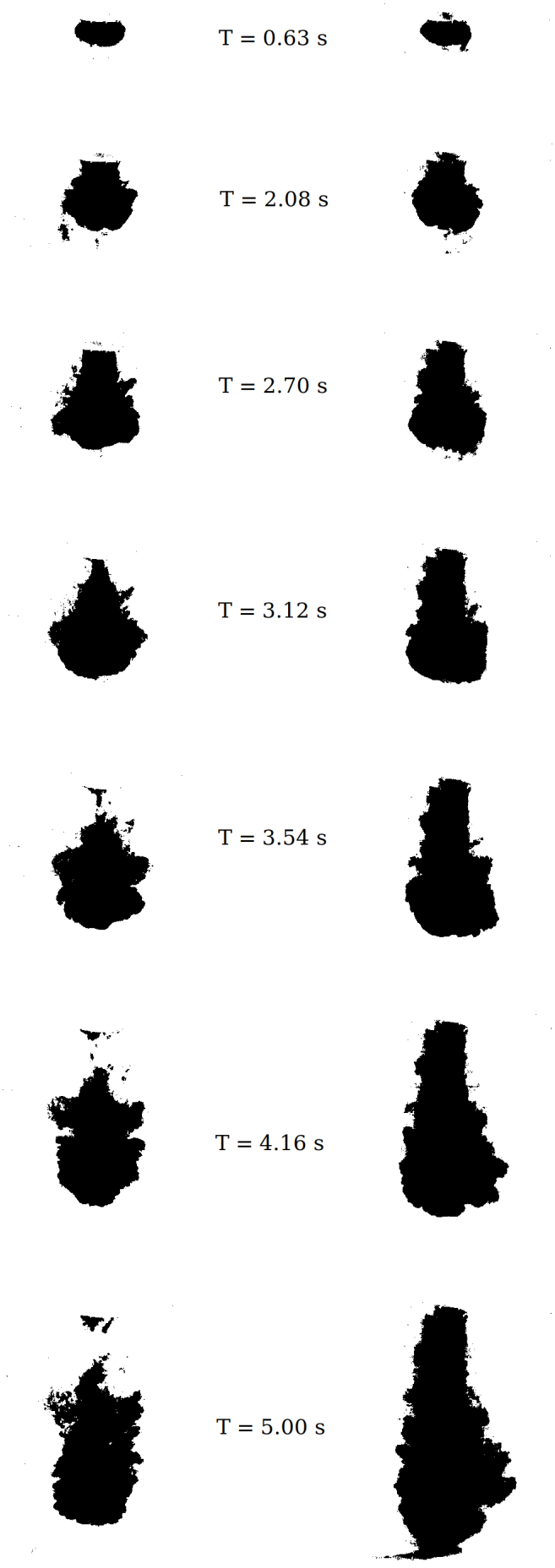


FIGURE 3.8: Stills from the Highspeed Camera from the vertical descent of F2s2p_01 (left) and F5s2p_01 (right)

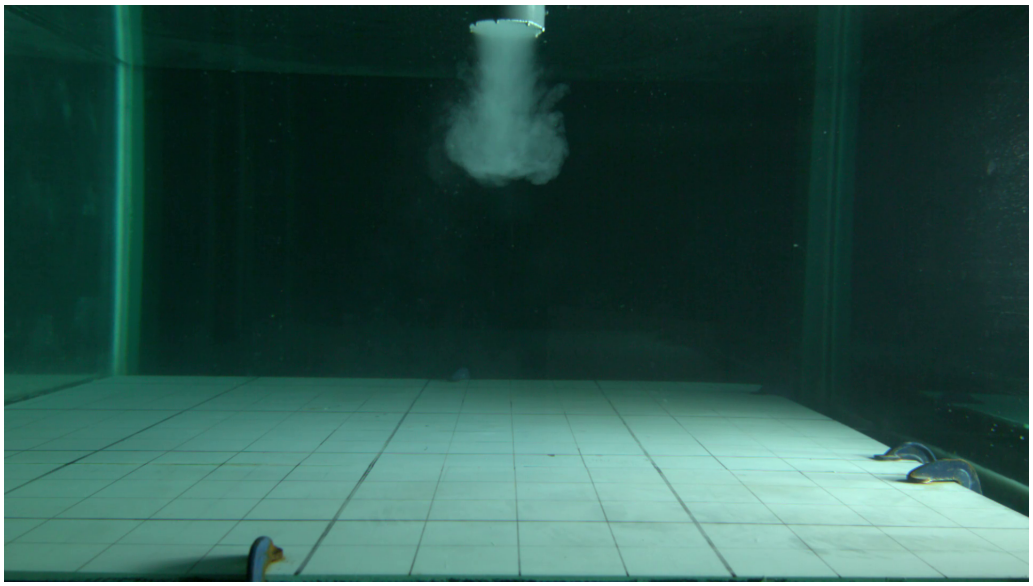

FIGURE 3.9: An unedited still from the Highspeed Camera from the vertical descent of a 2 s release F2s2p_01 at $t = 2.5$s

sub-divided the initial impacting fluid into different vortex structures (primary, secondary, intermediate ect.), in these experiments the leading vortex ring was a single structure. This is one advantage of conducting experiments in liquid, the complexity of the system can be reduced to a simplified idealised model which is consistently repeatable and approximately axisymmetric.

F2s2p_01 was entirely dominated by the formation of the vortex ring which encompassed almost all of the buoyant fluid. However, F5s2p_01 consisted of two distinct components; the leading vortex ring and the secondary after flow (Fig. 3.10). No obvious entrainment was observed after the head of the vortex ring, which is consistent with Britter (1979) who found that little, if any, mixing occurs between the different density gravity currents after the leading edge has passed. F5s2p_01 also exhibited a 'pulsing' tendency observed in several other steady plume studies (Proctor, 1988; Anabor et al., 2011), where baroclinic instabilities causes secondary surges after the leading vortex.

### 3.3.3 Characterisation of Pipe Outflow

One of the aims of this study is to relate experimental starting conditions to the characteristics of the resulting horizontal outflow, therefore it is important to know

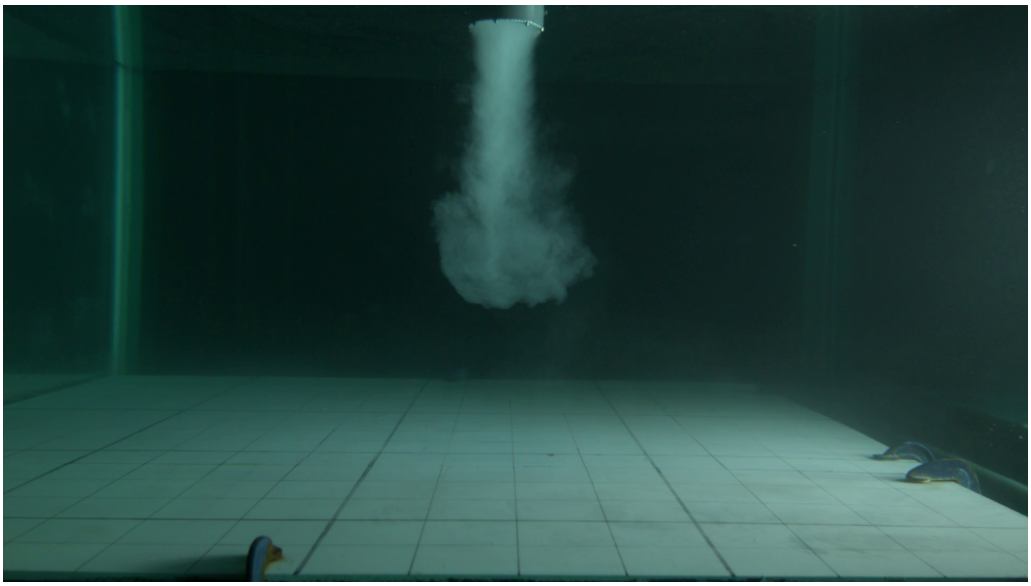

FIGURE 3.10: An unedited still from the Highspeed Camera from the vertical descent of a 5s release F5s2p_01 at $t = 2.7$s

the flow speeds and volumetric releases at the pipe outlet. Vertical velocities were measured using stacks of vertically aligned UDVP transducers aimed at the pipe outlet. The initial post processing of UDVP data was done by Hannah Kreczak who used phase unwrapping, applied data quality filters and an 11 point moving average (Kreczak, 2015). This study then used the processed vertical velocity data to estimate characteristic outlet velocities and volumetric releases.

Time averaged vertical velocity outflow profiles are shown in Figures 3.12 and 3.13 at approximately 5 cm below the outlet pipe. Figure 3.12 shows the averaged velocity at different widths from the centre of the pipe outlet for a 2 s release. A characteristic profile is created from averaging over the individual events (bold line). Similarly Figure 3.13 shows the same for a 5 s release. Both the releases have similar outflow profiles, although the outflow velocities for V5_01-03 are of greater magnitude to the velocities seen in V2_01-V2_04. From Figures 3.12 and 3.13, characteristic outflow velocities will be taken as 0.15 $ms^{-1}$ for 2 s releases and 0.2 $ms^{-1}$ for 5 s releases.

The UDVP transducers fire individually in a continuous cycle, at any given time the UDVP records instantaneous velocity measurements at a fixed $x$ along the $z$-axis of the transducer currently firing. Cycling through the transducers gives an overall

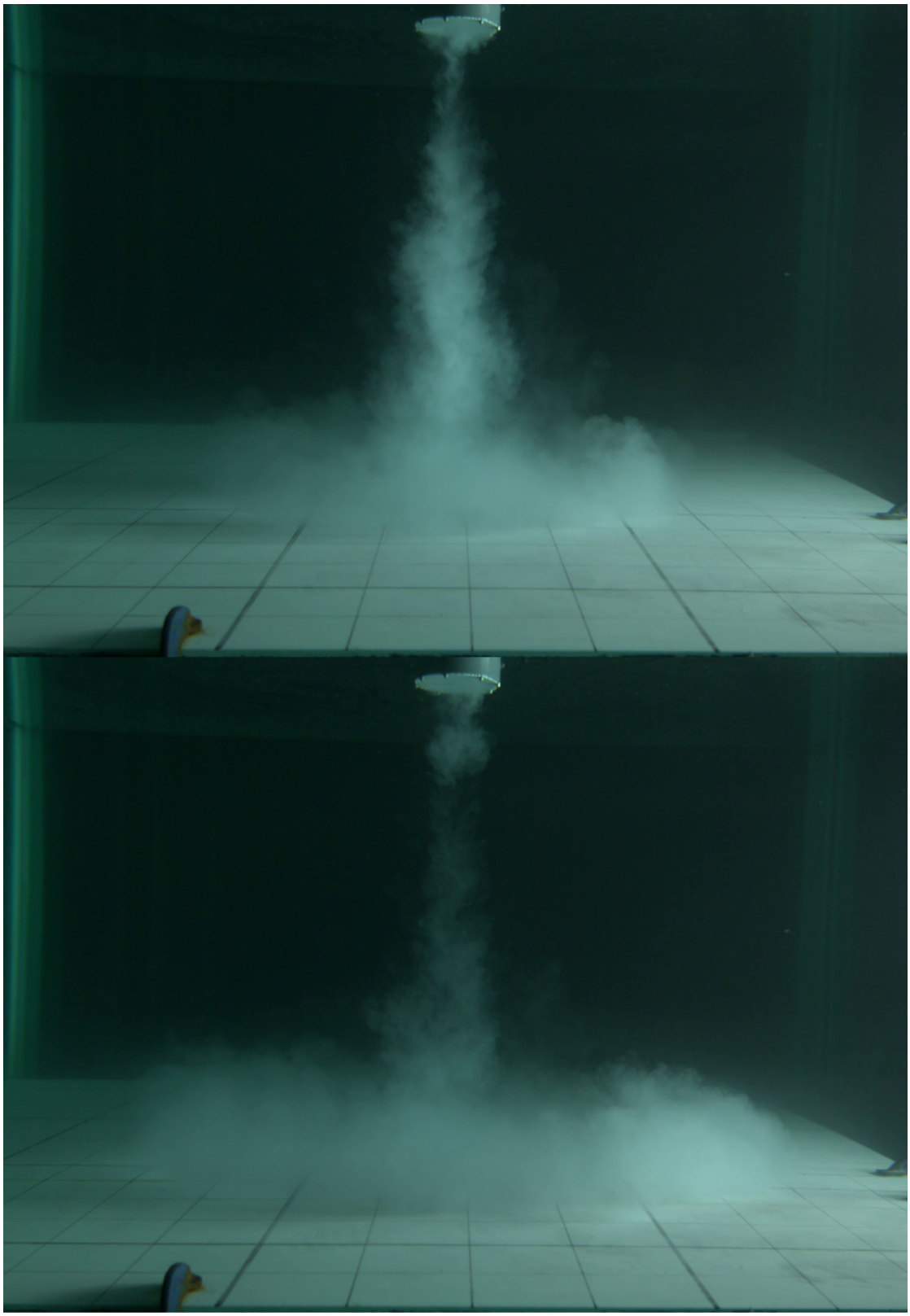

FIGURE 3.11: An unedited still from the Highspeed Camera from the vertical descent of a 5s release F5s2p_01 at $t = 6.5$s (top) $t = 8.4$s (bottom)

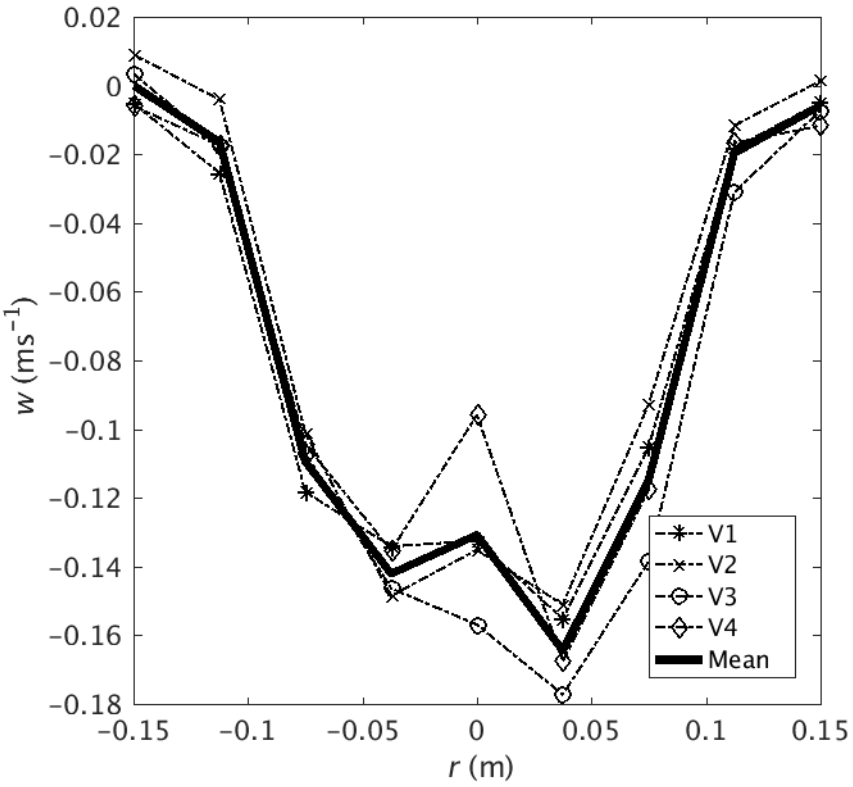


FIGURE 3.12: Vertical velocity (m $s^{-1}$) profiles at the outlet pipe for V1-V4 2s releases

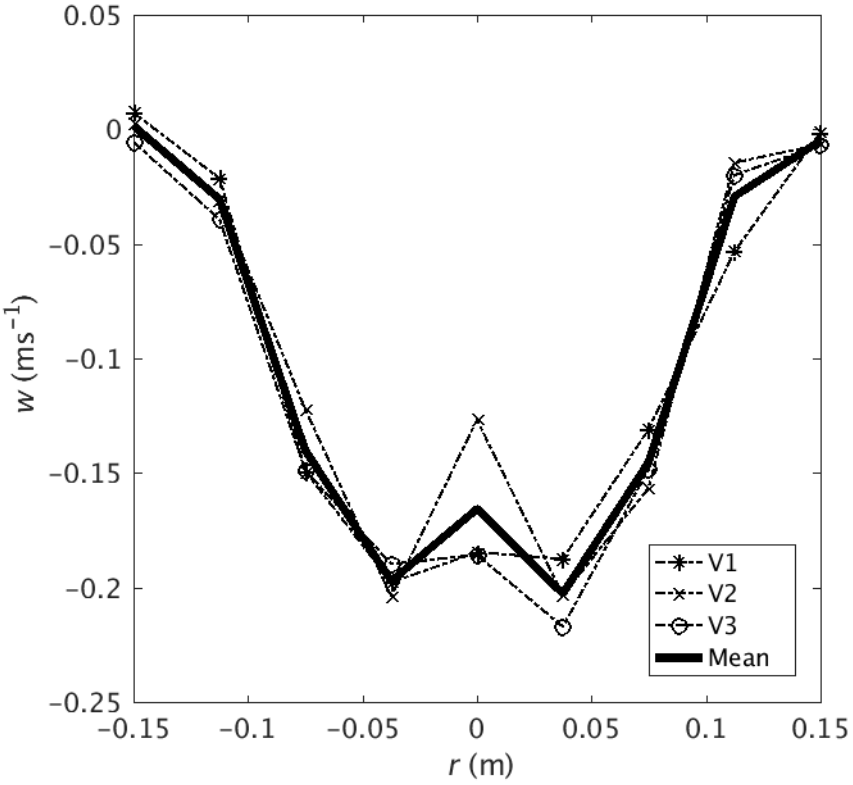


FIGURE 3.13: Vertical velocity (m $s^{-1}$) profiles at the outlet pipe for V5-V7 5s releases

picture of the flow field but staggered in time. Therefore, a linear interpolation was applied to the data to find the entire $(x-z)$ flow field at a specific time t,

$$w_{t_q} = w_{t_m} + (w_{t_{m+1}} - w_{t_m})\frac{t_q - t_m}{t_{m+1} - t_m}, \tag{3.7}$$

where $t_m$ is the time a given transducer fires, $t_{m+1}$ is the time that the given transducer next fires and $t_q$ is an imposed equally spaced time vector that can be used to compare all transducers against each other, where $t_m < t_q < t_{m+1}$. Here $t_q$ was chosen to give a linear interpolation most accurate for the middle transducers (responsible for the bulk of the velocity measurements). Typically, the error associated with the linear fit was between 0.5-1.0%. Velocities in the $z$ direction were then averaged to give $(\hat{w} - x)$ velocity profiles at times $(t_{q_1}, t_{q_2}, ..., t_{q_{end}})$. The volume $V$ was then found by integrating over the time of release,

$$V = \rho \int_{t_i}^{t_F} Q \, dt = \rho A \int_{t_i}^{t_F} \hat{w} \, dt \tag{3.8}$$

where $t_i$ is the time at release, $t_F$ is the time at end of release, volumetric flow rate is given by $Q(t) = A \cdot w(x,t)$ where $A$ is cross-sectional area of the pipe outlet and $\rho$ is density of fluid released. Using the trapezoidal rule,

$$L = \frac{(t_F - t_i)}{2n}(\hat{w}_{t_i} + \hat{w}_{t_F}) + 2\sum_{t=t_1}^{t=t_{f-1}} \hat{w}_t \tag{3.9}$$

where $L$ is the integrated velocity, the volume could be estimated from the data. It was found that for a 2 s release, 25.0 $dm^3$ of fluid was released while for a 5 s release, 51.0 $dm^3$ of fluid was released. The discrepancy between a $\times 2.5$ increase in release time resulting in a $\times 2.0$ volumetric release can be explained by (i) there is an error in the actual release time, the release time is set by a hand operated dial with uncertainty $\pm 0.5$ s. (ii) the $(\hat{w} - t)$ velocity profile becomes more 'U' shaped in the 5 s release than the 'V' shape in the 2 s release, suggestion a terminal outflow velocity is reached.

### 3.3.4 Entrainment

The experimental results allow two estimations of entrainment, from i) the vertical descent profiles taken from the highspeed camera and ii) the radius of impingement taken the GoPro camera. Applying the assumption used by Morton, Taylor, and Turner (1956) that the rate of entrainment $\alpha$ at the edge of the thermal is proportional to some characteristic velocity of the thermal at that given height, then the radius of thermal can be related to its height by

$$b = b_0 + \alpha z \tag{3.10}$$

where $b_0$ is the initial radius of thermal and $\alpha$ is assumed to be constant. The radius of impingement can then be estimated by simply taking $z = H$

$$R_i = b_0 + \alpha H. \tag{3.11}$$

The same assumptions for a steady plume yield a similar entrainment relationship

$$b = b_0 + \frac{6}{5}\alpha z. \tag{3.12}$$

Comparing (3.10) with the experimental results allows an estimation of entrainment. Figure 3.14 compares the radius with height for experiments F2s2p_01 and F5s2p_01 using the outline images from highspeed camera videos. F2s2p_01 descends as a discrete parcel of fluid, therefore radius is estimated instantaneously at different times (blue stars). After impacting the ground, F5s2p_01 resembles a quasi-steady plume for over 2 s since there is buoyant fluid continuously from source to floor. The radius of the quasi-steady plume is then averaged over time to produce a continuous profile of width (solid blue line).

There is little variation in the evolution of the radius with height between F2s2p_01 and F5s2p_01, which reflects the similarity between (3.10) and (3.12). Interestingly, there appears to be little variation in radius with time (Fig. 3.8) which suggests the bulk of the entrainment must be confined to the head of the saline release. A best

fit between the radius from highspeed camera stills and (3.10) suggests a value of $\alpha = 0.3$. This value for entrainment is within a sensible region for plumes and thermals (Turner, 1979; Rooney and Linden, 2012) and $\alpha = 0.3$ will be used throughout the analysis of the vertical descent. Figure 3.14 supports the classical assumption of a constant rate of entrainment in Morton, Taylor, and Turner (1956) in plumes and thermals.

Camera footage from the GoPro mounted above the tank allowed for another estimation of the radius of impingement $R_i$. Typically for a 2% saline experiment, the radius of impingement was between 250-325 mm. This rather large range of impingements does not seem to correlate to the experimental conditions, specifically there appears no difference between a 2 s and 5 s release on impingement radius. It is therefore likely that radius of impingement was heavily influenced by the uncertainty in release mechanism of the pneumatic valve, certain saline releases were more turbulent than others. Again comparing the estimated radius of impingement from GoPro stills and (3.10), suggests $\alpha = 0.3 - 0.4$. The estimation of $\alpha$ from the GoPro is higher than from the highspeed camera, a potential explanation for this discrepancy is that the entrainment rate is not entirely linear. The GoPro provides an estimation of $\alpha$ as the saline release impacts the floor, while the highspeed camera only measures the initial descent stage. It is conceivable that near impact, the leading edge of the release 'feels' the presence of the floor and entrainment is enhanced. A more rigorous investigation is needed to test this hypothesis.

### 3.3.5 Vertical Descent

The vertical descent of buoyant fluid was tracked using highspeed camera footage. Vertical propagation is defined as the vertical distance the leading edge of buoyant fluid has travelled from the outlet pipe. Individual stills from the highspeed footage were compared to a background image, pixel changes above a threshold of 0.02 were identified as buoyant fluid (see Section 3.2.2). The centre line of outflow pipe was estimated from the background image and vertical propagation measured along this

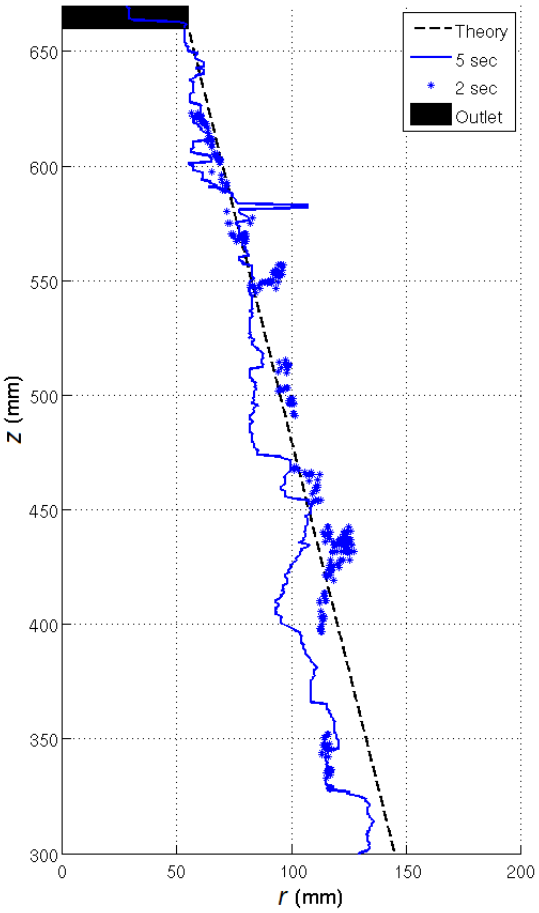


FIGURE 3.14: Horizontal radius (mm) of saline release against height (mm) for i) 5 s release, a time averaged profile of the quasi-steady plume is plotted as the blue solid line. ii) 2 s release, the instantaneous maximum radius at different times is plotted as the blue '$*$'. The theoretical radius of descending thermal from (3.10) is plotted as the black dashed line, where the value of $\alpha = 0.3$ is taken as the best fit to the experimental data.

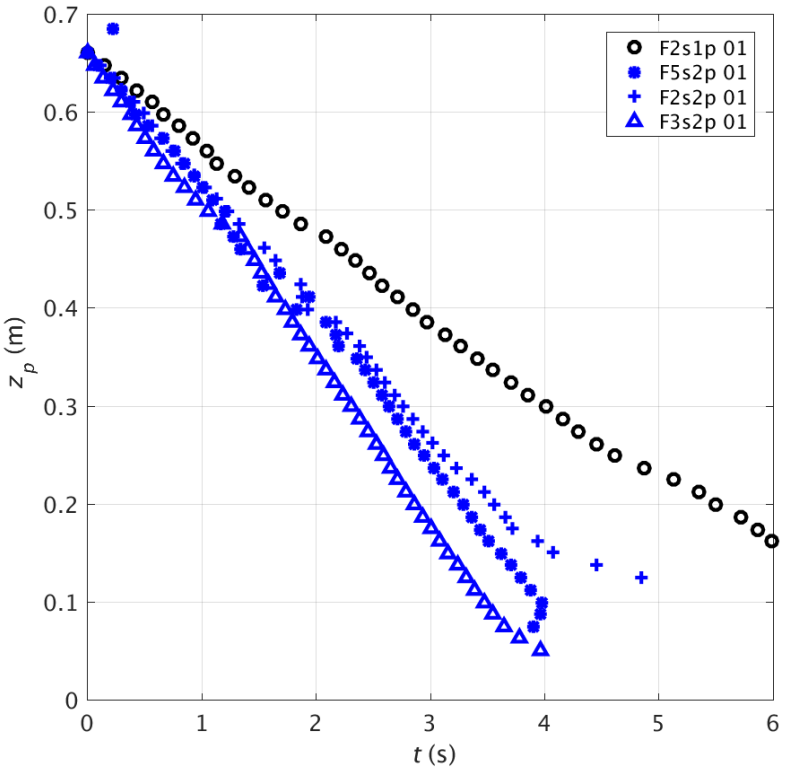


FIGURE 3.15: Vertical descent of the leading edge of experimental downburst for experiments F2s1p_01 F2s2p_01, F3s2p_01, and F5s2p_01.

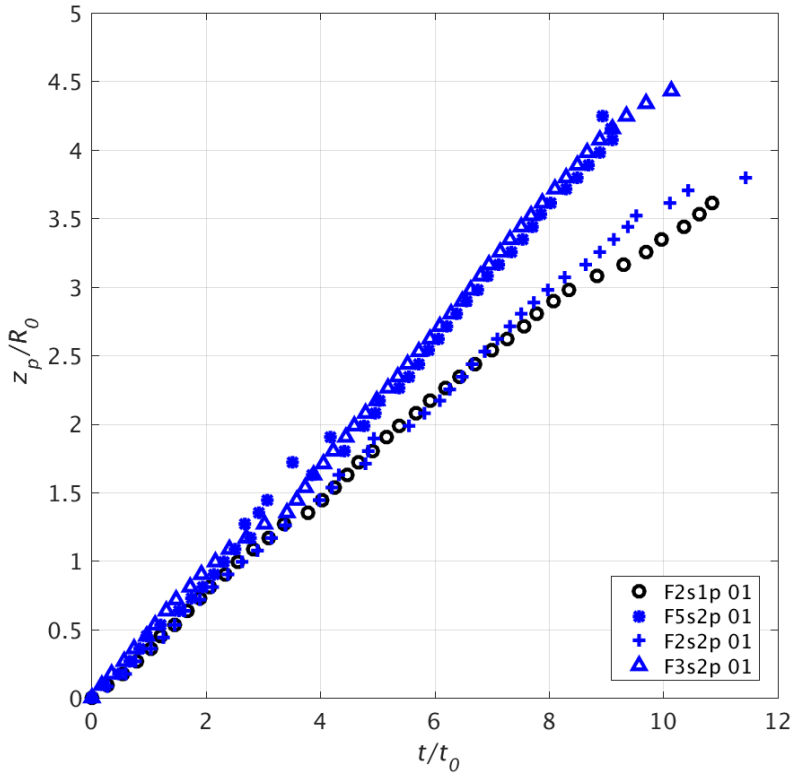


FIGURE 3.16: Vertical descent of the leading edge of experimental downburst for experiments F2s1p_01 F2s2p_01, F2s2p_02, and F5s2p_01 scaled by $R_0$ and $t_0$

FIGURE 3.17: Highspeed Camera stills for F2s2p_01 (left) and F3s2p_01 (right) at $t = 2.6$ s or $t/t_0 = 5.2$

line. The centre line was divided into a number of 'checkpoints' and the buoyant flow was considered to have reached this checkpoint if every touching pixel (including diagonals) was identified as moving fluid. Close to the surface of the table it becomes difficult to distinguish between the white of the fluid and the white of the table and therefore measurements were are limited to $> 100$ mm above the surface.

Figure 3.15 shows 4 experiments: F2s1p_01, F2s2p_01, F3s2p_01, F5s2p_01 captured by highspeed camera. An anomaly filter was applied to experiments F2s2p_01 and F5s2p_01, where differences $> 20\%$ between the line of best fit and data were considered to be erroneous speckles instead of actual fluid and disregarded. This filter removed 4 and 3 data points respectively from each experiment. No filter was needed for F2s2p_01 and F3s2p_01. Data are plotted starting at 660 mm (the height of outlet pipe) and with $t = 0$ s as the first time fluid movement is detected.

All experimental runs descend towards the surface in a linear fashion. There are not any major changes in vertical propagation, or regions of acceleration over the descent. Close to the surface of the table the experimental runs exhibit a slight change of behaviour, potentially experiencing the presence of the table (although this is where the identification method for vertical descent is most uncertain).

As expected for a partially density driven flow, the three 2% density experiments propagate towards the surface faster than the 1% density experiment because of the greater negative buoyancy in the 2% experiments. There appears good agreement between 2% density experiments, particularly for $0 < T < 2$s. After 2 s, agreement remains relatively good although there is divergence in propagation speeds. Figure 3.16 plots the same four experiments with the scaling developed by Lundgren, Yao, and Mansour (1992). $R_0$ is taken as the radius, $t_0$ is $(R_0/g_0')^{1/2}$. The scaled results are plotted from origin of pipe, taken to be $z/R_0 = 0$ and where $z$ is in the direction of the downward flow.

The scaled results collapse onto two lines, representing two different regimes of

buoyant transport for this experimental configuration: i) discrete parcel and ii) continuous source. Before $t/t_0 = 4$, the four experiments are indistinguishable in both flow visualisation (Figure 3.8) and propagation speed (Figure 3.16). This similarity is not unexpected, at this stage approximately the same volume of buoyant fluid has been released at a similar flow rate in all experiments. However at $t/t_0 = 4$, the valve is closed for F2s1p_01 and F2s2p_01. Closing the valve leads to significant changes in the development of the buoyant fluids. Consider the outline images of F2s2p_01 and F3s2p_01 at $t/t_0 = 5.2$ in Figure 3.17. F2s2p_01 has begun to resemble a discrete parcel of fluid, whilst F3s2p_01 is analogous to a starting plume. It appears that the continued supply of buoyant fluid and momentum causes the longer experimental releases to propagate faster.

Interestingly, the propagation rate does not differ between F3s2p_01 and F5s2p_01, despite valve opening times of 3 and 5 s respectively. Why then would a 2 s release propagate differently, whilst longer releases appear identical? To answer this discrepancy, remember the two stages of descent identified in Section 3.3.2. Initially, a vortex ring would form at the pipe outlet. Depending on the length of valve opening time, this vortex ring would for 2 s releases, contain the majority of the fluid released. Whilst longer releases developed a supporting 'column' or plume of fluid trailed behind the leading vortex ring. Shusser and Gharib (2000) shows that vortex rings develop over a characteristic time $t_F$ which is related to the scaled time $t_0$ by

$$t_F = 4.73 t_0 \tag{3.13}$$

This study suggests that the vertical propagation of the leading edge is characterised by the properties of the leading vortex ring. For 1% density experiments, $t_F \approx 3.5$ s and for 2% density experiments, $t_F = 2.5$ s. If the experiments are split two categories: i) where the valve opening time is less than the theoretical vortex formation time and ii) where the valve opening time is greater than the vortex formation time. Then F2s1p_01 and F2s2p_01 can be considered as 'weak' vortex rings since the supply of buoyancy is cut before the vortex ring has time to fully form (valve opening 2s). F3s2p_01 and F5s2p_01 have 'strong' vortex rings since they develop vortex

rings which have received the maximum theoretical energy available (valve opening times 5s). Consequentially, the vortex rings for F3s2p_01 and F5s2p_01 have the same properties despite F5s2p_01 receiving a greater total buoyancy over the entire release. It is only the supplied buoyancy and momentum that enters the leading vortex ring which determines the rate of propagation. The properties of the subsequent 'tail' do not determine the properties at the leading edge (at least over the scales of this study). Figure 3.15 shows the descent time for 2s releases is around 4s until impingement, which suggests that the vortex ring has just had time to fully form ($T_F = 3.25$s) at around 10cm above the surface. At this point, it is expected that the thermal will be influenced by the presence of the floor.

Most previous studies are either entirely momentum or buoyancy-driven. It is therefore not expected that theoretical buoyancy relations will fit well with these experimental results. However, it is of interest to examine the scale of the divergence between theory and experiments. Atmospheric downdraughts receive both momentum from precipitation and negative buoyancy from (Proctor, 1988), yet previous studies (Lundgren, Yao, and Mansour, 1992; Rooney, 2015) have developed similarity solutions assuming only buoyancy-driven flow. These theoretical relations will be examined in the context of this studies less idealised experiments.

Experiments will be compared the theoretical model of a thermal in a uniform environment, described in Turner (1979). Turner (1979) shows that a thermal has horizontal radius, velocity and reduced gravity,

$$b = \alpha z \tag{3.14a}$$

$$w = B^{1/2} z^{-1} f_1\left(\frac{p}{b}\right), \tag{3.14b}$$

$$g' = B z^{-3} f_2\left(\frac{p}{b}\right), \tag{3.14c}$$

where $z$ is the vertical displacement, $p$ the position relative to the centre of the thermal and $\alpha$ is the entrainment constant. Rooney (2015) shows how (3.14b) can also be expressed as

$$w = \left(Fr_T \, m^{-1/2} \alpha^{-1}\right) B^{1/2} z^{-1} \tag{3.15}$$

where $Fr_T = w/(g'b)^{1/2}$ is the Froude number and $m$ is a thermal shape factor, suggested as $m \approx 3$ by Scorer (1957). One may notice that (3.15) has an unphysical origin at $z = 0$. Since this study is considering atmospheric thermals with physical initial radius, it becomes convenient to introduce a virtual origin $z_v$ so that an initial radius $b_0$ can be related to a virtual point source by

$$z_v = \alpha^{-1} b_0. \tag{3.16}$$

Replacing $w$ with $\mathrm{d}z/\mathrm{d}t$ and integrating relates the vertical position of a thermal with time by

$$z + z_v = \left(2Fr_T \, m^{-1/2} \alpha^{-1} B^{1/2} t\right)^{1/2}. \tag{3.17}$$

Figure 3.18 plots (3.17) against the experimental results. Total buoyancy release $B$ was estimated using the volumetric release calculated in Section 3.3.3, entrainment was found in Section 3.3.4 as $\alpha = 0.3$. The Froude number was calculated at the pipe outlet using the characteristic outflow velocity found in Section 3.3.3 and ranged from 1.36 - 1.44, this is similar to Rooney (2015) (see Figure 4b) who found $Fr_T = 1.4$ for their experimental set-up. From Scorer (1957) the thermal shape factor was taken as $m = 3$.

There is reasonable agreement between the thermal similarity solutions and the experimental results. F2s1p_01 and F2s2p_01, which are the shorter thermal-like releases, fit the thermal vertical propagation (3.17) well. Perhaps counter-intuitively, (3.17) predicts a faster rate of descent than the experiments releases; which have the benefit of additional momentum. However, remember that (3.17) assumes an instantaneous release of buoyancy, whilst buoyancy is released over a finite time in the experiments. As an illustrative example, for an 'instantaneous' release from a virtual point source, with negative buoyancy equivalent to that of F2s2p_01, would from (3.15) would have a descent velocity of $\approx 0.3$ ms$^{-1}$ upon reaching the height of the pipe outlet. Compare this to the actual measured velocities of $\approx 0.2$ ms$^{-1}$ at pipe outlet and it can be seen that the added momentum from the experimental set-up results in smaller velocities that an 'instantaneous' release would achieve at the same height.

Unsurprisingly, the fit of (3.17) is weakest when compared to the longer F5s2p_01 release (Figure 3.19). F3s2p_01 and F5s2p_01 are more similar in nature to a starting plume and the assumptions of an instantaneous release in (3.17) leads to an overcompensation of the total buoyancy and subsequent speed of descent. It is advantageous in parameterizations for numerical weather modelling to limit the required number of equations and therefore generalise for as wide a regime of events as possible, therefore this study suggests a simple adaptation of (3.17). It was earlier established that the dominate structure of the descent is the leading vortex ring, and this vortex ring forms over a characteristic time. Using the assumption that it is the properties of this leading vortex ring that determines the rate of descent, (3.17) is re-calculated where instead of using the total buoyancy $B$, the estimated buoyancy within the vortex ring $B_v$ is used. This adaptation of (3.17) is plotted in pink in Figure 3.19 and provides a much better representation of rate of descent.

In summary so far, a theoretical expression for the vertical descent of negatively buoyant fluid (3.17), has been compared with laboratory saline releases. Figures 3.18 and 3.19 show reasonable verification of this theoretical relation. However, there is one important discrepancy throughout the results. Although at an instantaneous time, there is small difference between the theory and experiments, the actual curve of the theory and experimental data are significantly different. The theory (3.17) is dependent on a $r \propto t^{1/2}$ relationship, whilst the experiments appear to be more linear (curve fitting models suggest for a best fit $r = k_* t_*^n + c_*$, where $k_*, n_*, c_*$ are constants, $n_* = 0.75 - 0.9$). Additionally, all of the experimental descents are slower than the theoretical expressions. There are two potential reasons for these discrepancies. Firstly, errors in the measurement and post-processing of the vertical descent. The highspeed camera relied on identifying the moving dyed fluid, however the leading edge of release was identified as the region of greatest entrainment and therefore where the dye would be most diluted. Secondly, and perhaps more fundamentally the releases may not have had sufficient height to fully develop and descend at the expected theoretical rate. For example consider F2s2p_01, the vortex ring was identified as forming over 2 s whilst the experimental release impacted on

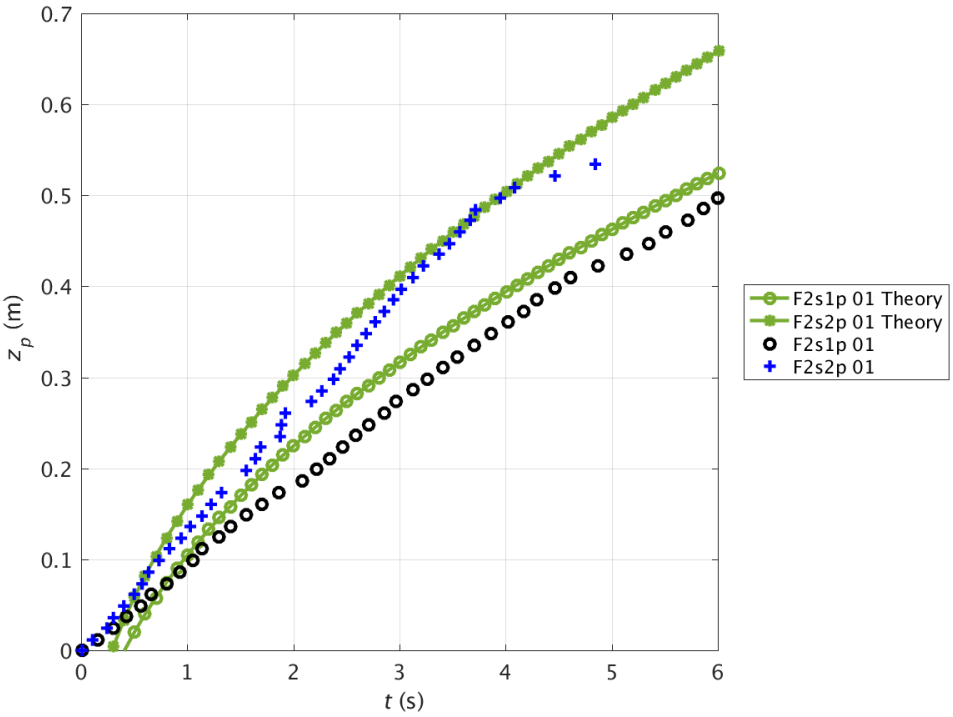


FIGURE 3.18: Vertical descent of the leading edge of experimental downburst for F2s1p_01 and F2s2p_01. Theoretical vertical descent (green) plotted using Equation (3.17)

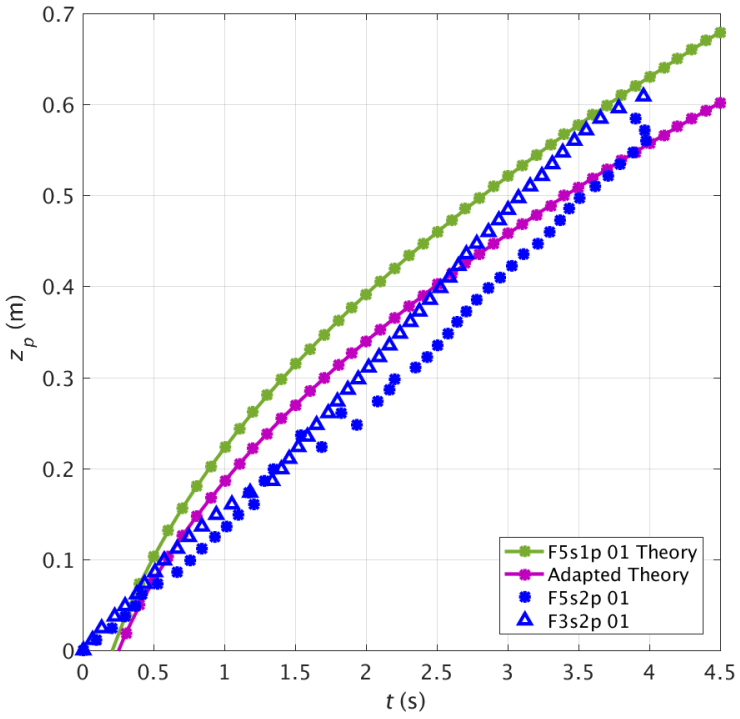


FIGURE 3.19: Vertical descent (m) of the leading edge of experimental downburst for F3s2p_01 and F5s2p_01. Theoretical vertical descent (green) plotted using Equation (3.17), adapted (pink)

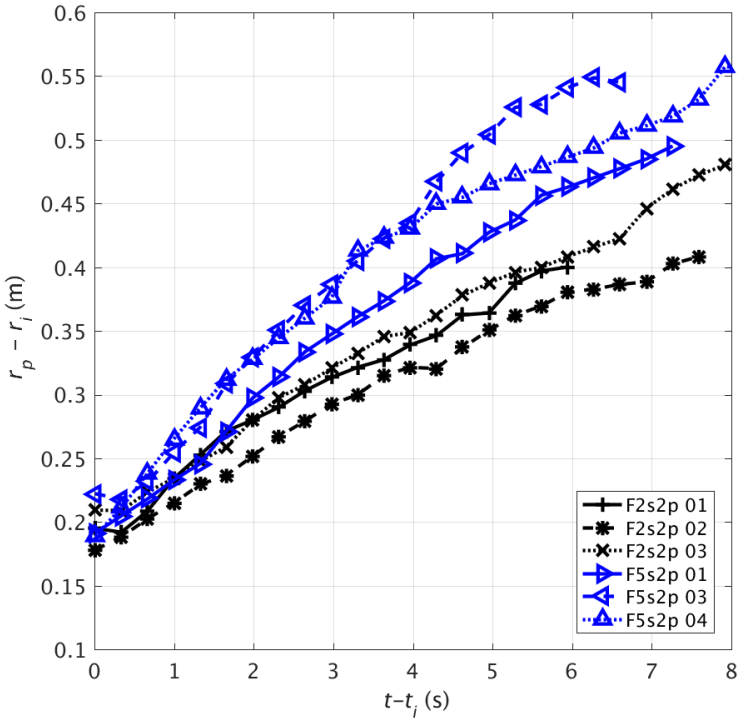


FIGURE 3.20: Radial spread (m) of the gravity current from assumed centre of impact.

the surface around 5-6 s. That only leaves a short period where F2s2p_01 has developed from the source and has not experienced any effects from the surface. Similar results are observed by Rooney (2015), who found it took released negatively buoyant bubbles in numerical LES simulations around 1600 s (by which the bubble had fallen 3000 m) to adapt to a $r \propto t^{1/2}$ relationship. Despite the limitations of (3.17), the fit between theory and experiments is still reasonable and will therefore be used in future parts of this study to determine vertical propagation.

### 3.3.6 Radial Propagation

After impact, the experimental downburst propagates radially. The radial spread of buoyant fluid was tracked using camera footage from a GoPro mounted above the tank, providing a 'birds eye' view of the experimental table. Individual stills from the GoPro footage were compared to a background image, pixel changes above a threshold of 0.02 were identified as buoyant fluid. Various post-processing methods were used to un-distort and tidy up the images, allowing radial propagation to be automatically identified, see Section 3.2.2 for a detailed description.

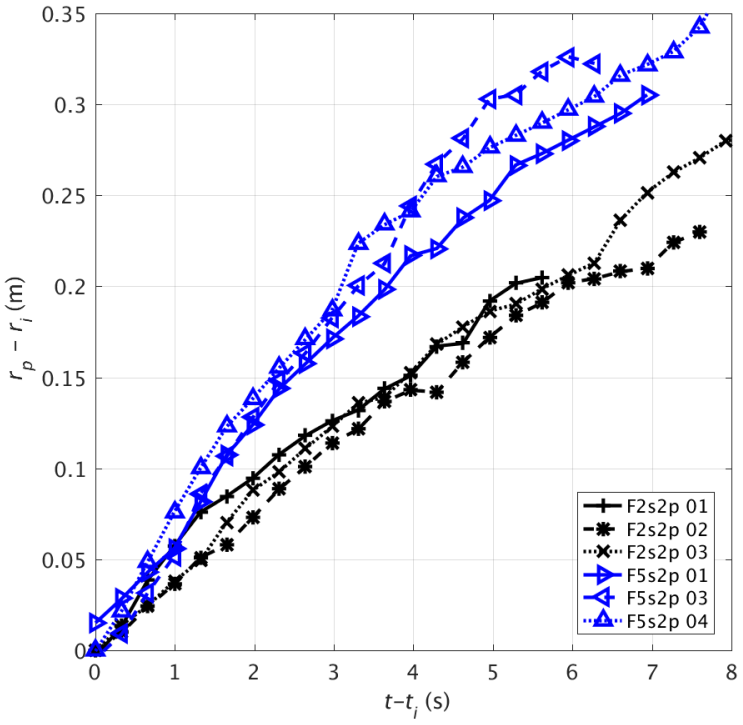


FIGURE 3.21: Radial spread of the gravity current. Time after impact (s) versus horizontal radial propagation normalised by radius of impact (m)

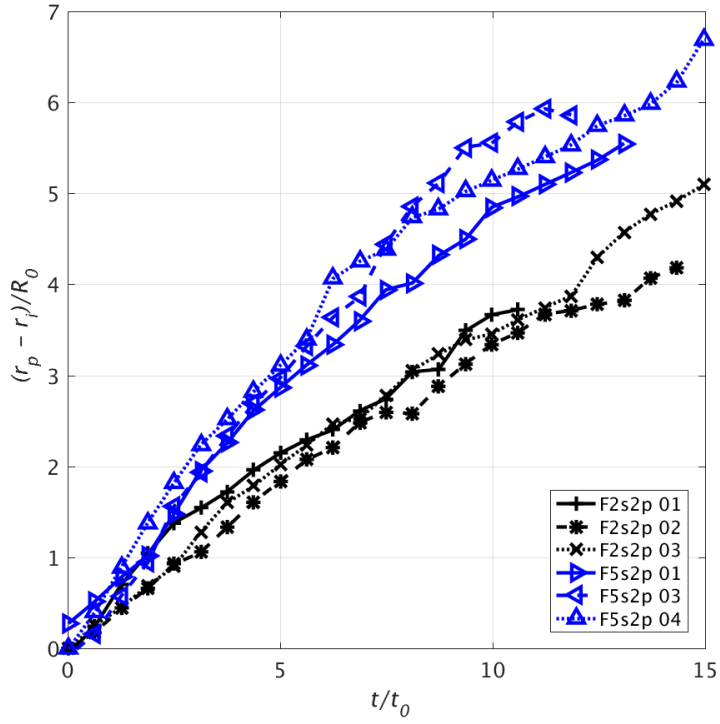


FIGURE 3.22: Radial spread of the gravity current. Time after impact (s), scaled by total buoyancy versus radial propagation normalised by radius of impact (m)

Radial propagation is defined as the horizontal distance the leading edge of the buoyant fluid has travelled along the surface of the experimental table from the estimated centre of impingement. The horizontal outflow propagates axisymmetrically from impact, therefore it is convenient to adopt a radial coordinate system $(r, \theta)$ throughout this section, where $r$ is measured from the centre of impingement. The centre of impingement for each experiment was estimated from three GoPro stills at or around the moment of impact. A best fit circle was drawn over the horizontal outflow and the centre of this circle was assumed to be the centre of impact. Time, unless otherwise stated, is the time after impingement.

Figure 3.20 shows the radial propagation versus time of 6 experiments, F2s2p_01,02,03 and F5s2p_01,02,04. Two of these experiments F2p2p_01 and F5s2p_01 were simultaneous filmed by GoPro and Highspeed camera footage and their vertical motion is discussed in Section 3.3.5, the rest of the experiments only have the horizontal part of their motion recorded. The six experiments are 3 ensembles of 2 different set-ups, i) three experiments with 2 s releases of buoyant fluid from the outlet pipe and ii) three experiments with 5 s releases. Apart from release time, these experiments are all identical in set-up. Figure 3.20 perhaps raises concern then that each of these supposedly identical experiments seems to have slightly different rates of horizontal propagation. However, notice the wide range of radius of impingement - identical experiments can have discrepancies of up to 5 cm in their radius of impingement. This wide range of radius of impingement is not in itself too surprising due to the highly turbulent nature of the experimental release. Therefore, if the results are normalised by the radius of impingement, as in Figure 3.21 then some coherency in the radial propagation becomes apparent. The experiments are split by their time of release, with F5s2p_01,02,04 propagating faster than F2s2p_01,02,03. In general there is good agreement for each class of release, particularly in the early stages $t < 4$ s. For $t > 4$ s there is greater variance in the radial propagation. However, it is in this later region that i) reflections or interference from the tank walls become more likely and ii) the measurement techniques for tracking the buoyant fluid become less accurate as the fluid is increasingly diluted.

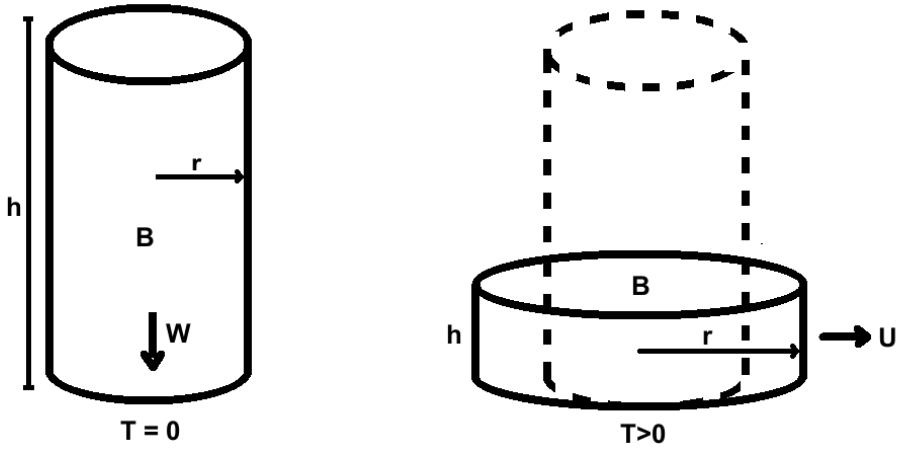


FIGURE 3.23: Conceptual box model collapse of into a gravity current of a fixed volume cylinder of fluid with negative buoyancy $B$, height $h$, radius $r$, vertical velocity $W$ and horizontal velocity $U$. The cylinder is instantaneously released at $t = 0$ and at time $t > 0$ has collapsed and spread axisymmetrically to form a gravity current.

Continuity suggests that experiments F5s2p_01,02,04 should spread faster than F2s2p_01,02,03 since it was established in Section 3.3.5 (Figure 3.16) that the 5 s releases descended at a greater speed than the 2 s releases. The aim now is to determine if that difference in propagation rate is scalable by some fundamental property of experiment at source. An obvious place to begin is by adopting the same scaling of Lundgren, Yao, and Mansour (1992) as applied in Section 3.3.5. Figure 3.22 plots the radial propagation, now scaled by $R_0$ and $t_0 = (R_0/g_0')^{1/2}$. It is immediately apparent that this scaling, so effective for the vertical descent, has made little difference to scaling the radial propagation. The lack of scaling in Figure 3.22 prompts two important questions: i) Why does this scaling work in the vertical descent but not the radial propagation? ii) Why does this scaling work in Lundgren, Yao, and Mansour (1992) but not these experiments? Before answering these questions, it is helpful to think about the simplest conceptual model of this set-up.

Imagine an experimental release that has fully developed and fallen far from the source above. At the moment of impact, represent the experimental release as a non-entraining cylinder falling at velocity $W$, with height $h$, radius $r$ and reduced

gravity $g'$ (see Figure 3.23). The volume is

$$V_c = \pi r^2 h. \tag{3.18}$$

After impact, the cylinder will collapse and spread out axisymmetrically. The horizontal velocity has two components $U_0$ from the collapse and spread of negatively buoyant fluid, and $U_*$ from the translation of vertical velocity to horizontal,

$$U = U_0 + U_*. \tag{3.19}$$

One might now realise there is nothing unique about this conceptual model. The horizontal intrusion of fluid with one density into fluid of a different density is well known across atmospheric science and fluid dynamics as a 'gravity current'. The release and spread of an axisymmetric volume of fluid from rest ($U_* = 0$) is a well studied problem. The forward velocity $U(t)$ of an inviscid, relatively dense, Boussinesq gravity current propagating over a horizontal surface is related by the Froude number,

$$Fr_c = U/(g'h)^{1/2}. \tag{3.20}$$

where the subscript $c$ denotes this is the Froude number for the gravity current instead of the vertical component. Hallworth et al. (1996) show, using a similar simple box-model collapse, that the radius of the current $r$ is related to $U$ by

$$U = \frac{\mathrm{d}r}{\mathrm{d}t} = Fr_c(g'h)^{1/2}. \tag{3.21}$$

By substituting the volume of the cylinder (3.18) into (3.21) and integrating, the radius of current as a function of time is given by

$$r = (4g'V_c Fr_c^2/\pi)^{1/4} t^{1/2}. \tag{3.22}$$

Grundy and Rottman (1985) show that (3.22) can also be derived from the shallow water equations.

Reviewing (3.22) answers the first of our scaling questions: why does the scaling

from Lundgren, Yao, and Mansour (1992) work for the vertical descent but not the radial propagation? In Section 3.3.5 it was found that the properties of the leading vortex ring largely determined vertical descent. This vortex ring formed over a characteristic time $t_F$ and it was the buoyancy within this vortex ring that was important rather than the total buoyancy of the whole release. The only two determining variables for the vortex ring were the radius of pipe outlet and the reduced gravity $g'$, which are both represented in $t_0 = (R_0/g'_0)^{1/2}$ and therefore the scaling works. However, (3.22) has a dependence on the total volume and therefore total buoyancy of release. $t_0$ does not represent the total buoyancy of experimental releases and therefore does not scale with the radial propagation. In answer to the second question: why does this scaling work in Lundgren, Yao, and Mansour (1992) but not with these experiments? Lundgren, Yao, and Mansour (1992) kept the volume of their experiments constant but varied the reduced gravity, this meant that density became a proxy for total buoyancy.

The radial propagation can now be described by properties of the fluid at impingement. However, the primary objective is to relate the radial propagation to properties at the source. Rooney (2015) examines this problem, combining the thermal similarity solutions described by Turner (1979) with the gravity current similarity solutions described by Grundy and Rottman (1985) and Hallworth et al. (1996) by assuming that the volume of the descending thermal at impingement $V_i$ is that of the gravity current and that buoyancy is conserved throughout. Rooney (2015) re-writes (3.22) as

$$r = (2Fr_c)^{1/2}\lambda^{1/4}B^{1/4}(t - t_i)^{1/2} + R_0, \tag{3.23}$$

where $\lambda$ is a constant, $t_i$ is the time of impingement and $R_0$ is the source length scale. Rooney (2015) verified (3.23) in Large Eddy Simulations, but (3.23) has not previously been tested in a laboratory.

Figure 3.24 plots the experimental radial propagation with the corresponding theoretical spread from (3.23). Two important adaptations to (3.23) from Rooney (2015) are made. From Large Eddy Simulations Rooney (2015) (Figure 4b.) finds a best

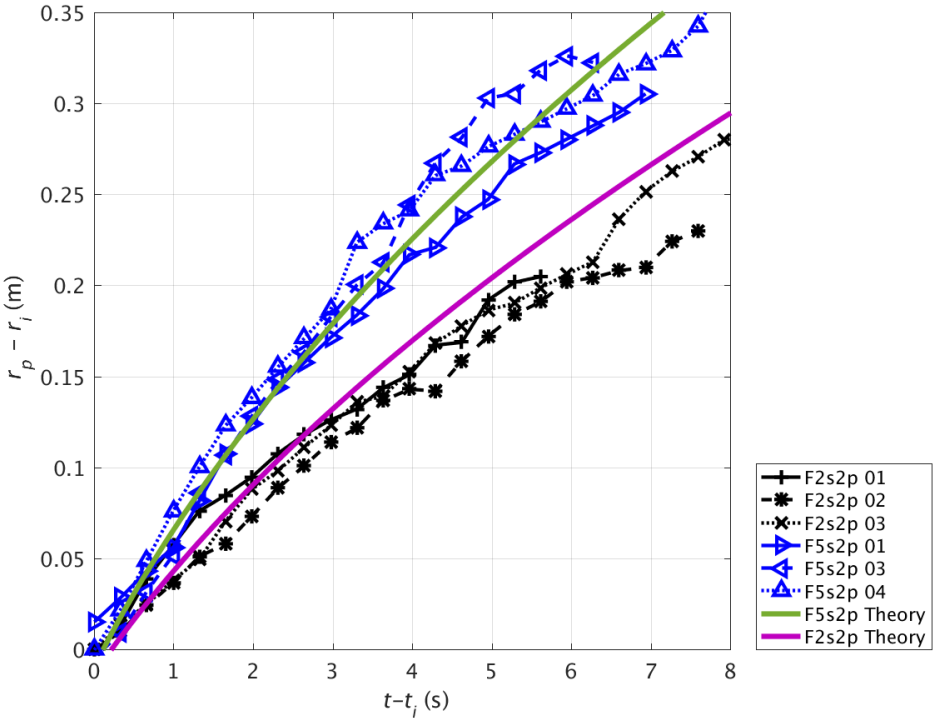


FIGURE 3.24: Spread of the gravity current. Time after impact (s) versus horizontal radial propagation normalised by radius of impact (m). Theoretical lines are plotted using (3.23) where following Hallworth et al. (1996), $Fr_c = 1.19$ and $\lambda = \pi^{-1}$. $R_0$ is taken as the theoretical radius of impingement.

fit to their numerical results, inferring $Fr_c = 1.4$ and $\lambda = 1$. However, this study finds much better agreement with Hallworth et al. (1996) who suggest $Fr = 1.19$ and $\lambda = \pi^{-1}$ from their volumetric gravity current releases from laboratory saline experiments. There could be a multitude of reasons why numerical simulations and laboratory experiments offer different Froude numbers and constants, ranging from numerical diffusions, different roughness lengths and real fluids exhibit an extra retarding effect due to Reynolds stresses and viscous drag at the head of the current (Bonnecaze, Huppert, and Lister, 1993). It is beyond the scope of this chapter to explore this issue further and is sufficient to conclude that the radial propagation of this studies experiments is in-line with that of other previous saline laboratory experiments. The second important distinction from Rooney (2015) is the value of $R_0$. Rooney (2015) takes $R_0$, which is itself a constant arising from the integration of $U = \mathrm{d}r\,/\,\mathrm{d}t$, assuming that the thermal descends as a quasi-spherical volume of fluid gives

$$R_0 = \left(\frac{3m}{4\pi}\right)^{1/3}(b_0 + \alpha H). \tag{3.24}$$

This approach worked well for the Large Eddy Simulations of instantaneously released negatively buoyant spheres. However depending on the valve opening times, the experiments could resemble either quasi-spherical parcels or appear more cylindrical in shape. $R_0$ was therefore taken as the theoretical radius of impingement, which from (3.14) and (3.16) is

$$R_0 = (b_0 + \alpha H). \tag{3.25}$$

The resulting equations are plotted in Figure 3.24. Experiments F2s2p_01,02,03 and F5s2p_01,02,04 represent three ensembles of two different volumetric releases with the same 2% reduced density, and therefore represent two different quantities of negative buoyancy. With the above modifications, the theoretical relations derived from (3.23) fit both sets of releases well. One of the primary objectives of this chapter has now been achieved: Figure 3.24 suggests that it is possible to determine the properties of the resulting radial outflow from an elevated source.

It is now finally possible to develop a scaling for the horizontal outflow. From (3.23)

it is clear that the total buoyancy is the important variable, rather than either density or volume alone. Therefore if the scaling developed by Lundgren, Yao, and Mansour (1992) is adapted as in Rooney (2015) (see Section 3.3.1) to

$$t_0 \sim \frac{R_0^2}{B_0^{1/2}}, \tag{3.26}$$

then a time scaling dependent on buoyancy can be used. Figure 3.25 plots experiments F2s2p_01,02,03 and F5s2p_01,02,04 now scaled by the pipe outlet $R_0$ and the modified $t_0$. All experiments collapse onto one line. There is a particularly good fit in the early stages of development $((R_p - R_i)/R_0) < 3$, beyond this radius there is greater variation, but as previously discussed it is in the later regions of experimental spread that there is the greatest uncertainty in measurement, along with the highest chance from interference from the tank walls, therefore some divergence at this stage is expected. The scaled results should now allow for these experiments to be compared to the full regime of buoyant release. For completeness, experiments F2s2p_01,02,03 and F5s2p_01,02,04 are now compared with the numerical results from Rooney (2015). The experimental results seem to differ to Rooney (2015) by a factor of 20. Again this difference is consistent with the difficulty of reconciling atmospheric scale numerical simulations to real laboratory saline experiments. Although, the general curve in propagation of laboratory and numerical results is of similar shape.

So far, the radial propagation of laboratory results has been compared narrowly to one set of similarity solutions and LES results from Rooney (2015). However, Chapter 2 demonstrated the wide range of previous studies that consider similar experiments. Instead of describing the release of a saline as an 'instantaneous' release of buoyancy $B$, and rather considering the release as a quasi-steady buoyancy flux $F$, which is arguably more representative of the experimental set-up (specifically the 5s releases), then this studies experimental results can be placed in the context of the wider literature.

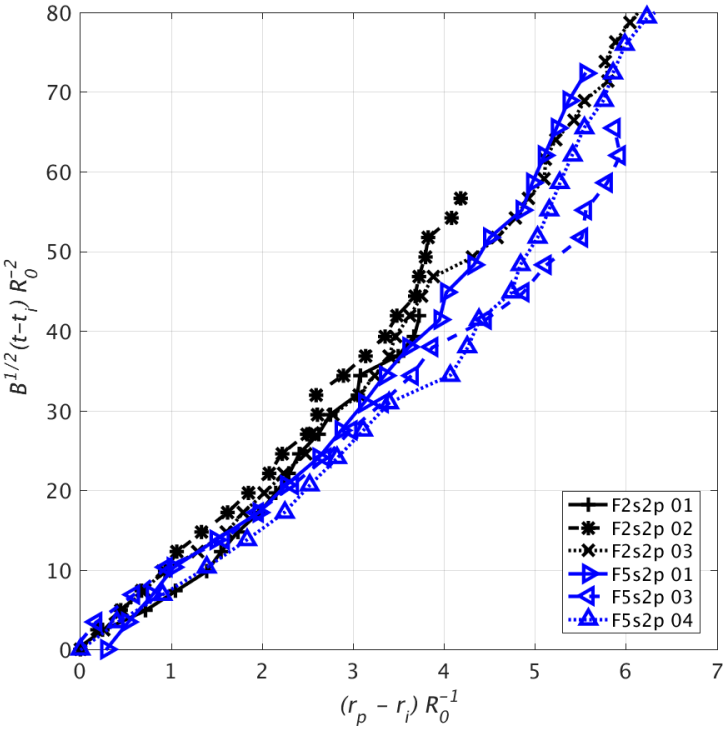


FIGURE 3.25: Radial spread of the gravity current. Time after impact (s), scaled by total buoyancy versus radial propagation (m) normalised by radius of impact.

Figure 3.27 plots the radial propagation of gravity against time after impingement. Scalings proposed by Kaye and Hunt (2007) (see Section 2.2.1) are used to non-dimensionlise length and time as

$$\tau = \frac{t}{H^{4/3}F^{-1/3}} \tag{3.27}$$

and

$$\phi = \frac{r}{H}. \tag{3.28}$$

Applying this scaling allows comparison between this studies experimental results and other previous studies focused either on i) axisymmetric lock gate experiments or ii) impinging constant flux plume studies (see Table 2.1). $F$ is calculated for this studies release of $B$ by assuming a normal distribution of buoyancy release over the time of valve opening and then averaging to give a constant $F$.

Firstly considering solely this studies laboratory results; there is an imperfect col-

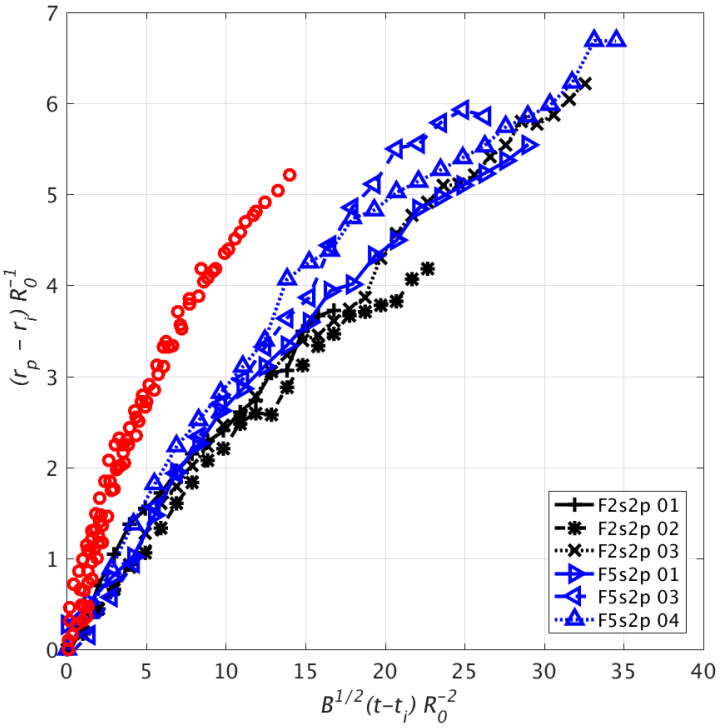


FIGURE 3.26: Radial spread of the gravity current. Time after impact, scaled by total buoyancy versus radial propagation normalised by radius of impact. For comparison, the numerical results from Rooney (2015) are plotted in red.

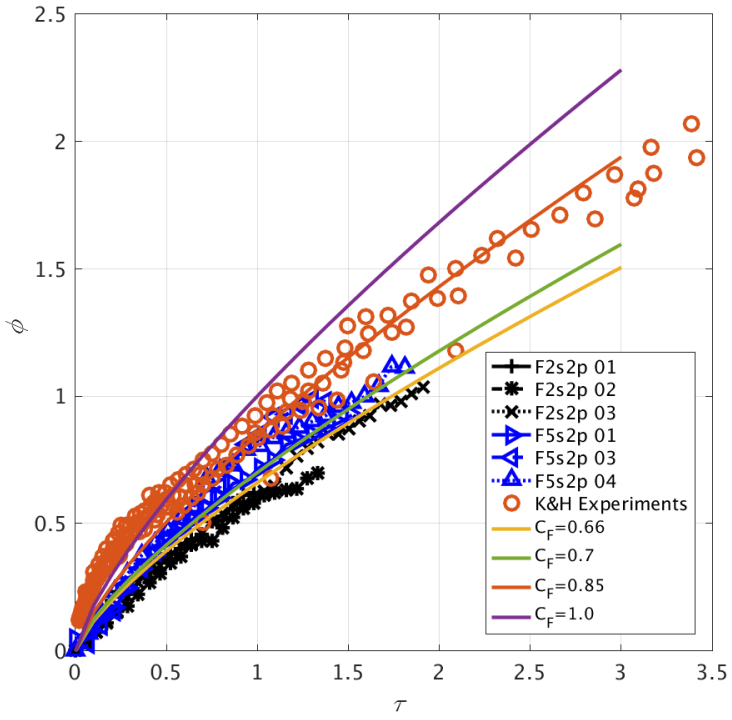


FIGURE 3.27: Radial spread of the gravity current. $(t - t_i)$ and $r$ are non-dimensionalised from (3.27) and (3.28) as described in Kaye and Hunt (2007). This studies laboratory experiments are plotted in black (2s releases) and blue (5s releases). In addition, laboratory experiments of constant buoyancy flux plumes impinging upon a surface from Kaye and Hunt (2007) are plotted as orange circles. Different values of $C_F$ are taken from previous studies. ($C_F = 0.66$ from Rooney and Linden (2012), $C_F = 0.7$ from Linden and Simpson (1994), $C_F = 0.85$ from Britter (1979) and Kaye and Hunt (2007) and $C_F = 1.0$ from Chen (1980).)

lapse of the experimental data set. The data has not collapsed onto one line when following the scalings from Kaye and Hunt (2007). This is not unexpected, the 2s release did not form a steady plume but instead a discrete volume of fluid, and even the 5s release only had continual saline release from outlet to floor for 2s of the release time. It is not surprising then that similarity solutions assuming a constant $F$ do not collapse the data onto a single line. However, when compared to previous studies on gravity currents with constant buoyancy flux, this studies experiments do actually fall into a similar flow regime. Numerous studies suggest a value for the constant of radial propagation $C_F$, which ranges from 0.6-1.0 (see Table 2.1). This studies experiments appear to fit the lower end of the value range, with $C_F = 0.7$ as seen in Linden and Simpson (1994) appearing to predict the radial outflow well. However, it should be noted that the method used to estimate $F$ for this study was crude and likely to overestimate the actual rate of $F$ ($F$ was not measured during the experiments and is therefore inferred from the total buoyancy release). A smaller value of $F$ would mean the experimental results were more consistent to $C_F = 0.85$ as seen by Britter (1979) and Kaye and Hunt (2007). The 2s releases are at the lowest end of the range of suggested propagation rates, which is consistent with the idea that using a constant buoyancy flux would provide the poorest estimation for a thermal 2s release. The 5s, which could be considered as a quasi-steady plume, is seen to behave more consistently with previous studies that have constant $F$.

### 3.3.7 Properties of the Gust Front

So far, this chapter has confined itself to examining how the bulk properties of buoyant fluid, such as propagation rate and radius, develop with time. For a meteorological audience, these bulk properties are of primary importance because of their role on atmospheric processes through their fluxes of heat or moisture, or in generating convection. However for the communities and industries who experience downdraughts more directly, through devastating storms and haboobs, knowledge or forecasting of the specific wind profile at surface is of paramount importance. Therefore this section will devote its attention to examining the instantaneous peak winds, and the structure found in the head of the resulting gravity current, defined as the 'gust front'.

Velocities around the surface of the experimental table could be measured at specific points using Acousitic Dopppler Velocity Profilers (ADVPs). The ADVPs measured 3 components of velocity $(u, v, w)$ at 100 Hz, along a vertical line of 20 equally spaced points at certain radial locations. The ADVPs have a range of 64 mm, whilst the head of the gravity current was around 100 mm, therefore two ADVPs were used to cover the entire height of the structure. The lower ADVP measured 2 - 66 mm from the floor of the tank table, while the higher ADVP measured between 72 - 136 mm. There was an 8 mm gap between the two ADVPs, where no data were collected (see Section 3.2.2 for more details).

Figures 3.28 and 3.29 are plotted from VM2s2p_04 and VM5s2p_02 and provide an insight into the velocity structure of the gravity current. In both figures, the velocity maximums are concentrated at two heights. Close to the surface $z/R_0 < 0.4$, there are strong positive velocities (positive is in the radial direction $r$ away from centre of impingement). In contrast at $z/R_0 = 0.8$, there are strong negative velocities registered. For VM2s2p_04, the negative velocities slightly precede the positive velocity, with similar magnitudes of 0.25 $\text{ms}^{-1}$, indicating a strong overturning of fluid. This circulating body of fluid is the head of the gravity current. After the head of the gravity current has passed, there is little subsequent flow, although there is a secondary positive maxima of 0.25 $\text{ms}^{-1}$ at $t/t_0 = 68$. This secondary maxima is consistent with Vermeire, Orf, and Savory (2011) who observed a strong secondary (and sometimes tertiary) pulse in their experiments in air. VM5s2p_02 has a similar general structure to VM2s2p_04, in that there is a strong positive velocity maximum at the surface, whilst there is a strong negative maximum at $z/R_0$=0.8. As expected, for the longer 5 s experiment, there is a more sustained flow after the head of the gravity current has passed through. Interestingly, this secondary flow appears slightly elevated at around $z/R_0 = 0.3$.

Certain specific times are extracted from the data used in Figures 3.28 and 3.29 to provide instantaneous vertical profiles of the horizontal velocity for VM2s2p_04 and

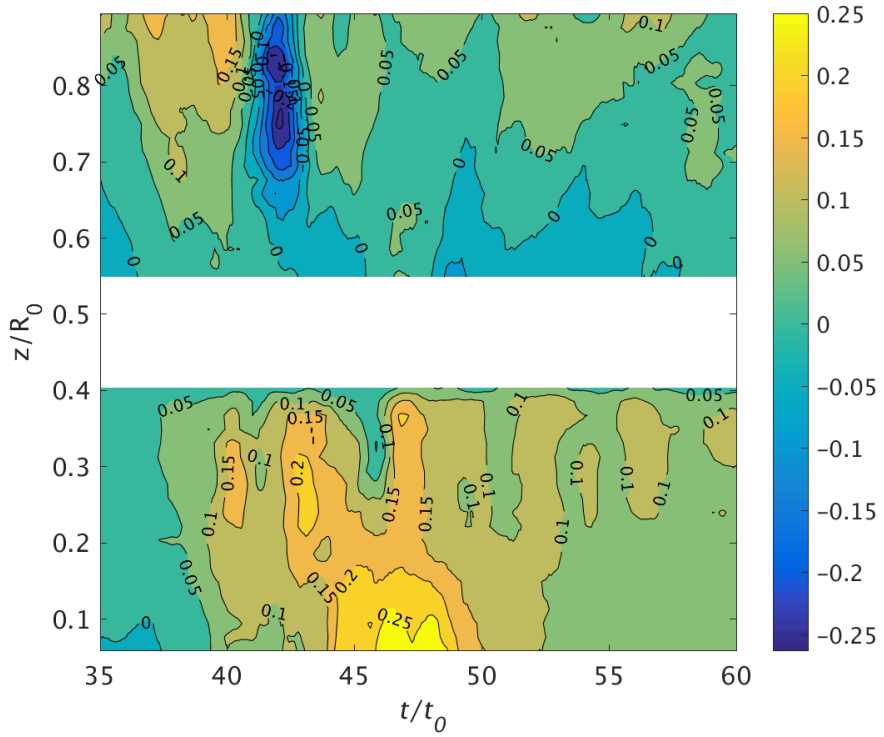


FIGURE 3.28: Velocity contour (m $s^{-1}$) plots at $r/R_0$ for VM2s2p_04

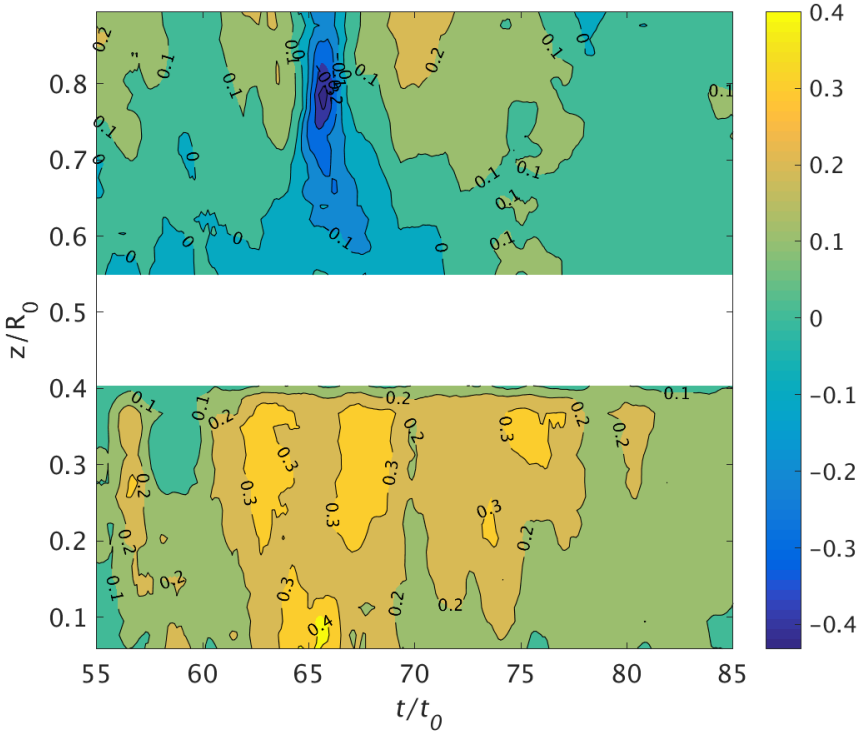


FIGURE 3.29: Velocity contour (m $s^{-1}$) plots at $r/R_0$ for VM5s2p_02

VM5s2p_02. In Figures 3.30 and 3.31, both experimental releases initially have a traditional nose profile, where at $0 < z/R_0 < 0.1$, velocity rapidly increases from 0 to a maximum ($U_r/U_0 \approx 0.4$) and then gradually reduces to 0 at around $z/R_0 \approx 0.8$. It is possible this initial nose profile could either be the very start of negatively buoyant fluid from the experimental release reaching the measurement location or could be ambient fluid pushed ahead of the gravity current. Certainly the strong negative velocities associated with the presence of the vortex ring, which has formed the head of the gravity current, then arrives a few time steps later. During the passage of the gravity current head, the vertical profile of horizontal velocity forms an 'S' shape, with strong positive velocities between $0 < z/R_0 < 0.4$ and strong negative velocities between $0.4 < z/R_0 < 0.8$. The elevated negative velocities are lower in magnitude than the bottom positive velocities, which is to be expected since the bulk of the fluid is still propagating in the postive direction despite the strong overturning in the head of the gravity current. After the vortex ring passes, the flow returns to a similar nose profile. The vertical profiles of horizontal velocity are reasonably similar for VM2s2p_04 and VM5s2p_02, the main differences occurring in magnitude of velocities rather than fundamental differences in velocity profile. An interesting feature from VM2s2p_04 is (Fig. 3.28, at $t/t_0 = 13.20$) what appears to be a secondary smaller elevated eddy. This secondary structure arriving after the main vortex ring supports observations from Mason, Letchford, and James (2005) who found primary and secondary vortex structures in their pulsed wall jet experiments.

The focus of this chapter has been on trying to link properties of downbursts to fundamental properties at source, however is useful to compare these experimental results to previous studies from a range of disciplines to ensure the experiments are representing the downburst accurately. The nose profile of the vertical profile of horizontal velocity from Figures 3.28 and 3.29 is a feature observed in many studies into downbursts and microbursts (Fujita, 1985; Hjelmfelt, 1988; Wood et al., 2001; Sengupta and Sarkar, 2008; Anabor et al., 2011). For the benefit of the aeronautical and engineering communities, several studies (Sengupta and Sarkar, 2008; Wood et al., 2001; Anabor et al., 2011) have proposed an empirical relationship of the vertical

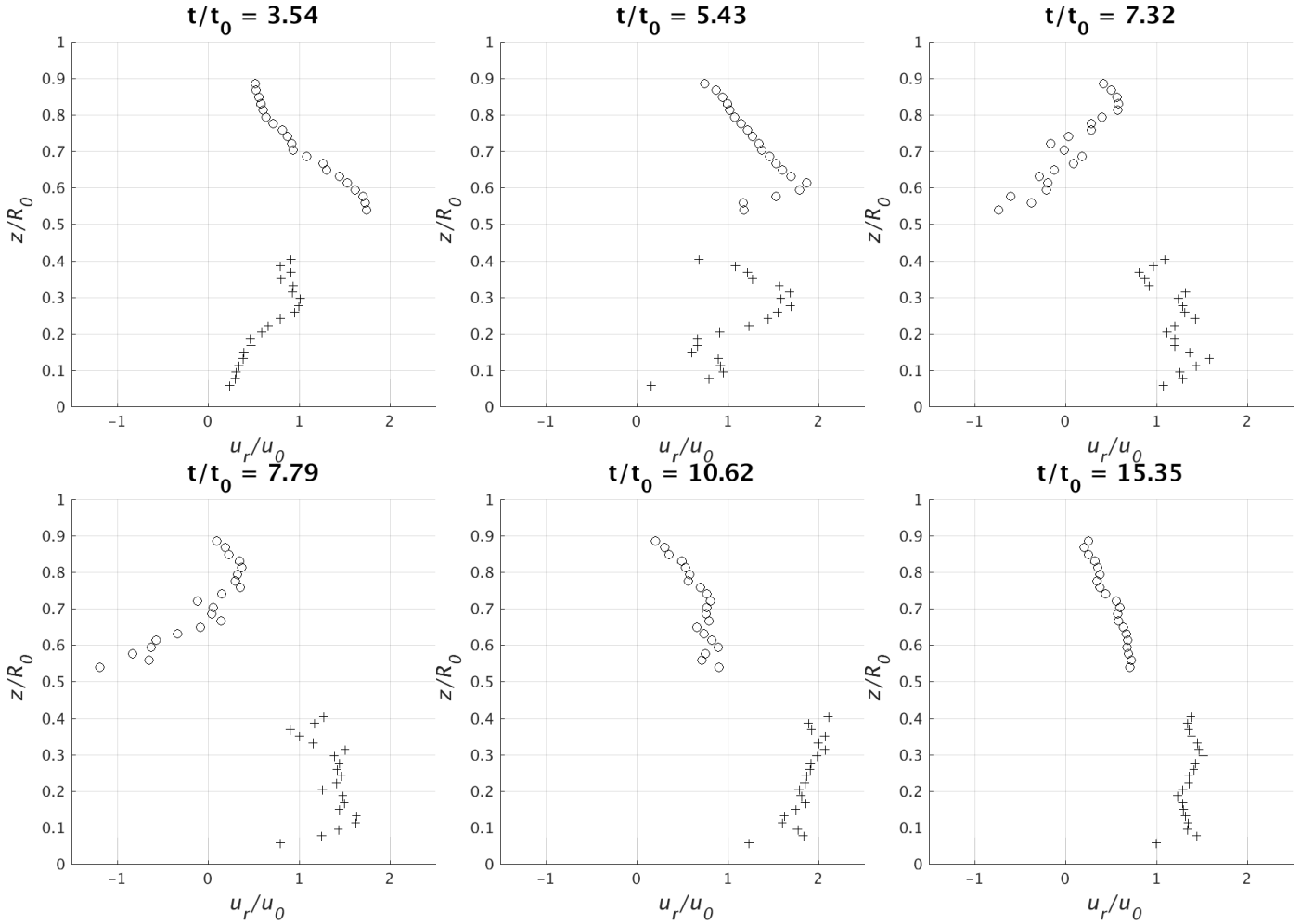


FIGURE 3.30: Plots of the instantaneous wind profiles at various $t/t_0$ for VM2s2p_04

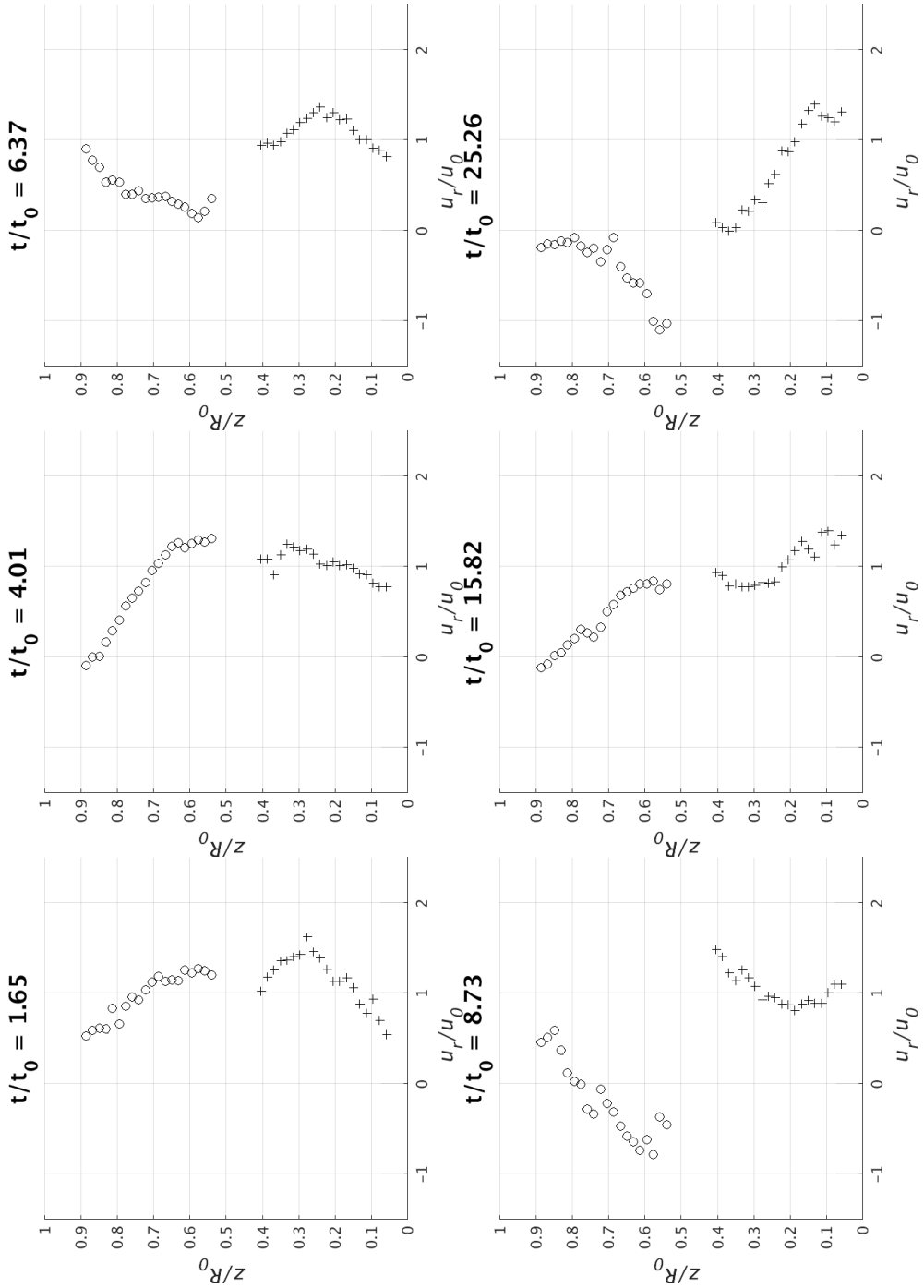


FIGURE 3.31: Plots of the instantaneous wind profiles at various $t/t_0$ for VM5s2p_02

profile of horizontal velocity for microburst events,

$$\frac{u_r}{u_m} = C_4 \left(\frac{z}{n_1}\right)^n_1 \left[1 - \text{erf}\left(C_5 \frac{z}{h_m}\right)\right] \tag{3.29}$$

where $u_r$ is the horizontal (or in these experiments the radial) velocity, $u_m$ is the maximum velocity, $h_m$ is the elevation at which $u = u_m/2$. $C_4, C_5$ and $n_1$ are empirically determined constants and erf() is the error function.

Figure 3.32 plots the time averaged vertical profile of horizontal velocity of VM2s2p_04-07 and VM5s2p_02. Since some studies only consider the steady state outflow (impinging jet experiments) whilst others include impact and development of gravity current, two averaged vertical profiles are plotted in Figure 3.32; i) the average horizontal velocity with height, excluding the passage of the vortex ring (black). ii) the same, but including the vortex ring. The green line is the best fit of (3.29) to the experimental results. Following Wood et al. (2001), $C_4 = 1.48$ and $n_1 = 1/7$. However, the best fit to the experiments found $C_5 = 1.2$ instead of 0.55. This difference of $C_4$ by roughly a factor of 2 is not surprising considering Wood et al. (2001) and Sengupta and Sarkar (2008) examine steady-state impinging jets in air (experimentally and using CFD), versus these transient experiments in water.

### 3.3.8 Maximum Horizontal Velocity

Section **??** examined the time averaged profile of the horizontal wind speed. However, for assessing the threat downbursts pose to communities, aircraft and infrastructure, studies suggest that it is not the median wind speed that is important but rather the top 1% of a storms wind speed probability function, i.e. the maximum wind speeds that are responsible for the highest damage (Chay, Albermani, and Wilson, 2006; Zhang, Sarkar, and Hu, 2014).

Figure 3.33 plots the maximum horizontal velocity for two 1% density releases with identical setups, VM2s2p_03 and VM2s2p_04, at fixed radial location, $r = 270$ mm from the centre of impingement. ADVPs measured the 3 components of velocity between 0 and 90 mm at 100 Hz. An 11-point moving average is applied to

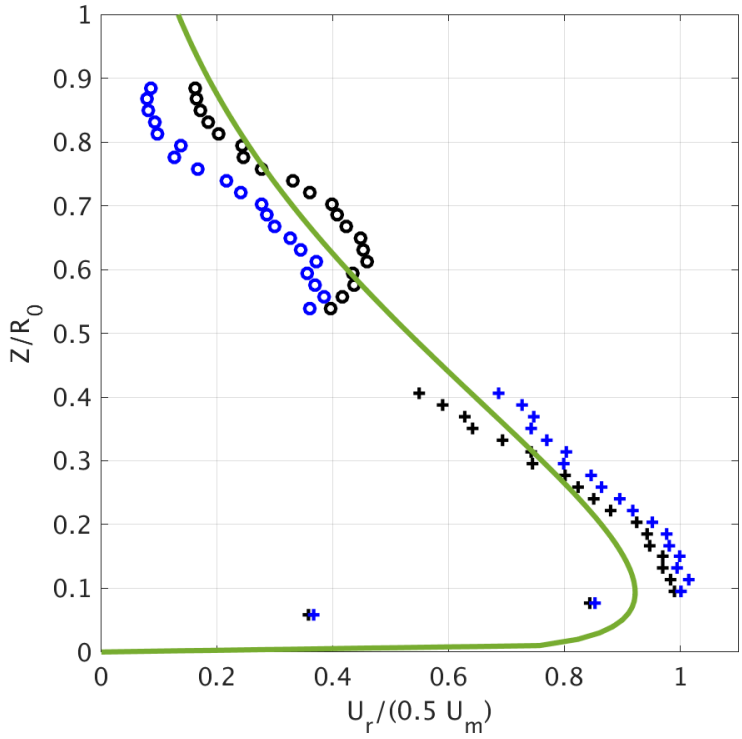


FIGURE 3.32: Time averaged vertical profile of horizontal velocity (m $s^{-1}$). Black denotes vertical profile excluding the identified gust front. Blue denotes vertical profile including the identified gust front. Green shows (3.29) with $C_4 = 1.48$, $n_1 = 1/7$ and $C_5 = 1.2$.

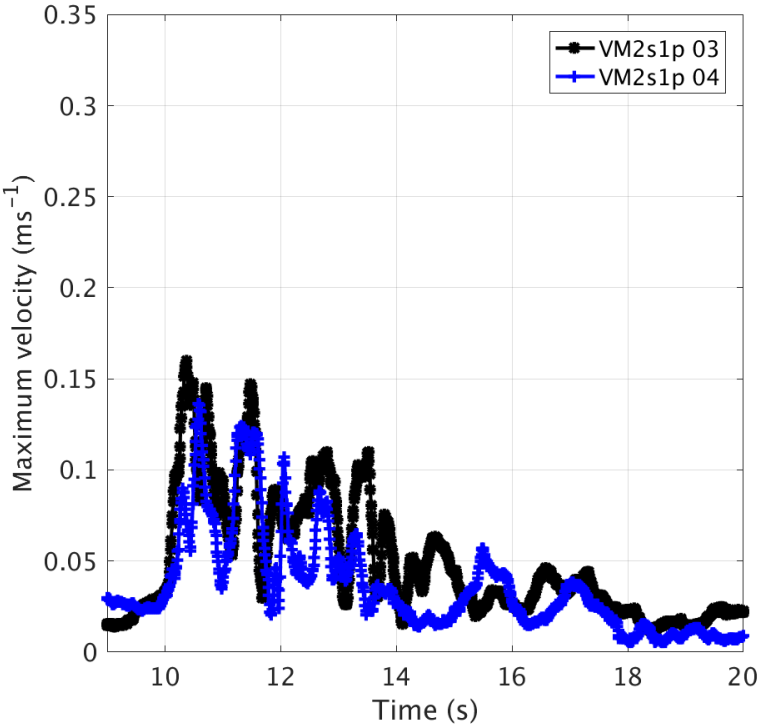


FIGURE 3.33: ADVP time series plot of the maximum horizontal velocity (m s$^{-1}$) across all heights for VM2s1p_03 (black) and VM2s1p_04 (blue). Measured at $r = 270$mm from centre of impingement.

the data, this average does smooth the data somewhat, both removing erroneous spikes but also slightly suppressing the maximums. The averaging was deemed acceptable since the purpose of analysing the data is to develop representative maximum velocities for experimental releases rather than single maximum points which could either be erroneous or random eddy fluctuations. Unfortunately, the time axis should be regarded as somewhat arbitrary, relating to when the ADVP was switched on instead of time after impact.

For two different turbulent events, there is good agreement in the magnitude of velocities seen. For both releases, the maximum velocity occurs at the arrival of the gravity current ($\sim$ 0.15 ms$^{-1}$ at 10 s). This initial maximum is then followed by 3-4 'pulses' of reducing magnitude over 2 s period, the 'pulsing' tendency has been observed by a number of previous studies (Hjelmfelt, 1988; Holmes and Oliver, 2000; Vermeire, Orf, and Savory, 2011). To put the maximum velocity of 0.15 ms$^{-1}$ into the context of the overall event, VM2s1p_03 and VM2s1p_04 hit the surface with a vertical descent speed of 0.1 ms$^{-1}$ (Figure 3.18) and by 270 mm are radially propagating at approximately 0.05 ms$^{-1}$ (Figure 3.21).

Similarly, Figure 3.34 plots the maximum horizontal velocity for two 2% density releases with identical setups, VM2s2p_04 and VM2s2p_05 at the same fixed $r = 270$ mm from centre of impingement. Compared to VM2s2p_03 and VM2s2p_04, there is more variation in the maxima of VM2s2p_04 and VM2s2p_05. VM2s2p_04 observes a peak at 0.3 ms$^{-1}$ compared to 0.2 ms$^{-1}$ for VM2s2p_05. This discrepancy is considered natural variation for two highly turbulent flows, a particularly strong eddy may have occurred just as VM2s2p_04 passed through the measurement location resulting in a higher spike than seen in VM2s2p_05. As previously seen, for VM2s2p_04 the maximum velocity co-insides with the arrival of gravity current, followed by a strong secondary pulse 2 s later. Interestingly, VM2s2p_05 does not have a maximum at the arrival of gravity current but instead roughly 1 s later. Again putting the maximum velocity into the context of the overall event, VM2s2p_04 and VM2s2p_05 hit ground with vertical speed of about 0.15 ms$^{-1}$ (Figure 3.18) and at r=270 mm have a radial propagation speed of 0.1 ms$^{-1}$ (Figure 3.21). As discussed

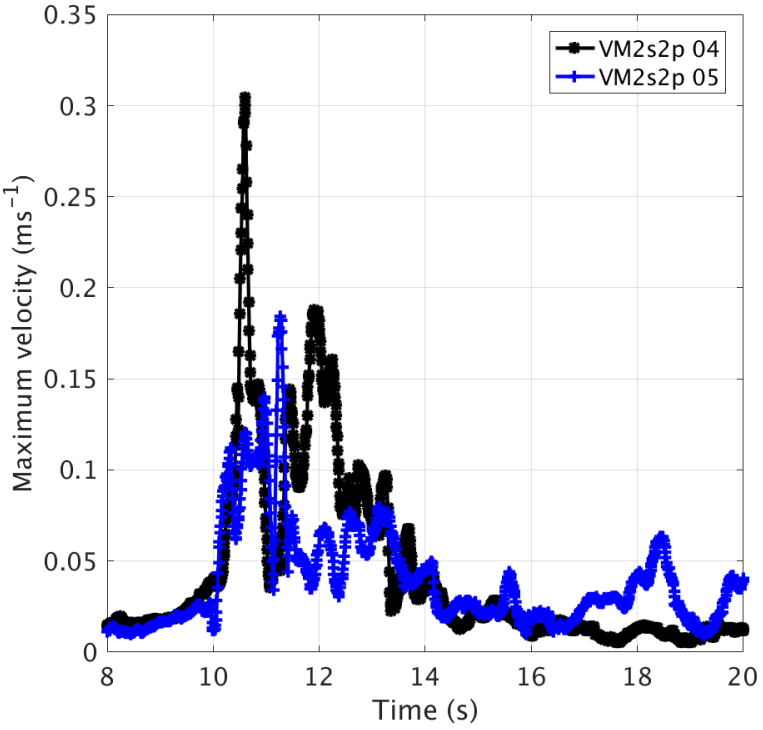


FIGURE 3.34: ADVP time series plot of the maximum horizontal velocity (m s$^{-1}$) for VM2s2p_04 (black) and VM2s2p_05 (blue). Measured at $r = 270$mm from centre of impingement.

in Section 3.3.5 and 3.3.6, the releases with higher density differences (resulting in a greater total buoyancy) both descended and spread faster than those with lower density differences, it is therefore not surprising that the maximum densities also reflect this difference with maximums velocities of 0.15 ms$^{-1}$ for 1% releases VM2s1p_03 and VM2s1p_04 versus 0.2-0.3 ms$^{-1}$ for 2% releases VM2s2p_04 and VM2s2p_05.

One of the aims of this chapter has been to relate bulk fluid properties at source to vertical and horizontal rates of propagation. In Section 3.3.6, experiments verified (3.23) from Rooney (2015) similarity solutions. Is it possible to use similar arguments to relate the maximum velocities from an experimental release to conditions of at the source? Note that (3.23) is only an integration of (2.43), so that the radial propagation speed can be expressed as

$$u_r = Fr_c \lambda^{1/2} B^{1/2} r^{-1}. \tag{3.30}$$

Where Section 3.3.6 found that $Fr_c = 1.19$, and $\lambda = \pi^{-1}$.

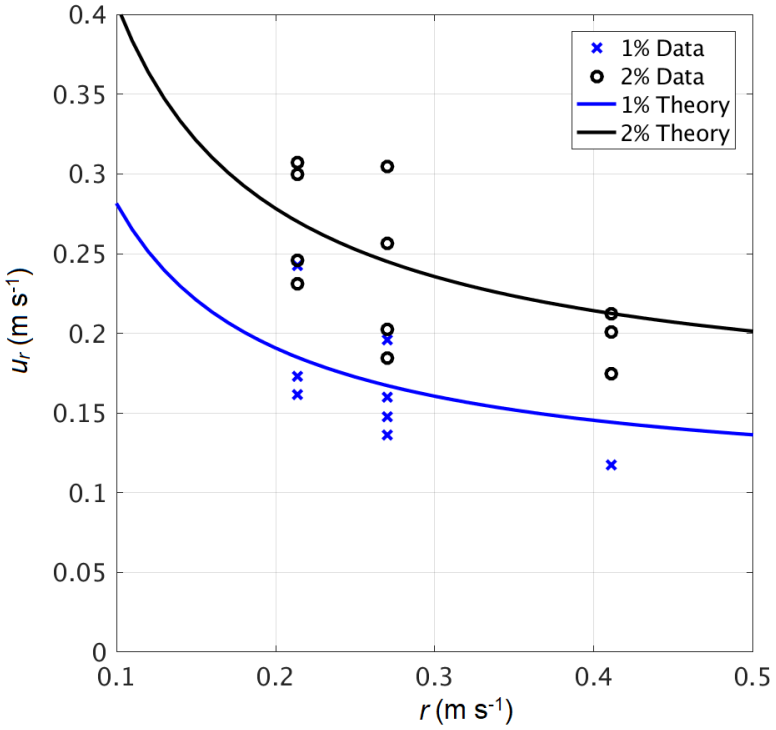


FIGURE 3.35: Plot of maximum velocity (m s$^{-1}$) from all 2s ADVP measurements, VM2s1p 01-08 (blue) and VM2s2p 01-10 (black) taken at 3 radial locations.

This study proposes that the maximum horizontal velocity is only a function of the gravity current velocity, $u_{rmax}$=$f(u_r)$ which from 3.30 is itself only a function of buoyancy and radius. The maximum velocities occur in the head of the gravity current, and the properties of the head of the gravity current are determined by buoyancy and radius of source. It is therefore not unreasonable that there is a simple scaling between maximum velocities and propagation speed. Figure 3.35 plots the maximum horizontal velocity of VM2s1p_01-08 (blue) and VM2s2p_01-10 (black) at the three ADVP measurement locations $r = 214, 270, 411$ mm (see Figure 3.5). As expected for turbulent events, there is a relatively wide spread of maxima. However, there is a general trend that maximum velocities decrease with radial distance and that the releases with greater density differences (2% instead of 1%) have larger maximum velocities. From comparing the maximum velocities to the horizontal propagation speed, a simple empirical relation is proposed,

$$u_{rmax} = ku_r = kFr_c\lambda^{1/2}B^{1/2}r^{-1}. \tag{3.31}$$

where from experiments $k = 3$ is seen to fit.

## 3.4 Summary

As part of an MSc project, laboratory experiments designed to simulate atmospheric downbursts, were conducted by releasing a volume of excess density fluid into a tank of water. The study focused on the descent, impact onto a horizontal surface and subsequent radial spread of the heavier fluid. Video camera footage was used to track vertical and horizontal propagation. Instantaneous velocities at the source and in the radial gravity current were measured by Ultrasonic (UDVPs) and Acoustic (ADVPs) Doppler Velocity Profilers. Apart from the previous work by Kreczak (2015), which is specifically cited, analysis of those experimental results has been conducted as part of this PhD and is presented in this chapter.

There were three aims to this experimental chapter:

1. Analyse the data from laboratory saline releases of momentum driven negatively buoyant fluid designed to simulate atmospheric downbursts.

2. Determine the properties of the descending saline release and resulting radial gravity current from the properties of an experimental set-up at the source.

3. Determine the structure of the radial gravity current, specifically the vertical profile of the horizontal wind and the associated wind maxima.

Flow visualisation indicated that Aim 1. was partially met, experimental releases contained all of the salient features of an atmospheric downburst as identified by previous studies ((Lundgren, Yao, and Mansour, 1992; Hjelmfelt, 1988; Vermeire, Orf, and Savory, 2011)). Specifically, i) as dense fluid is released, a vortex ring formed, ii) the dense fluid propagates vertically downwards, steadily growing in width, iii) upon impact, the vortex ring 'billows' up and begins to propagate radially forming a gravity current. Experimental releases were sub-divided into two extremes of transport of buoyant fluid - an instantaneous thermal and quasi-steady plume.

In order to achieve Aim 2, and determine the properties of the resulting gravity

current, the behaviour of the vertical descent of the saline release had to be first understood. Analysis of highspeed camera footage found in the vertical descent stage:

- Entrainment was constant. Comparing the horizontal radius of saline experiment with height showed constant entrainment $\alpha = 0.3$, between experiments. There was minimal difference in width between 2 s and 5 s saline releases. $\alpha = 0.3$ is reasonable for buoyancy driven thermals (Turner, 1979; Lundgren, Yao, and Mansour, 1992).

- Experimental releases were shown to have reasonably reproducible rates of vertical descent. The results were non-dimensionalised by a scaling proposed by Lundgren, Yao, and Mansour (1992), where $R_0$ is pipe outlet and $t_0 = (R_c/g_0')^{1/2}$. This scaling worked well, propagation rates of experiments with different density releases collapsed onto one line.

- The formation of the vortex ring was identified as the determining mechanism for the rate of vertical descent. Experiments with release times greater than their theoretical vortex formation time, had the same rate of vertical descent.

- Vertical descent of experiments was in good agreement with thermal similarity solutions described by Turner (1962) and modified by Rooney (2015) to be,

$$z + z_v = \left(2Fr\, m^{-1/2}\alpha^{-1}B^{1/2}t\right)^{1/2}.$$

  where the virtual origin is defined as $z_v = \alpha^{-1}b_0$. This study did not consider the work of Hunt and Kaye (2001) or Ciriello and Hunt (2020) who suggest different solutions for the virtual origin for constant and variable rates of entrainment respectively. An interesting extension of this work would be to determine the sensitivity of the similarity solution to the formulation of the virtual origin.

- Since this theory was developed for quasi-spherical thermals, this study proposed a simple adaptation for vertical descent rate of longer saline releases. Instead of using the total buoyancy $B$, only the buoyancy in the vortex ring $B_v$ is used. This adaptation provided a better, although still imperfect fit to the experimental results.

- A caveat of the matching of vertical theory with experiments is that the shape of the vertical descent rate was different. Theory suggests a $r \propto kt^{1/2}$ relationship whilst the experimental results were behaved more like $r \propto kt^{n}$ where $n = 0.75 - 0.9$. This discrepancy was attributed to i) measurement error, ii) insufficient time for experiments to reach their theoretical propagation before impacting the surface. For 1% density experiments, $t_F \approx 3.5$ s and for 2% density experiments, $t_F = 2.5$ s, which was similar for the time required for impingement.

Utilising the above findings from the vertical descent of negatively buoyant fluid, the radial propagation of the subsequent gravity current was examined. This study found that:

- Experiments had reproducible propagation rates, particularly when adjusted by the radius of impact. Larger volumetric releases resulted in faster rates of propagation.

- The similarity solution, developed by Rooney (2015) for the spread of negatively buoyant fluid,

$$r = (2Fr_c)^{1/2}\lambda^{1/4}B^{1/4}(t - t_i)^{1/2} + R_0,$$

  was validated by the experiments subject to several adaptations. Supporting previous experimental gravity current experiments by Hallworth et al. (1996), $Fr$ and $\lambda$ were changed from 1.4 and 1.0 to 1.19 and $\pi^{-1}$. Experimental releases were not quasi-spherical in origin, therefore $R_0$ was taken as the radius at impact $R_0 = b_0 + \alpha H$, instead of the radius of the quasi-spherical volume of fluid.

- The scaling of Lundgren, Yao, and Mansour (1992) depends on the reduced gravity rather than total buoyancy and did not scale the results in the radial propagation. Instead results scaled by total buoyancy, $t_0 \sim R_0^2/B_0^{1/2}$. This scaling was used to compare experiments to Rooney (2015) LES simulations, with good agreement of shape. However, the magnitude of the results differed

by a factor of 20. This difference in magnitude is attributed to fundamental differences in saline laboratory experiments and numerical simulations.

By using adaptations of similarity solutions developed by Rooney (2015), which combine the vertical descent of negatively buoyant thermals with the radial spread axisymmetric gravity currents from fixed volumetric releases, Aim 2. has been achieved; the propagation rate of an experimental release with known pipe outlet, buoyancy and release time can be determined.

In addition to focusing on the bulk fluid properties, attention was given to the instantaneous velocities that occurred in the head of the gravity current, analogous to an atmospheric gust front. Analysis of UDVP and ADVP measurements found that:

- Strong circulation was identified in the head of the gravity current.
- Secondary pulses following the head of the gravity current were observed, containing velocities close to the maximum.
- In shorter experimental releases most significant velocities were confined to the head of the gravity current, in longer releases a secondary flow, elevated at $z/R_0 = 0.3$ was observed.
- The vertical profile of the horizontal velocity was compared with an empirical profile developed by previous experimental and numerical studies (Wood et al., 2001; Sengupta and Sarkar, 2008), where

$$\frac{u}{u_m} = C_4 \left(\frac{z}{n}\right)_1^n \left[1 - \text{erf}\left(C_5 \frac{z}{b}\right)\right].$$

  This study's experiments were found to fit well with this empirical profile (Figure 3.32). However, $C_2$ was found to be 0.55 instead of 1.2.
- The maximum velocity at a given radial location, always occurs within the head of the gravity current.
- This study proposes that the maximum horizontal velocity is simply a function of the gravity current propagation speed $u_{rmax} = f(u_r)$, where the gravity

current propagation speed is itself only a function of buoyancy and radius of pipe outlet. A simple relation is suggested,

$$u_{rmax} = ku_r = kFr_c\lambda^{1/2}B^{1/2}r^{-1}$$

where from experiments $k = 3$. Figure 3.35 supports this relation for the maximum velocities in the gravity current.

The three aims of this chapter have been broadly met. A study of the descent and spread of experimental saline releases has provided both validation of existing theory and insight into new behaviour. Hopefully, these findings can be adapted from the laboratory to help provide a better understanding of atmospheric downdraughts.

# Chapter 4

# Numerical simulation of downdraughts: model sensitivity in MONC

## 4.1 Introduction

The remainder of this thesis is concerned with the numerical simulation of downdraughts. Using numerical simulations has several advantages over laboratory experiments; i) the information available in numerical simulations is more extensive than can be gathered using instrumentation in the laboratory, numerical simulations provide full 3D fields, written out at a frequency specified by the user, ii) using numerical simulations, the parameter range of experiments is far greater. Radius, height and buoyancy differences are not limited by the diameter of available pipes, density of saline or size of tank, but instead can be freely altered. However, any numerical model is only as useful as the confidence one has in it. It is difficult to achieve complete confidence in ones numerical set-up and properly achieving grid independence. If domains and grid resolutions are two small/low then the numerical model risks failing to resolve the dynamics system properly. Additionally, numerical errors may create artificial behaviour that either mask or superimposes upon the actual dynamical behaviour of the system.

This chapter presents the methodology used to set-up Large Eddy Simulations (LES),

designed to investigate the descent and near-surface evolution of idealised downdraughts. This study takes advantage of the new Met Office and NERC Collaboration (MONC Beta version) LES model, based on the well established Met Office Large Eddy Model (LEM), but completely re-written to utilise the present and future developments in high performance computing. However, the novelty of this model presents a problem; MONC has not previously been used for many idealised studies, and therefore it is not clear what resolution and settings can be used. Significant time was undertaken to establish the sensitivities of MONC set-up and grid parameters. The aim of this chapter is to perform a sensitivity study in order to determine an appropriate model set-up for further investigation into the descent and near-surface evolution of atmospheric downdraughts. This set-up will then be used for Chapters 5 and 6.

Downdraughts and downbursts have been studied numerically before. In almost all global numerical weather prediction models, downdraughts are parameterized as part of atmospheric convection (see Jun-ichi (2015) for a good summary). However, in order to understand the complex descent and evolution of downdraughts, a numerical model is needed that explicitly resolves the downdraught. Some numerical studies attempt to create atmospheric conditions favourable for the formation of strong downdraughts, using high-resolution cloud models and microphysics schemes (Proctor, 1988; Orf, Anderson, and Straka, 1996; Orf, Kantor, and Savory, 2012). Whilst, using realistic cloud models is perhaps the best approach for simulating a downdraught as observed in nature, it is hard to construct a comprehensive and reproducible set of model runs that systematically cover specific parameter regimes. Instead many other studies adopt the approach of imposing the downdraught or downburst artificially using either i) an impinging jet or ii) a cold source. There is a significant body of engineering literature that conducts Reynolds Averaged Navier-Stokes (RANS) CFD simulations of downbursts and microbursts. Typically, those that use a velocity-inlet as the source of the downdraught, have an emphasis on downburst loading of infrastructure (Chay, Albermani, and Wilson, 2006; Mason, Letchford, and James, 2005; Sengupta and Sarkar, 2008; Kim and Hangan, 2007; Abd-Elaal, Mills, and Ma, 2013; Aboshosha, Bitsuamlak, and El Damatty,

2015).

The limitation with velocity-inlet based studies, is there inability to model the buoyancy based aspects of downdraught evolution. Vermeire, Orf, and Savory (2011) use their LES to directly compare velocity-inlet models to cooling source models and concluded that the impinging jet model is not capable of capturing the outflow features predicted by the cooling source model, and therefore is unable to capture the physics of an actual downburst event. Therefore, this study will use a cooling source instead of an impinging jet.

LES is a type of computational fluid dynamics (CFD) for simulating turbulent flows. LES separates the velocity field into two parts: i) resolved and ii) sub-grid. The large scale eddies in the resolved part are then explicitly solved using the Navier-Stokes equations, whilst the small scale scale eddies are parameterized by a sub-grid scheme, reducing the computational cost. Table 4.1 details the previous LES studies that have been made on downdraughts, downbursts or cold pools that use either an instantaneous or constant cooling of a region to simulate the event. Bryan and Fritsch (2002) suggest their instantaneous release of a cold bubble as a benchmark for nonhydrostatic numerical models (the properties listed in Table 4.1 are for their dry thermal case). Rooney (2015) has already been introduced in Chapter 3 and has tested their similarity solutions for the descent and spread of negatively buoyant thermals against cold bubble numerical runs. Anabor et al. (2011) constantly cools a region of the domain to create a microburst like outflow, they only present one case. Lastly, Romps and Jeevanjee (2016) represents a cold pool outflow but instead of a bubble, a cold cylinder is released at the surface. This study now outlines a methodology for modelling idealised atmospheric downdraughts, conducted to the author's best knowledge, at the finest resolution ($\Delta x = 25$m, $\Delta z = 10$ m), over one of the largest domains ($X = 25.6$ km, $Z = 4$km), using a grid of $N = 5.37$e8 points.

TABLE 4.1: Previous LES Cooling Source Studies. $\Delta x$ and $\Delta z$ are the horizontal and vertical model resolution. $X$ and $Z$ are the horizontal and vertical model domain. $b_0$ and $h_0$ are the initial or fixed width and height of cold source.

| **Study** | $\Delta x$ **(m)** | $\Delta z$ **(m)** | **X (km)** | **Z (km)** | $b_0$ **(km)** | $h_0$ **(km)** | **Cold Source** |
|---|---|---|---|---|---|---|---|
| Bryan (2002) | 100 | 100 | 20 | 10 | 2.0 | 2.0 | Bubble |
| Anabor (2011) | 80 | 15.6 | 10 | 2.0 | 2.0 | 1.8 | Cooled region |
| Rooney (2015) | 50 | 50 | 25.6 | 12 | 0.238-0.756 | 3.0-12 | Bubble |
| Romps (2016) | 50 | 10-50 | 38.4 | 3.0 | 1.0 | 1.0 | Cylinder |
| This Study | 10-25 | 4-8 | 25.6 | 4.0 | 0.3-0.7 | 3.0 | Bubble |

## 4.2 Met Office and NERC Collaboration Model

Large Eddy Simulation is a computational fluid dynamics technique used to study turbulent flows. Eddies (large scale turbulent motions) are explicitly resolved, while small scale motions are parametrized by a sub-grid scheme. The Met Office and NERC Cloud (MONC) model is a newly developed large eddy simulation model, based on a complete re-write of the well established Met Office Large Eddy Model (LEM). The LEM is the principle LES used by the Met Office and academia within the UK, and whilst the science underpinning the LEM is consistently updated, the code from the 1980s has become outdated (Brown et al., 2015). MONC uses the same trusted science as the LEM, but has been re-written with modern software engineering and parallelisation techniques, that take advantage of current and future developments in high performance computing (HPC). Consequentially, it is now possible to conduct simulations in MONC at resolutions previously impossible to achieve in the LEM.

MONC solves a Boussinesq-type equation set,

$$\frac{Du_i}{Dt} = -\frac{\partial}{\partial x_i}\left(\frac{p'}{\rho_s}\right) + \delta_{i3}B' + \frac{1}{\rho_s}\frac{\partial \tau_{ij}}{\partial x_j} - 2\epsilon_{ijk}\Omega_* j u_k \tag{4.1a}$$

$$\frac{\partial}{\partial x_i}(\rho_s u_i) = 0 \tag{4.1b}$$

$$\frac{D\theta}{Dt} = \frac{1}{\rho_s}\frac{\partial h_i^\theta}{\partial x_i} + \left(\frac{\partial \theta}{\partial t}\right)_{mphys} + \left(\frac{\partial \theta}{\partial t}\right)_{rad} \tag{4.1c}$$

$$\frac{D\hat{q}_n}{Dt} = \frac{1}{\rho_s}\frac{\partial h_i^{\hat{q}_n}}{\partial x_i} - \left(\frac{\partial \hat{q}_n}{\partial t}\right)_{mphys} \tag{4.1d}$$

| | |
|---|---|
| $\chi_s$ | denotes a reference state of $\chi$ |
| $\chi'$ | denotes a perturbation from reference state of $\chi$ |
| $\mathbf{u}$ | is vector flow velocity |
| $\theta$ | is potential temperature |
| $\hat{q}_n$ | is all other scalar variables |
| $p$ | is pressure |
| $\rho$ | is density |
| $B'$ | is buoyancy |
| $\tau$ | is subgrid stress |
| $h^\theta$ | is subgrid scalar flux of $\theta$ |
| $h^{\hat{q}_n}$ | is subgrid scalar flux of $\hat{q}_n$ |
| $\omega_{i3}$ | is the Kroneker delta function |
| $\Omega_*$ | is Earth's angular velocity |
| $\epsilon_{ijk}$ | is the alternating pseudo-tensor |
| $\left(\frac{\partial\theta}{\partial t}\right)_{mphys}$ | is source term of $\theta$ due to microphysics |
| $\left(\frac{\partial\theta}{\partial t}\right)_{rad}$ | is source term of $\theta$ due to radiation |
| $\left(\frac{\partial q_n}{\partial t}\right)_{mphys}$ | is source term of $\hat{q}_n$ due to microphsyics |

TABLE 4.2: List of MONC variables

as described in Gray et al. (2001b). The mean reference state is defined by $\rho_s$, $\theta_s$ and $p_s$, and perturbations from this state (denoted by prime superscript) are assumed to be small. The buoyancy is given by $B' = g\theta'_v/\theta_s$ where $\theta'_v$ is the virtual potential temperature. MONC uses an adaptation of the Smagoringsky-Lilly approach for subgrid component. The classical Smagoringsky-Lilly subgrid approach sets the subgrid eddy-viscosity $\nu$ as

$$\nu = \hat{\lambda}_0^2 S, \tag{4.2}$$

where $\hat{\lambda}_0$ is the basic mixing length and $S$ is the modulus of the rate of strain tensor $S_{ij}$,

$$S = \frac{1}{\sqrt{2}}||S_{ij}|| = \left(\frac{1}{2}\sum_{i,j=1,3} S_{ij}^2\right)^{1/2}. \tag{4.3}$$

MONC uses an extension of (4.2) which also uses the Richardson number and a length scale $\hat{\lambda}$. Here, $\hat{\lambda}$ is dependent on both the basic mixing length $\hat{\lambda}_0 = C_s\Delta x$ where $C_s = 0.23$ is the Smagorinsky coefficient and $\Delta x$ is the horizontal grid spacing. $k = 0.4$ is the von Karman constant, and $z_0$ is the surface roughness,

$$\frac{1}{\hat{\lambda}^2} = \frac{1}{\hat{\lambda}_0^2} + \frac{1}{[k(z+z_0)]^2}. \tag{4.4}$$

When $z$ is large (far from the surface) $\hat{\lambda} = \hat{\lambda}_0$, but close to the surface the length scale becomes a function of distance from the surface, providing a smooth transition from surface to the main body of the fluid (Gray et al., 2001b). The resulting eddy viscosity and diffusivity are then,

$$\nu = \hat{\lambda}^2 S f_m(R_{i_p}) \tag{4.5a}$$

$$\nu_h = \hat{\lambda}^2 S f_h(R_{i_p}), \tag{4.5b}$$

where $Ri_p = (1/S^2)\partial B'/\partial z$ is the local Richardson number and $f_m$ and $f_h$ are Richardson number dependent functions. This is the standard subgrid mixing set-up for both the LEM and MONC, for further details see Mason (1989) and Gray et al. (2001b). The momentum equations are solved using a centred-difference (PW) method from Piacsek and Williams (1970). The potential temperature equation is solved using a total variation diminishing (TVD) method from Leonard, MacVean, and Lock (1993). The Poisson equation for pressure is solved using a fast Fourier transform. MONC is used in Boussinesq mode. This choice of numerical set-up is keeping with previous LES studies on the atmospheric boundary layer and the transport of buoyant fluid (Mason, 1989; Devenish, Rooney, and Thomson, 2010; Rooney, 2015).

The timestep of the numerical simulations needs to be carefully considered to ensure the stability of the simulation. MONC uses a variable time step and the user can chose a minimum CFL condition to prevent computational instability. Both advective and viscous terms independently place constraints on the time step. Across the entire grid, the model is constrained by the behaviour of the 'worst' individual grid point. In MONC the CFL number is calculated from

$$CFL = \frac{CVIS}{CVIS_{max}} + \frac{CVEL}{CVEL_{max}} \tag{4.6}$$

where $CVEL$ is the largest advective Courant number

$$CVEL = \Delta t \left( \left( \frac{|u|}{\Delta x} \right)_{max} + \left( \frac{|v|}{\Delta y} \right)_{max} + \left( \frac{|w|}{\Delta z} \right)_{max} \right) \tag{4.7}$$

and $CVIS$ is the worst case viscous stability parameter

$$CVIS = \max\left[4\Delta t \nu_{max}\left(\frac{1}{\Delta x^2}\right) + \left(\frac{1}{\Delta y^2}\right) + \left(\frac{1}{\Delta z^2}\right)\right]. \tag{4.8}$$

The model timestep is set so that $CFL = 1$, subject to a user specified acceptable timestep minimum and rate of timestep increase (see Gray et al. (2001b), for more information).

Backscatter is an extension to the subgrid model, commonly used in MONC. Backscatter, 'scatters' back a portion of the energy dissipated by the model into the resolved fields. In regions of poor resolution or close to the surface, the subgrid fluxes of momentum and scalars may not be properly determined by the resolved fields. The viscous drain of the model, that is the energy dissipated by the model each timestep, is

$$\epsilon = S^2(\nu - \nu_h Ri_p). \tag{4.9}$$

The addition of backscatter reduces (4.9) to

$$\epsilon = \frac{S^2(\nu - \nu_h Ri_p)}{1 + C_b}, \tag{4.10}$$

where $C_b$ is

$$C_b = C\left(\frac{\hat{\lambda}_r}{\hat{\lambda}_0}\right)^5. \tag{4.11}$$

$\hat{\lambda}$ is the length scale defined in (4.4) and $\hat{\lambda}_0$ is the basic mixing length. $C$ is a constant of 1.4 for velocity fields and 0.45 for scalars. More information on backscatter can be found in Mason and Thomson (1992), Brown, Derbyshire, and Mason (1994), and Gray et al. (2001a).

### 4.2.1 Initial Configuration

Numerical experiments are conducted in a three dimensional box filled with a Cartesian grid of $N_x \times N_y \times N_z$ grid points in $(x, y, z)$, where the Boussinesq equation set (4.1) is solved at each grid point for every model time step. In all simulations, the length and width of domain was 12.8 km and the height of domain was 4 km. The

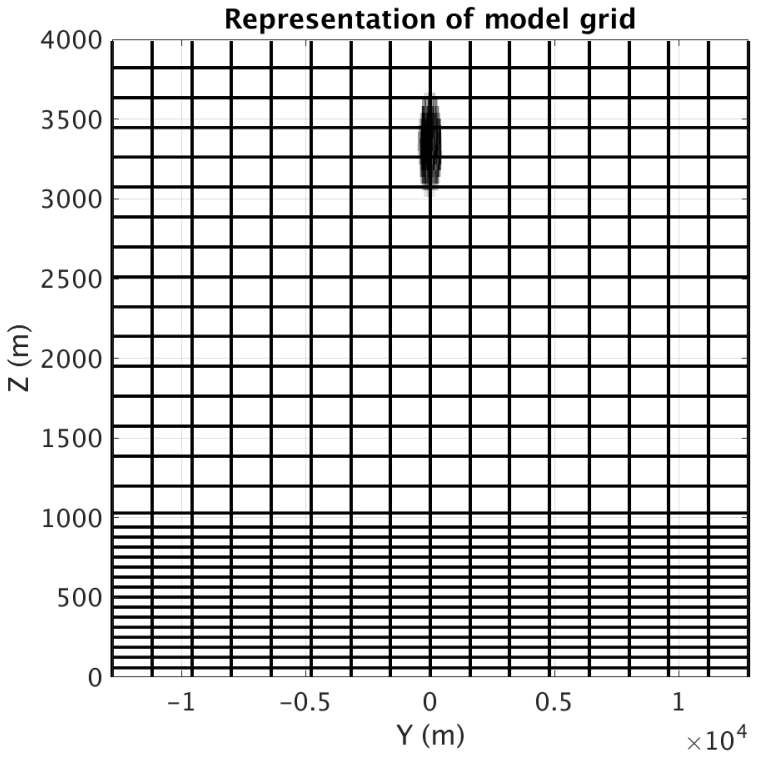


FIGURE 4.1: Representation of a typical grid set-up, with horizontal domain of -12.8 to 12.8 km and vertical domain of 0 to 4.0 km. Horizontal lines are plotted every 8th Z grid point (variable vertical resolution), vertical lines are plotted for every 64th Y grid point (horizontal resolution 25m).

horizontal grid spacing is fixed, while the vertical grid spacing linearly increases from 0 to 1000 m, before being fixed from 1000 to 4000 m (the top of the domain). A representative grid for a typical cold bubble release is shown in 4.1. The version of MONC used (Beta) for this study, does not allow for horizontal grid refinement i.e. the horizontal spacing is fixed. The necessary vertical and horizontal grid resolutions for mesh sensitivity are determined in Section 4.2.3. A background potential temperature of 300 K was applied to the entire domain, similarly the surface was given a temperature of 300 K, a pressure of 1000 hPa and surface fluxes were switched off.

Periodic boundary conditions are imposed on the lateral boundaries, while the bottom and top boundaries are given no-slip and free-slip boundary respectively. The imposition of periodic boundaries required the size of the domain is large enough to

prevent one side of the model from influencing the other. The size of domain was estimated by assuming that thermals would propagate at approximately $r = k_r B t^{1/2}$, where $k_r = 2.6$ is determined from Chapter 3. It was determined that the thermal fastest travelling thermal should take >5000s to reach the domain boundaries (results were only analysed for <3000s), which should prevent any influence of the domain. Internal gravity waves triggered by the thermal travel much faster than the buoyant fluid. However, in an ambient background fluid, it was decided that the influence of those waves would be small. The resolution of domain are determined in the grid sensitivity study, detailed in Section 4.2.3. The roughness length $z_0$ was set to $2.0 \times 10^{-4}$ m. Rooney (2015) tested the sensitivity of the Smagorinksky coefficient and roughness length to their model results in the LEM and found little dependence. Given the scale of the numerical experiments is limited to <20 km, the Coriolis force was deemed unimportant and is switched off.

MONC allows for complex microphysics and radiation schemes, however in order to both limit computation expense and study the simplest model of buoyant transport, all experiments in this chapter are conducted with these schemes switched off. Instead of creating a downdraught through microphysical processes, a downdraught is initiated by applying constant cooling to a spherical region of the domain. Cooling was applied with the function,

$$\hat{Q}(x,y,z,t) = \begin{cases} \hat{g}(t), & \kappa \leq (1-\hat{\phi}), \\ \hat{g}(t)\cos\frac{\pi}{2}\frac{\kappa-(1-\hat{\phi})}{\hat{\phi}}, & (1-\hat{\hat{\phi}}) < \kappa \leq 1, \end{cases} \tag{4.12}$$

where $b_0\kappa$ is the distance from the centre of the spherical region and $\hat{\phi} = 0.25$ is the proportion of edge region of sphere where the relatively cold fluid is blended with the ambient background temperature. The rate of cooling $\hat{g}(t)$ could be modified to represent different extremes of buoyant fluid release. For an instantaneous release of negative buoyancy (equivalent to a bubble of fluid released at $t = 0$),

$$\hat{g}(t) = \begin{cases} \Delta\theta', & t = 0, \\ 0 & t > 0, \end{cases} \tag{4.13}$$

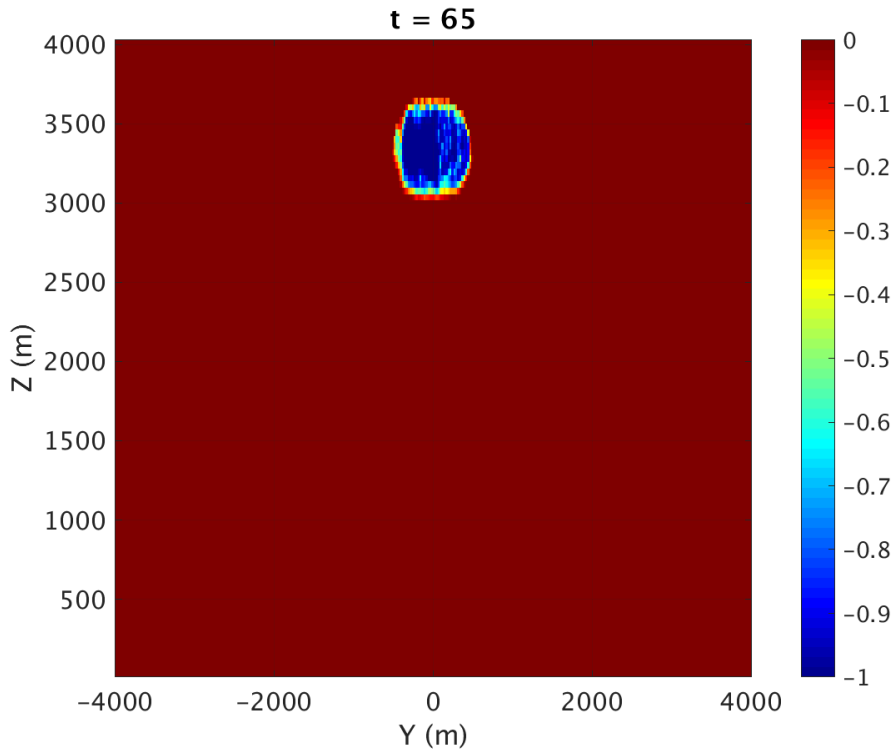


FIGURE 4.2: Potential temperature (K) contour plot for a typical instantaneous release at t = 65 s. The colour bar is from 0 K potential temperature perturbation (red) to -1 K (blue)

where $\Delta\theta$ is a negative temperature perturbation.

Following Rooney (2015), after the cooling is initially applied to the spherical region, random points within the cooling sphere's interior have their potential temperature perturbations swapped. This randomisation has the effect of bringing some reduced buoyancy points from the edge of the sphere, into the centre and therefore breaking the flow symmetry. Although somewhat artificial, this randomisation was decided upon in an attempt to make the numerical simulations more analogous to an atmospheric downburst. An example of a typical initial set-up is shown in Figure 4.2. In this example, the cooling is applied instantaneously as a temperature perturbation of -1 K. The cooled region is then allowed to fall freely and develop according to its own properties.

### 4.2.2 Tracking of Negatively Buoyant Fluid

The simulated downdraught is identified at all stages of descent and spread by its negative temperature perturbation. The only source of cooling in the entire model, is the spherical source that creates the downdraught. It is therefore assumed that all negative temperature perturbations are associated with the passage of the downdraught from either the initial body of the fluid or subsequent mixing and entrainment. One might be tempted to then identify the downdraught as comprising of all grid points with a negative temperature perturbation, however, there are two problems with this approach. Firstly, the role of numerical diffusion means that small temperature perturbations are diffused are at an artificial rate, at a scale that is insignificant to this problem. Secondly, this study is primarily interested in the bulk properties of the downdraught and less so in the motions of small scale eddies that spin off the main buoyant core. Therefore, it becomes useful to introduce a threshold of temperature perturbation that will be used to identify negatively buoyant fluid,

$$|\Delta\theta - \Delta\theta_{max}| < \Omega\Delta\theta_{max}, \tag{4.14}$$

where $\Delta\theta$ is the temperature perturbation at a given grid point, $\Delta\theta_{max}$ is the maximum absolute value of the temperature perturbation across the whole 3D field and $\Omega$ is the threshold value at each model output time. Volumes where the condition (4.14) is met, are considered to be negatively buoyant fluid forming the downdraught.

Over the duration of a simulation, $\Delta\theta_{max}$ reduces as relatively warm fluid is entrained into the core of the downdraught. Figure 4.3 plots the development of the minimum temperature perturbation for an instantaneous release with initial temperature perturbation of -1 K. Note that the minimum temperature perturbation is equivalent to the maximum absolute temperature $\Delta\theta_{max}$ and henceforth the results will be discussed in terms of absolute values. Over 2000s, $\Delta\theta_{max}$ reduces around 85% from 1 K to 0.15 K, with the sharpest gradient between 500 and 1500 s. Therefore instead of having one global $\Delta\theta_{max}$ across the entire model run, $\Delta\theta_{max}$ is calculated for each diagnostic time dump and then applied to that 3D field for that specific time.

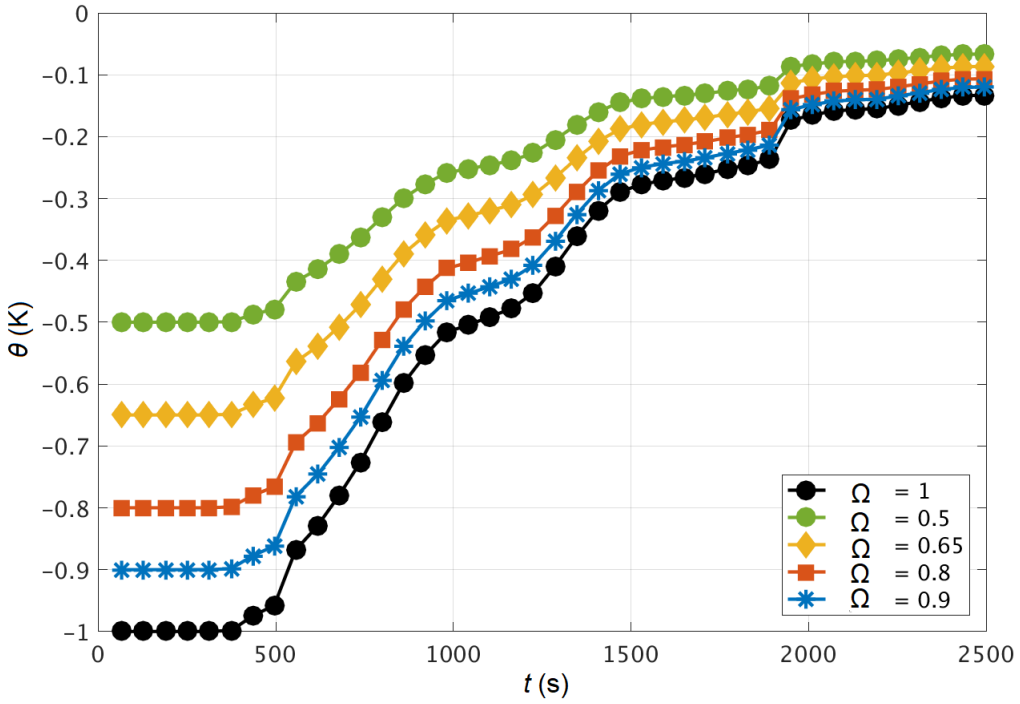


FIGURE 4.3: Time (s) versus minimum temperature perturbation (K) for an instantaneous release with initial temperature perturbation of -1 K for different values of Ω. Model run: Gx25z20.

This allows the threshold condition to dynamically change as the downdraught entrains and becomes closer to the ambient background temperature. The value of Ω determines what proportion of $\Delta\theta$ is identified as being part of the downdraught. A value of 0.5 means that $\Delta\theta$ within 50% of $\Delta\theta_{max}$ is identified, while a value of 0.8 means $\Delta\theta$ within 20% of $\Delta\theta_{max}$ is identified. Figure 4.4 illustrates how the number of identified buoyant points varies with time for different threshold values. Obviously the value of Ω has repercussions on the subsequent results, Ω is determined as part of the grid sensitivity study in Section 4.2.3 and subsequently taken as $\Omega = 0.8$. This methodology for identifying negatively buoyant fluid and the value of Ω is consistent with Devenish, Rooney, and Thomson (2010) and Rooney (2015).

After developing a condition to identify the downdraught, it is now possible to develop post-processing tools to extract key diagnostics such as the rate of vertical descent, rate of radial propagation and kinetic energy of the downdraught.

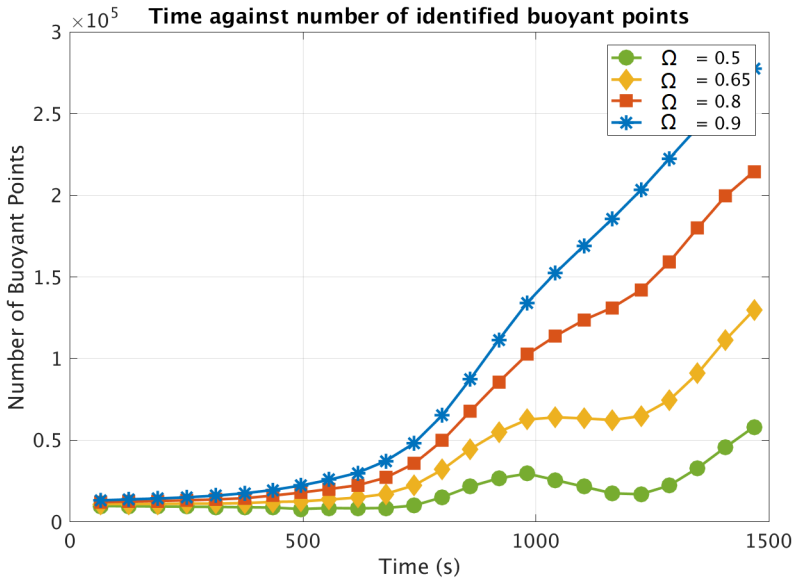


FIGURE 4.4: Time (s) versus number of identified buoyant points. Buoyant points are identified by condition (4.14).

### Tracking Vertical Descent

Tracking the rate of vertical descent is done using the 3D $\Delta\theta$ fields and condition (4.14). A typical 500s of numerical simulation creates a diagnostic file of over 60GB, this amount of data is computationally expensive therefore the diagnostic file was sliced using netCDF Kitchen Sink (`ncks`) to extract only a central volume of the grid. For all runs, this volume $V = X \times Y \times Z$ where $X$ and $Y$ were 8 times the initial radius of cooling sphere $8R_i$ and $Z$ was the entire height of the domain. For example, a typical experimental run with initial cooling sphere $R_i = 500$ m, centred at a height of 3000 m, the extracted grid would be $X, Y = -2000 < x \leq 2000$ and $Z = 0 < z \leq 4000$.

Rate of vertical descent is determined by applying condition (4.14) to the 3D $\Delta\theta$ fields over the entire extracted grid. Grid points across the extracted grid are given a value of 1 if they meet this condition or 0 if not. Starting at the surface (z = 0), the extracted grid is then looped over z. A sum of all identified buoyant points is taken for each z plane, until an area fraction $A_f = A^* N_x^2$ is exceeded, vertical propagation

$Z_p$ is then determined by

$$Z_p(t) = \begin{cases} NaN & \sum N_B < A^* N_x^2, \\ Z_p & \sum N_B \geq A^* N_x^2, \end{cases} \tag{4.15}$$

where $A^*$ is a percentage area, $N_B$ is the total number of identified buoyant points (each individual buoyant point has a value 1), $N_x$ is the number of $x, y$ grid points ($N_x = N_y$).

Vertical descents, calculated with different values of $\Omega$ and $A^*$ are plotted in Figure 4.5 for a control run Gx25z20 (see Table 4.3). Figure 4.5a shows only slight differences in vertical descent for 4 values of $\Omega$ between 0.5 and 0.9. Between 600 and 850 s, more pronounced differences develop, although still small in size. Figure 4.6 plots potential temperature contours for Gx25z20, the identified outline of the downdraught is superimposed. These contour plots reflect the trends seen in Figure 4.5a. In the early stages of descent, the downdraught falls as one discrete object (Fig. 4.6a,b) making it easier to track. However, closer to the surface, this particular model run splits (Fig. 4.6c). The splitting of the downdraught makes determining the vertical propagation more sensitive to the value of $\Omega$. Figure 4.5b plots vertical descent for 4 different area fractions $A^*$ between 1.0e-5% and 1.0e-4%, this is equivalent to between 1 and 105 grid points being identified as negatively buoyant on a $1028 \times 1028$ grid. The value of $A^*$ makes only a slight difference to the vertical descent. In the early stages, vertical descent is almost identical. Similarly, between 600 to 900 slight differences occur, where as expected the smallest area fraction predicts the greatest vertical descent. Encouragingly, identifying the vertical descent is not sensitive to $\Omega$ or $A^*$.

**Tracking Radial Propagation**

This methodology defines radial propagation as the outer leading edge of the downdraught or buoyant fluid. Tracking of radial propagation follows a similar methodology to that of vertical descent. The 3D $\Delta\theta$ fields and condition (4.14) are used to analyse an extracted region of the grid. For all runs, this volume $V = X \times Y \times Z$

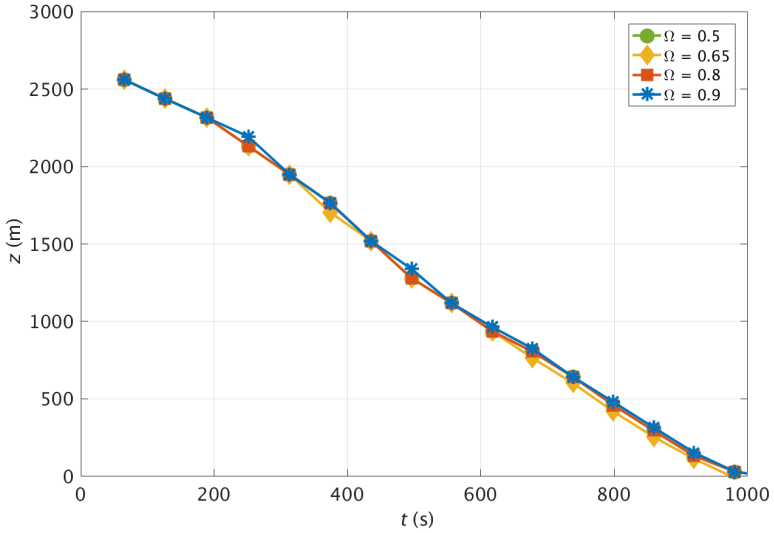


(A) Vertical descent (m) calculated using 4 different values of $\Omega$ in condition (4.14). $A^* = 5.0e-5\%$ for all.

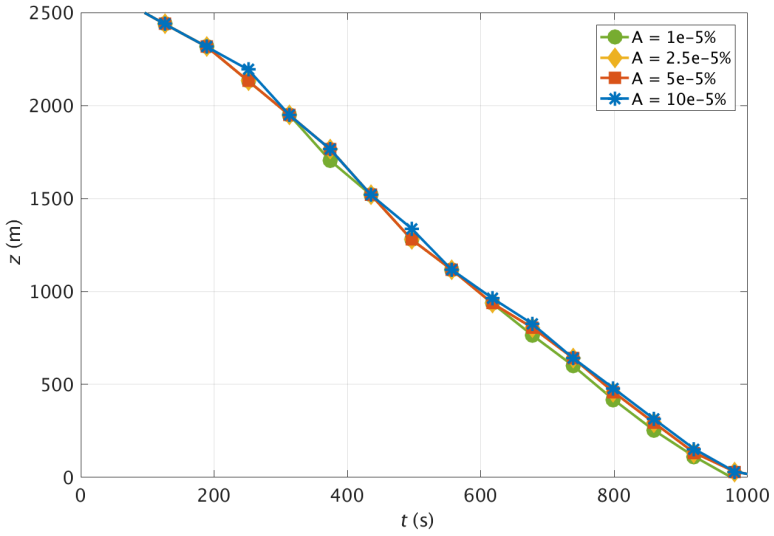


(B) Vertical descent (m) calculated using 4 different values of $A^*$ in condition (4.15). $\Omega = 0.8$ for all.

FIGURE 4.5: Vertical descent of Gx25z20.

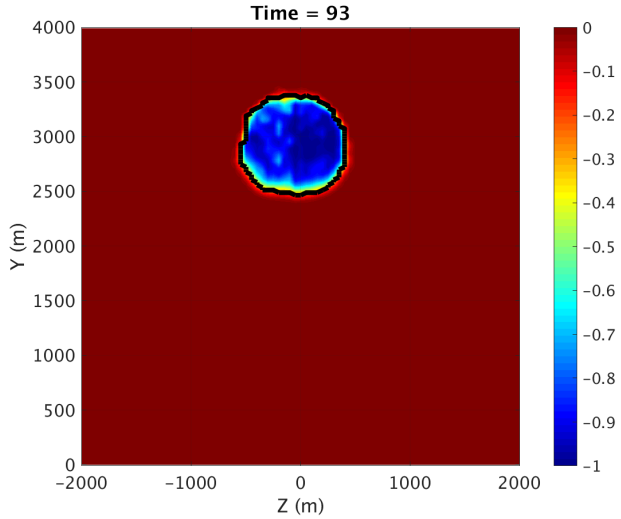


(A) Initial set-up

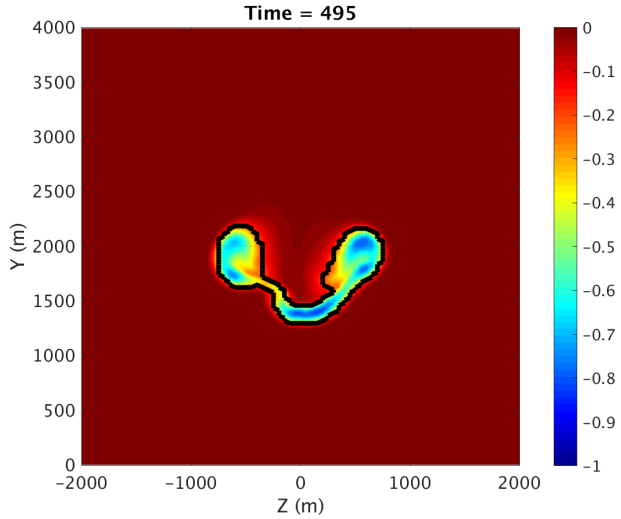


(B) Mid-descent

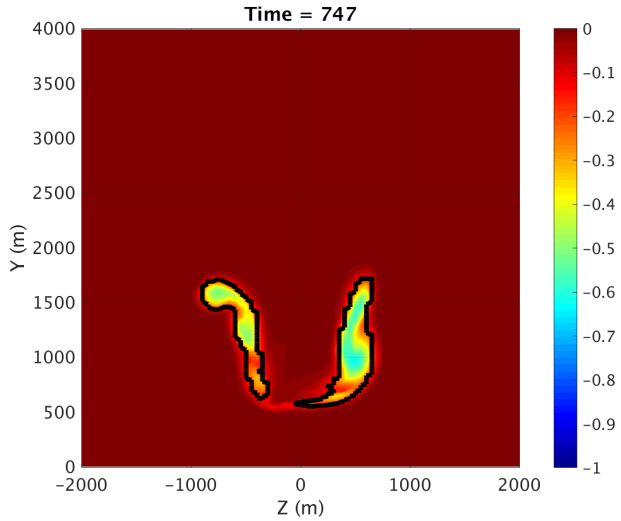


(C) Close to impact

FIGURE 4.6: Potential temperature (K) contour plots for Gx25z20 at times $t = 93, 495$ and 747s, taken on a vertical slice through the centre of the domain. The black solid line is the identified outline of the downdraught. The outline is determined by condition (4.14), with $\Omega = 0.8$.

where $X, Y$ is 24 times the initial radius of cooling sphere $24R_i$ and $Z$ is half the entire height of the domain. For example, a typical experimental run with initial cooling sphere $R_i = 500$ m, centred at a height of 3000 m, the extracted grid would be $X, Y = -6000 < x \leq 6000$ and $Z = 0 < z \leq 2000$.

The main difference between analysing the vertical descent and radial propagation is that instead of descending in the $z$-direction, the downdraught now spreads axisymmetrically. This axisymmetric spread is harder to track over the Cartesian numerical grid. Figure 4.7 demonstrates the methodology for identifying radial propagation. Firstly, condition (4.14) is applied to the $\Delta\theta$ 3D fields, buoyant fluid is identified as either 1 or 0 (Fig. 4.7). The Cartesian coordinates are then converted to radial using

$$r = \sqrt{x^2 + y^2}. \tag{4.16}$$

For a $1028 \times 1028$ grid, that creates over 13 000 unique values of $r$, therefore $r$ is binned into 10m intervals. Figure 4.8 shows the identified radial locations of buoyant fluid versus frequency of occurrence. The leading edge of radial propagation is identified when the frequency of radius exceeds an area fraction $A_f = A^* N_x^2$, radial propagation is then determined by

$$R_p(t) = \begin{cases} NaN & \sum N_B < A^* N_x^2, \\ R_p & \sum N_B \geq A^* N_x^2,. \end{cases} \tag{4.17}$$

This methodology for identification of radial propagation does have its limitations. From Figure 4.7 it can seen that this method tends to overestimate the radial propagation in the early stages of downdraught impact. This problem is created (or at least exacerbated) by the unsymmetrical impact of downdraught, where one part of the downdraught reaches the surface faster than the main body of fluid. After the first 100s, the radial propagation methodology achieves a far better representation of the horizontal outflow. On reflection, future studies might simply identify the centre of mass as the radius of propagation.

Radial propagation, calculated with different values of $\Omega$ and $A^*$ is plotted in Figure 4.9 for a control run Gx25z20 (see Table 4.3). Figure 4.9a shows almost no difference in radial propagation for 4 values of $\Omega$ between 0.5 and 0.9. Similarly, Figure 4.9b plots radial propagation for 4 different area fractions $A^*$ between 1.0e-5% and 5.0e-4%, this is equivalent to between 10 and 528 grid points being identified as negatively buoyant on a $1028 \times 1028$ grid. The value of $A^*$ similarly makes almost no difference to identifying radial propagation. The resulting identification of radial propagation is demonstrated in Figure 4.10, where the black circle is the identified leading edge of downdraught.

The differences in both vertical descent and radial propagation have only slight dependencies on the choice of $\Omega$ and $A^*$. For the rest of this study, $\Omega$ is taken as 0.8. This value is in keeping with Rooney (2015) and represents a balance between identifying the downdraught and mitigating against the impact of numerical diffusion. $A^*$ is taken as 5e-5%.

### 4.2.3 Grid Spacing Test

The benefits of diagnostics from complete 3D fields can shed insight otherwise impossible to obtain. However, any numerical model is only as useful as the confidence one has in it. There is always a balance of computational cost to accuracy of results; if domains and grid resolutions are two small then the numerical model risks failing to resolve the dynamics system properly. If they are too large, then the computational cost becomes prohibitive as the grid size increases and model timestep decreases.

The grid resolution test determines an appropriate domain and grid size for the whole study. A unique feature of this study is capitalising on the advances in parallization that MONC has over the older LEM model. It is now possible to run higher resolution models, the most recent large-eddy simulations of atmospheric downdraughts typically have horizontal resolutions between 50 and 100 m (see Section 4.1, Table 4.1). By contrast, in using MONC, this study has been able to run simulations up to 10m in horizontal resolution and 4m in the vertical resolution. Table 4.3 contains the list of model runs used for the grid sensitivity test. The name of

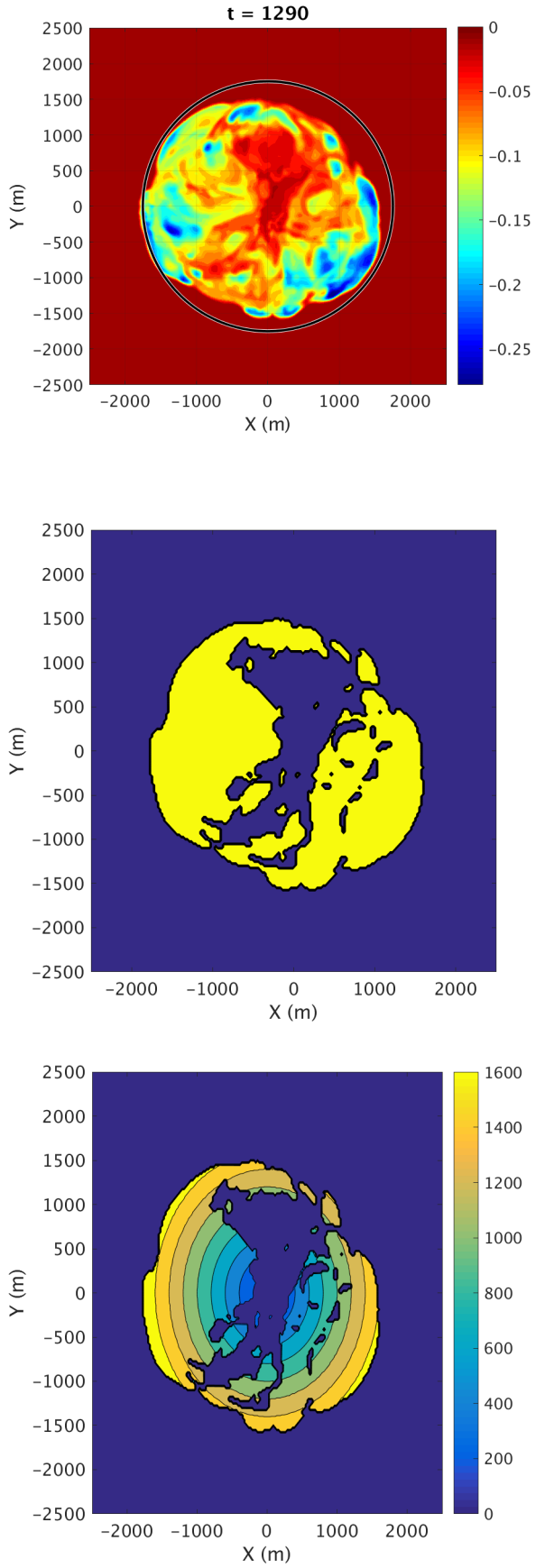


FIGURE 4.7: The methodology for identifying radial propagation. Plots shown are horizontal slices at $z = 10$ m from Gx25z20. Top is an instanteneous $\Delta\theta$ contour plot, with outer radius shown as the black circle from estimated radius of impingement. Middle shows the identified negatively buoyant fluid. Bottom is a contour of the radial propagation of identified negatively buoyant fluid (now in radial coordinates).

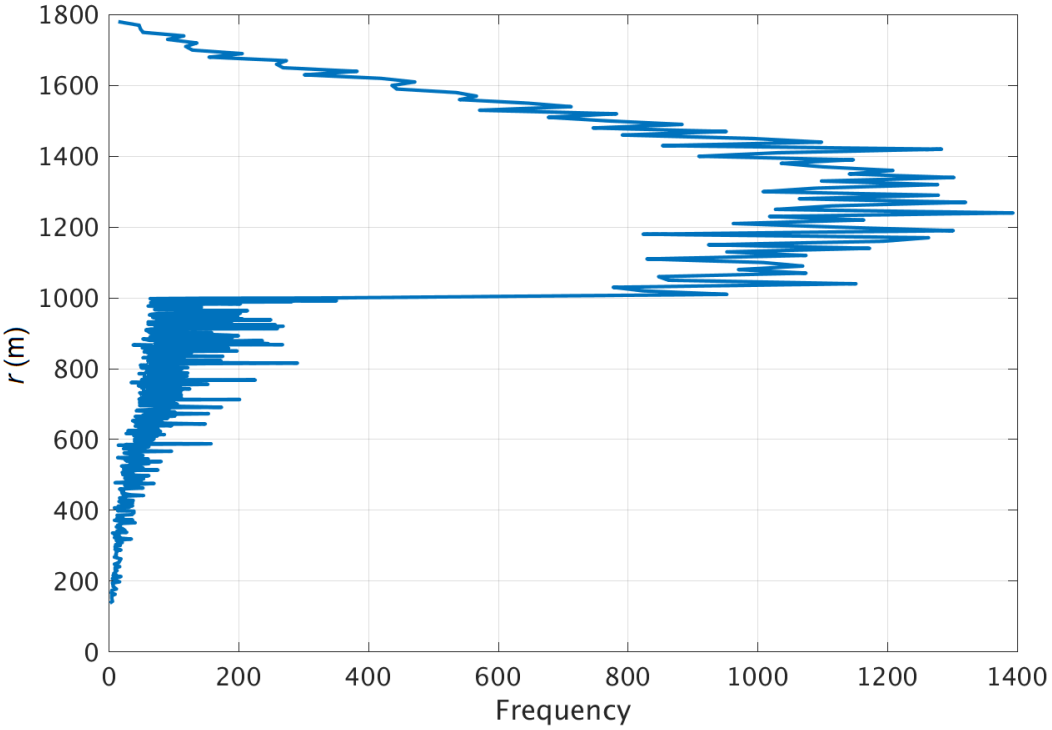


FIGURE 4.8: Radius of identified buoyant fluid (m) versus frequency of 10m bin from Gx25z10, $t = 1290$ s at $z = 10$ m.

each model run contains its properties, the G signifies that it is a grid sensitivity run, the x is the horizontal resolution and z is the minimum vertical resolution e.g. Gx50z20, has $dxx = 50$m and $dzz_{min} = 20$m. The letter b denotes model runs where backscatter was turned off. The main variables of interest for this study are the vertical descent, radial propagation and kinetic energy. Therefore, these are used to determine grid sensitivity. A representative model grid is shown in Figure 4.1. The grid sensitivity test is conducted using the same initial set-up for each model run, the only difference is the properties of the grid. For all runs, a cold bubble with $\Delta\theta = -1$ K is instantaneously released at a height of 3 km and allowed to fall freely. The initial radius of bubble is $b_0$ =500 m. A snapshot of the initial configuration of the grid sensitivity runs is shown in Figure 4.2.

Figure 4.11 plots the vertical descent of 8 different model runs. Two different vertical grid resolutions are shown, i) $dzz_{min} = 20$m (Fig. 4.11a) and ii) $dzz_{min} = 8$m (Fig. 4.11b). The coarser vertical resolution has relatively large variation of rate of vertical descent, while the finer vertical resolution has almost identical vertical descents.

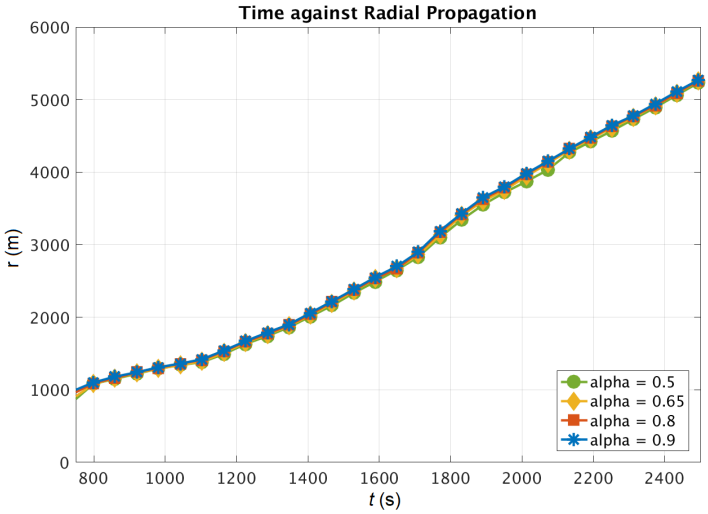


(A) Radial propagation (m) calculated using 4 different values of $\Omega$ in condition (4.14). $A^* = 5.0e - 5\%$ for all.

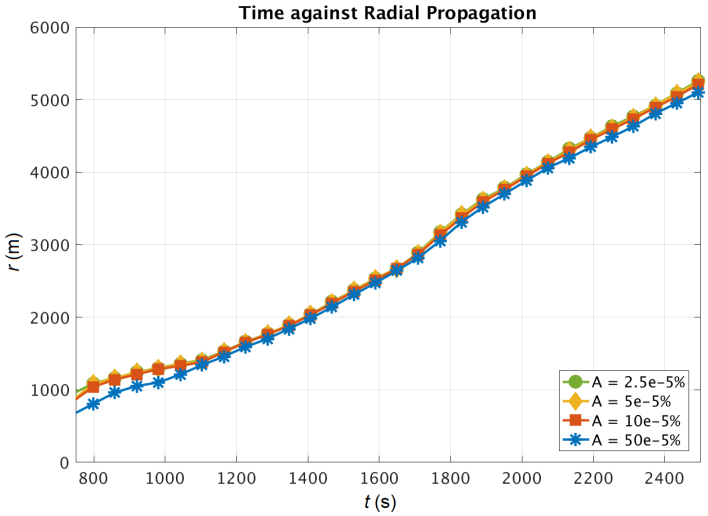


(B) Radial propagation (m) calculated using 4 different values of $A^*$ in condition (4.15). $\Omega = 0.8$ for all.

FIGURE 4.9: Radial propagation for Gx25z20

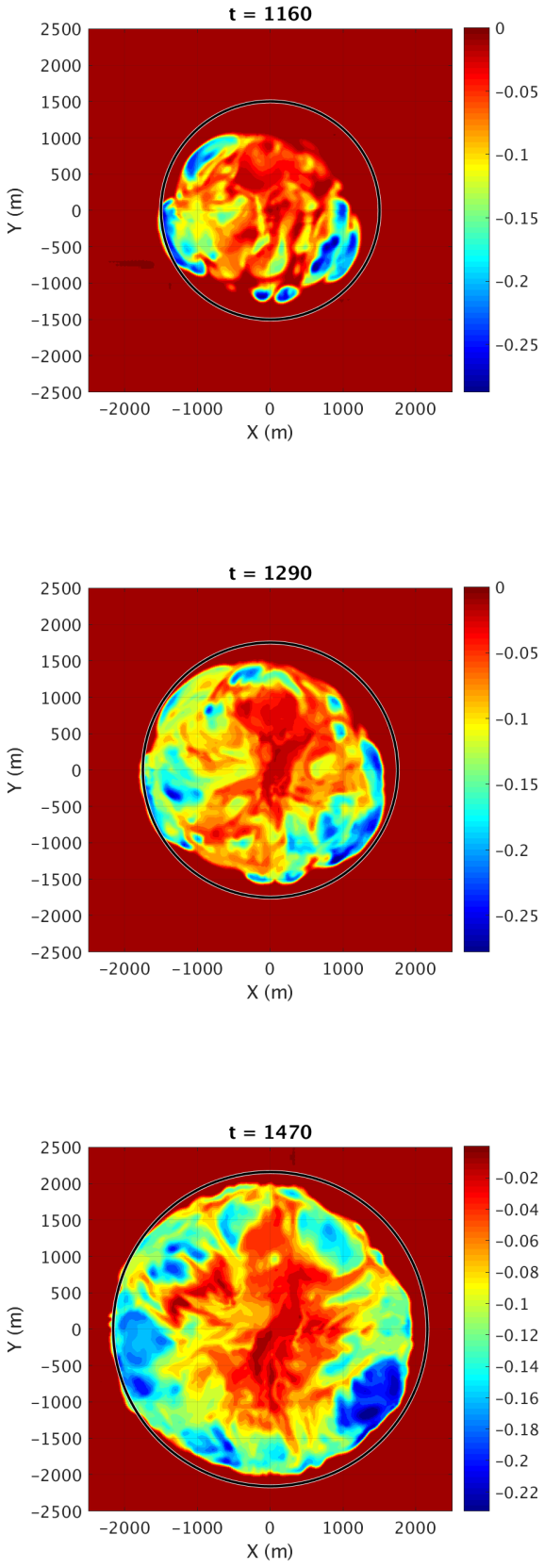


FIGURE 4.10: Potential temperature (K) contour plots at different times for Gx25z20 taken at $z = 10$ m. The black circle is the identified radial propagation from condition (4.14) with the applied radial coordinate system.

TABLE 4.3: Grid sensitivity runs. dxx and dzz are the horizontal and vertical resolution. $N_x$ and $N_z$ are the number of horizontal and vertical grid points.

| **Simulation Number** | **Horizontal Domain (m)** | **dxx** (m) | $N_x$ | **Vertical Domain (m)** | **dzz**$_{min}$ (m) | $N_z$ |
|---|---|---|---|---|---|---|
| Gx50z20 | 25600 | 50 | 512 | 4000 | 20 | 99 |
| Gx33z20 | 25608 | 33 | 776 | 4000 | 20 | 99 |
| Gx25z20 | 25600 | 25 | 1024 | 4000 | 20 | 99 |
| Gx10z20 | 25600 | 10 | 2560 | 4000 | 20 | 99 |
| Gx50z08 | 25600 | 50 | 512 | 4000 | 7.9 | 256 |
| Gx33z08 | 25608 | 33 | 776 | 4000 | 7.9 | 256 |
| Gx25z08 | 25600 | 25 | 1024 | 4000 | 7.9 | 256 |
| Gx10z04 | 25600 | 10 | 2560 | 4000 | 3.9 | 512 |
| Gx25z20 | 25600 | 25 | 1024 | 4000 | 20 | 99 |

Figure 4.11b shows that vertical descent is independent of horizontal resolution, as might be expected at a stage where the flow is dominated by movement in the $z$ coordinate, with relatively small variations in $(x, y)$. $dzz_{min} = 8$m is chosen as the vertical spacing for this study.

Figure 4.12 plots the radial propagation for all of the different grid sensitivity model runs. There is reasonable agreement for all model runs for $t < 1800$s, afterwards there is greater divergence. There appears little dependence on the vertical resolution in the radial propagation stage, as the dotted and solid lines tend to overlay each other. An exception to this is Gx33z08 and Gx33z20 (red lines) which diverge significantly after 1800s. Figure 4.13 plots the mean kinetic energy of the entire grid against time. The bubble impacts the surface around 1300 s, in conjuction with the maximum of the mean kinetic energy. Before, $t = 1300$s, all model runs contain almost identical mean kinetic energy. At impact, there are complex turbulent interactions between the bubble and the surface as it 'splashes' down, and therefore it is here that the mean kinetic energies diverge slightly. The coarsest horizontal resolution $dxx = 50$m (blue) has the lowest value of mean kinetic energy, $dxx = 33$m has the highest. $dxx = 25$m lies roughly between the two. $dxx = 25$m is chosen as the horizontal spacing for this study, representing the best balance of consistency versus computational cost.

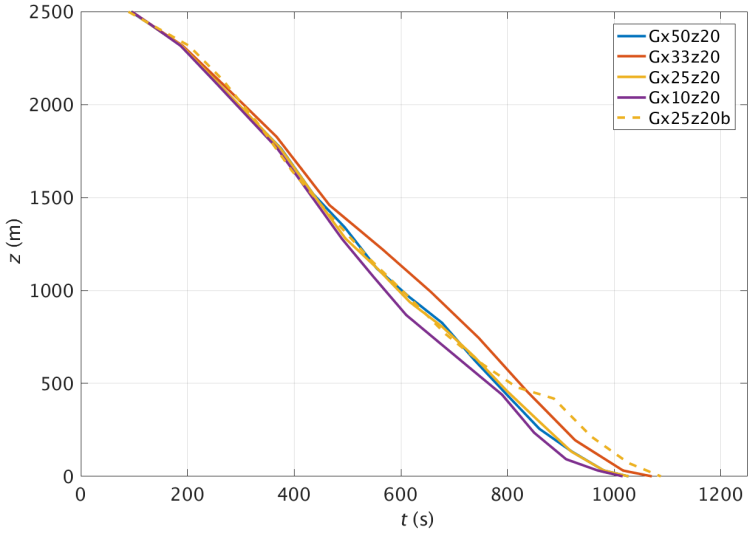


(A) 5 different horizontal resolutions, $dzz_{min} = 20$ m for all.

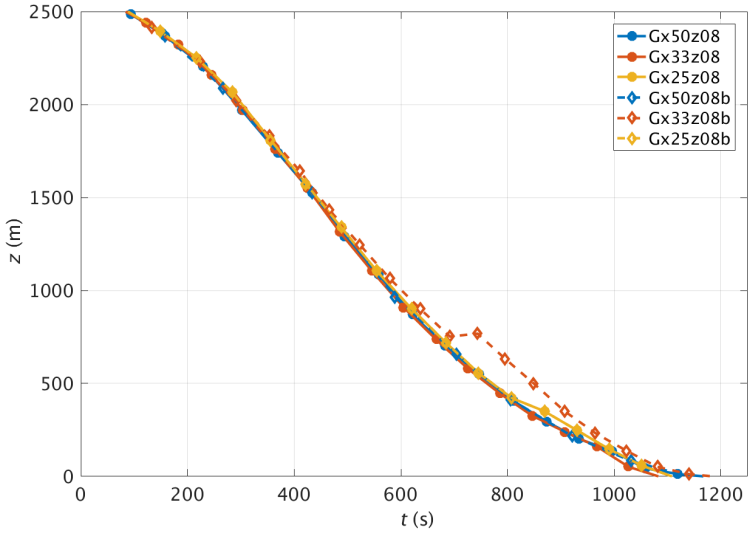


(B) 3 different horizontal resolutions, $dzz_{min} = 8$ m for all.

FIGURE 4.11: Vertical descent (m) for different grid resolution test runs.

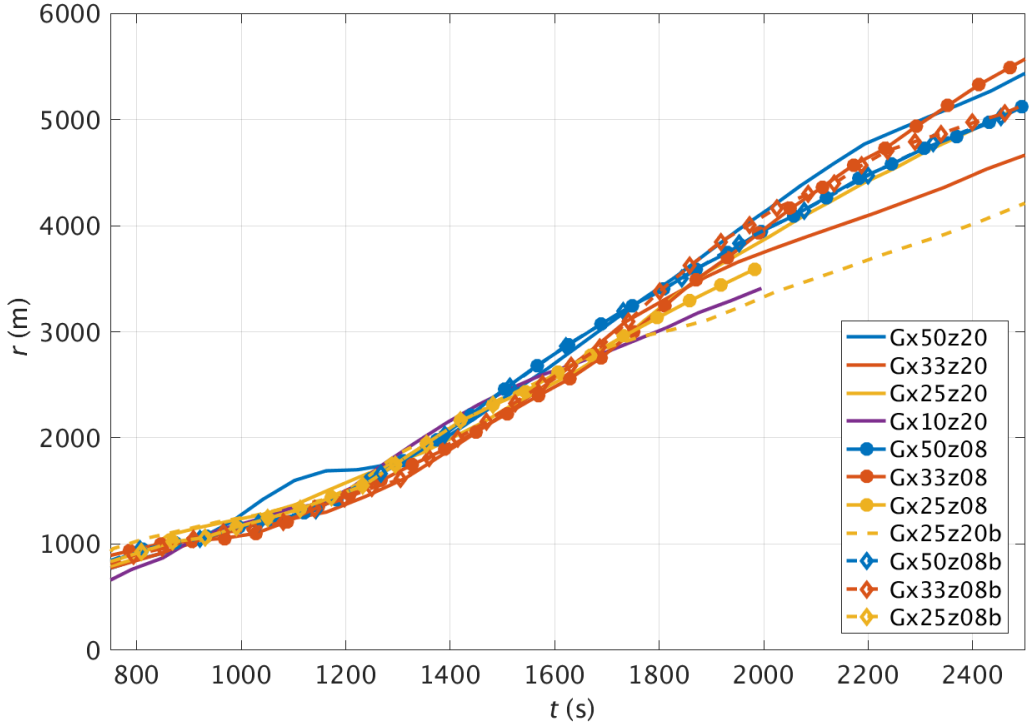


FIGURE 4.12: Radial propagation (m) for different grid resolution test runs. Showing 4 horizontal resolutions and 2 vertical resolutions. Gx10z20 ran for a reduced time to save computational cost.

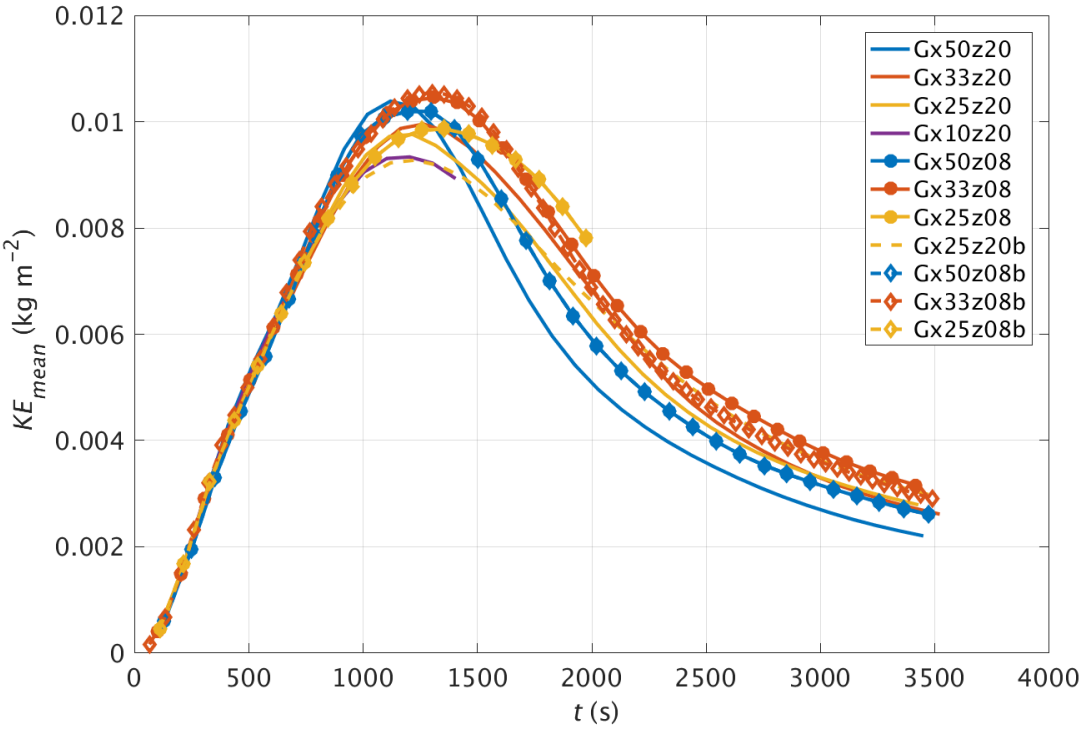


FIGURE 4.13: Mean kinetic energy (kg $m^2$ $s^{-2}$ for the whole domain against model time for different grid resolution test runs. Showing 4 horizontal resolutions and 2 vertical resolutions.

## 4.3 Summary

This chapter outlines a methodology for modelling idealised atmospheric downdraughts. The new Met Office and NERC Collaboration (MONC) model is used to conduct large eddy simulations of idealised downdraughts. The downdraught is represented using a cold bubble which is instantaneously released and allowed to fall freely during the simulation. The methods used for identifying and tracking buoyant fluid are described, and the thresholds needed for those identifications are found. A grid sensitivity test is conducted to determine the necessary grid spacing of model runs. A horizontal resolution of $dxx = 25$ m and $dzz_{min} = 8$m is suggested as representing a reasonable compromise between consistency and computational cost. Despite the limitation that MONC cannot use a grid with variable areas of refinement, grid independence is still achieved. The model configuration described in this Chapter is now employed throughout the remainder of thesis to provide insight into the descent and near-surface evolution of idealised atmospheric downdraughts.

# Chapter 5

# Numerical simulations on the descent and near-surface evolution of atmospheric downdraughts

## 5.1 Introduction

This chapter presents analysis of Large Eddy Simulations (LES) for the descent and near-surface evolution of idealised downdraughts. Both existing theory and new theory is compared against these simulated downdraughts. In Chapter 3, laboratory experiments simulating atmospheric downbursts made a number of findings:

- The radial propagation of resulting gravity current was found to spread at

$$r = (2Fr_c)^{1/2}\lambda^{1/4}B^{1/4}(t - t_i)^{1/2} + R_0.$$

  However, $Fr_c$ and $\lambda$ were changed from 1.4 and 1.0 to 1.19 and $\pi^{-1}$. $R_0$ was taken as the radius at impact $R_0 = b_0 + \alpha H$, instead of the radius of the quasi-spherical volume of fluid.

- The maximum horizontal velocity of outflow is simply a function of the gravity current propagation speed $u_{rmax} = f(u_r)$. A simple relation is suggested,

$$u_{rmax} = ku_r = kFr_c\lambda^{1/2}B^{1/2}r^{-1},$$

  where from experiments $k = 3$.

- The vertical profile of the horizontal velocity was compared with an empirical profile developed by previous experimental and numerical studies (Wood et al., 2001; Sengupta and Sarkar, 2008), where

$$\frac{u}{u_m} = C_4 \left(\frac{z}{n}\right)_1^n \left[1 - \text{erf}\left(C_5 \frac{z}{b}\right)\right].$$

  The experiments were found to fit well with this empirical profile. However, $C_5$ was found to be 0.55 instead of 1.2.

Using MONC provides an opportunity to verify these findings using a new method, that of numerical simulation instead of laboratory experiments.

An advantage of numerical simulations is the ability to analyse the full 3D velocity and potential temperature fields at each time dump. This proliferation of data, allows CFD to examine subjects difficult in an experimental facility. The energetics of a cold bubble's descent and spread, would be difficult to measure in the laboratory but are intrinsic within the model. This chapter firstly extends the theoretical similarity solutions of Rooney (2015) to include the potential and kinetic energy, secondly compares this extended theory to LES results, and finally uses the extended theory to compare and contrast between different similarity solutions for cold pool outflow proposed by Romps and Jeevanjee (2016).

Specifically, this chapter has four aims:

1. Conduct detailed LES of an idealised atmospheric downdraught using MONC.
2. Compare the results of MONC cold bubble simulations with the new findings of the laboratory experiments in Chapter 3.
3. Extend the similarity solutions of Rooney (2015) to include expressions for the potential and kinetic energy.
4. Compare the similarity solutions of Rooney (2015) and Romps and Jeevanjee (2016) to MONC simulations.

## 5.2 Developing Energy Relations of Thermals

In this section, the thermal similarity solutions from Rooney (2015) are developed further to create new expressions that relate the kinetic and potential energy of the thermal throughout the thermal's descent and spread to the initial buoyancy, radius and height. This new treatment not only builds on the work of Rooney (2015) by expanding the similarity solutions, but also allows comparison of these buoyancy based relations to an alternative energy based theory proposed by Romps and Jeevanjee (2016). The work from the point on is original, unless otherwise referenced.

### 5.2.1 Potential Energy in Thermals

The negatively buoyant thermals are released from rest at $t = 0$, therefore the entirety of the initial energy of the thermal is gravitational potential energy. As the thermal falls, this potential energy is primarily converted to kinetic energy. The gravitational potential energy of the thermal is simply,

$$PE = \Delta\rho g h V, \tag{5.1}$$

where $\Delta\rho$ is relative density, $g$ gravitational acceleration, $h$ height at time $t$ above the surface.

Using reduced gravity $g' = (g\Delta\rho/\rho_0)$ and buoyancy $B = g'V$, the potential energy can be written in terms of buoyancy,

$$PE = \rho_0 B h. \tag{5.2}$$

$h$ is the height of thermal above surface at a given time $t$ and can therefore be written as $h = H - z(t)$ where $H$ is the initial height of thermal and $z$ is the vertical distance the thermal has travelled. Therefore,

$$PE = \rho_0 B H - \rho_0 B z. \tag{5.3}$$

Using (5.24), an expression for how potential energy develops with time is developed

$$PE = \rho_0 BH - \rho_0 B \left[2Fr_T m^{1/2} \alpha^{-1} B^{1/2} t\right]^{1/2}. \tag{5.4}$$

Let a constant $k_1^2 = \left[2Fr_T m^{1/2} \alpha^{-1}\right]$ giving

$$PE = \rho_0 BH - k_1 \rho_0 B^{5/4} t^{1/2}. \tag{5.5}$$

### 5.2.2 Kinetic Energy in Descending Thermals

As the thermal descends, PE is converted into kinetic energy (KE). The kinetic energy of the thermal is

$$KE_v = \frac{1}{2}\rho V \mathbf{u}^2, \tag{5.6}$$

where $\mathbf{u}$ is the velocity field. Using radial coordiates, $\mathbf{u}$ comprises of the vertical velocity $w(z,t)$ and the radial velocity $u_r(r,t) = \sqrt{u^2 + v^2}$, therefore

$$KE_v = \frac{1}{2}\rho V (u_r^2 + w^2). \tag{5.7}$$

In the vertical descent stage, radial velocities are governed by the increasing radius of thermal through entrainment and the internal circulation of the descending vortex ring. From (2.37), the radius of thermal $b$ is only a function of $z$. Therefore, the radial velocity can be assumed to be related to the vertical velocity through some relationship $u_r(r,t) = f(w(z,t)$. For now, it will be assumed that this relationship is linear, so that

$$u_r(r,t) = k_2 w(z,t), \tag{5.8}$$

where $k_2 < 1$ is a constant. Assuming no dissipative energy low, kinetic energy is now,

$$KE_v = \frac{1}{2}\rho V (k_2 + 1) w^2. \tag{5.9}$$

As for the potential energy relation, it is desirable to express the kinetic energy in terms of the characteristics of thermal at origin. From (2.43b)

$$w = Fr_T m^{-1/2} \alpha^{-1} B^{\frac{1}{2}} z^{-1}. \tag{5.10}$$

Substituting in (5.10) into (5.9) gives

$$KE_v = \frac{1}{2}\rho V Fr_T^2 m^{-1}\alpha^{-2}(k_2+1)Bz^{-2}. \tag{5.11}$$

The volume of the quasi-spherical thermal is $V = mb^3$, and using $b = \alpha z$ gives an expression for kinetic energy in the vertical dependent on: the density $\rho$, entrainment $\alpha$, the Froude number $Fr_T$ and buoyancy $B$.

$$KE_v = \frac{1}{2}\rho\alpha Fr_T^2(k+1)Bz. \tag{5.12}$$

### 5.2.3 Kinetic Energy in Gravity Currents

After the thermal has hit the surface, it propagates out radially from the centre of impingement. The thermal has transitioned to an axisymmetric gravity current. Huppert and Simpson (1980) show how a simple box-model collapse can be used to model slumping gravity currents. For axisymmetric cases, Hallworth et al. (1996) show how this box-model approach can be adapted to the collapse of cylinders. Using this cylindrical approximation for gravity current collapse and spreading, means the kinetic energy is

$$KE_r = \frac{1}{2}\rho\int_0^r 2\pi r\mathrm{d}r\int_0^h \mathrm{d}z(u_r^2+w^2). \tag{5.13}$$

For the simplest case, assume $u_r >> w$. Kinetic energy is then,

$$KE_r = \frac{1}{2}\rho\pi r^2 h u_r^2. \tag{5.14}$$

Rooney (2015) combines (2.43) with similarity solutions proposed by Grundy and Rottman (1985) for the axisymmetric release of a finite volume of negatively buoyant fluid (see 2), to show that

$$u = Fr_c\lambda^{1/2}B^{1/2}r^{-1}, \tag{5.15a}$$

$$g' = c^{-1}\alpha^{-3}BH^{-3}\left(1+\frac{b_0}{\alpha H}\right)^{-3}f^{-1}, \tag{5.15b}$$

$$\frac{h}{H} = \lambda c\alpha^3\left(1+\frac{b_0}{\alpha H}\right)^3\left(\frac{r}{H}\right)^{-2}f. \tag{5.15c}$$

By substituting (5.15a) and (5.15c) into (5.14), the kinetic energy of the resulting gravity current can be related to the initial properties of the thermal by

$$KE_r = \frac{1}{2}\rho\pi H^3\lambda^2 c\alpha^3 Fr_c^2 \left(1 + \frac{b_0}{\alpha H}\right)^3 Br^{-2} f. \tag{5.16}$$

$\alpha, \lambda, Fr_c, \pi$ are dimensionless. $f$ is an empirical function proposed as $(r'_{max}/R_0)^{-1.3}$ by Rooney (2015).

These new expressions for potential and kinetic energy are compared against the LES model in Section 5.5.

## 5.3 Design of Numerical Simulations

The technical description and methodology followed for the set-up of the LES runs used for the analysis is described in Chapter 4. This section is devoted only to the specific properties of the numerical simulations used for analysis of this chapter.

The purpose of these numerical simulations is to help provide better understanding of the descent and near-surface evolution of atmospheric downdraughts. Several of the research questions this study aims to answer, stem directly from the laboratory experiments discussed in Chapter 3. Therefore these numerical simulations are designed to be broadly analogous to the laboratory experiments. However, it is important to make clear that it is not the intention to replicate the exact properties of the laboratory experiments using MONC. There are two reasons for this: i) practically it is difficult to quantify the exact role that the opening valve of the experiments had on injecting momentum into the experimental releases, therefore replication of these releases would be difficult and ii) more fundamentally, the purpose of these numerical simulations is to investigate atmospheric buoyant transport, why then constrain this study to the practical limitations of the laboratory when one of the main advantages of the numerics is the ability to model a wide regime of initial properties.

TABLE 5.1: Scaled Atmospheric Values of Laboratory Experiments

| Experimental Property | Symbol | Value | Atmospheric Value | Unit |
|---|---|---|---|---|
| Radius of pipe outlet | $R_0$ | 0.0055 | 550 | m |
| Characteristic length | $R_0$ | 0.0055 | 550 | m |
| Volume release - 2s | $V_{v2}$ | 0.0026 | 2.6e9 | $m^3$ |
| Volume release - 5s | $V_{v5}$ | 0.0051 | 5.1e9 | $m^3$ |
| Reduced gravity | $g'$ | 0.01-0.02 | 0.01-0.02 | $m\ s^{-2}$ |
| Buoyancy release - 2s2p | $B_0$ | 5.1e-4 | 5.1e8 | $m^4\ s^{-2}$ |

Lundgren, Yao, and Mansour (1992) introduce a simple scaling based on the equivalent spherical radius $R_0$ of downburst parcel or fluid released, and a characteristic time $t_0$ dependent on $R_0$ and reduced gravity $g'_0$. Rooney (2015) adopts the scaling of Lundgren, Yao, and Mansour (1992) for the descent and spread of negatively buoyant thermals, where $R_0$ is taken as the 'equivalent spherical radius of thermal',

$$R_0 = \left(\frac{3m}{4\pi}\right)^{1/3} (b_0 + \alpha H). \tag{5.17}$$

However, experiments in Chapter 3 found that an adaptation of $R_0$ provided an improved scaling of results (see Section 3.3.6), $R_0$ is therefore taken as the theoretical radius of impingement,

$$R_0 = (b_0 + \alpha H). \tag{5.18}$$

Using the initial buoyancy of thermal as $B_0 = g'V$, allows $t_0$ to be expressed as

$$t_0 = \left(\frac{R_0}{g'_0}\right)^{1/2} = \frac{R_0^2}{B_0^{-1/2}}\,. \tag{5.19}$$

These scalings are now employed to create analagous atmospheric numerical simulation of the experiments in Chapter 3. Table 5.1 contains the scaled atmospheric values of the laboratory experiments. These scaled values are broadly in keeping with both previous studies of downdraughts (Anabor et al., 2011; Rooney, 2015) and atmospheric observations (Fujita, 1985; Hjelmfelt, 1988). These scaled values form the basis of the variables chosen for model runs chosen for analysis. The characteristics of the analysis runs are given in Table 5.2.

TABLE 5.2: Characteristics of Analysis Runs. $\theta_0$ is the initial potenital temperature perturbation of bubble, $H$ is the release height of the centre of bubble, $b_0$ is the initial width of bubble, $z_v$ is the location of the virtual origin, $t_0$ is the characteristic time.

| **Name** | $\theta_0$ (K) | $H$ (m) | $b_0$ (m) | $B/B*$ | $z_v$ (m) | $t_0$ (s) |
|---|---|---|---|---|---|---|
| B1r5 | -1 | 3000 | 500 | 1 | 1923 | 60.4 |
| B2r5 | -2 | 3000 | 500 | 2 | 1923 | 42.7 |
| B3r5 | -3 | 3000 | 500 | 3 | 1923 | 34.9 |
| B4r5 | -4 | 3000 | 500 | 4 | 1923 | 30.2 |
| B6e5 | -6 | 3000 | 500 | 6 | 1923 | 24.7 |
| B0.1r5 | -0.1 | 3000 | 500 | 0.1 | 1923 | 191.0 |
| B0.5r5 | -0.5 | 3000 | 500 | 0.5 | 1923 | 85.4 |
| B1r3 | -4.63 | 3000 | 300 | 1 | 1154 | 21.8 |
| B0.5r3 | -2.31 | 3000 | 300 | 0.5 | 1154 | 30.8 |
| B0.1r3 | -0.46 | 3000 | 300 | 0.1 | 1154 | 68.8 |
| B1r7 | -0.36 | 3000 | 700 | 1 | 2692 | 118.4 |
| B0.5r7 | -0.18 | 3000 | 700 | 0.5 | 2692 | 167.5 |
| B2r7 | -0.73 | 3000 | 700 | 2 | 2692 | 83.7 |

## 5.4 Vertical Descent and Radial Propagation of Thermals

Whether downbursts are studied by atmospheric scientists, aeronautical engineers or the wind industry, the key parameters common to all are the rate of vertical descent of downdraught and resulting radial spread of gust front or gravity current. Furthermore, in creating a theoretical model of downburst behaviour, developing an understanding of how that downburst propagates and develops with time is perhaps the most fundamental component of that model. Each phase of the downburst's development; vertical descent and radial spread, are well studied scientific problems. Work on the vertical transport of buoyant fluid is a classical fluid dynamics problem dating back to the 1950s (Morton, Taylor, and Turner, 1956). Whilst the gravity current is found in such diverse settings, it deserves study regardless of application (Huppert and Simpson, 1980; Simpson, 1999). Rooney (2015) combines similarity solutions for buoyant descent with axisymmetric gravity currents to propose expressions that detail a negatively buoyant thermal's descent and subsequent spread as a gravity current based only on the initial properties of that thermal. These expressions, were examined experimentally in Chapter 3, where good agreement between laboratory experiments and theoretical expressions for vertical descent and radial propagation from Rooney (2015) was found, subject to several modifications

proposed by this study. Specifically, the rate of propagation was found to be

$$r = [2Fr_c\lambda^{1/2}B^{1/2}(t - t_i)]^{1/2} + R_0, \tag{5.20}$$

where the Froude number $Fr_c$ and $\lambda$ are suggested as 1.19 and $\pi^{-1}$ (instead of 1.4 and 1 in Rooney (2015)), and the length scale $R_0$ is taken as the radius of impingement $R_0 = b_0 + \alpha z$. The aim of this section is both to check the consistency of this study's numerical model (described in Section 4) with the experimental findings in Chapter 3 and evaluate the similarity solutions from Rooney (2015).

### 5.4.1 Flow visualisation

Before delving into substantial diagnostics generated in these numerical simulations, it is useful to first develop a visual understanding for how the thermal descends and spreads. Figures 5.1 and 5.2 show potential temperature and resultant velocity ($u_{res} = \sqrt{u^2 + v^2 + w^2}$) contour plots of B1r5. Note the colour bar of the plots dynamically changes as the thermal falls, this is to better visual the thermal. For example, the minimum potential temperature perturbation changes by roughly a factor of 10 between $t = 68$ s and $t = 2024$ s.

At $t = 68$s, the thermal is still close to initiation and has not significantly altered from the spherical initial condition. Most of the thermal is still at the initial temperature perturbation of -1K. Although there are some internal pockets of fluid at a smaller perturbation, this is most likely from the initial randomisation process which swaps points of buoyant fluid at the edges of the thermal into the centre (see Section 4.2.1). As the thermal descends, this spherical shape breaks up into a more irregular object. As viewed in the vertical plane, the thermal appears to split at around $(t = 448)$. The thermal now becomes more similar to a vortex ring.

Between $t = 990$ s and $t = 1294$ s, the thermal impacts the surface and begins to spread rapidly. It is possible to see the strong rotation that has developed in the core of the thermal in Figure 5.2 at $t = 1294$s. The thermal, or vortex ring, continues to spread radially with time. It appears that the bulk of the negatively buoyant fluid

remains in the head of the gravity current. In fact, the entire feature is largely contained in this gravity current head, with little to no secondary flow or 'tail' following.

Throughout the descent and spread, the thermal maintains a reasonable symmetry, although at $t = 2024$ s it is clear some asymmetries are developing. These asymmetries are perhaps more clearly seen in Figure 5.3 which plots potential temperature and resultant velocity for the same model run B1r5 at a horizontal slice at the surface ($z = 7$ m). Figure 5.3 demonstrates the axisymmeteric spread of the gravity current. The vortex ring structure is clearly visible in the resultant velocity contour plots. Again, it is possible to see that the bulk of the higher speed fluid remains in concentrated in that gravity current head. Interestingly, the potential temperature is not as uniformly distributed around the entire vortex ring, there are pockets of more concentrated cold fluid at seemingly random points around the head of the gravity current. These pockets of cold fluid have only a weak connection with the local maxima of the resultant velocities.

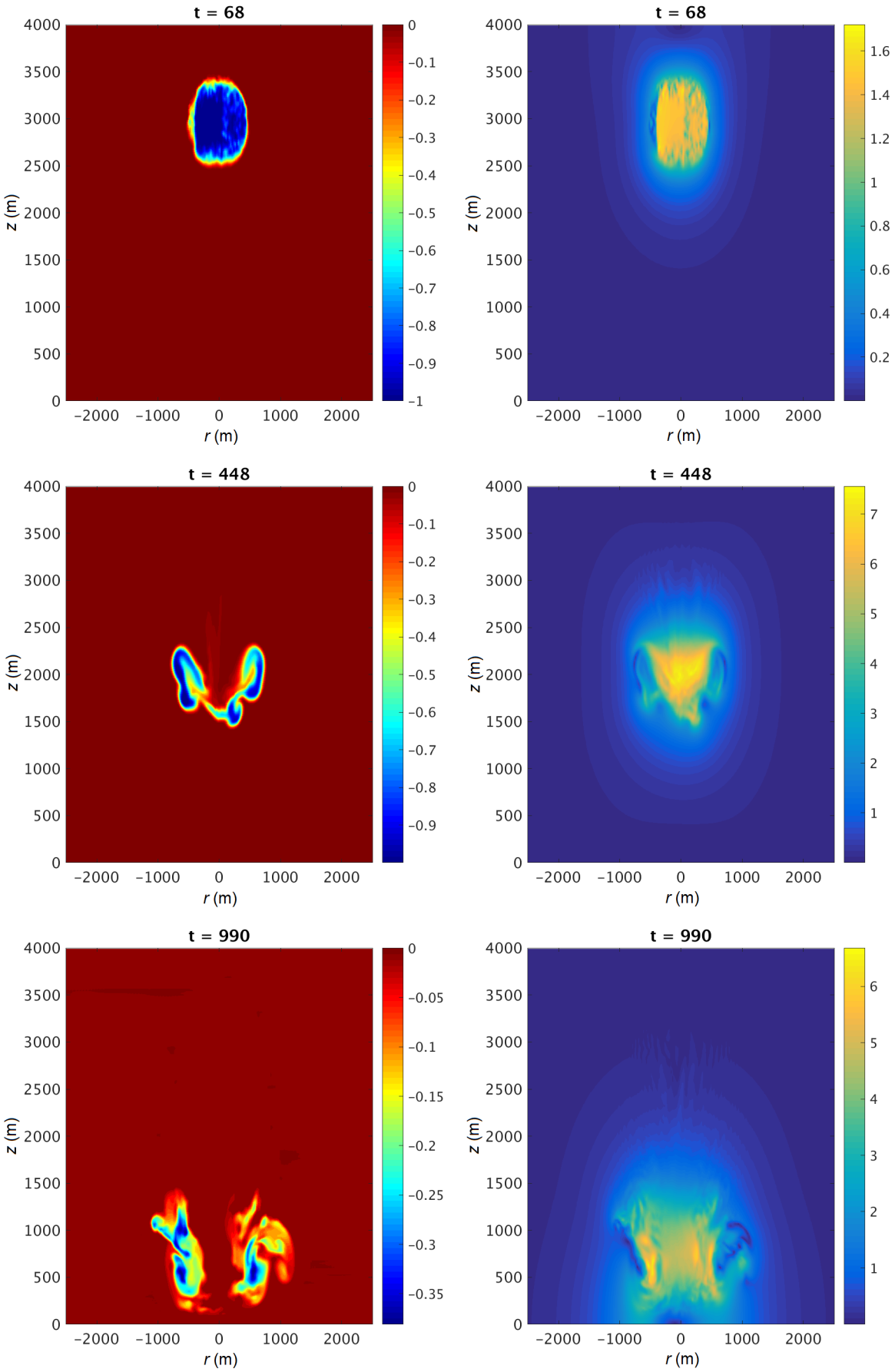


FIGURE 5.1: Potential temperature (K) (left) and resultant velocity (m $s^{-1}$) (right) plots of B1r5, taken at a vertical slice through the centre of the domain ($r = 0$ m). Note i) the colour bar dynamically changes to better illustrate the thermal and ii) the changing $r$ scale.

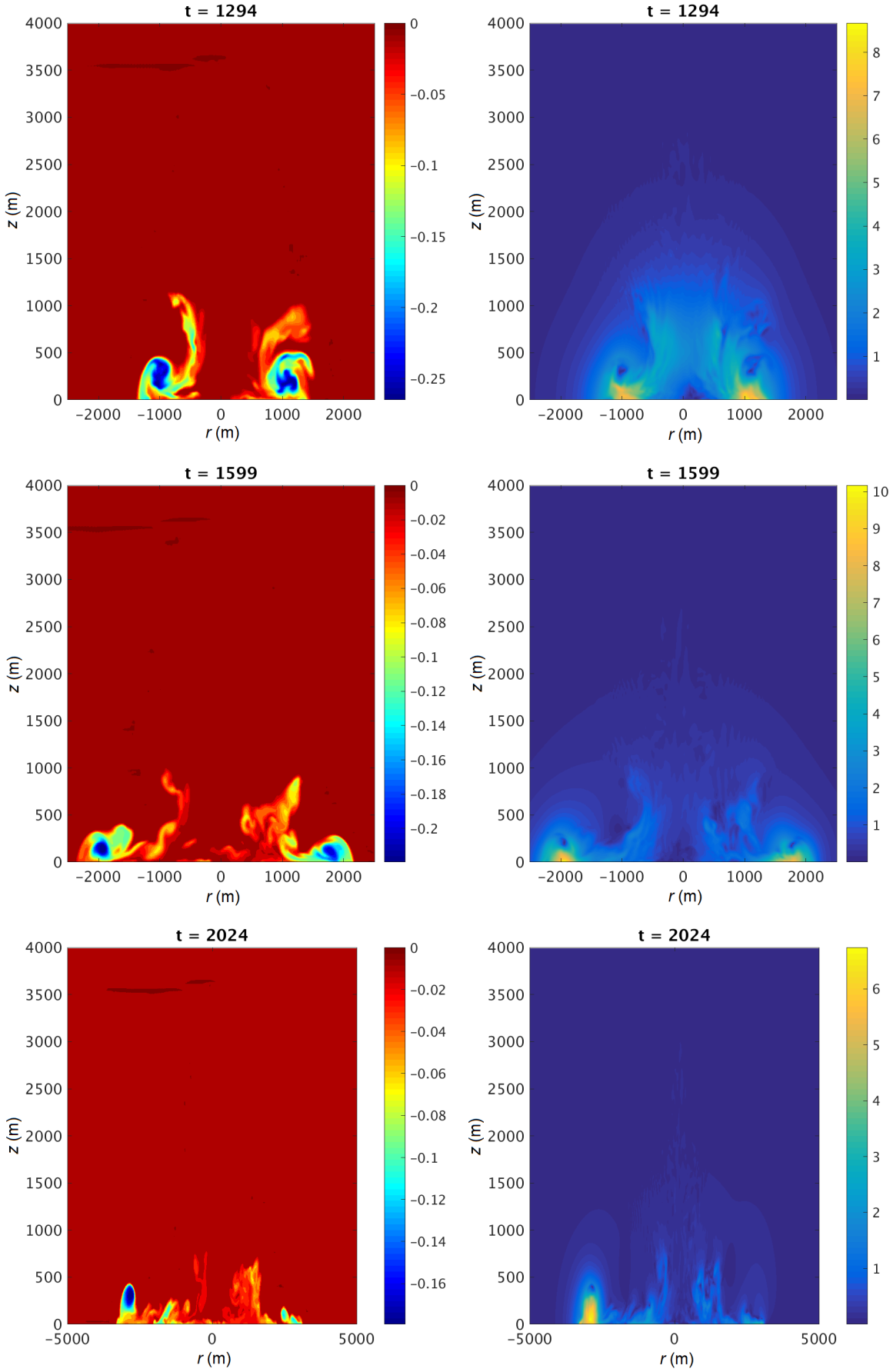


FIGURE 5.2: Potential temperature (K) (left) and resultant velocity (m $s^{-1}$) (right) plots of B1r5, taken at a vertical slice through the centre of the domain ($r = 0$ m). Note the colour bar dynamically changes to better illustrate the thermal.

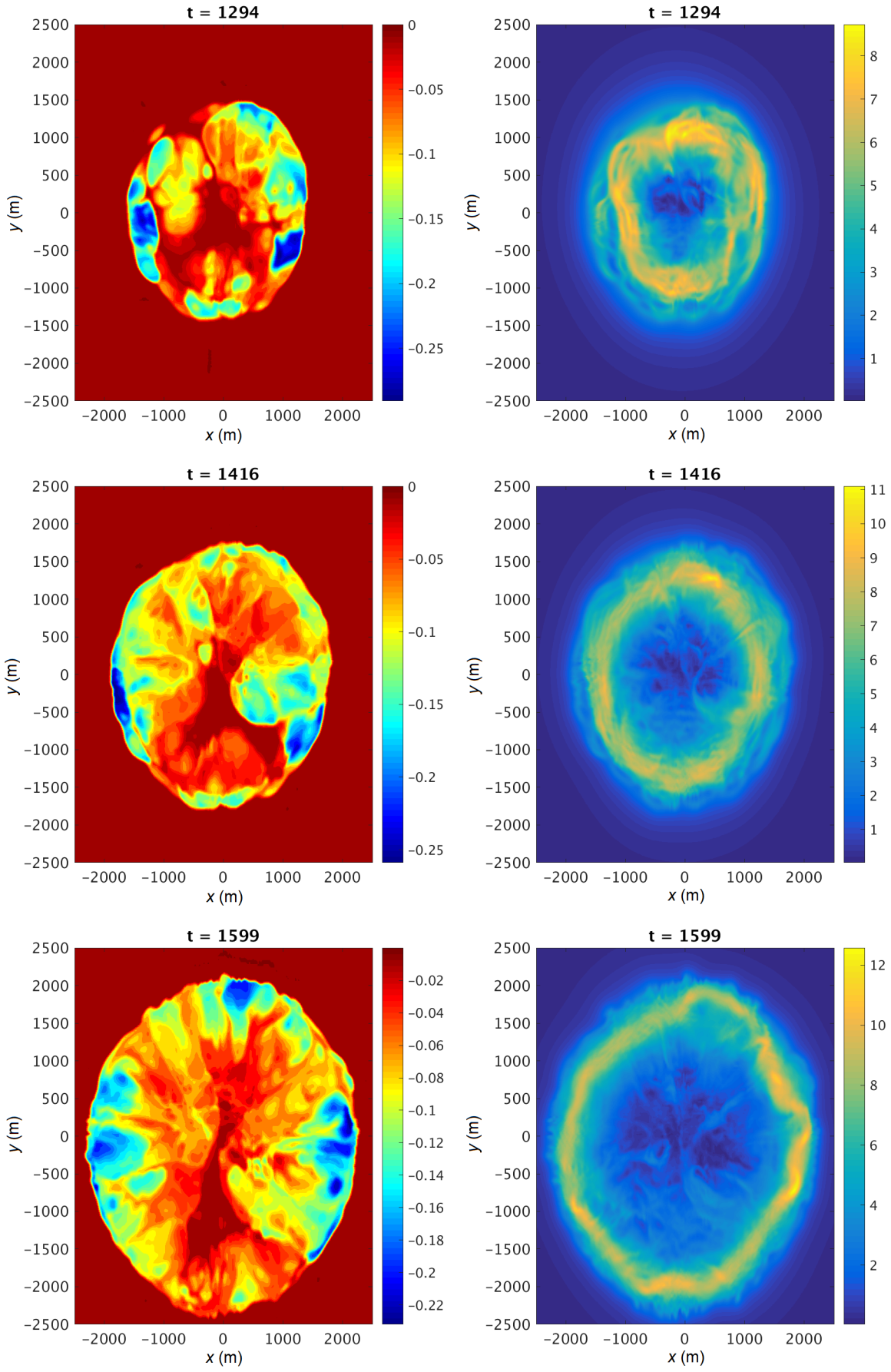


FIGURE 5.3: Potential temperature (K) (left) and resultant velocity (m $s^{-1}$) (right) plots of B1r5, taken for a horizontal slice at ($z = 7$ m). Note the colour bar dynamically changes to better illustrate the thermal.

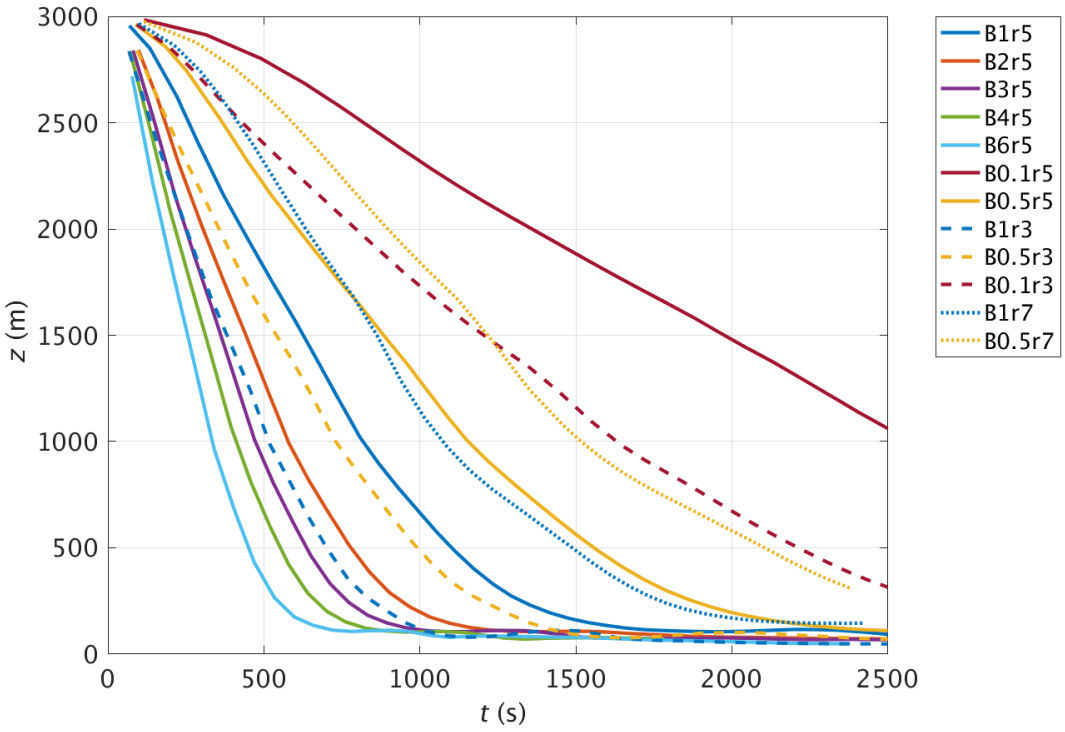


FIGURE 5.4: Vertical descent (m) of all runs. Colour of line denotes buoyancy, line style denotes radius.

### 5.4.2 Vertical Descent

Vertical descent is calculated using two methods: i) when 'vertical descent' of thermal or bubble is discussed, this refers to the location of the centre of mass. The centre of mass is calculated as the averaged height of all identified points of buoyant fluid. Identification of buoyant points depends on a threshold value $\alpha$. ii) when 'leading edge' is discussed, this refers to the outer edge, closest to the ground, of the thermal. The leading edge is calculated using an area fraction $A^*$ and the buoyant threshold value $\alpha$. A detailed discussion of this methodology and the values of $\alpha$ and $A*$ is available in Section 4.2.2.

The vertical descent of all numerical runs is plotted in Figure 5.4. There are three trends to extract from this plot. Firstly, vertical descent is related to buoyancy. For thermals with equivalent radius, those with a greater buoyancy (i.e. a larger potential temperature perturbation) descend faster. Secondly, vertical descent is related

to radius. For thermals with equivalent buoyancy, those with a smaller radius descend faster. Lastly, it is possible for thermals with different buoyancy and radii to descend at approximately the same rate. A good example of this is B0.5r5 (solid yellow line) and B1r7 (dotted blue line) which have relative buoyancy of 0.5 and 1 and radii of 500 and 700 m, yet descend at almost the same rate. The first two trends are consistent with what one should expect. For two identical parcels of fluid, the one with greatest buoyancy descends the fastest. The reduced gravity $g'$ is related to buoyancy $B$ by $B = g'V$, so if the volume $V$ is consistent between thermals then the thermal with the greater buoyancy has a larger reduced gravity and therefore descends faster. The third trend - similar descents for thermals of different properties is not as immediately intuitive and requires examination of the similarity solutions for a descending thermal.

From Morton, Taylor, and Turner (1956), Rooney (2015) adapts thermal similarity solutions to express the width $b$, vertical velocity $w$ and the reduced gravity $g'$ in terms of the buoyancy $B$ and $z$,

$$b = \alpha z, \tag{5.21a}$$

$$w = (Fr_T c^{1/2} \alpha^{-1}) B^{1/2} z^{-1}, \tag{5.21b}$$

$$g' = (m^{-1} \alpha^{-3}) B z^{-3}, . \tag{5.21c}$$

where $Fr_T$ is the Froude number of thermal, $m$ is the thermal shape factor and $\alpha$ is the entrainment constant. Notice that (5.21) has an unphsyical origin at $z = 0$, it is expected that an atmospheric thermal originates with some finite initial radius $b_0$. Therefore Rooney (2015) introduces the concept of a distance $z_v$ which is the distance that a thermal with initial radius would have travelled from a virtual point source,

$$z_v = \alpha^{-1} b_0. \tag{5.22}$$

The solutions (5.21) are now re-written using (5.22) instead of $z$ as:

$$b = b_0 + \alpha z, \tag{5.23a}$$

$$w = (Fr_T c^{1/2} \alpha^{-1}) B^{1/2} (z + z_v)^{-1}, \tag{5.23b}$$

$$g' = (m^{-1} \alpha^{-3}) B (z + z_v)^{-3}. \tag{5.23c}$$

Lastly, by integration of (5.23b) the vertical descent and time are related by

$$z + z_v = (2 Fr_T c^{-1/2} \alpha^{-1} B^{1/2} t)^{1/2}. \tag{5.24}$$

Figure 5.5 plots time, non-dimensionalised by $t_0 = b_0^2 B^{-1/2}$ against the thermal radius $b$ divided by the vertical descent. A constant value of approximately $\alpha = 0.26$ is found in the descent stage, before $t/t_0 = 10$. Similarly, the Froude number is defined as

$$Fr_T = \frac{w}{(g'b)^{1/2}}, \tag{5.25}$$

and is plotted in Figure 5.6 against non-dimensional time. There large variation in Froude number as the thermal accelerates and then begins to experience the surface. Since the entrainment relationship only appears to hold before $t/t_0 = 10$, it seems logical to apply the same constraint to the Froude number. A representative value of 1.2 is selected. Using these values of $\alpha$ and $Fr_T$, and taking the thermal shape factor $m = 3$ as found by Scorer (1957), gives the relation

$$z + z_v = 2.63 B^{1/4} t^{1/2}. \tag{5.26}$$

To allow comparison with thermals across scales, the vertical descent is non-dimensionalised in Figure 5.7. In this plot, $(z + z_v)$ is translated to 0 for all runs and scaled by initial radius $b_0$. Time is non-dimensionalised by $t_0 = b_0^2 B^{-1/2}$. Figure 5.7 shows a strong collapse of the different thermals onto one line, suggesting that the scaling works well. The dashed line is the linear best fit to the data, and this study suggests the

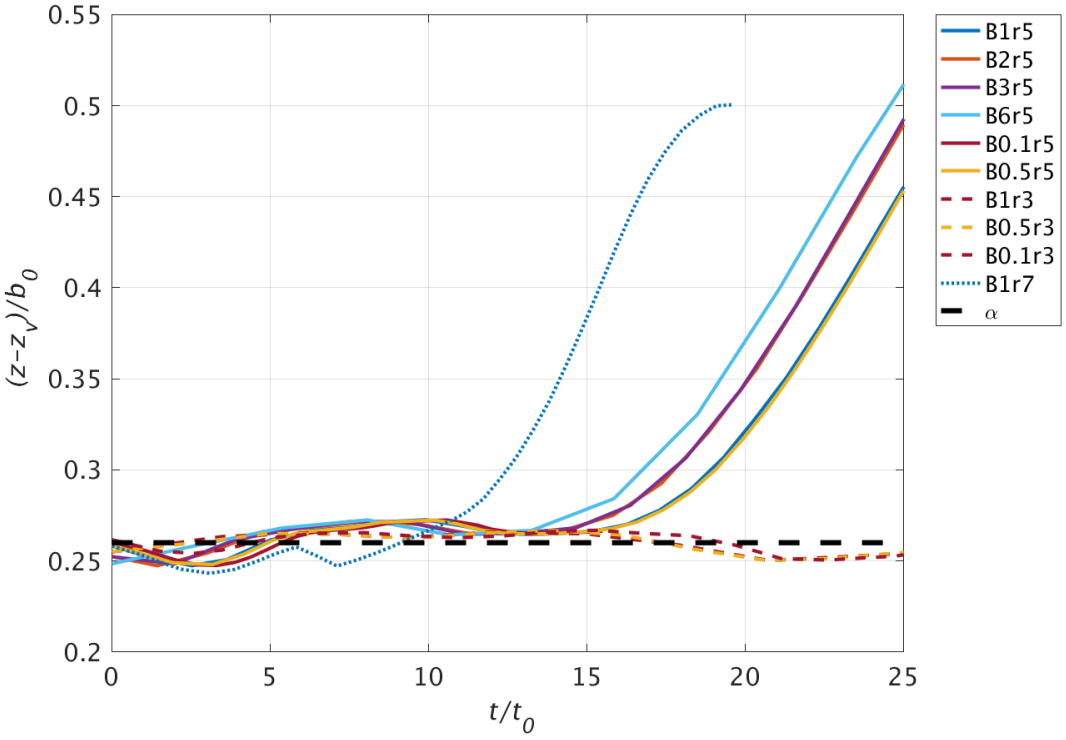


FIGURE 5.5: Non-dimensionalised time versus vertical descent divided by radius. The black dashed line is a value of 0.26.

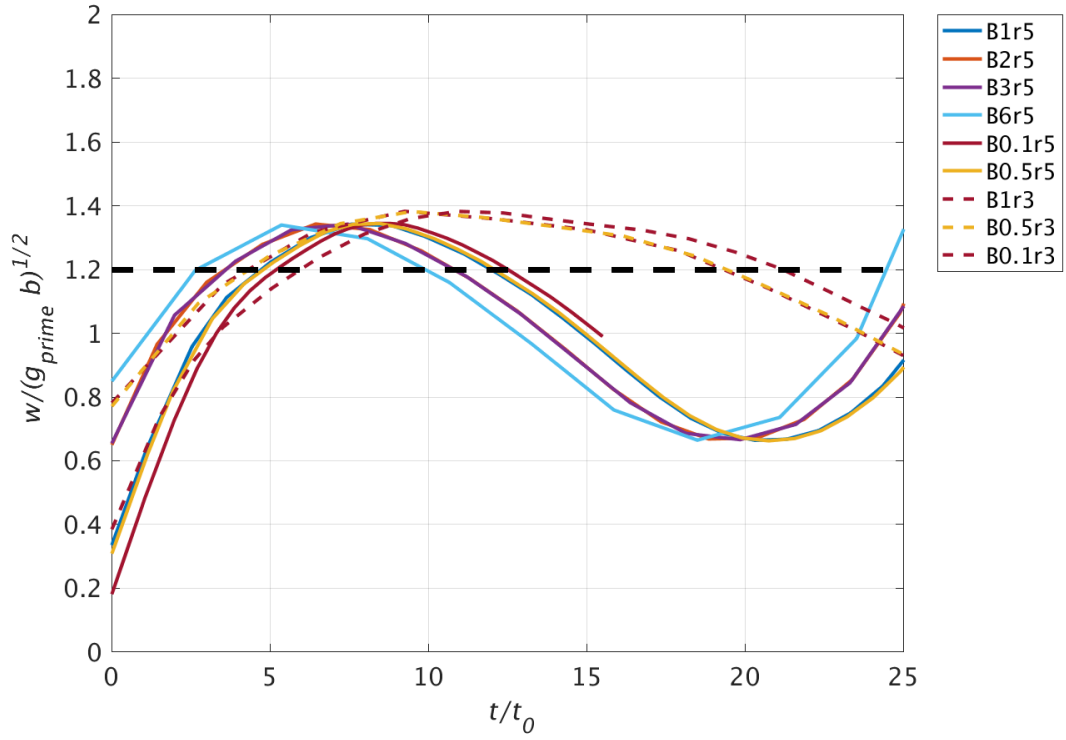


FIGURE 5.6: Non-dimensionalised time versus the Froude number. The black dashed line is a value of 1.2.

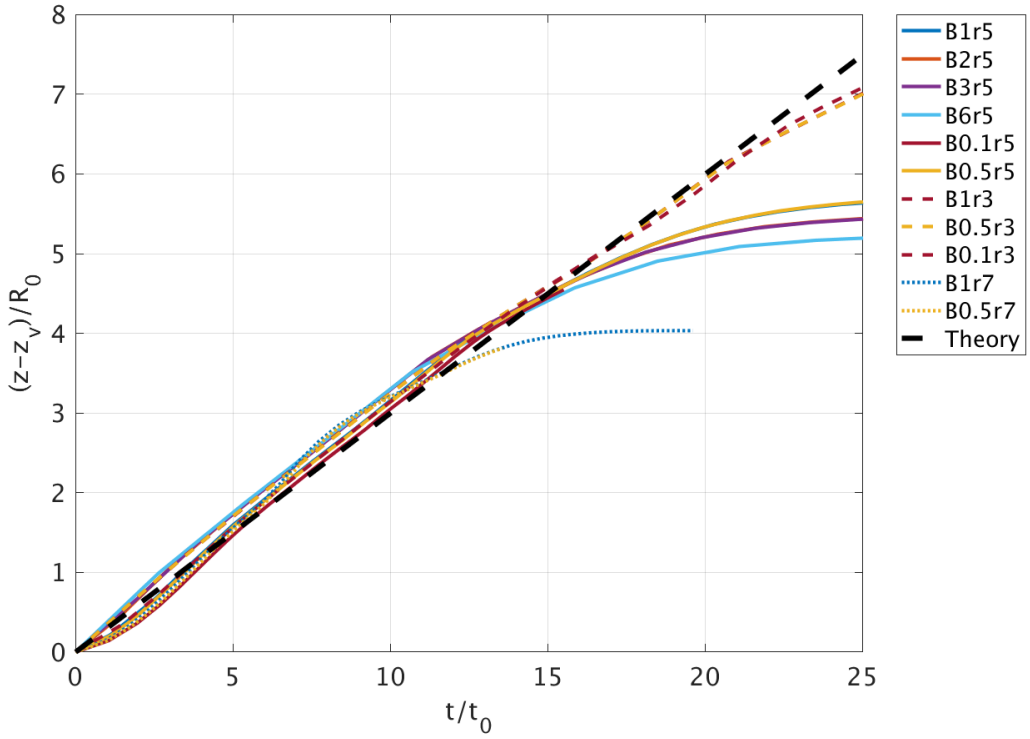


FIGURE 5.7: Vertical descent of all model runs, non-dimensionalised by initial radius $b_0$ and $t_0 = b_0^2 B^{-1/2}$. The dashed black line is the best fit.

functional relationship

$$\frac{z - z_v}{b_0} = 0.3\frac{t}{t_0}. \tag{5.27}$$

Notice that this functional relationship is not consistent with the similarity solutions from Rooney (2015) where a $z \propto B^{1/4}t^{1/2}$ relationship is expected. However, there is an argument that for thermals within this study's parameter range of $H = 3000$ m and radii $300 - 700$ m, never fall far enough for a convincing $z \propto B^{1/4}t^{1/2}$ relationship to develop. Rooney (2015) did show thermals that fitted this curve, but those thermal required release heights of 9000 m. This study suggests that for atmospheric cases originating below 3 km, (5.27) provides a simple estimation of vertical descent versus time. The non-dimensionalised vertical descent of the model runs can be compared the non-dimensionalised laboratory experiments from Chapter 3. Figure 5.8 is the same as Figure 5.7 but with the $x$-axis reduced and the vertical descent of all laboratory experiments added (see Section 3.3.5, Figure 3.16). Four laboratory experiments are plotted, two 2s saline releases designed to be quasi-thermal and two 5s saline releases designed to be a continuous source. The 2s saline releases have

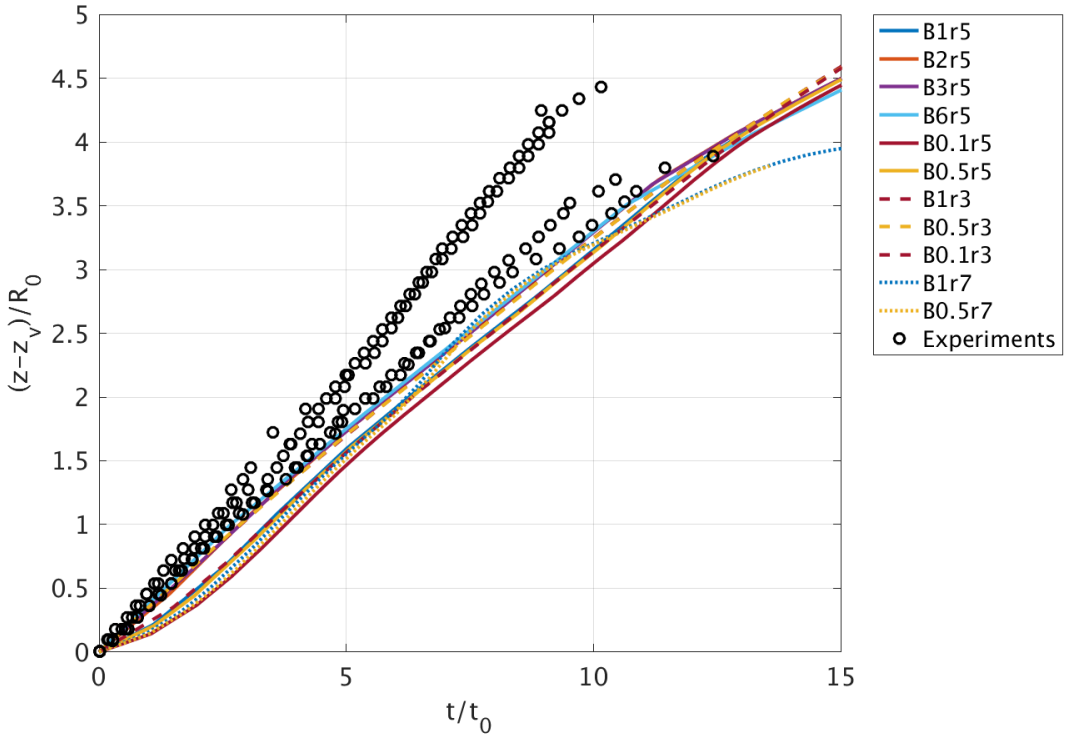


FIGURE 5.8: Vertical descent of all model runs, non-dimensionalised by initial radius $b_0$ and $t_0 = b_0^2 B^{-1/2}$. The dashed black line is the best fit. Vertical descent of all laboratory experiments from Chapter 3 are plotted as the black circles.

a descent rate in good agreement with the numerical runs. The 5s saline release is initially in good agreement until diverging from the numerical runs at $(t/t_0 > 4)$, this faster rate of descent is attributed to the greater negative buoyancy within the head of the descending fluid (discussed in Section 3.3.5). In the early stages of release $(t/t_0 < 5)$, the experimental releases descent faster than in the numerics. This speed up is probably down to the method of fluid release. In the LES the thermal is generated by an instantaneous release of cold fluid at rest, while in the laboratory experiment a pneumatic valve was opened from a header tank to release a controlled volume of saline, which added an extra initial momentum in the saline releases. The consistency in rate of vertical descent between scaled laboratory and numerical simulations provides confidence in each respective methodology and the results they generate.

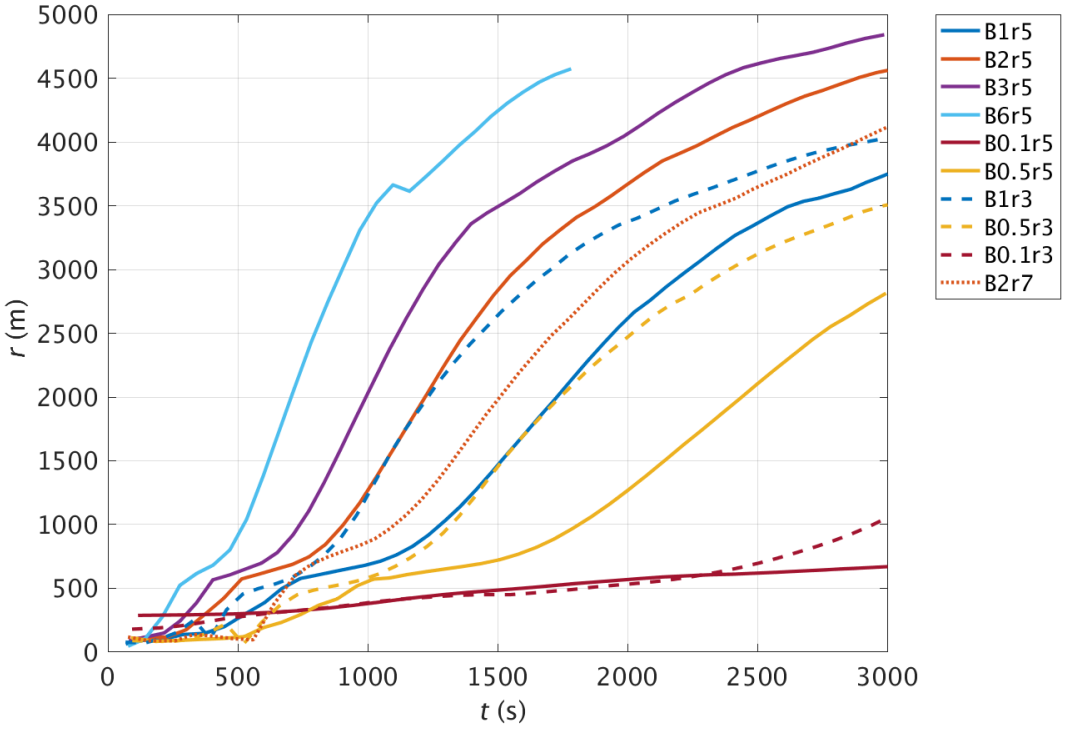


FIGURE 5.9: Radial propagation (m) against time (s) for all model runs

### 5.4.3 Radial Propagation

Radial propagation is calculated using a similar methodology to vertical descent. The 'radial propagation' of thermal is the horizontal distance the centre of mass in a 2D slice of the domain has travelled from the origin. Since all thermal releases are symmetric and centred at the middle of the domain, the centre of mass always originates at $r = 0$. The centre of mass is calculated as the averaged radius of all identified points of buoyant fluid. Identification of buoyant points depends on a threshold value $\alpha$. A detailed discussion of this methodology and the values of $\alpha$ is available in Section 4.2.2.

The radial propagation of all numerical runs is plotted in Figure 5.9. Time is measured from the release of thermal at $H = 3000$ m, therefore $r$ plotted in Figure 5.9 shows the radius of thermal and subsequent gravity current throughout both the descent and radial spread. It is possible to estimate the time of impact of thermal

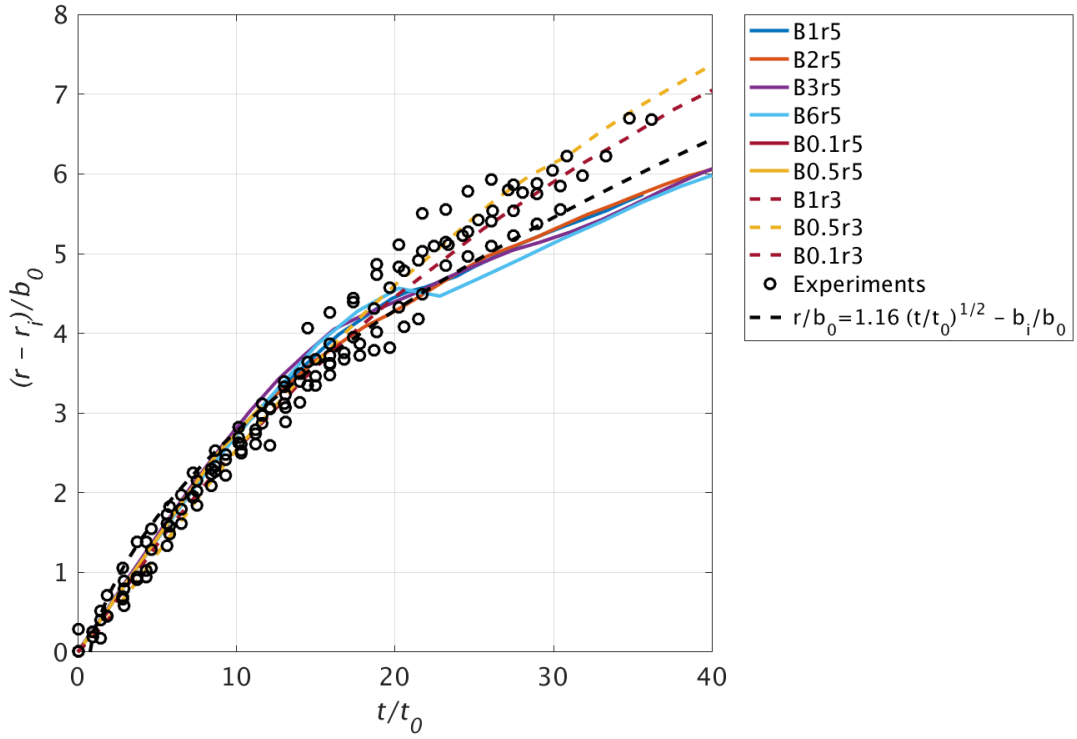


FIGURE 5.10: Time versus radial spread, using the scaling of the initial radius $b_0$ and $t_0 = b_0^2/B^{1/2}$
. The numerical runs are plotted as the coloured lines, the scaled experimental results from Figure 3.22 are plotted as black circles and (5.28) is plotted as the dashed black line.

from the rapid increase of radius, for example the time of impact for B1r5 is approximately 1250s, B6r5 is 500s and B0.1r5 and B0.1r3 do not hit the surface before the end of the model run. As seen in the vertical descent, there are two trends to extract from this plot. Firstly, radial propagation is related to initial buoyancy, thermals with equivalent radius and greater buoyancy travel faster. The importance of initial radius seems less clear in Figure 5.9, thermals with the same buoyancy but a smaller initial radius spread faster across the combined descent and spread phases. However, the actual rate of spreading of thermals with different radii after impact appears harder to distinguish. For example, if B1r7 is translated by it's time of impact, it has a similar profile to B1r5. The similarity solutions proposed by Rooney (2015) are now considered to help shed light on this relationship between thermal and rate of propagation.

In Section 3.3.6, this study proposed

$$r = k_2 B^{1/4}(t - t_i)^{1/2} + r_i, \tag{5.28}$$

where $R_0$ is taken as the radius of impact $r_i = b_0 + \alpha H$.

By using the length scale of the initial radius of thermal $b_0$ and the characteristic time $t_0 = b_0^2/B^{1/2}$, it is now possible to compare the radial spread of the laboratory experiments with the numerical runs. Figure 5.10 plots the scaled radial propagation of both the numerical runs and the laboratory experiments from Chapter 3, along with (5.28), this study's proposed theoretical relation. The result is a agreement of theory, experiments and numerical simulations, suggesting that (5.28) can be used to calculate the radial spread of thermals across both scales.

## 5.5 Energy Relations of Thermals

So far in this chapter, numerical simulations of negatively buoyant thermals have been created and used to validate proposed similarity solutions in Rooney (2015) and experiments in Chapter 3. In Section 5.2, the thermal similarity solutions from Rooney (2015) were developed further to create new expressions that relate the kinetic and potential energy of the thermal throughout the thermal's descent and spread to the initial buoyancy, radius and height. This new treatment not only builds on the work of Rooney (2015) by expanding the similarity solutions, but also allows comparison of these buoyancy based relations to an alternative energy based theory proposed by Romps and Jeevanjee (2016).

### 5.5.1 Potential Energy in Thermals

Section 5.2 showed that the potential energy of a thermal is

$$PE = \rho_0 BH - k_1 \rho_0 B^{5/4} t^{1/2}, \tag{5.29}$$

where $k_1 = [2Fr_T c^{1/2} \alpha^{-1}]^{1/2}$. In Section 5.4.2, this study found $\alpha = 0.26$ and $Fr_T = 1.2$, and $c = 3$ from Scorer (1957), which implies $k_1 \approx 4$.

The potential energy (PE) for all model runs is plotted against the distance $z$ that

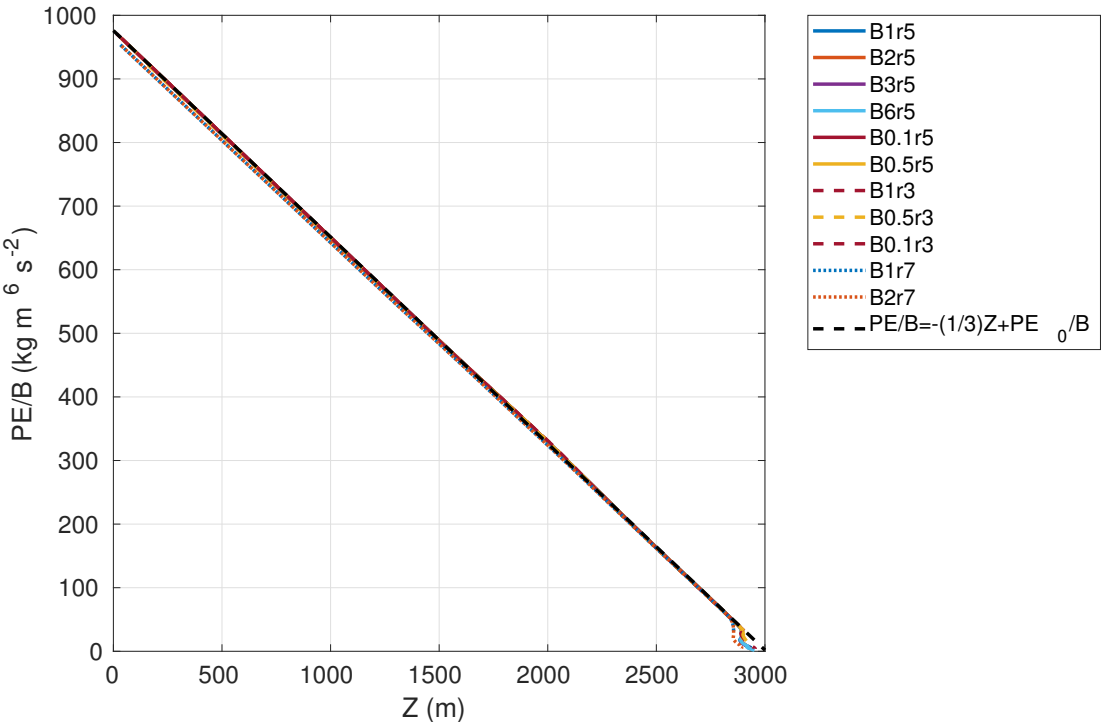


FIGURE 5.11: Potential energy (kg $m^2$ $s^{-2}$) versus height of thermal (m)

the thermal has travelled from source in Figure 5.11. PE is calculated across the entire grid in the model. MONC does not output 3D density fields, therefore the potential temperature fields are used to estimate $\Delta\rho$ using the assumption

$$\frac{\Delta\rho}{\rho_0} = \frac{\Delta\theta}{\theta_0} \tag{5.30}$$

where $\rho_0$ and $\theta_0$ are background reference densities and potential temperatures. Since all model runs are released from the same height, the PE can be simply scaled by the initial buoyancy of thermal (the total potential temperature or density difference providing the only difference in initial PE). All model runs collapse onto a single line which, as expected, reduces from a maximum value to close to 0 as the thermal reaches the surface.

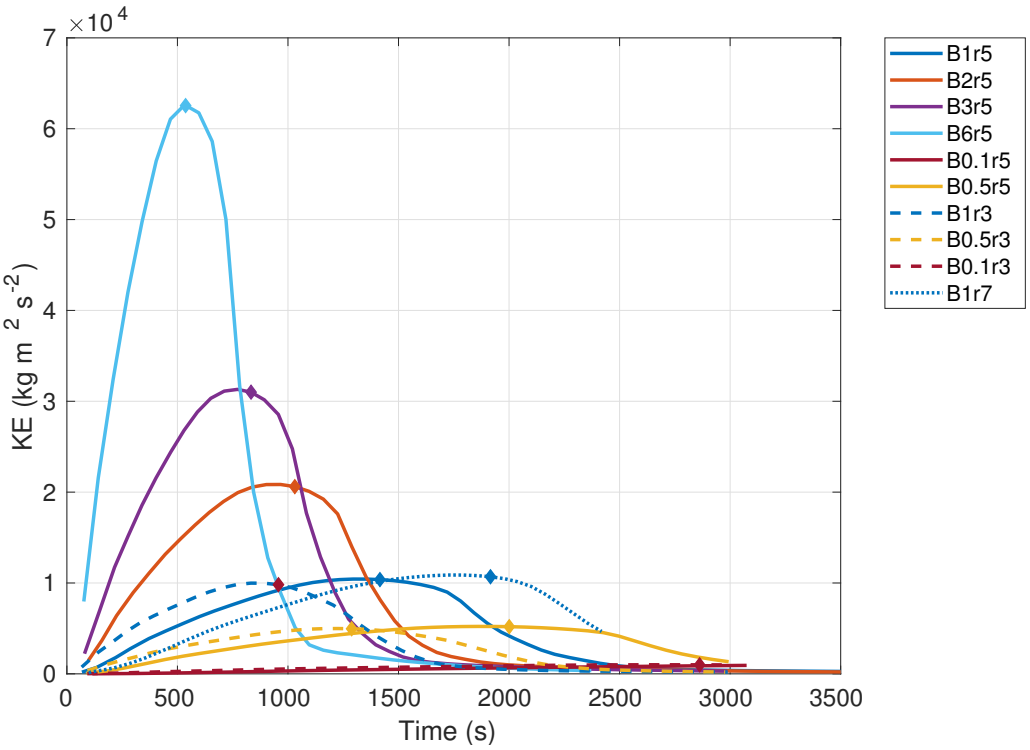


FIGURE 5.12: Time (s) versus kinetic energy (kg m$^2$ s$^{-2}$) across the grid domain. The point of impact is marked on each line.

### 5.5.2 Kinetic Energy in Descending Thermals

As the thermal descends, PE is converted into kinetic energy (KE). From Section 5.2, the KE of the descending thermal is:

$$KE_v = \frac{1}{2}\rho\alpha Fr_T^2(k_2+1)Bz. \tag{5.31}$$

where $k_2$ is an empirically determined constant.

The KE for all numerical model runs is plotted in Figure 5.12. Resultant KE is a output diagnostic from MONC (`reske`) and is calculated by integrating the three components of velocity $(u, v, w)$ over the entire grid. Since the thermal is the only source of energy in the model, the KE for the entire grid can be attributed to the behaviour of the thermal. Figure 5.12 shows KE is related to initial buoyancy and radius. For equivalent radii, larger initial buoyancy results in a greater maximum KE. Whilst thermals with the same buoyancy but different initial radii have approximately the same maximum KE release. However, that maximum occurs at different times, smaller radii result in a maximum KE occurring sooner. These trends are

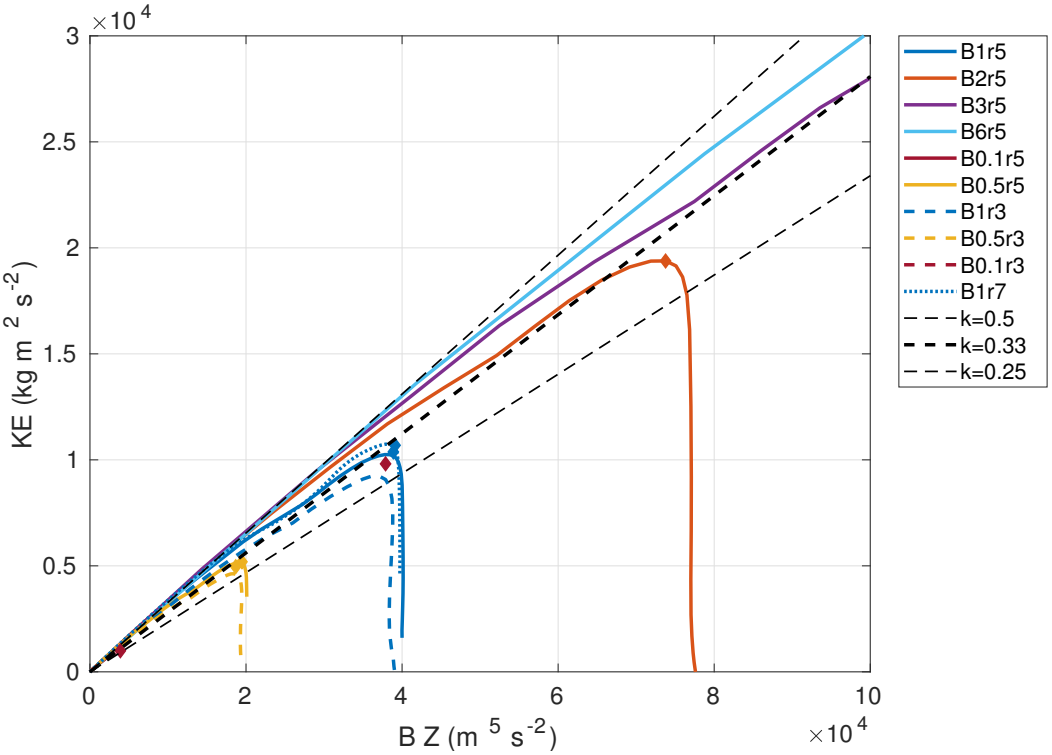


FIGURE 5.13: Buoyancy scaled vertical propagation versus kinetic energy (kg m$^2$ s$^{-2}$) over the entire grid

not surprising, all of the energy in the system results from the negative buoyancy. Therefore, larger negative buoyancy result in greater KE. Similarly, thermals with different radii but the same buoyancy generate the same KE because they have the same amount of initial integrated energy. The estimated time of thermal impact is marked on each line on Figure 5.12. In all cases, the maximum KE is at the point of impact (the condition for a thermal to impact is $z < b_0/2$).

The relationship between KE and vertical descent is plotted in Figure 5.13. Vertical descent has been scaled by initial buoyancy. The point of thermal impact is marked for each thermal. All of the model runs collapse onto approximately a single line for the extent of their vertical descent, although runs with greater B have slightly steeper gradients. The derived expression for KE in the vertical (5.31) is plotted as the dashed black lines. As in Section 5.4.2, the Froude number and entrainment constant are taken as 1.2 and 0.26 respectively. Three different values for $k_2$, are plotted in Figure 5.13. $k$ defines the assumed relationship between $w$ and $u_r$ by $u_r = k_2 w$. There is good agreement between (5.31) and the model results when

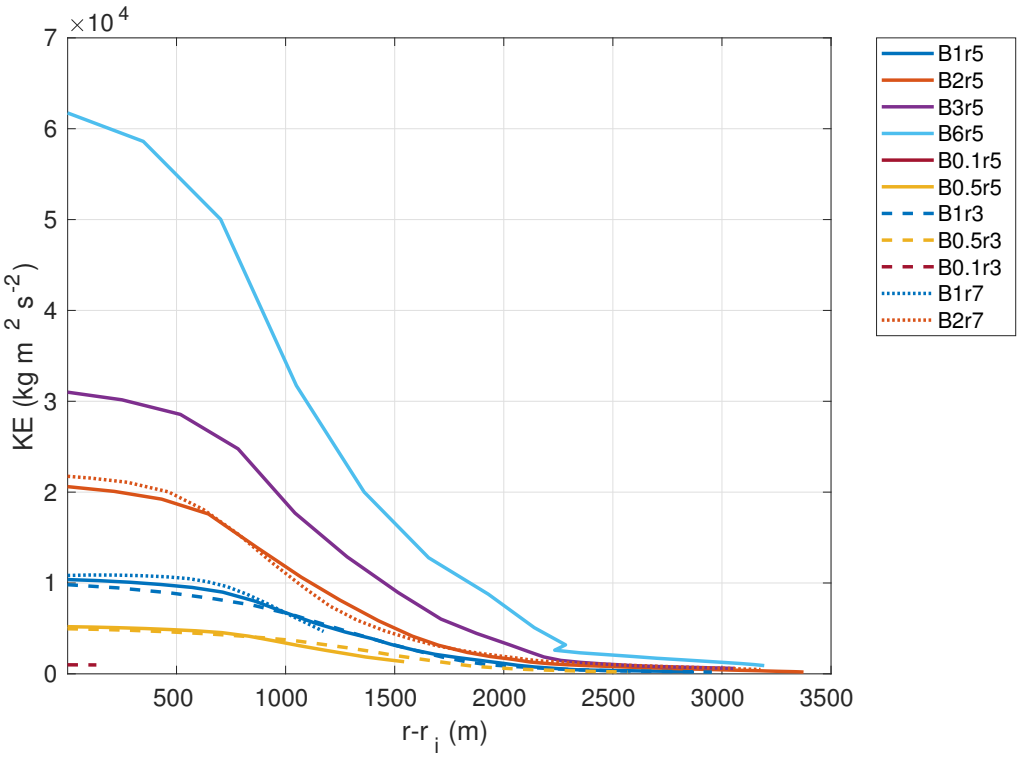


FIGURE 5.14: Radial propagation (m) after impact versus total kinetic energy (kg m$^2$ s$^{-2}$) across the domain grid.

a value of $k_2 = 0.33$ is selected. One could dedicate a significant amount of time to exploring the relationship between $u_r$ and $w$ and perhaps suggest a value of $k_2$ based on more fundamental principles, however, it appears that the assumption of a simple linear relationship is one that is both practical and works well.

### 5.5.3 Kinetic Energy in Gravity Currents

After the thermal has hit the surface, it propagates out radially from the centre of impingement. The thermal has transitioned to an axisymmetric gravity current. Radial propagation is plotted against the total KE of the grid domain in Figure 5.14. Following the assumption that at initiation, all of the bubbles energy is PE, then at impact, the vast majority of that TE has been converted to KE (i.e $TE \sim KE_r$. Therefore, Figure 5.14 plots the energy dissipation of the bubble with radial propagation. As the gravity current propagates, KE is dissipated primarily through entrainment, surface drag and form drag (Simpson, 1999). At impact, $(r - r_i = 0)$ the amount of KE is proportional to the initial buoyancies of bubbles. For example, B6r5 has approximately double the KE at impact as B3r5, which supports Fig. 5.13 which showed that

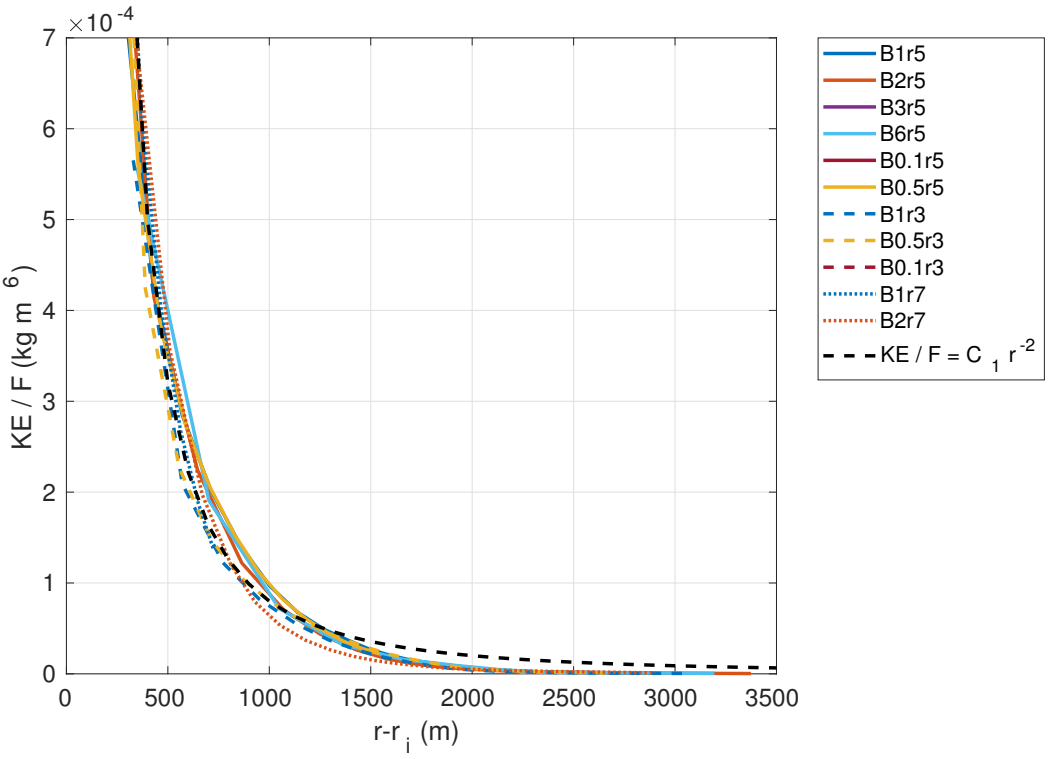


FIGURE 5.15: Buoyancy scaled KE versus radial propagation. KE is calculated across the entire domain. The dashed line is (5.32).

the bubbles gained KE at rate proportional to their initial buoyancy and height. For example, B1r3 (blue dotted line), B1r5 (blue solid line) and B1r7 (blue dashed line) are roughly superimposed upon each other. Interestingly, the KE for all bubbles is essentially dissipated around $(r - r_i = 3000)$ m, regardless of the bubbles initial energy or buoyancy. Zooming into the $2500 < (r - r_i) < 3000$ m section of Figure 5.14 shows that KE is still monotonically ordered by buoyancy. However, both the total magnitudes and differences of KE between bubbles has become negligible. The implications for this are that downbursts have a finite lifetime determined by the sinks of energy rather than their initial properties.

Section 5.2 suggested that the KE of the spreading gravity $KE_r$ is of the form:

$$KE_r = \frac{1}{2}\rho\pi H^3\lambda^2 c\alpha^3 Fr_c^2 \left(1 + \frac{b_0}{\alpha H}\right)^3 Br^{-2} f, \tag{5.32}$$

where $\rho$ is the density, $H$ is the initial height of bubble, $\lambda$ is a dimensionless constant, $m$ is the thermal shape factor, $\alpha$ is the entrainment constant and $Fr_c$ is the gravity current Froude number. $f$ is an empirical function proposed as $(r'_{max}/R_0)^{-1.3}$ by

Rooney (2015). For simplicity, two variables are defined:

$$K_1 = \frac{1}{2}\rho\pi H^3\lambda^2 c\alpha^3 Fr_c^2, \tag{5.33}$$

and

$$F_1 = \left(1 + \frac{b_0}{\alpha H}\right)^3 Bf. \tag{5.34}$$

(5.33) and (5.34) reduce (5.32) to

$$KE_r = K_1 F_1 r^{-2}. \tag{5.35}$$

Both $K_1$ and $F_1$ are constants, although $F_1$ is different for each individual bubble while $K_1$ is the same for all of these runs (with fixed height $H = 3000$ m).

Radial propagation is plotted against $KE_r/F_1$ in Figure 5.15. In these experiments, $f$ is defined differently to Rooney (2015). Instead of considering the maximal radial propagation $r'_{max}$, the centre of mass after impact is used $(r - r_i)$. Furthermore, the length scale is simply taken as $b_0$ instead of $R_0$ ($R_0$ is approximately the radius of thermal at impact). Therefore,

$$f = \left(\frac{r - r_i}{b_0}\right)^{-1.3}. \tag{5.36}$$

This formulation of $f$ was found to yield a better collapse of all model results. In Figure 5.15, all bubbles collapse onto a single line, suggesting that the form of (5.36) and therefore (5.35) is valid. Using (5.32), the KE of bubble in the spreading phase can be estimated as function of i) the bubble's initial properties at origin and ii) the radial propagation of bubble. A complete set of KE and PE equations in both the descent and spreading phase, based on the similarity solutions from Rooney (2015), have now been presented and validated using LES numerical simulations.

## 5.6 Comparison of Two Methods for Modelling Cold Pools

A significant part of the work in this study has focused on validating, modifying and expanding on the similarity solutions proposed by Rooney (2015). However, Rooney (2015) does not possess a monopoly on the spread of downbursts. Section 5.2 devoted significant effort to establishing if the work of Rooney (2015) could be extended to the energetics. The motivation for that section, beyond offering an extension to Rooney (2015), is the opportunity to now compare those buoyancy-based relations with an energy-based theoretical model proposed by Romps and Jeevanjee (2016) (referred to from now on as RJ).

RJ construct analytical equations based on kinetic and potential energy balances for the collapse and spread of a cold cylinder of fluid. The application of their theory is to determine the size and lifetimes of 'cold pools'. The cold pool is modelled as a cylinder with initial radius $R_0$, height $H_0$ and density different $\rho_0'$. The cylinder is initially at rest at the surface. After release, the cylinder collapses and spreads axisymmetrically with radius $R(t)$, height $H(t)$ and $\rho'(R)$. A conceptual schematic of this set-up is shown in Figure 5.16.

By considering the energy equation, where change of the cold pool's total energy TE, which is the sum of its potential energy PE and its kinetic energy KE is equal to the sinks of energy

$$\frac{\mathrm{d}}{\mathrm{d}t}TE = \frac{\mathrm{d}}{\mathrm{d}t}(KE + PE) = \text{sinks}. \tag{5.37}$$

RJ suggest there are five sinks of energy, which are caused through entrainment, surface drag, form drag, other pressure forces and surface enthalpy fluxes. An assessment of these sinks, and subsequent simplification of higher order terms provides an equation set for the development of the cold pool,

$$R(t) = R_0 + \frac{1}{\epsilon}\log(1 + t\epsilon U_0), \tag{5.38a}$$

$$H(R) = H_0\left(\frac{R_0}{R}\right)^2 \exp\left[\epsilon(R - R_0)\right], \tag{5.38b}$$

$$\rho'(R) = \exp^{-\epsilon(R-R_0)}\left(\rho_0' + \frac{2}{9}c_{ds}\rho_s'\frac{1}{R_0^2 H_0}(R^3 - R_0^3)\right). \tag{5.38c}$$

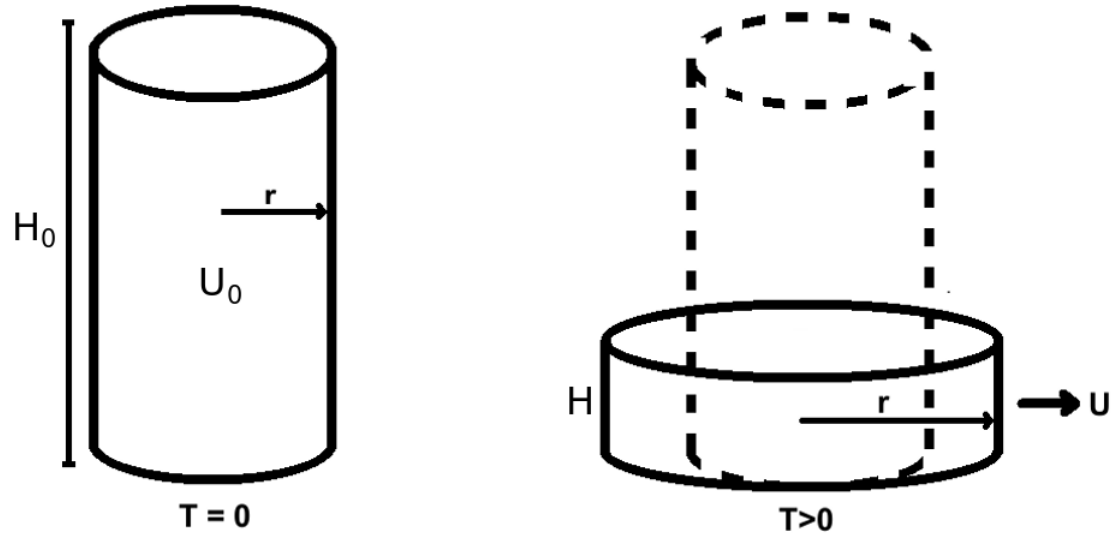


FIGURE 5.16: Conceptual schematic of collapsing cold pool cylinder model proposed by RJ. At time $T = 0$ the cylinder has height $H_0$ and radius $R_0$. The complex initial change of KE to PE in the collapse of the cylinder is not modelled, instead the cylinder is prescribed with an initial horizontal velocity $U_0$. At time $T > 0$, the height $H(t)$, radius $R(t)$ and $\rho'(R)$ are time dependent functions, in the radial co-ordinate $r$.

$c_{ds}$ is the surface drag coefficient, $\rho'_s$ is the 'density of air that would be in equilibrium with the surface'. $\epsilon$ is the fractional entrainment per distance travelled by the cold pool, with units $\mathrm{m}^{-1}$. $U_0$ is a concession to the complex interaction between PE and KE during the initial collapse of cylinder. Instead of modelling these detailed interactions, the cold pool is prescribed with an initial horizontal velocity $U$ equal to

$$U_0 = \sqrt{\frac{2\beta g \rho'_0 H_0}{\rho}}, \tag{5.39}$$

where $\beta$ is the 'fraction of the cold pool's initial potential energy that is immediately or eventually converted to kinetic energy of the cold pool'. A detailed discussion of these assumptions and derivation of RJ is available in Chapter 2, Section 2.3.

Before starting any analysis using the MONC numerical runs, it is useful to first think about the fundamental similarities and differences between these two proposed theories. Both of these theories demand: i) conservation of volume, ii) conservation of momentum and (iii) conservation of density deficiency. The differences

TABLE 5.3: Comparison of theories for buoyant spread

| | **Rooney (2015)** | **Romps and Jeevanjee (2016)** |
|---|---|---|
| **Origin** | Sphere at height | Cylinder at surface |
| **Equation Shape** | Power | Logarithmic |
| **Radial Propagation** | $[2Fr_c\lambda^{1/2}B^{1/2}(t-t_i)]^{1/2}+R_0$ | $R_0+\frac{1}{\epsilon}\log(1+t\epsilon U_0)$ |
| **Entrainment** | Dimensionless constant | Fractional entrainment ($m^{-1}$) |
| **Froude Number** | Constant | 0 to inf. |
| $U_0$ | $Fr_c\lambda^{1/2}B^{1/2}R_0^{-1}$ | $(2\beta H_0)^{1/2}B^{1/2}$ |
| **Buoyancy** | Constant, conserved, global | 'Effective buoyancy' |
| **Radius of Death** | Inf | $R_0\left(\frac{9}{2c_{ds}}\frac{H_0}{R_0}\frac{\rho_0'}{\rho_s'}\right)^{1/3}$ |

are only in how these conservation equations are implemented and the assumptions in simplification. This study does not aim to determine which theory is 'right' or 'wrong' since clearly both approaches are valid methodologies for tackling the spread of negatively buoyant fluid, instead the differences will be considered and suggestions made for which theory best fits the numerical set-up of this study.

Table 5.3 summarises the key physical and conceptual differences between the two theories. Firstly, the theories are formulated for different purposes. Rooney (2015) offers a similarity solution for a negatively buoyant sphere that falls, impacts the ground and spreads radially. Whilst, RJ models the spread of a cold pool as a negatively buoyant collapsing cylinder on the surface. Obviously, the descent stage from Rooney (2015) is not relevant to RJ, other than the initial conditions of the spreading gravity current in Rooney (2015) are determined by the thermal's behaviour in the descent stage. The gravity current in RJ, has no prior 'knowledge'

of where it originated or any properties before cylinder release apart from the prescribed $U_0$. Despite this difference in origin, comparing the two theories is still relevant since the initial velocity scale of the gravity currents are analogous to each other. RJ prescribes $U_0 = (2\beta H_0)^{1/2} B^{1/2}$, while the equivalent from Rooney (2015) is $U_0 = Fr_c \lambda^{1/2} B^{1/2} R_0^{-1}$.

A fundamental difference is the nature of the 'shape' of each equation set. Despite being formulated using similar conservation equations, the actual form of the equation set is quite different; Rooney (2015) similarity solutions are all power laws, whilst RJ are logarithmic. This difference in shape will inevitably create differences in the estimation of the radial propagation, gravity current height and density difference. The two different expressions for radial propagation are shown in Table 5.3. Rooney (2015) has a $r \propto t^{1/2}$ relation, while RJ suggest $r \propto \log t$.

Definitions of buoyancy, entrainment and the Froude number are also different. RJ argues that the total buoyancy B is not as important in the collapse and spread of a cold pool as the 'effective buoyancy', or the buoyancy of the leading edge (Davies-Jones, 2003). This 'effective buoyancy' can be only 25% of the total buoyancy. This study used a similar argument in the descent stage of the laboratory releases in Chapter 3, when in Section 3.3.5 it was suggested that the rate of vertical descent depends on the buoyancy within the leading vortex ring rather than the total buoyancy of the entire saline release. RJ then argues that an assumption of a constant Froude number is inadequate for modelling cold-pool dynamics and entrainment is defined as a fractional entrainment per distance travelled by the cold pool's front.

In order to compare RJ to the MONC numerical runs, which are all spherical and start elevated at 3000m, this study proposes some adaptations to RJ. Firstly, $U_0$ is defined at the surface to represent the complex transition of PE to KE in the cylinder collapse. Now, in the model runs the thermal impacts the ground and adjusts into a gravity current, in a similarly complex transition. Following in the same vein as RJ, instead of trying to provide an analytical solution for this chaotic stage, a modified

characteristic velocity $U_{0M}$ is prescribed,

$$U_{0M} = \sqrt{\frac{2\beta g \kappa \rho_t' (b_0 + \alpha H)}{\rho}}. \tag{5.40}$$

(5.40) is this study's modified version of (5.39), where the initial characteristics of the cylinder are replicated by the properties of the thermal at impact. There are two differences: i) the initial density difference of cylinder $\rho_0'$ is replaced by $\rho_t'$, where $\rho_t'$ is the initial density difference of thermal, at the origin height $H = 3000$ m. As the thermal falls, entrainment causes the density difference to reduce, $\kappa_i$ is the fraction of the remaining density difference of thermal at impact (analogous to the initial density difference of cylinder in RJ). ii) $H_0$, the height of cylinder is replaced with the radius of bubble impact, $r_i = (b_0 + \alpha H)$ where $H = 3000$ m is the height of the bubble above the ground. Using $r_i$ assumes that the bubble is quasi-spherical when it impacts, and therefore the distance from centre of bubble to the top edge is also approximately $r_i$.

Figure 5.17 plots the $\theta$ perturbation of descending bubble, divided by the initial $\theta_p$ perturbation of source against buoyancy scaled time ($t_0 = (b_0^2/B_0^{1/2})$) for the modelled bubble runs. The impact time for all bubble runs is marked with the black vertical line at ($t/t_0 \approx 22$). In the initial stages of descent ($0 < (t/t_0) < 10$), $\theta$ remains constant as the core of the bubble has not yet been entrained. $\theta$ subsequently reduces as the ambient fluid and bubble are mixed. Bubbles with the same radius, all collapse onto a single line. However, those with different initial radii, lose $\theta$ at slightly different rates. The smallest radii bubbles initially lose their $\theta_p$ at the fastest rate, but then after impact the magnitude of the $\theta_p/\theta_i$ ratio is maintained at a higher rate, with the equivalent being true for larger radii bubbles. In (5.39), $\rho_0'$ is the density perturbation of cylinder in release. $\rho_0'$ is replaced with $\kappa\rho_t'$ in (5.40), where from Figure 5.17 and using the assumption that small density differences are equivalent to small potential temperature differences, $\kappa$ is the fraction of remaining density difference, estimated as 0.4. The use of the modified $U_{0M}$ allows the theory of Rooney (2015) and RJ to be compared. To illustrate how the two conceptual theories compare

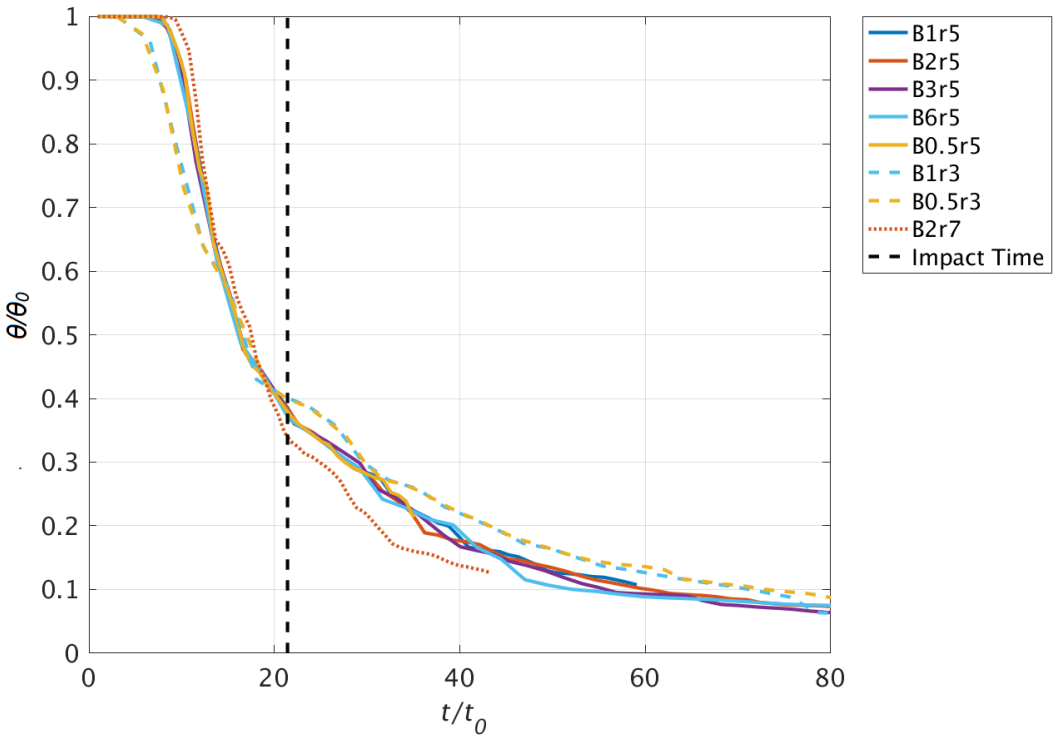


FIGURE 5.17: $\theta$ perturbation of descending bubble (K), divided by the initial $\theta_p$ perturbation of source against buoyancy scaled time ($t_0 = (b_0^2/B_0^{1/2})$). Time of all bubble impacts is plotted as the vertical black dashed line.

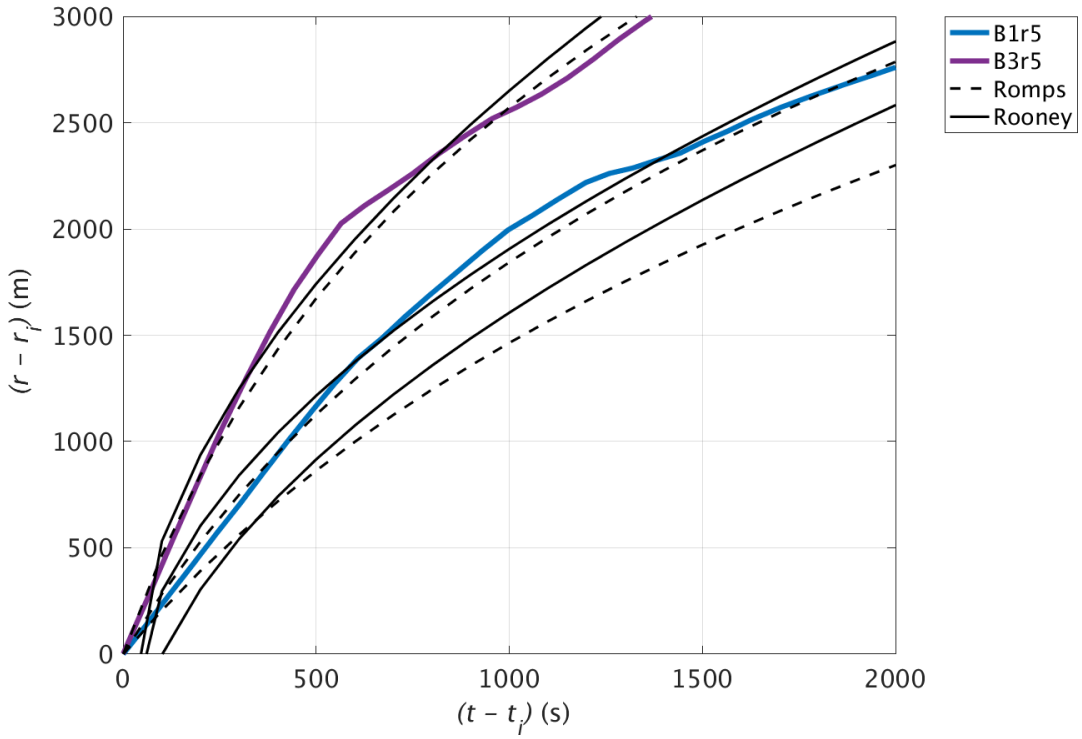


FIGURE 5.18: Radial propagation (m) for 3 different numerical model runs, displaced by radius of impact plotted against time after impact (s). Two theoretical radial propagations are also plotted, i) from (5.28) based on Rooney as the solid line and ii) from (5.40) based on Romps as the dashed line

against each other and typical numerical runs, Figure 5.19 plots the radial propagation, displaced by radius of impact, of three numerical runs: B1r5, B3r5 and B1r7. Additionally, two theoretical radial propagations for each model run are plotted i) this study's adapted radial propagation based on Rooney (2015), (5.28) (solid black line, note that these lines do not start at $(t - t_i) = 0$ because of the virtual origin) and ii) the radial propagation from RJ, (5.38a) (dashed black line) using this study's definition of $U_0 M$. Both theories suggest similar rates of radial propagation and match the modelled bubble runs relatively well. In the early stages of radial spread, RJ provides a better fit.

To quantitatively compare the two theories against the numerical runs, the ratio (RD) of radial propagation between the theory and model is plotted in Figure 5.19. RD is defined as

$$RD = \frac{r_{theory}}{r_{numerics}}. \tag{5.41}$$

Figure 5.19a plots RD using (5.28) and Figure 5.19b plots RD using (5.38a). In the far field, both theories approach RD = 1 suggesting good agreement between numerics and theory. However, around the thermal impact both theories break down. Figure 5.19 provides an indicative time scale for each theory for the readjustment phase of thermal impact as the thermal transition from vertical descent to horizontal outflow. The similarity solutions from Rooney (2015) provide an accurate estimate of radial propagation after 600 s, whilst RJ becomes accurate after 1000 s.

More fundamentally, the 'shape' of the radial propagation of the two theories is compared in Figure 5.20. Rooney (2015) proposes a power law $r \propto B^{1/2}t$, whilst RJ proposes a logarithmic function $r \propto \log B^{1/2}t$. A power law relationship can be tested by taking the natural log of both sides to provide a linear relationship, Figure 5.20a plots $\log(r)$ against $\log\left(B^{1/2}t\right)$. Similarly, the RJ relationship can tested by taking the time derivative $1/(\mathrm{d}r/\mathrm{d}t)$, which should provide a linear relationship. 5.20a plots $1/(\mathrm{d}r/\mathrm{d}t)$ against $(B^{1/2}t)$. The linear best fit of all model runs is plotted as the solid black line. The best fit is compared against the mean of all model runs (dashed line) to provide $R^2$ correlation values. $R^2$ values of 0.96 and 0.86 found for the power

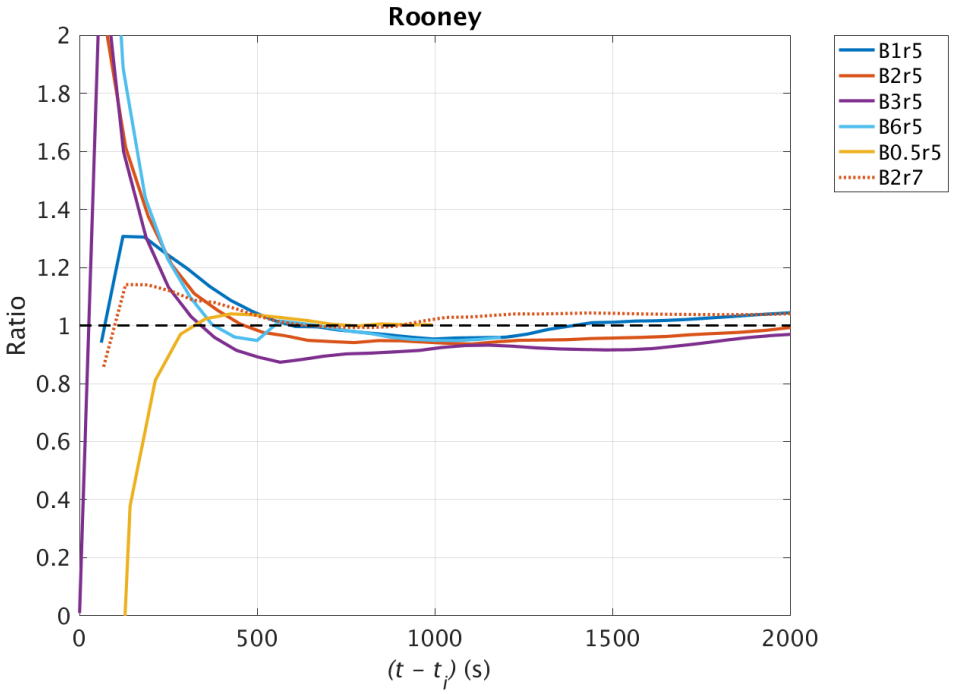


(A) Ratio of radial propagation between (5.28) and numerical models runs.

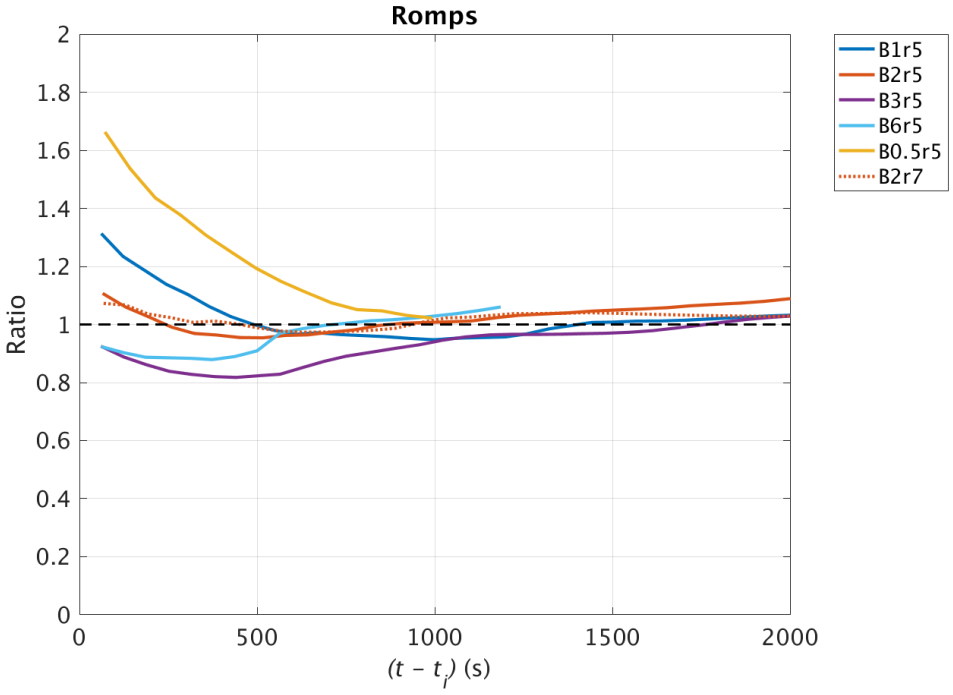


(B) Ratio of radial propagation between (5.38a) and numerical models runs.

FIGURE 5.19: Ratio between theory and numerical model runs

law relation of Rooney (2015) and the logarithmic relation of RJ. The better correlation for Rooney (2015) suggests that for this type of modelled runs, the power law relation performs better. However, there is an important caveat; this study is using the RJ theory for an application that the equation set was not originally intended for, and a series of modifications were used to make RJ applicable to descending thermals instead of collapsing surface cylinders. It is possible that the assumption of using the impact radius as a proxy for height and using $\kappa\rho_t'$ used in creating $U_0M$ (5.40), weaken the estimation of the radial propagation.

## 5.7 Summary

LES experiments using the new model MONC were conducted to provide a better understanding of the descent and near-surface evolution of atmospheric downdraughts. The downdraught was represented in the simulations by an instantaneously released bubble of cold fluid, which was allowed to fall freely and then spread outwards.

This chapter had three aims:

1. Compare the results of MONC cold bubble simulations with the findings from the laboratory experiments in Chapter 3.

2. Extend the similarity solutions of Rooney (2015) to include expressions for the potential and kinetic energy.

3. Compare the similarity solutions of Rooney (2015) and Romps and Jeevanjee (2016) to MONC simulations.

Aim 1. was achieved in Section 5.4, where the similarity solutions developed by Rooney (2015) and modified by this study in Chapter 3 in laboratory experiments, were compared against the numerical bubble runs. Analysis of the modelled vertical descent and radial propagation found:

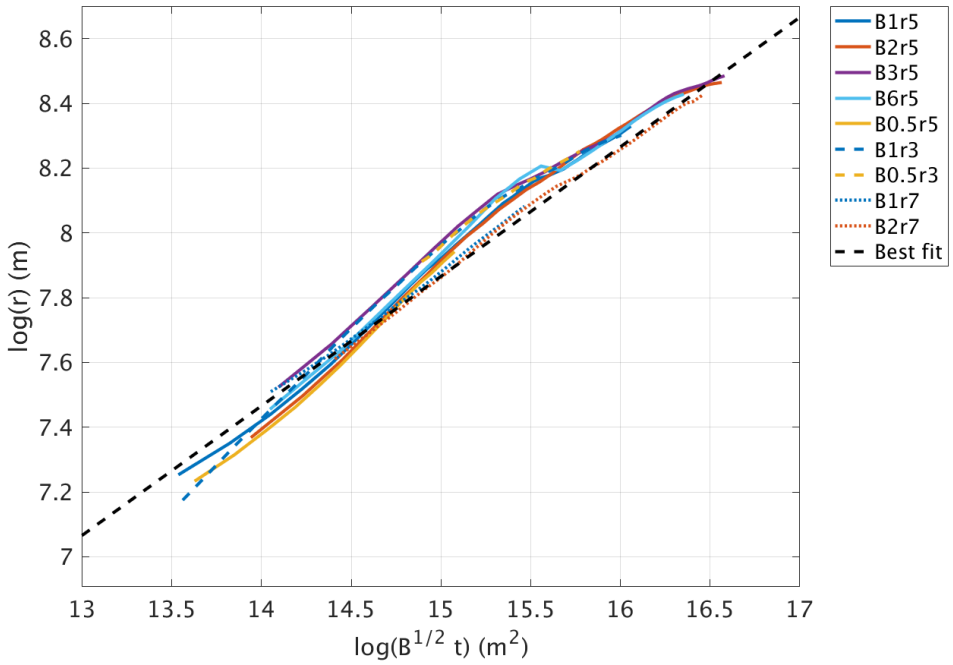


(A) The log of buoyancy scaled time against the log of radial propagation.

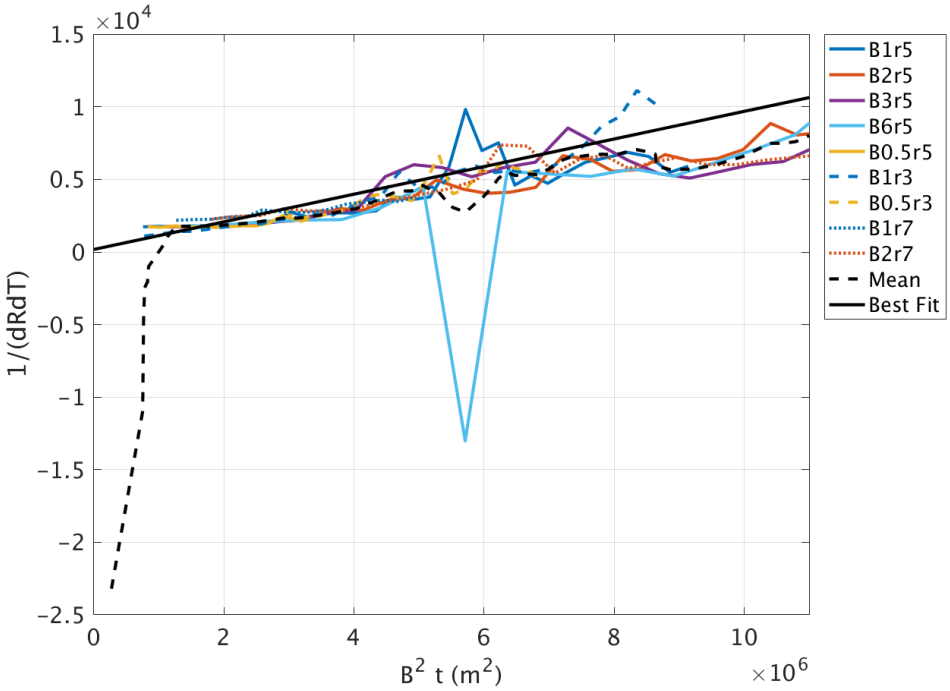


(B) Buoyancy scaled time against $1/(\mathrm{d}r/\mathrm{d}t)$.

FIGURE 5.20: Logarithmic and $1/(\mathrm{d}r/\mathrm{d}t)$ plots of radial propagation of all numerical model runs.

- The vertical descent was evaluated using similarity solutions from Rooney (2015). The proposed adaptation is suggested

$$z + z_v = kB^{1/4}t^{1/2} \tag{5.42}$$

where this study suggests $k = 2.63$ due to differences in calculating the Froude number ($Fr = 1.2$) and the entrainment constant ($\alpha = 1.26$).

- The rate of radial propagation for spreading thermal as suggested by Rooney (2015) and modified in Chapter 3, is evaluated.

$$r = (2Fr_c)^{1/2}\lambda^{1/4}B^{1/4}(t - t_i)^{1/2} + r_i. \tag{5.43}$$

The proposed adaptations to Rooney (2015) are: i) that the radius of impingement $r_i$ is included, and ii) the Froude number is taken as $Fr_c = 1.19$ and $\lambda = \pi^{-1}$, which supports the findings in Chapter 3.

- The laboratory experiments in Chapter 3 are compared to the numerical bubble runs using an adapted scaling from Lundgren, Yao, and Mansour (1992), where the length scale is initial radius of bubble (or pipe outlet diameter in the experiments) $b_0$ and the characteristic time is $t_0 = b_0^2 B^{-1/2}$. Figure 5.8 plots the vertical descent of numerical results and laboratory experiments, supporting (5.42). Similarly, Figure 5.10 plots the radial propagation of numerical simulations and laboratory experiments in support of (5.43).

Section 5.2 presented new expressions for the potential and kinetic energy for the descent and spread of negatively buoyant thermals, derived from Rooney (2015).

- In the vertical stage, this study suggests the potential energy ($PE_v$) and kinetic energy ($KE_v$) are:

$$PE_v = \rho_0 BH - \rho_0 Bz, \tag{5.44}$$

$$KE_v = \frac{1}{2}\rho V Fr_T^2 m^{-1}\alpha^{-2}(k_2 + 1)Bz^{-2}, \tag{5.45}$$

where $k_2 < 1$ is a constant.

- In the radial stage, this study suggests the kinetic energy ($KE_r$) is:

$$KE_r = \frac{1}{2}\rho\pi H^3\lambda^2 c\alpha^3 Fr_c^2\left(1+\frac{b_0}{\alpha H}\right)^3 Br^{-2} f, \tag{5.46}$$

  where $f$ is an empirical function proposed as $(r'_{max}/R_0)^{-1.3}$ by Rooney (2015).

- The numerical simulations support (5.44) and (5.45), as shown in Figure 5.11 and Figure 5.15. A value of $k_2$ is suggested between 0.25 and 0.5.

- The numerical simulations support the estimation of $KE_r$ (5.46), as shown in Figure 5.15.

Having established expressions for KE and PE, the buoyancy based similarity solutions from Rooney (2015) were then compared to the energy balance similarly solutions from Romps and Jeevanjee (2016) (referred to as RJ). This study demonstrated how RJ could be modified from initial conditions of a collapsing cylinder to that of a thermal at impact, through adaptation of the initial velocity $U_0$ and the radius of thermal at impact, to give the radial propagation $R$:

$$R(t) = R_0 + \frac{1}{\epsilon}\log(1+t\epsilon U_0 M), \tag{5.47}$$

where

$$U_{0M} = \sqrt{\frac{2\beta g\kappa\rho'_l(b_0+\alpha H)}{\rho}}. \tag{5.48}$$

Comparison of (5.43) and (5.47) to the numerical simulations showed both theories provided good estimations of the radial propagation of thermal after impact with time. In the near field, (5.47) from RJ provides a better estimation of radial propagation to (5.43) because of the formulation of the radius of impact. However, Figure 5.20 demonstrated that when the fundamental shape of each theory is compared to the numerical runs, buoyancy based similarity solutions from Rooney (2015) achieve a better $R^2$ value to RJ.

Using two different methodologies; laboratory experiments in Chapter 3 and numerical simulations in this chapter, similarity solutions that estimate a thermal's descent and radial spread based only on the initial conditions of source and the time passed,

have been shown to provide accurate estimates of the thermals behaviour. Across different mediums (water and air) and different scales, the same equation set can be used to predict the behaviour of negatively buoyant fluid. Hopefully, this work can be used to study actual atmospheric downdraughts and downbursts.

# Chapter 6

# Near-surface evolution of atmospheric downdraughts impacting a stable boundary layer

## 6.1 Introduction

This chapter presents the first study into idealised downdraughts impacting a stable boundary layer. The descent and near-surface evolution of downdraughts, represented by parcels of negatively buoyant fluid has been discussed in Chapters 3 and 5. In both these experimental and numerical investigations, the ambient background fluid was of constant density or potential temperature. However, the background atmospheric profile is rarely as simple. The atmospheric boundary layer (ABL) is the bottom layer of the troposphere that feels the effect of the Earth's surface. In general, the ABL over land experiences a diurnal cycle as solar radiation heats the land surface over the daytime. During the evening and night, the surface then cools creating a stable boundary layer (SBL). The SBL is an interesting atmospheric phenomenon that is not clearly understood, governed by radiative cooling, turbulent mixing and surface interaction. The SBL can host gravity waves, katabatic flows and fog (Mahrt, 1999). The introduction of a SBL to the previous uniform environment, adds an element of complexity. The turbulent mixing of downdraught and SBL, and the excitement of internal gravity waves creates a more complex problem than the previous case of downdraughts descending through a neutrally stratified background.

Various observations from field campaigns and numerical weather models have shown that compared to downdraughts from surface-based convection, it is more difficult for downdraughts from elevated convection to reach the surface and form a cold-pool outflow (Crook, 1988; Schmidt and Cotton, 1990; Stoelinga et al., 2003; Parker, 2008). Downdraughts not strong enough to reach the surface have been seen to generate waves and bores (Browning et al., 2010; Marsham et al., 2010; Marsham et al., 2011; Marsham et al., 2013). Marsham et al. (2011) observes a case from the IHOP_2002 field campaign over the Great Plains of the United States, where a surface wind speed increase from a downdraught outflow did not coincide with any significant surface temperature or water vapor mixing ratio change. This was attributed to the secondary initiation by a bore generated by downdrafts from the elevated convection interacting with the stable nocturnal boundary layer. Similarly, Marsham et al. (2013) observes the strong noctural SBL of the Sahara can prevent downdraught events from reaching the ground, and instead of a cold surface signal as expected for a cold pool, the disturbed SBL air can cause a slight surface temperature increase. Heinold et al. (2013) proposes a mechanism where an aged cold pool can interact with a SBL to form an elevated density current. In the Plains Elevated Convection at Night (PECAN) field campaign, cold pool outflows from nocturnal mesoscale convective systems were regularly seen to trigger undular bores and gravity waves within the SBL (Geerts et al., 2017). Undular bores are atmospheric wave disturbances (a type of gravity wave) typically caused with the collision of two air masses. Gravity waves transfer energy and momentum throughout different layers of the atmosphere. This transfer of energy and momentum is responsible for the forcing of the many large-scale dynamical features of the atmosphere.

There are complex interactions between downdraughts and SBL with repercussions that are poorly understood. Numerical weather models do not have the vertical or horizontal grid resolution to resolve these complex interactions well. Typical parametrizations of downdraughts use an inverted plume entraining plume model where the magnitude of the downdraught mass flux has to be determined (Gregory, 1997). These parametrizations may not account for an interaction with a SBL, which could lead to misrepresentations of wave-turbulence interactions, surface winds,

dust uplift and the triggering of convection (Sun et al., 2015).

To our knowledge, there are no previous studies that numerically model idealised atmospheric downdraughts impacting a stable boundary layer. However, there are some relevant experimental papers that examine similar problems. In laboratory experiments, Manasseh, Ching, and Fernando (1998) release dense fluid into a 20 cm deep channel with a 2cm stratified layer at the bottom, to model the 2D transition of density-driven to wave-dominated flows. They suggested two scalings, firstly for the density-driven regime and secondly for the wave-dominated regime. Their study provided inconclusive results, with only 'plausible' scalings for the density-driven regime, whilst the wave-dominated regime did not appear to scale. Furthermore, their experiments were limited to thermals with length scales much larger than the depth of the stratified layer, meaning that all resulting flows travelled along the tank floor.

There has naturally been substantial work on gravity currents propagating in stratified fluid, when that gravity current originates from the conventional lock-gate release and not from a descending thermal. Stratification of the ambient fluid increases the complexity of the gravity current's interaction with it's environment. The reduced gravity $g'$ is still the key physical parameter; however oscillations within a continuously stratified fluid do not depend solely on $g'$ but instead on the buoyancy frequency (also known as the Brunt–Väisälä frequency) where

$$N(z) = \left( -\frac{g}{\rho_0} \frac{\mathrm{d}\rho}{\mathrm{d}z} \right)^{1/2}. \tag{6.1.1}$$

The Brunt–Väisälä frequency is a measure of a vertically perturbed parcel of fluids tendency to return it's original position. In atmospheric science, the Brunt–Väisälä frequency provides an understanding of the stability of a certain layer and the capacity of that layer to host vertical motion of fluid, for example convection. A detailed background on the buoyancy frequency and internal gravity waves can be found in Sutherland (2010). The relevant gravity wave theory for this Chapter is reproduced

in Section 6.3. Holyer and Huppert (1980) considers steady gravity currents in two-layer fluids, observing the perhaps intuitive relationship of: if the gravity current is i) sufficiently heavy, it travels along the bottom surface, ii) sufficiently light, it travels along the top surface forming a boundary gravity current or iii) when the gravity current is of a density between the densities of the upper and lower layers, the current will travel at that intermediate height to form an intrusion. White and Helfrich (2012) provide a detailed extension of this two-layer theory. Maxworthy et al. (2002) presents a generalisation of classical results from Benjamin (1968) for a steady gravity current propagating into a stratified fluid. The governing parameters are:

$$a = \frac{h}{h_b}, \tag{6.1.2}$$

where $h$ is the depth of gravity current and $h_b$ is the height of stratified fluid,

$$R = \frac{\rho_s - \rho_0}{\rho_c - \rho_0}, \tag{6.1.3}$$

where $\rho_s$ is the density at the surface, $\rho_c$ is the density of current and $\rho_0$ is a reference density. These governing parameters are validated in laboratory lock gate experiments by Maxworthy et al. (2002) for a range of $a$ and $R$ values. Maxworthy et al. (2002) observed two regimes i) current and ii) wave, which were dependent on the Froude number.

This chapter presents a study of idealised downdraught-SBL interactions, where an overview of the diverse range of resulting behaviours from the impact and evolution of a downdraught on a SBL is provided using large-eddy numerical simulations (LES). A schematic of the proposed problem is shown in Figure 6.1. The downdraught will be modelled, as in previous chapters, by a relatively cold bubble of fluid that is allowed to descend freely. However, instead of simply falling through an unstratified background fluid as in Chapter 5, a SBL is added at the surface. The SBL has a linear potential temperature gradient, from the coldest at the surface, rising to the ambient background temperature.

Conceptually, the two ends of the regime diagram are perhaps simpler to understand: i) the strongest downdraughts impacting the weakest SBL, are likely to behave close to the ambient background fluid cases previously considered (as if there were no SBL at all) and ii) the weakest downdraughts impacting the strongest SBL, might barely register a significant interaction within the SBL. However, the middle regimes where the both downdraught and SBL play significant roles in the flow development, is an area full of exciting, unanswered questions. It is not obvious how the downdraught will behave. When the bubble descends towards the SBL, it is not clear whether or not it will be able to reach the surface. In particular, it may only be able to penetrate through part of the SBL before it reaches its level of neutral buoyancy, and it may then spread out. This study performs experiments with a range of cold bubbles, designed to span two parameter regimes: i) strongly negatively buoyant bubbles that are expected to penetrate through the SBL and reach the surface and spread out as a gravity current (similar to those studied in Chapter 3 and 5), ii) weaker negatively buoyant bubbles which are expected to only penetrate into the upper part of the SBL before spreading.

## 6.2 Methods

The numerical simulations for this investigation have the same initial set-up as those in Chapter 4, apart from the addition of a SBL. A sphere of fluid at a height $z = H$ is given an instantaneous negative potential temperature perturbation $\theta_b$ and allowed to fall freely towards the ground $z = 0$. The unique feature of these numerical simulations is the addition of a stable boundary layer (SBL), extending horizontally across the whole domain, and vertically from the surface to the height of boundary layer $z = h_b$. This SBL is generated by imposing a linear negative potential temperature gradient from the surface to $h_b$. The set-up for a typical SBL numerical simulation is shown in Figure 6.2 (left) and the vertical profile of potential temperature far from the cold bubble is shown on the right.

The methodology for the Large Eddy Simulations used for this study is provided

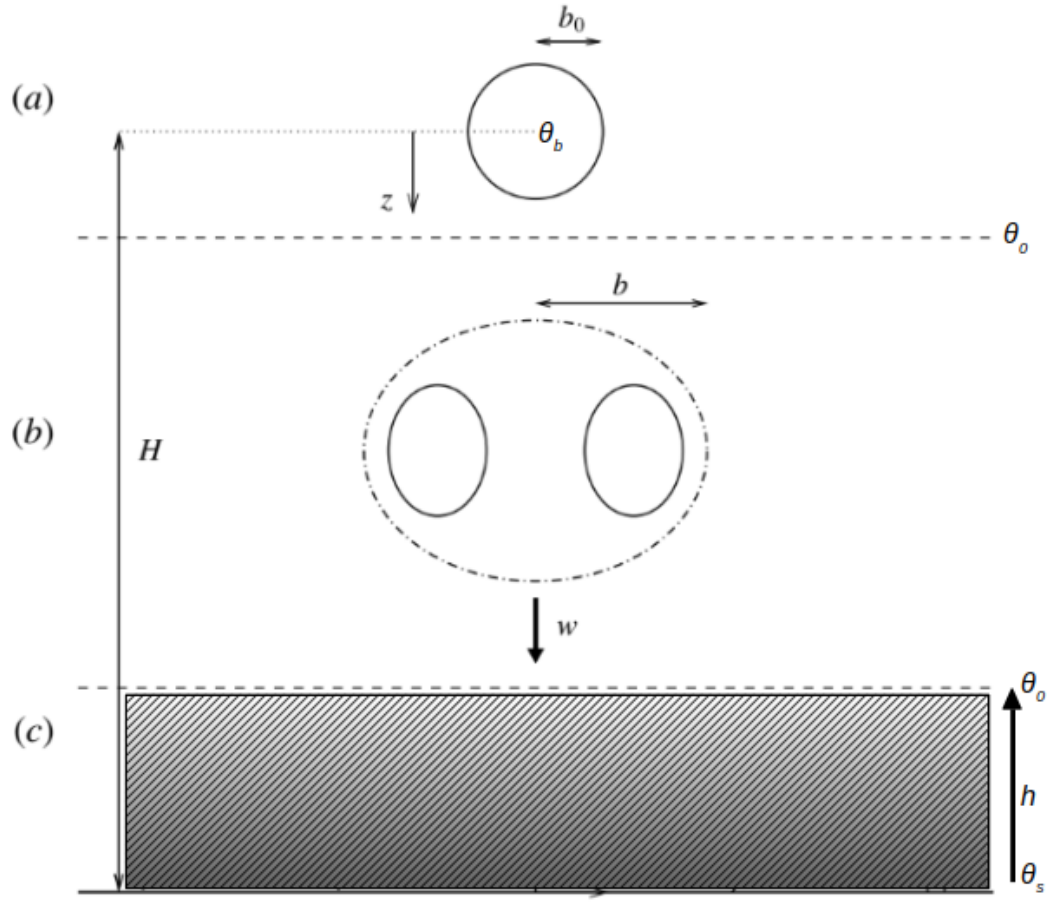


FIGURE 6.1: Schematic of the idealised impact of downdraught on a SBL. (a) At $t = 0$ , the downdraught is represented as a cold bubble with width $b_0$ and initial temperature perturbation $\theta_0$, at a height $H$ above the surface. (b) $t > 0$, the cold bubble is allowed to fall freely towards the surface. (c) a SBL is represented by a potential temperature gradient, with $\theta_s$ at the surface, linearly increasing to $\theta_0$ at height $h$.

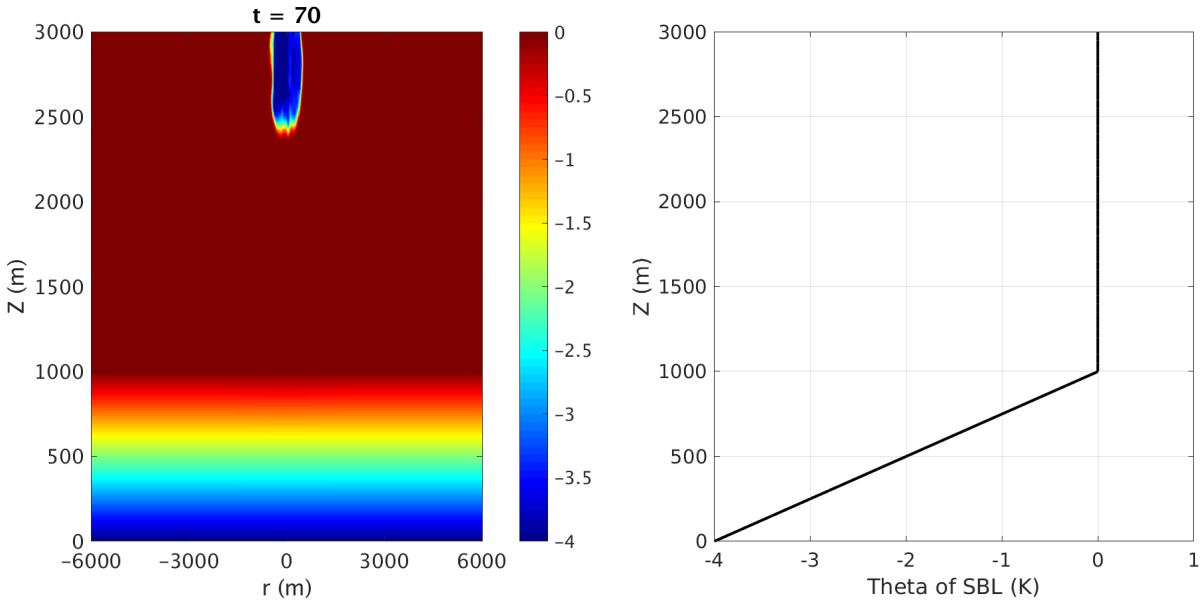


FIGURE 6.2: Left: A potential temperature contour plot of B04_SBL04 at $t = 70$ s. Right: Vertical profile of potential temperature for B04_SBL04 where $\theta_s = -4$K and $\theta_0 = 0$K. The vertical temperature profile is taken far away from the bubble.

in Chapter 4. Rather than repeat methods previously described, this section will instead focus on the aspects of the numerical work that are entirely new and specific for this chapter. An explanation of LES numerical model, bubble source, grid resolution test, tracking of buoyant fluid etc. can be found in Chapter 4. The set-up of the grid the same as was chosen after the grid sensitivity test in Chapter 4, and the grid properties are shown again in Table 6.1.

Table 6.2 contains the SBL numerical model runs analysed in this chapter. Initially, a

TABLE 6.1: SBL Grid Properties. Horizontal domain is the entire width of the domain, e.g. for a 25.6km domain, bubble is centred at 12.8km. dxx is the horizontal grid spacing (same in $x$ and $y$), $N_x$ is the horizontal number of grid points. Vertical domain is the height from surface to the top of the domain. $\mathrm{dzz}_{min}$ is the minimum vertical grid spacing (spacing increases with height). $N_z$ is the number of vertical grid points.

| **Simulation Number** | **Horizontal Domain (m)** | **dxx (m)** | $N_x$ | **Vertical Domain (m)** | $\mathbf{dzz}_{min}(m)$ | $N_z$ |
|---|---|---|---|---|---|---|
| B01_SBL04 | 25600 | 25 | 1024 | 4000 | 7.9 | 256 |
| B02_SBL04 | 25600 | 25 | 1024 | 4000 | 7.9 | 256 |
| B04_SBL04 | 38400 | 25 | 1536 | 4000 | 7.9 | 256 |
| B08_SBL04 | 51200 | 25 | 2048 | 4000 | 7.9 | 256 |
| B16_SBL04 | 51200 | 25 | 2048 | 4000 | 7.9 | 256 |

TABLE 6.2: SBL Numerical Runs. $\theta_b$ is the initial potential temperature perturbation of bubble. $H$ is the release height of the centre of bubble. $b_0$ is the initial width of bubble. $\theta_s$ is the initial potential temperature difference at the surface of the SBL. $h_b$ is the height of the SBL.

| **Simulation Number** | $\theta_b$ **(K)** | $H$ **(m)** | $b_0$ **(m)** | $\theta_s$ **(K)** | $h_b$ **(m)** |
|---|---|---|---|---|---|
| B01_SBL04 | -1 | 3000 | 500 | 4 | 1000 |
| B02_SBL04 | -2 | 3000 | 500 | 4 | 1000 |
| B04_SBL04 | -4 | 3000 | 500 | 4 | 1000 |
| B08_SBL04 | -8 | 3000 | 500 | 4 | 1000 |
| B16_SBL04 | -16 | 3000 | 500 | 4 | 1000 |

far more extensive set of model runs (>30) was produced, spanning a wider parameter range. A wide range of bubble and SBL heights, SBL strength and SBL profile (linear and step functions) were considered. However, such was the diverse range of resulting behaviours and flow regimes, that it became necessary to restrict the scope of the investigation. Therefore, the height and strength of SBL and the initial release height and width of bubble are kept constant throughout all of the analysed numerical runs in this chapter. The only variable is the initial potential temperature perturbation of the bubble.

### 6.2.1 Influence of Domain Width

The main additional consideration for the SBL numerical runs is the effect of the finite domain width. The model domain sides have periodic boundary conditions, which means any signals that reach one edge of the model domain, are experienced on the opposite edge. In the previous numerical runs, the fastest gravity currents reached 6.0 km at around 3000 s (end of the model run), which is sufficiently far from the edge of the domain at 12.8 km to not pose any concern. However as shall be seen, SBLs have the capacity to propagate waves that travel much faster than actual displaced fluid from the bubble. Figure 6.3 plots the resultant velocity ($\bar{u} = \sqrt{u^2 + v^2 + w^2}$) from a numerical run (B04_SBL04_test) with the standard 25.6 km wide grid used in Chapter 5. Time is measured from the release of bubble. The bubble impacts around $t = 250$s, causing disturbances that last for the entirety of the modelled run ($t_{end} = 6000$s). The velocity field is first disturbed around 2000 s, whilst stronger signals follow with a period of 750-1000 s. Based on this data, the

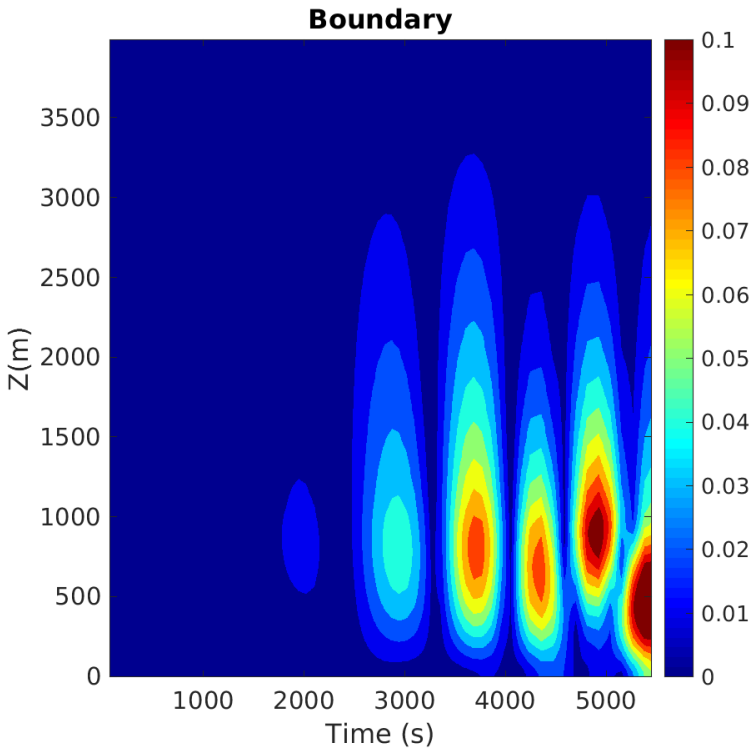


FIGURE 6.3: Resultant speed ($t - z$) contour plot in (m/s) of a test numerical run (B04_SBL04_test) at $x = 12.8$km, which is the edge of the domain width.

decision was taken to expand the domain size for the runs with large initial $\theta_b$. The properties of the different grids used can be found in Table 6.1.

## 6.3 Gravity waves in a SBL

A characteristic of stably stratified fluid is their ability to support wave motions. Any perturbation of a SBL will generate waves as gravity or the force buoyancy tries to restore the equilibrium. These gravity waves act as a mechanism to transport energy away from the disturbances that generate them and redistribute this energy throughout the atmosphere. As Figure 6.3 shows, this redistribution of energy can occur faster than the mean flow. Without the SBL, the equivalent 4K bubble run (B4r5, see Figure 5.9 in Chapter 5) reaches around 4.5 km in 2000 secs, whilst the first wave disturbance seen at the edge of the domain (12.8km) for B04_SBL04_test at the same time. Readers with an atmospheric science background may be familiar with the theory for vertically propagating gravity waves in the troposphere; which can be generated by orography, frontal systems, and deep tropical convection (Fritts,

1984; Lane, Reeder, and Clark, 2001; Nappo, 2013). However, gravity waves in SBLs have different boundary conditions to those in the troposphere. Instead of the usual rigid lower and upper boundaries at $z = 0$ and $z = H$, the vertical displacement $\zeta_*(x, z, t)$ is continuous at $z = H$. Furthermore, this study is primarily concerned with $u$ instead of $w$. Therefore, this section presents a summary of the well established Boussinesq linear theory for gravity waves in stable boundary layers as described by Sutherland (2010), which will be of use for interpreting the results of the SBL numerical simulations. In addition, the wave speeds and modes for the stratification of the SBL used throughout this study are provided.

The governing Boussinesq equations for 2D disturbances to a non-hyrdostatic stratified shear flow $U(z)$ are

$$u_t + Uu_x + U'w = -p_x, \tag{6.3.1a}$$

$$(w_t + Uw_x) = -p_z + \theta, \tag{6.3.1b}$$

$$\theta_t + U\theta_x + N^2 w = 0, \tag{6.3.1c}$$

$$u_x + w_z = 0. \tag{6.3.1d}$$

Where $p$ is the pressure. The vertical displacement is $\zeta_*(x, z, t)$, which in the linear limit satisfies $w = \zeta_{*t} + U\zeta_{*x}$.

For a stably stratified boundary layer with $U(z) = 0$ and

$$N^2(z) = \begin{cases} N_0^2 & 0 < z < H, \\ 0 & z > H, \end{cases} \tag{6.3.2}$$

with $N_0$ a constant. Then

$$\zeta_{*zz} + \left(\frac{N_0^2}{c^2} - k_w^2\right)\zeta_* = 0 \text{ for } 0 < z < H, \tag{6.3.3a}$$

$$\zeta_{*zz} - k_w^2\zeta_* = 0 \text{ for } z > H. \tag{6.3.3b}$$

At the rigid surface at $z = 0$, the relevant solution with $\zeta_* = 0$ at $z = 0$, and $\zeta_*$ continuous at $z = H$, is

$$\zeta_* = \frac{\sin mz}{\sin mH} \text{ for } 0 < z < H, \tag{6.3.4a}$$

$$\zeta_* = \mathrm{e}^{-|k_w|(z-H)} \text{ for } z > H, \tag{6.3.4b}$$

where

$$m = \sqrt{\frac{N_0^2}{c^2} - k_w^2}. \tag{6.3.5}$$

$k_w$ is the wavenumber. At $z = H$, we also require continuity of $\zeta_{*z}$, which gives $m \cot mH = -|k_w|$. Given $k_w$, this is only satisfied for certain values of $m$, or equivalently certain values of $c$ via (6.3.5), and thus serves as the dispersion relation. It is usefully rewritten in non-dimensional variables as

$$\cot M = -\frac{K}{M}, \text{ where } K = |k_w|H, \quad M = mH = \sqrt{\frac{N_0^2 H^2}{c^2} - K^2}. \tag{6.3.6}$$

There is one root for $M$ in each interval $(0, \pi)$, $(\pi, 2\pi)$, $(2\pi, 3\pi)$, whatever the value of $K$. Since $K/M$ is small for sufficiently large $M$ (or for sufficiently small $K$), the corresponding roots are approximately given by those of $\cot M = 0$, i.e.,

$$M \approx M_0 = \left(n + \frac{1}{2}\right)\pi \implies c \approx \frac{N_0 H}{\sqrt{(n+1/2)^2\pi^2 + K^2}}, \quad n \in \mathbb{N}. \tag{6.3.7}$$

In the long-wave limit, i.e., $K = |k_w|H \ll 1$, this simplifies further to

$$c \approx \frac{N_0 H}{(n+1/2)\pi}, \quad n \in \mathbb{N}. \tag{6.3.8}$$

The expected vertical structure of the mode 1 and mode 2 internal gravity waves are plotted in Figure 6.4 using the properties of the SBL from the numerical simulations. The height of the SBL $h_b = 1000$m, the potential temperature is $\theta_s = -4$K at $z = 0$ and $\theta = 0$K at $z = h_b$, which gives a corresponding buoyancy frequency of $N = 0.114\ \mathrm{s}^{-1}$. Each column in Figure 6.4 corresponds to a different wavenumber

$k_w$. The right end column is the approximate long wave limit, where $k_w = 1 \times 10^{-4}$ $\mathrm{m}^{-1}$ and wave speed $c \approx Nh_b/((n+1/2)\pi)$. The other columns from left to right are, $k_w = 2\pi/L, 2\pi/2L$ and $2\pi/4L$, where $L = 2b_0$ is the width of cold bubble ($b_0 = 500$m in all model runs).

## 6.4 Flow Visualisation

Before conducting these simulations, little was known about what behaviour would be seen in either the bubble or SBL. The first step to analysing this interaction was to build develop a coherent picture of what happens in the different regimes. This section presents a selection of contour plots of potential temperature, velocity and change in potential temperature. Each row of contour figures is an individual model run, that then shows a different snapshot in space or time for each column. In addition, the animated GIFs of potential temperature and velocities through a centre slice of the domain, which were invaluable throughout this study, are made available to the reader in the supplementary material.

Figure 6.5 plots potential temperature contour plots of model runs B01, B04, B08 and B16 for a $y$-slice through the centre of the domain, at different times. Velocity vectors $u$ and $w$ are represented by arrows. One half of the simulation is shown for clarity. All simulations behave reasonably axisymmetrically.

In the early descent stage, the cold bubbles behave as expected. B01 and B04 impact the SBL around 668 s and 328 s respectively. This is consistent with the time taken for cold bubbles in numerical simulations (B1r5 and B4r5) without the SBL from Chapter 5 to fall from 3000 m to 1000 m (see Figure 5.4), thus indicating that the descent stage of bubble before impact with the SBL remains unchanged with the addition on a SBL. Descent is characterised by the formation of a vortex ring, which both grows in width and decreases in density difference through entrainment. As seen in Chapter 5, Figure 5.17, the maximum potential temperature $\theta$ (or density) difference of bubble with $z$ scales with the initial $\theta_b$ perturbation. Therefore, the proportion that $\theta$ reduces by is approximately the same for all bubbles, although the

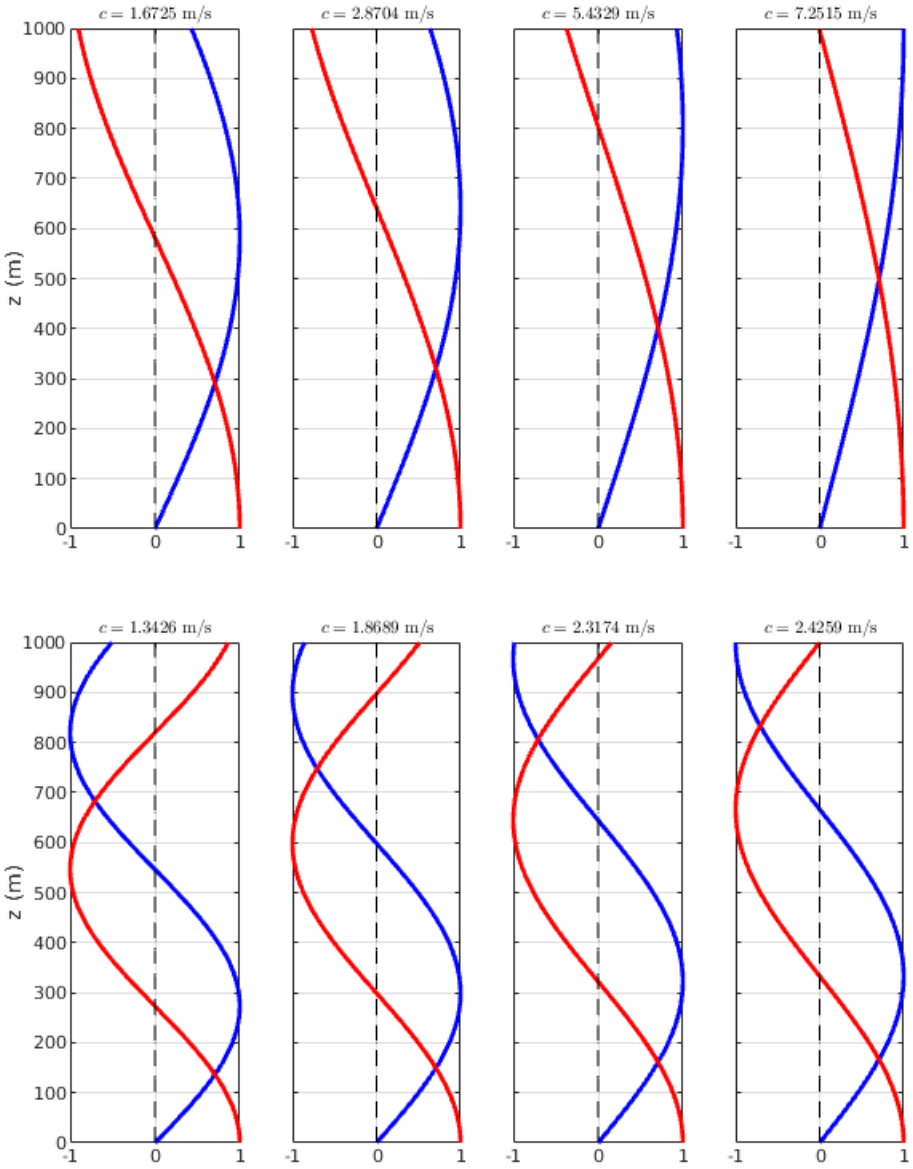


FIGURE 6.4: Expected vertical structure of the mode 1 (top row) and mode 2 (bottow row) waves. Red is $u$, blue is $w$ (or equivalently $\theta$). In all cases, the maximums have been normalised to 1. Different columns, show different wavenumbers. From left to right $k_w = 2\pi/L, 2\pi/2L, 2\pi/4L, 1 \times 10^{-4}$ m$^{-1}$, where $L = 2b_0$ is the width of cold bubble.

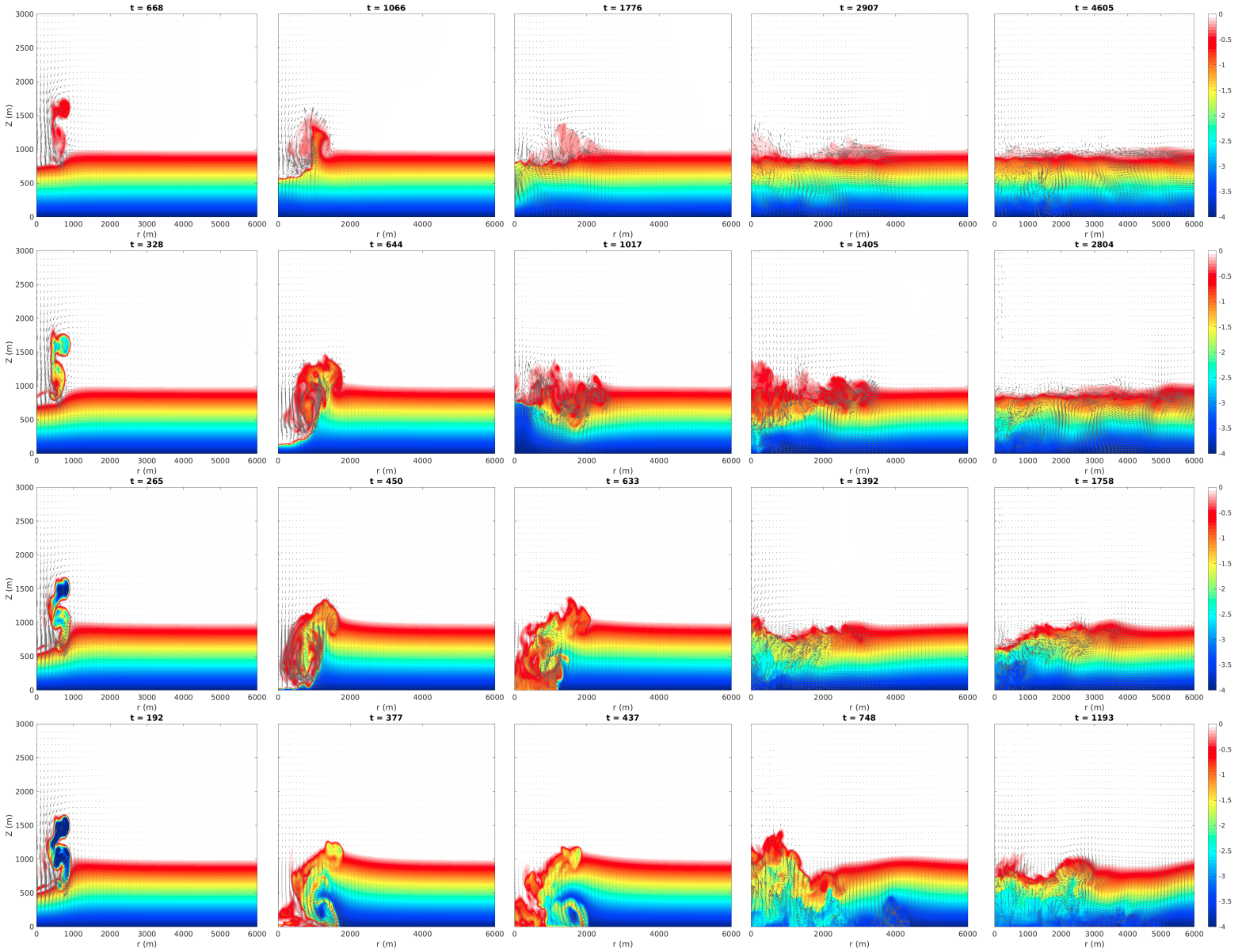


FIGURE 6.5: Potential temperature contour (K) plots of model runs B01, B04, B08 and B16 (top to bottom) for a $y$-slice through the centre of the domain, at different times. Arrows represent resultant velocity magnitudes and directions.

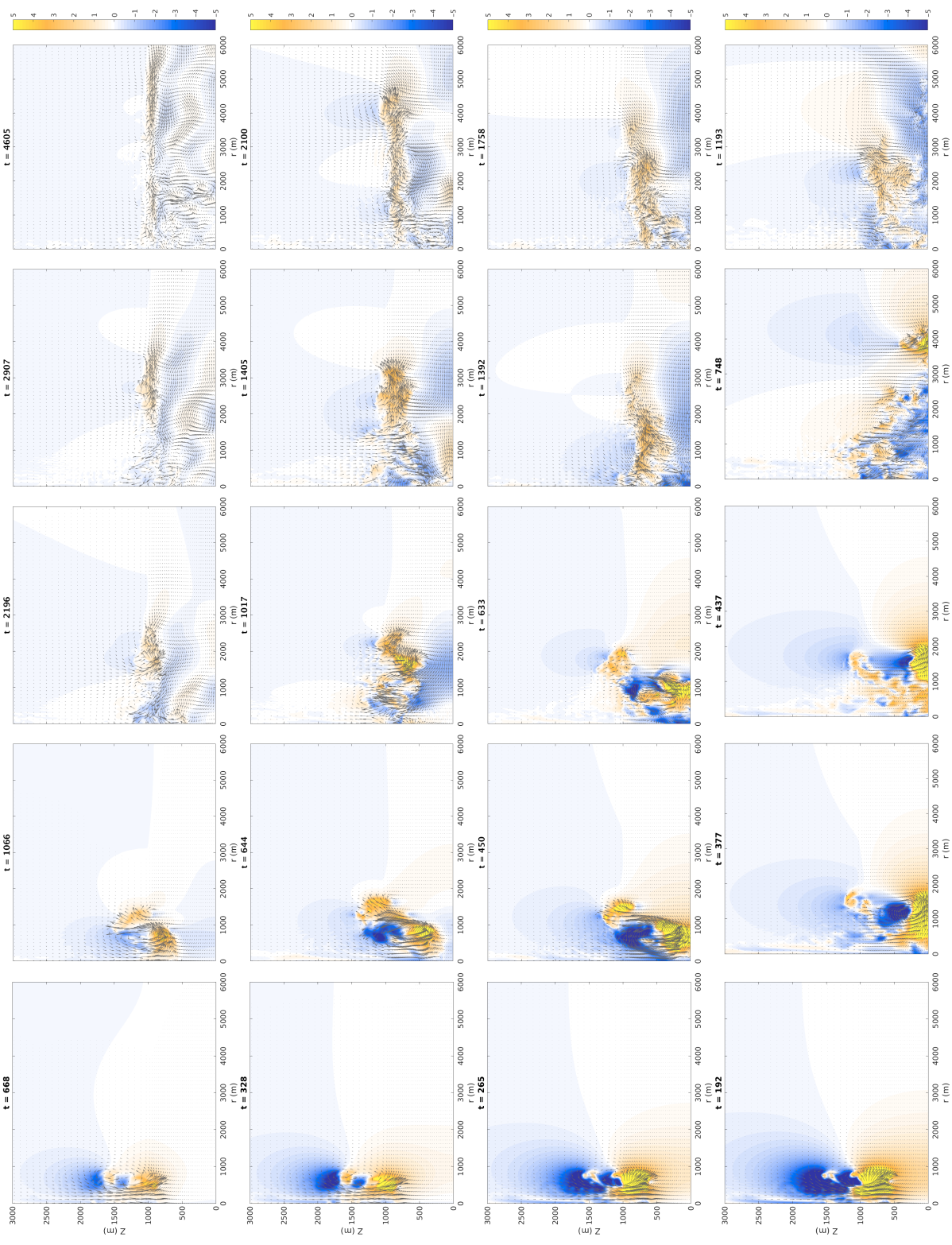


FIGURE 6.6: Horizontal velocity contour (m $s^{-1}$) plots of model runs B01, B04, B08 and B16 (top to bottom) for a *y*-slice through the centre of the domain, at different *z* heights. Arrows represent resultant velocity magnitudes and directions.

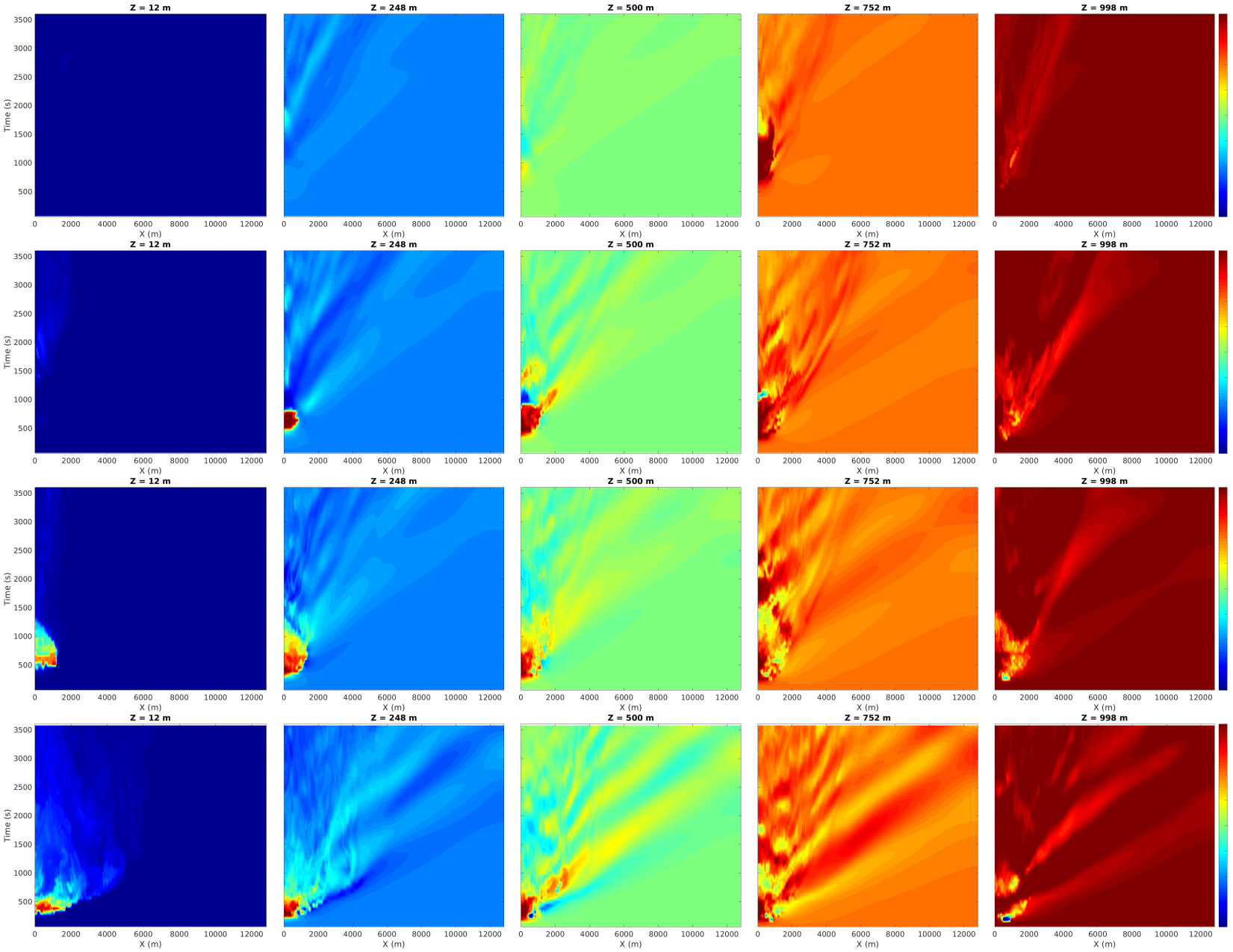


FIGURE 6.7: Potential temperature contour (K) plots of model runs B01, B04, B08 and B16 (top to bottom) for a $y$-slice through the centre of the domain, at different $z$ heights.

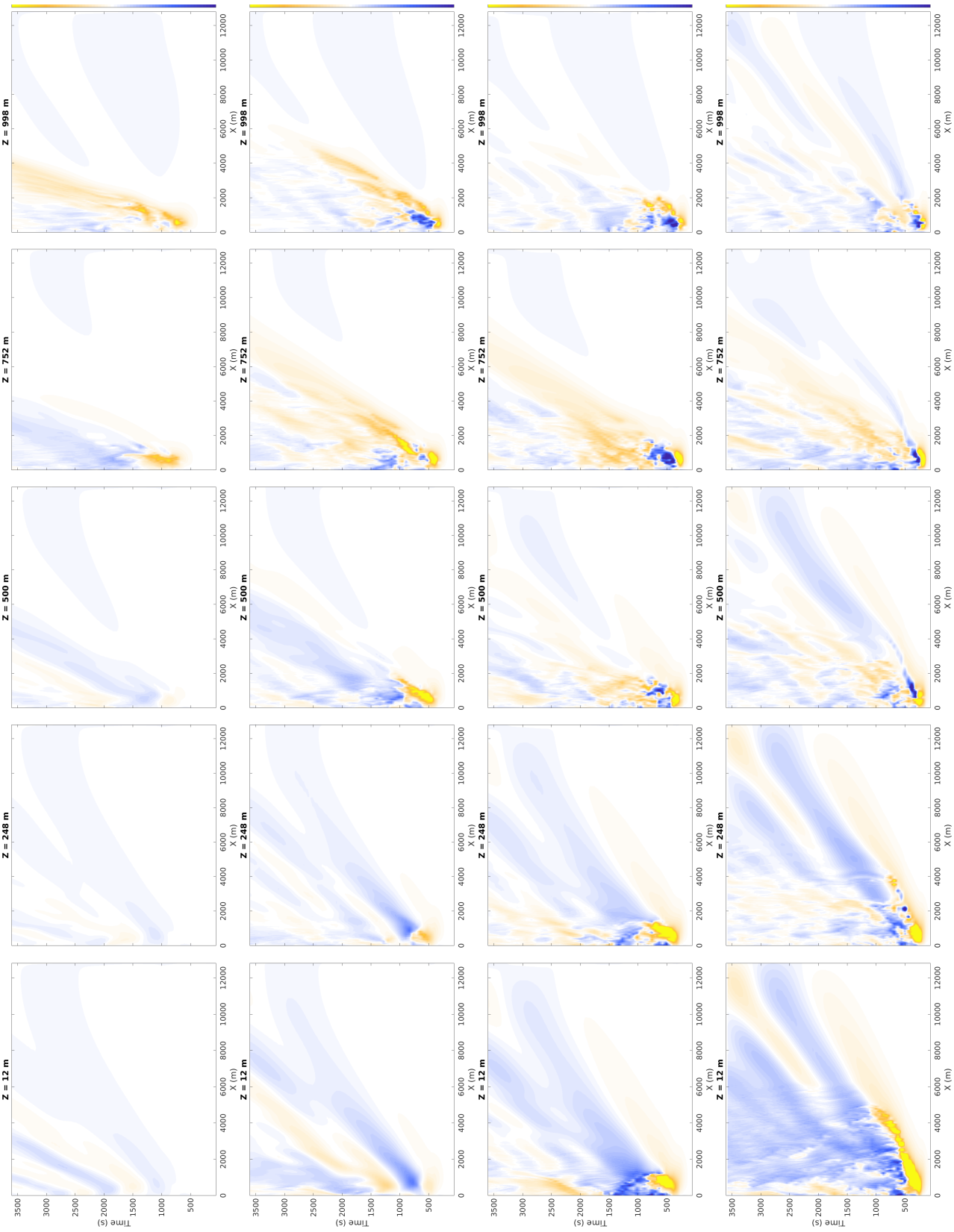


FIGURE 6.8: Horizontal $u$ velocity (m s$^{-1}$) contour plots of model runs B01, B04, B08 and B16 (top to bottom) for a $y$-slice through the centre of the domain, at different $z$ heights.

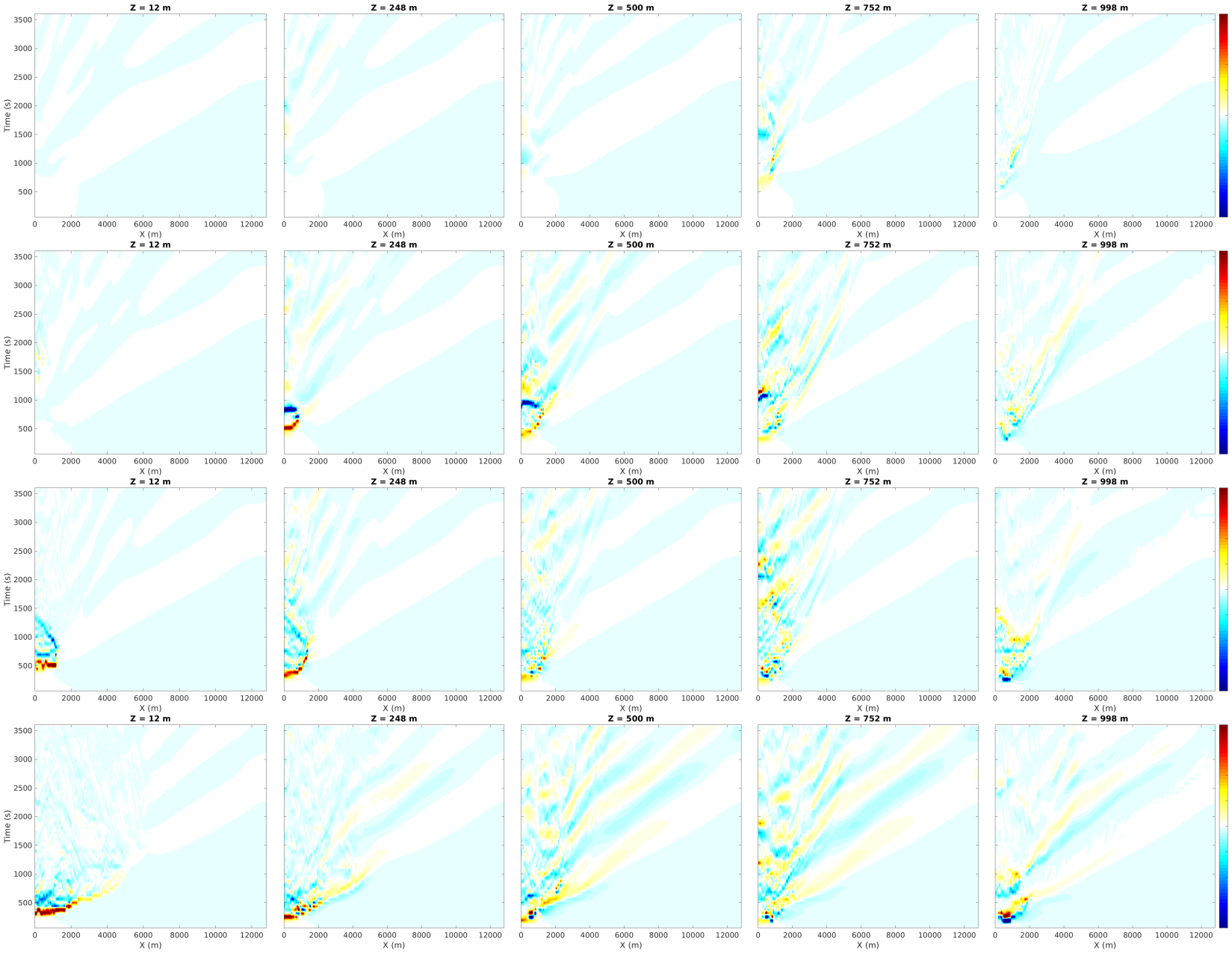


FIGURE 6.9: Change in potential temperature contour (K) plots of model runs B01, B04, B08 and B16 (top to bottom) for a $y$-slice through the centre of the domain, at different $z$ heights.

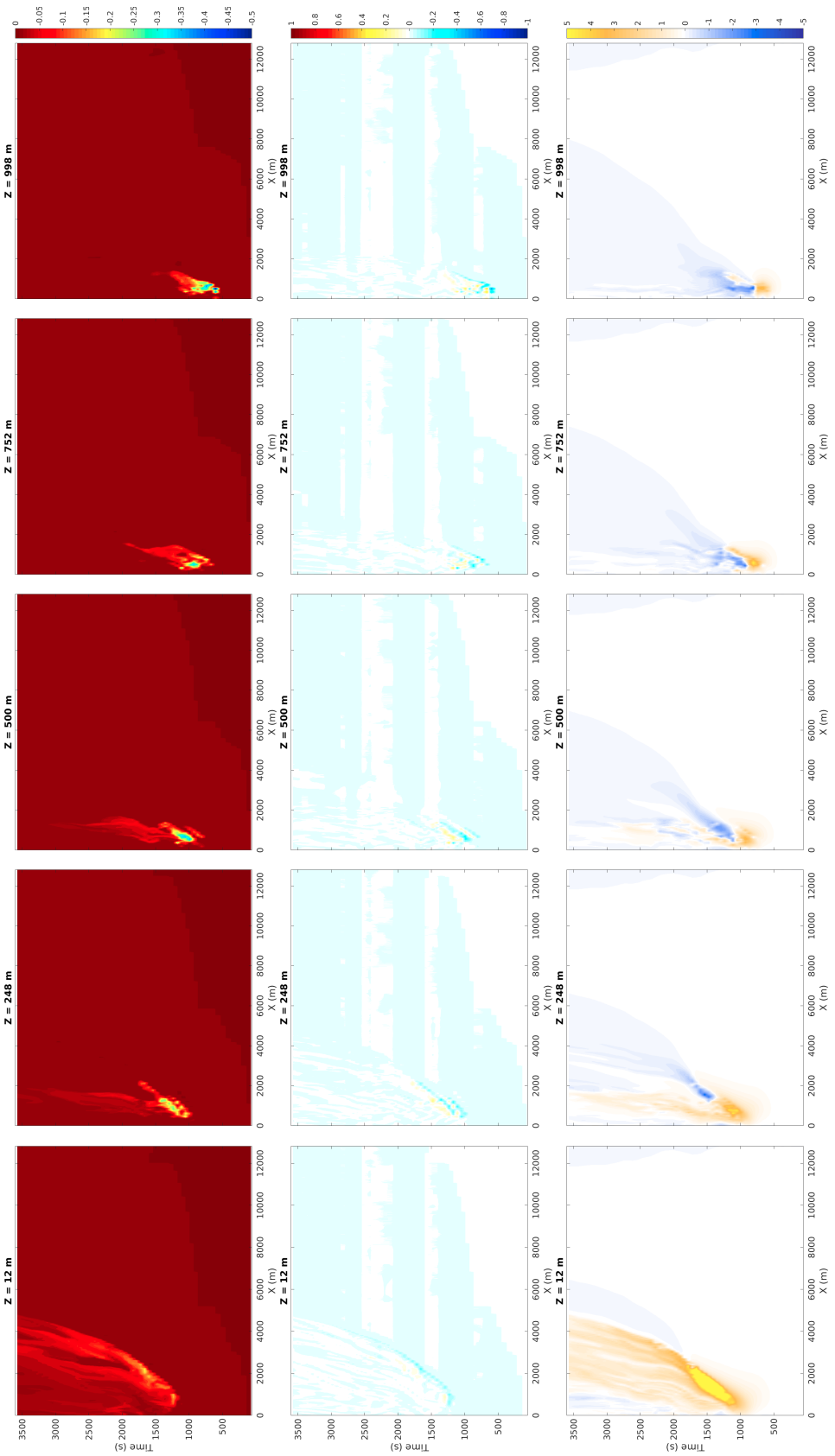


FIGURE 6.10: Potential temperature (top) (K), change in potential temperature (middle) (K) and horizontal velocity (bottom) (m $s^{-1}$) contour plots of model run B1r5 without a SBL for a $y$-slice through the centre of the domain, at different $z$ heights.

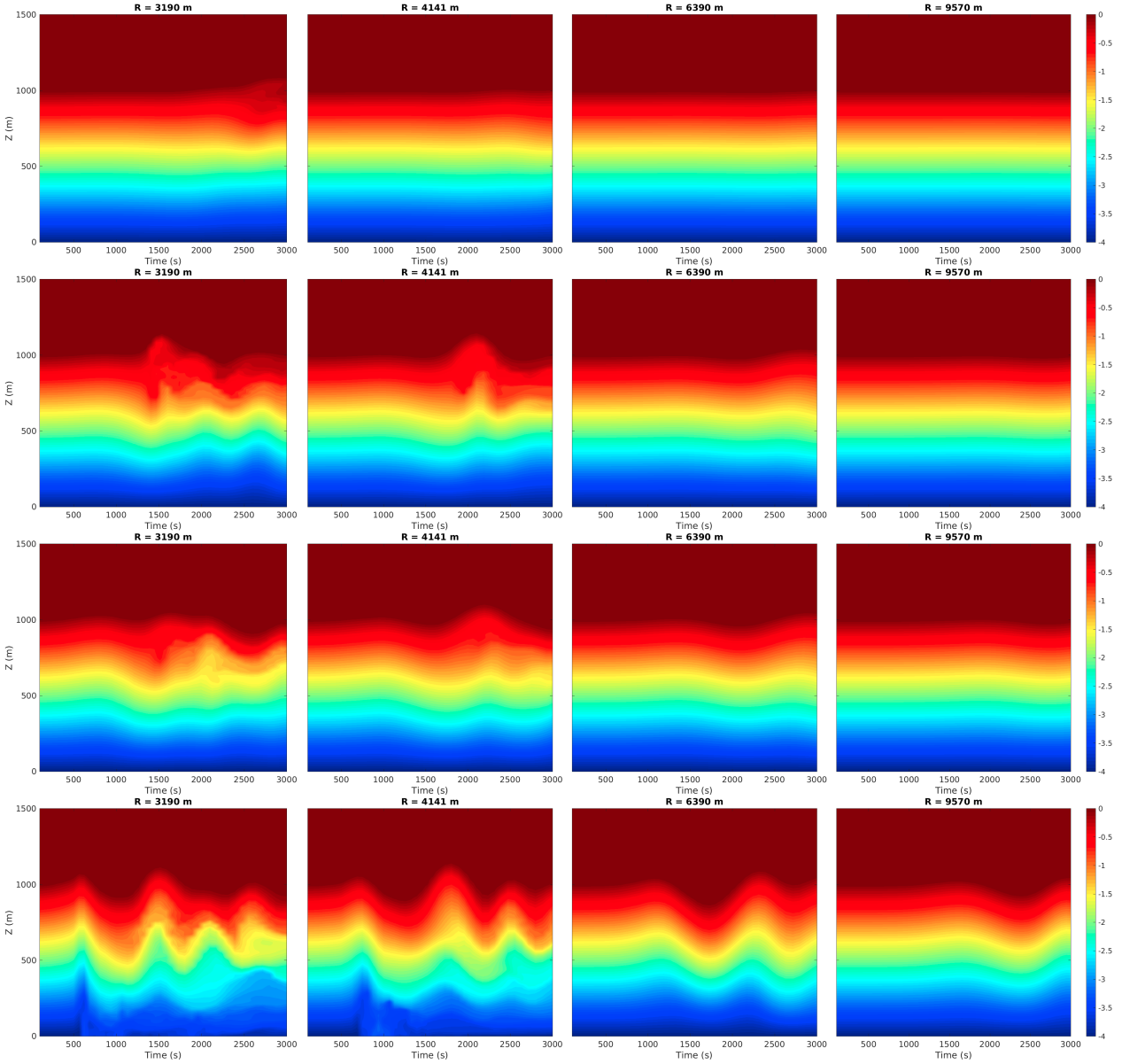


FIGURE 6.11: Potential temperature $(t - z)$ (K) contour plots of model runs B01, B04, B08 and B16 (top to bottom) for different $r$-slices.

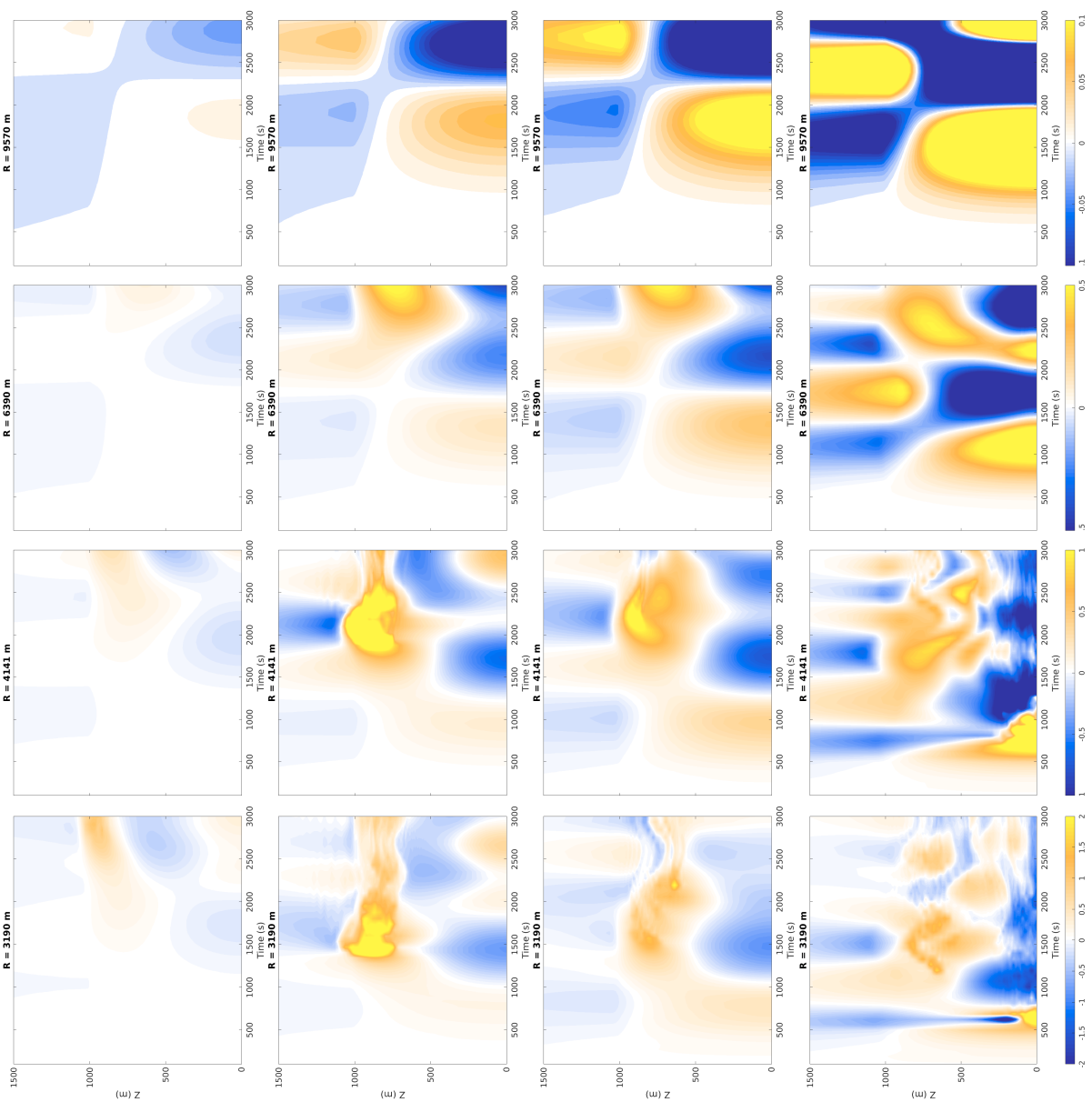


FIGURE 6.12: Horizontal velocity $(t - z)$ (m s$^{-1}$) contour plots of model runs B01, B04, B08 and B16 (top to bottom) for different $r$-slices. Note the change of colour scales for different $r$.

magnitude is obviously substantially different. In general at impact, the average $\theta$ across the bubble has dropped 50% from the initial potential temperature of bubble $\theta_b$; however the core at the centre of the vortex ring remains at $\theta_b$.

Before impact, the SBL experiences the presence of the bubble and deflects in advance. The magnitude of this deflection appears to scale with the initial $\theta_b$. At impact, both the fluid from the bubble and ambient background fluid (white) push into a region of the SBL. Depending on $\theta_b$, the SBL is temporarily deflected from the impact region. For B01 and B04, the SBL is deflected to a depth of 500 and 100 m respectively. For B08 and B16, the SBL is completely deflected to the surface, with both fluid from the bubble and ambient background fluid reaching the surface. The subsequent evolution of SBL and bubble after impact then appears to vary based on the magnitude of $\theta_b$.

Different model runs exhibit different behaviour depending on $\theta_b$. Beginning with B01, the impact of B01 on the SBL causes a splash to rise to around 1500 m, in conjunction with a region of strong re-circulation ($t = 1066$ s). At the same time, inside the SBL, the velocity arrows show the generation of a wave-like structure. This wave can be seen to travel radially outwards ($t = 2196$s and 2907s). Behind the leading wave, more complex wave modes follow. These waves can be seen in Figure 6.6, which shows $u$ velocity contour plots for B01-B16 for the same times as in Figure 6.5. Focusing just on B01 (top row), the generation of the different wave modes can be seen. At $t = 2196$s, between 4000 and 6000 m, there is a mode 2 wave going from positive (yellow) in the top half of the SBL, roughly 0 at $z = h_b/2$ and negative in the bottom of the SBL. The mode 2 wave, is followed by a mode 3 wave between 2000 and 3000 m, going from positive in the top third of the SBL, negative in middle third and positive again in the bottom third. The greater the time, the more complex wave modes form (see B01, $t = 2907$ and 4605 s). Throughout the impact and evolution of B01, the majority of the maximum velocities remain at the top interface of the SBL.

Now consider B16, the model run with the greatest initial $\theta_b$. The bubble in B16 naturally impacts the SBL with the greatest momentum and the largest temperature

difference between the bubble and the SBL. At impact, B16 is the only bubble that is significantly colder than the minimum potential temperature of the SBL. This combination of momentum and density difference, results in B16 crashing to the surface. In B01 at $r = 0$, there was almost no temperature or velocity change at the surface. In contrast in B16, there is a considerable mixing of the SBL and sustained wind speed increases of over $5\text{ms}^{-1}$. However, instead of a local temperature decrease, there is actually only a relative surface warming, as air is entrained from both above the SBL (white) and inside the SBL (red), leading to a temporary local increase of 3 to 4 K (this phenomenon is better seen in Figure 6.7, and will be discussed further on). Despite the relative warming of the surface, the B16 bubble still evolves in to something that resembles the head of a gust front, that spreads radially along the surface (see Figure 6.5 and 6.6, B16 at $t = 377, 437$ and 748 s). This gust front head is similar in structure to those seen in Chapter 5 for bubble runs without a SBL, characterised by strong rotation and a core of cold fluid. B16 still forms a surface current. However, B16 cannot be described as density driven at this point, given that the head of the current is not actually colder than the surroundings it is propagating in. Instead, the motion appears to be completely momentum driven from the descent and impact stage of the bubble. The head of the current propagates until around 4000 m before dying. The current head seems to be preceded by a wave (Figure 6.6), although it is hard to distinguish clearly the same generation of subsequent modes as seen in B01 - these signals may be lost in Figure 6.6 given the higher magnitudes of velocities in B16 compared to B01.

The behaviour of B01 and B16, although complex, is perhaps simple to categorise at a high level i) B01 impacts the SBL, generating waves in the SBL, i.e. is wave-dominated. ii) B16, impacts the SBL and forms a surface current, preceded and followed by waves. However, B04 and B08 are harder to neatly categorise. At impact, both B04 and B08 appear similar in structure, although B08 reaches the surface whilst B04 is stopped around 100-150 m (Figure 6.5, t=644 and 450 s for B04 and B08 respectively). At this point, both runs generated waves that proceed the bulk of the motion. In the next plotted times (Figure 6.5, $t = 1017$ and 633 s for B04 and B08), slight differences in the subsequent behaviours can be seen. The bubble in B04

'spills' over the depression in the SBL made by the impact and forms a current in the upper layers of the SBL. At the same time, B04 experiences significant up-welling of cold fluid (possibly also seen to a smaller extent for B03 at $t = 1249$ s, not plotted. See attached GIF.) to almost to the height of the original SBL around $r = 0$ m (Figure 6.5, $t = 1017$s for B04). This transition from bubble to elevated current can also be seen in Figure 6.6, between $t = 644$, 1017 and 1405 for B04. However at $t = 1405$ s, it also appears that internal waves have been created. Throughout the work in this chapter, it will prove difficult to distinguish between what is a current (the physical flow of fluid horizontally from A to B) and a wave. Interestingly, B08 also forms what appears to be an elevated current (Figure 6.6, $t = 1392$s for B08). There are several features of note here, firstly B08 has formed an elevated current at a lower height in the SBL than B04 (roughly 700 and 900 m respectively). This emulates findings by Holyer and Huppert (1980) and Maxworthy et al. (2002) who find that elevated density currents propagate at a height based on the ratio of their initial densities versus the stratification of boundary layer. Secondly, the B04 and B08 elevated currents have propagated at different rates. Figure 6.6, shows B04 and B08 at approximately the same time (1405 and 1392 s), the elevated currents for B04 is slightly advanced that of B08 (3500 versus 3000 m) despite having impacted the SBL at a later time. Furthermore, the velocity contour plots suggest the magnitude of the velocity in B04 is greater than B08. This is contradictory behaviour to that seen in Chapter 5, where the rule was established that bubbles with greater initial buoyancy (or $\theta_b$) propagate fastest. Why then is a 'weaker' bubble travelling faster than a 'stronger' bubble? The answer might lie in the depth that each bubble reaches. The B08 bubble impacts the ground, and is slowed by the surface roughness. In contrast, a thin layer of 100 to 150 m of the SBL is maintained throughout the B04 bubble. This thin layer may serve a dual purpose, i) reducing the friction experienced by the B04 bubble and ii) speeding the recirculation (seen in the upwelling) of the original SBL. Both B04 and B08 also experience internal waves, seen mostly clearly in Figure 6.6, B04 at $t = 2100$ s.

Hovmöller plots are useful for developing a temporal understanding of the wave and current structures present in these numerical runs. Figures 6.7, 6.8 and 6.9 plot

x-time contours of $\theta$, the change in potential temperature, and horizontal velocity $u$ for a centre slice through the $y$-axis, for different $z$ heights. Figure 6.7 gives a sense of the infiltration depth of the bubble at impact. The bubbles are the warm signals seen at the different heights throughout the SBL. Starting with the top row, B01 reaches around 752 m, whilst there is little change in $\theta$ at lower levels, and almost none at the surface. This is an example of a downdraught event that has excited significant waves within the SBL but would not be registered on a temperature scale at the surface. B04 propagates further to at least $z = 250$ m, although again at the surface there is negligible $\theta$ change. B08 does impact the surface and is seen as a warming signal that spreads to almost 2 km in radius over roughly 500 s. B16 is the only model run that creates a sustained change to the surface environment, impacting around 250 s with $\theta$ perturbations extending up to 6 km and lasting over 3000 s. However, despite the B16 bubble originally being 4 times colder than the bottom of the boundary layer, the $\theta$ change at the surface is still a warm one. It is only in the top two levels ($z$ =998 and 752 m) that there is a cold signal in association with the arrival of the bubble. It appears that the fluid of the bubble itself is mixed away in the upper 250 m and it is actually the background fluid that reaches the surface. This surface warming is consistent with observations from Marsham et al. (2011) and Marsham et al. (2013) where surface wind speed increases attributed to downdraughts either did not coincide with surface cooling, or actually had slight surface temperature increases.

Whilst the identification of the bubble impact is clear, it remains difficult to understand the resulting evolution of the bubble and SBL. Are the outflows from the bubble impact, wave-dominated or current dominated? Consider the $x$-time velocity Hovmöller plots in Figure 6.8, the behaviour at the surface ($z = 12$ m) is relatively straightforward. For B01, the fluid from the bubble does not reach the surface, and waves are generated. There are at least 5 waves, of decreasing wave speed (as viewed anti-clockwise) with the first ($n_w = 1$) wave having a negative signal. Similar characteristics can be seen at the surface for B04, B08 and B16, although the wave structure become less defined with increasing bubble strength, especially for the higher order waves. All bubble impacts generate an $n_w = 1$ wave, although it is clearest to see in the $z = 12$ and 248 m plots. The wave behaviour is easiest to see at

the depths in the SBL where bubble fluid does not reach, the turbulent mixing of the near-bubble environment makes identification of the higher order waves more difficult. The wave amplitudes vary between bubbles but it appears that the gradient of waves in the Hovmöller plots and hence the wave speeds, are independent of $\theta_b$. The wave speed is looked at quantitatively in Section 6.5.2.

B16 is an interesting case since it is the only run to have a sustained surface current. This current can be seen in Figure 6.8 at $z = 12$ m between 0 and 4000 m as the bright yellow region of high horizontal velocity. There is a wave associated with this current, that precedes it (faint orange contours). Around 4500 m at 1000 s, the current appears to die (also seen in Figure 6.5) and the rest of the flow behaviour beyond this distance is wave dominated. B16 is analogous to the laboratory experiments of Manasseh, Ching, and Fernando (1998), where the dominant feature was the 'density-driven' current that transitioned to wave-dominated behaviour. However, caution should be taken using the term 'density-driven' since the current in B16 is actually less dense than the bottom of the SBL, suggesting the current is momentum driven rather than density driven. Note that, Manasseh, Ching, and Fernando (1998) did not measure the density change of their bottom currents with time so would not have known if their experiments were negatively, neutrally or positively buoyant. Using the definition from Maxworthy et al. (2002), B16 is an example of a subcritical current (the current head moves slower than the leading gravity wave).

Over Chapter 3 and 5, a detailed understanding of the descent and radial spread of negatively buoyant fluid without a SBL was developed. It is useful to compare and contrast Hovmöller of a numerical run without the SBL. Figure 6.10 plots the potential temperature, change in potential temperature and horizontal velocity of numerical simulation B1r5 (see Chapter 5, Table 5.2), which is identical in set-up to B01_SBL04, except without the SBL. Starting with the similarities; as expected both B1r5 and B01_SBL04 descent at similar rates. The potential temperature contours show both bubbles reaching $z = 1000$m at around 500s (as expected since they are identical runs up until this point). Interestingly, the velocity signal for both experiments still occurs at similar times for different heights, despite the addition of the

boundary layer. For example, B1r5 impacts the surface just after 1000s, which approximately corresponds to the triggering of a wave at the surface for B01_SBL04. The second similarity is that B1r5 still triggers a wave (blue velocity signal in Figure 6.10), although this wave has a noticeably different speed to that of B01_SBL04 in the SBL. This different wave speed is expected since the wave is travelling through a different density fluid without the top of the SBL acting as a lid. The magnitude of the horizontal velocity and potential temperature signal at the surface is much higher and persistent for B1r5 than at any height for B01_SBL04, which is attributed to the greater mixing experienced by B01_SBL04. Examining B1r5 is useful in determining the 'shape' of a gravity current, there is a characteristic curve to the propagation of the surface current in B1r5 which from Chapter 5, is known to be $r \propto B^{1/4}t^{1/2}$. Perhaps the only SBL experiment that this shape is replicated in is B16_SBL04.

The horizontal extent of the gravity currents and waves is not the only feature of interest. As discussed in Chapter 2, the vertical profile of downbursts is a subject of great interest in the engineering and atmospheric community. Figures 6.11 and 6.12 are potential temperature and horizontal velocity ($t - z$) contour plots for B01, B04, B08 and B16 (Note the change colour axis scale between different $r$ values). Figure 6.11 gives a good sense of the scale of disturbance caused by a downburst impact into a SBL. At $r = 3190$m, B01 only causes a slight perturbation of the SBL at around 2500s and at further $r$, there is hardly any disturbance at all. In contrast in B16, large amplitude waves pass through $r = 3190 - 9570$m, resulting in substantial mixing of the SBL. At the surface, for B16 at $r = 3190$ and 4141m, the coldest -4K contour appears mixed away after $\approx$ 500s. This relative surface warming corresponds with the warming signal seen in Figure 6.7. B16 is the only run with clearly defined peaks and troughs throughout the potential temperature of the SBL, these might exist for B04 and B08 but the frequency and amplitude is harder to determine. The frequency of the SBL oscillations appear quasi-regular for B16.

The wave behaviour triggered in the SBL can be seen in horizontal velocity ($t - z$) contour plots in Figure 6.12. In the far field ($r = 6390$ and 9570 m), away from the impact zone, the horizontal motions are dominated by the waves. At $r = 6390$ for B04,

B08, and B16 (faintly for B01), the vertical structure of the waves is both identifiable and similar between model runs. At $r = 6390$, all model runs experience a mode 1 wave, where a positive horizontal signal, extending from the surface to around $z = 800$m. This first wave mode is followed by an equivalent negative signal for a similar duration. Above the height of the SBL, opposite signed co-current waves are triggered. The next wave mode is just visible at around 2500-3000s in B04, B08 and B16 as the velocity profile goes from maximum negative velocity, to 0 at half the height of the SBL ($z = 500$m) and then to a positive maximum at the top of the SBL. At radial distances closer to bubble impact ($r = 3190$ and 4141m) for B04 and B08, the pattern of waves is broken by an interesting addition at the height of the SBL. For both model runs, there is a 500m wide region of sustained positive horizontal velocity which does not appear consistent with the wave structures in the background. This velocity anomaly is further evidence for the bubble impact triggering an elevated current at the interface of the SBL. Comparing the location of these elevated currents with the potential temperature contours in Figure 6.11, shows that the elevated currents coincide with the peak change in potential temperature profile in the upper part of the SBL. However, this mixing predominantly occurs in the upper 500 m of SBL (as opposed to B16 which causes mixing throughout the entire SBL). In addition, the magnitude of the horizontal velocity is greater for B04 than B08, as also shown in 6.6. This difference of greater horizontal velocity for a weaker bubble is attributed to the additional mixing and surface interaction experienced by B08. B16 is the only bubble that generates a surface current, which can be seen arriving at $r = 3190$m at $t = 500$s and $r = 4141$ at $t = 600$s. The surface current is slightly preceded by the first wave signal which appears 100-200s before the surface current. The arrival of the surface current coincides with strong re-circulations throughout height of SBL. After the surface current has passed through each location, a subsequent negative re-circulation occurs. This suggests that at this stage, the surface current exclusively consists of the current head and there is no significant 'tail' or secondary flow that follows.

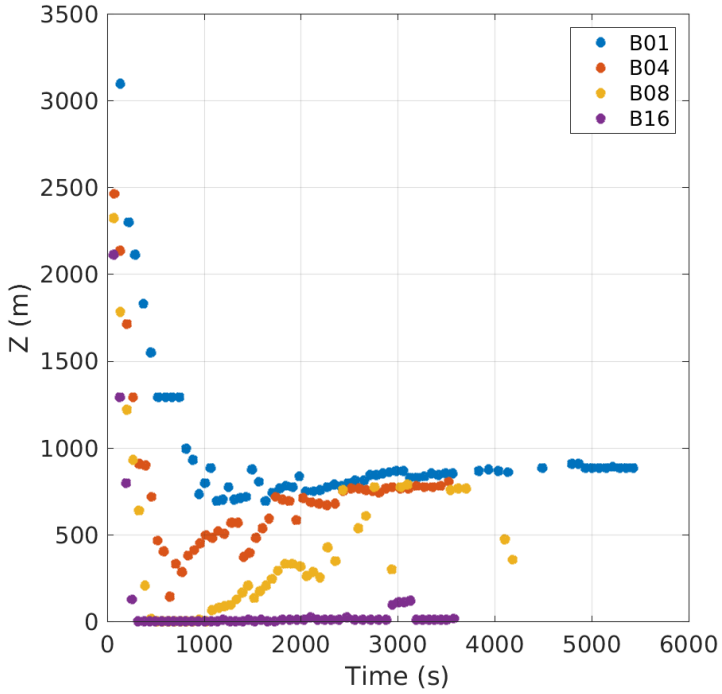


FIGURE 6.13: Vertical descent (m) of positive vorticity for B01-B16. The SBL extends to 1000 m.

## 6.5 Impact and evolution of thermal with a SBL

Flow visualisation has provided insight into the complex interaction between bubble and SBL. This section now apply quantitative techniques to assess the bubble's descent and radial propagation, the characteristics of gravity waves generated and the mixing length scale of the bubble in the SBL.

### 6.5.1 Bubble Descent and Propagation

Throughout the previous chapters, both the descent and spread of simulated downdraught has been shown to primarily depend on the total buoyancy $B$. Downdraughts with different initial radii and potential temperature perturbations scale by $B$. Chapter 5 found that the radial propagation $r$ of a negatively buoyant bubble can be related to the initial buoyancy by

$$r = kB^{1/4}(t - t_i)^{1/2} + r_i, \tag{6.5.1}$$

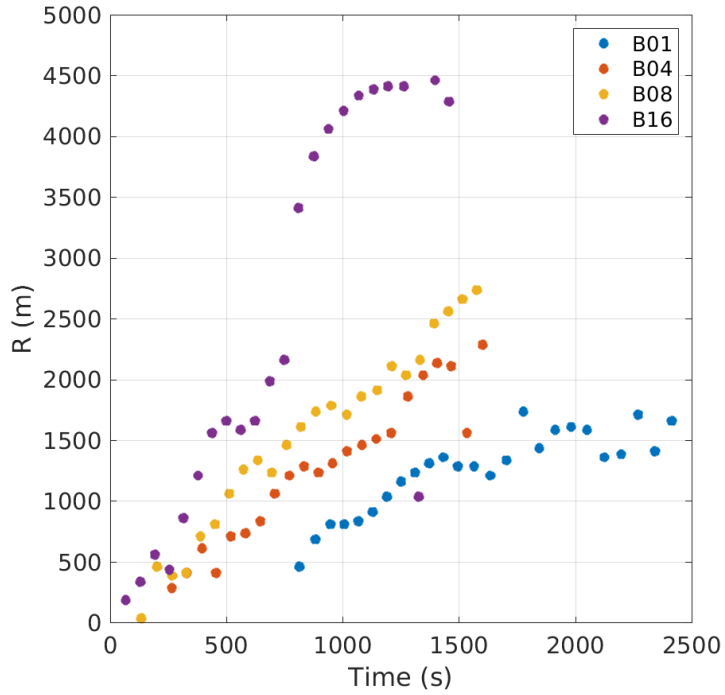


FIGURE 6.14: Radial propagation (m) of B01-B16. The SBL extends to 1000 m.

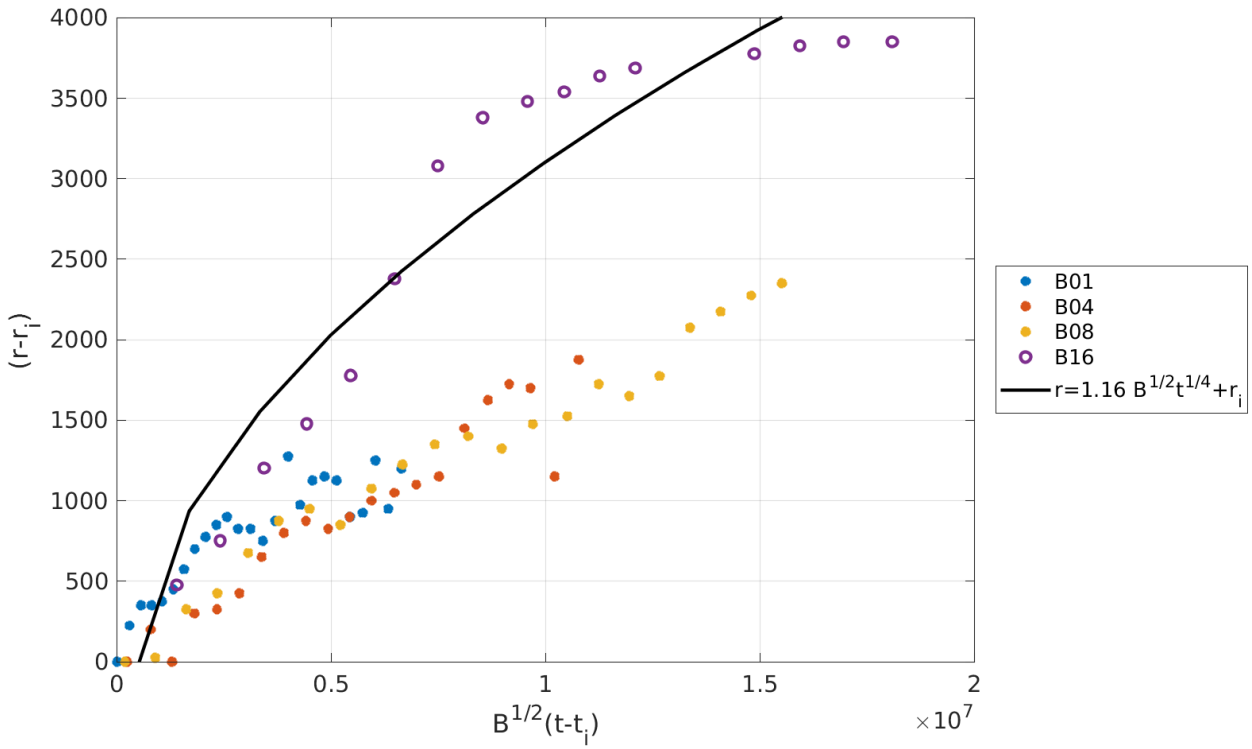


FIGURE 6.15: Radial propagation (m) of B01-B16, scaled by buoyancy and translated by radius and time of impact. The black solid line is (6.5.1).

where $r_i$ and $t_i$ are the radius and time of impact and $k$ is a constant, found to be 1.16 (see Chapter 5, Section 5.4.3). These expressions were shown to be valid for a bubble falling through an unstratified ambient background. The introduction of a SBL alters the background that the bubble descends through. Is (6.5.1) still valid for cases with a SBL and is the buoyancy still the primary parameter in the near-surface evolution?

As the bubble descends, positive vorticity is generated within the bubble. During impact, negative vorticity is induced in the SBL, however the positive vorticity is only lost at small scale mixing and therefore is quasi-conserved for much of the numerical run and is used to track the original bubble fluid. Figure 6.13 and Figure 6.14 estimate the vertical descent and radial propagation of the bubble fluid, using vorticity. Here, vertical descent and horizontal propagation are assumed to be that of the actual bubble rather than motion generated within the SBL during impact. Vorticity is tracked using a similar methodology to $\theta_p$ as described in Chapter 4, Section 4.2.2. The outline of vorticity is determined using the condition $\omega > 0.01$, vertical descent requires 20 grid points to be identified as within the outline for a given $z$ plane, radial propagation requires 10 grid points to be identified as within the outline for a given $r$ plane.

Figure 6.13 reflects trends seen in the previous Flow Visualisation section. The rate of vertical descent before impact with the SBL ($z$>1000 m), is monotonic with the bubble runs with greatest initial $\theta_b$, falling the fastest. Which layer of SBL the bubble fluid then resides in after impact also seems to depend on the initial buoyancy. B01 (blue), descends only to a depth of around 750 m (250 m into the SBL), before rising steadily to between $z$ =800 and 900 m. At the other end of the spectrum, B16 (purple) descends straight to the surface, almost as if there were no SBL, where the vorticity signal remains for the entirety of the run. B04 (red) and B08 (yellow) fall between the two extremes of B01 and B16, penetrating the SBL to different depths before rising back to the top interface of the SBL. B04 reaches around $z = 250$ m, whilst B08 hits the surface. The fact that both B04 and B08 rise to back to the interface of the SBL after impact, reflects that during descent and impact, the fluid of the

bubble has mixed away the majority of the density difference it originally held.

Figure 6.14 plots the radial propagation of the bubble against time. There is an increased rate of propagation for bubbles with greater $\theta_b$. Similarly, the maximum extent of the bubble (before radius of propagation decreases) is furthest for the strongest bubbles. Note that the decrease in propagation distance of the bubble is due to the mixing away of positive vorticity at longer times, and is not not an indication that bubble is being recirculated back towards the point of impact. The radial propagations in Figure 6.14 can be compared to (6.5.1). Figure 6.15 plots the radial propagation of all SBL model runs, scaled by buoyancy and translated by time and radius of impact. The original scaling of a thermal falling through an ambient background (6.5.1) is plotted as the black solid line. The four numerical runs collapse onto two different lines; B16 collapses onto line to similar to (6.5.1). As expected, the agreement between theory and modelled run is worse than seen for bubbles without the SBL in Chapter 5 because of the addition mixing in the SBL, however (6.5.1) still provides a reasonable estimation for B16. This good agreement can be attributed to the relative strength of B16 to the SBL (ratio of 4:1), and at least in the early stages of radial spread, B16 evolves almost as if the SBL was not there as a surface current. In the far field, B16 diverges from (6.5.1) as the head of the surface gravity current loses momentum and then dies (around at around $r = 4500$m). B01, B04 and B08 all collapse onto a slower trajectory (the collapse of B01 is questionable given the limited data points available). Remember that these runs with smaller initial buoyancies are propagating out with an entirely different mechanism, not as surface currents but as elevated currents or waves. However, despite this different mechanism of propagation, the buoyancy scaling that has been integral throughout the entirety of this study, remains relevant. The radial propagation of B04 and B08 still scales with initial buoyancy of bubble, albeit with a different relationship to (6.5.1).

There have not been any previous experiments of a descending thermal impacting SBLs, therefore it is difficult to put this study's results in the context of previous work. However perhaps the most comparable experiments are from Maxworthy et al. (2002), who conduct gravity current 2D channel lock release experiments into a

linearly stratified fluid. Experiments are catagorised by the ratio between the density of the lock release $\rho_c$ and the bottom density of the stratified fluid $\rho_b$,

$$R = \frac{\rho_c - \rho_0}{\rho_b - \rho_0}, \tag{6.5.2}$$

where $\rho_0$ is the density of the ambient fluid above the stratified layer. To both allow comparison between the laboratory experiments in water (saline solutions) and the atmospheric model runs of this study and highlight the dependency on properties of SBL, results are non-dimensionalised using the buoyancy frequency $N$ and a length scale $L$. Maxworthy et al. (2002) uses the length of lock release as the length scale (20 cm). The analogous length scale for the numerical runs is the radius of bubble at impact. Figure 6.16 plots the horizontal propagation of vorticity for B01, B04, B08 and B16, in addition to three experimental runs from Maxworthy et al. (2002) (data extracted from Figure 5. and Appendix A). The similarity solution for radial propagation (6.5.1) is plotted as the black dashed line. The seven experiments fall into two categories; B16 and Run 5, propagate faster than B01, B04, B08, Run 19 and 22. In addition, the shape of propagation between B16 and Run 5 (non-linear), and the other runs (linear) is different. Maxworthy et al. (2002) suggests that this difference is due to the value of the density ratio $R$ each experiment has and hence the method of propagation; i) density dominated or ii) wave dominated. For Run 5, $R = 3.41$, whilst Run 19 and 22 have $R = 1.40$ and 1.19 respectively. The equivalent for the numerical runs is $R = 4$ for B16, $R = 2, 1, 0.25$ for B08, B04 and B01. Certainly, this simple ratio of relative densities appears to work well in broadly sub-dividing the behaviour of the resulting propagation. To consider this second wave-dominated regime, the long-wave limit speeds are calculated from

$$c \approx \frac{N_0 H}{(n + 1/2)\pi}, \quad n \in \mathbb{N}. \tag{6.5.3}$$

The wave speeds for $n_w = 1, 2, 3$ are plotted as the solid black, red and blue lines (see Section 6.3 for derivation of (6.5.3). The mode 1 wave speed from Maxworthy et al. (2002) is plotted as the black dotted line. The purpose of these wave speed lines is to illustrate the mechanism of propagation. The applicability of the long-wave limit

assumption is discussed later in Section 6.5.2.

A reasonable hypothesis is that downbursts with a low $R$ values propagate linearly with a wave dominated mechanism, where the bubble fluid becomes coupled to a SBL wave speed. Maxworthy et al. (2002) finds their low $R$ value experiments propagate at the first long-wave limit mode $(Nh_b/\pi)$ whilst B01, B04 and B08 propagate in region between the second and third long-wave limit mode. This difference in wave speed could be down to the numerical experiments being axisymmetric versus quasi 2-D lock gate experiments, or a more fundamental reason to do with initiation of wave (bubble impact versus lock gate). Equivalently, downbursts with higher $R$ values behave more similarly to surface currents without the presence of the SBL and in the early stage can be represented well by (6.5.1). Future work is needed to determine the exact value of $R$ which determines the behaviour of the spreading bubble fluid. Although the experiments from Maxworthy et al. (2002) have a different buoyancy frequency and SBL, improving the parameter regime covered by Figure 6.16, future work which varied the properties of the SBL and hence the buoyancy frequency would allow greater understanding on how the propagation of bubble fluid is coupled to a wave speed or mode.

### 6.5.2 Waves

At impact, gravity waves are triggered in the SBL. These waves appear to travel both faster and further than the impact zone or the extent that the fluid from the actual downburst reaches (see Section 6.4) and therefore may be significant in breaking down the nocturnal SBL or triggering new convection. Figure 6.17 is an example of the methodology used for estimating wave speeds. Using the Hovmöller plots in Figure 6.7, straight lines are drawn through the velocity maximum or minimum of the waves. The gradient of these lines is then used as an estimate for the wave speeds.

All of the lines of identified waves for the five heights ($z = 12, 248, 500, 752$ and 1000m) from all model runs are plotted in Figure 6.18. Horizontal velocity contours at $z = 752$ m are plotted to give the reader a reference to the actual model run.

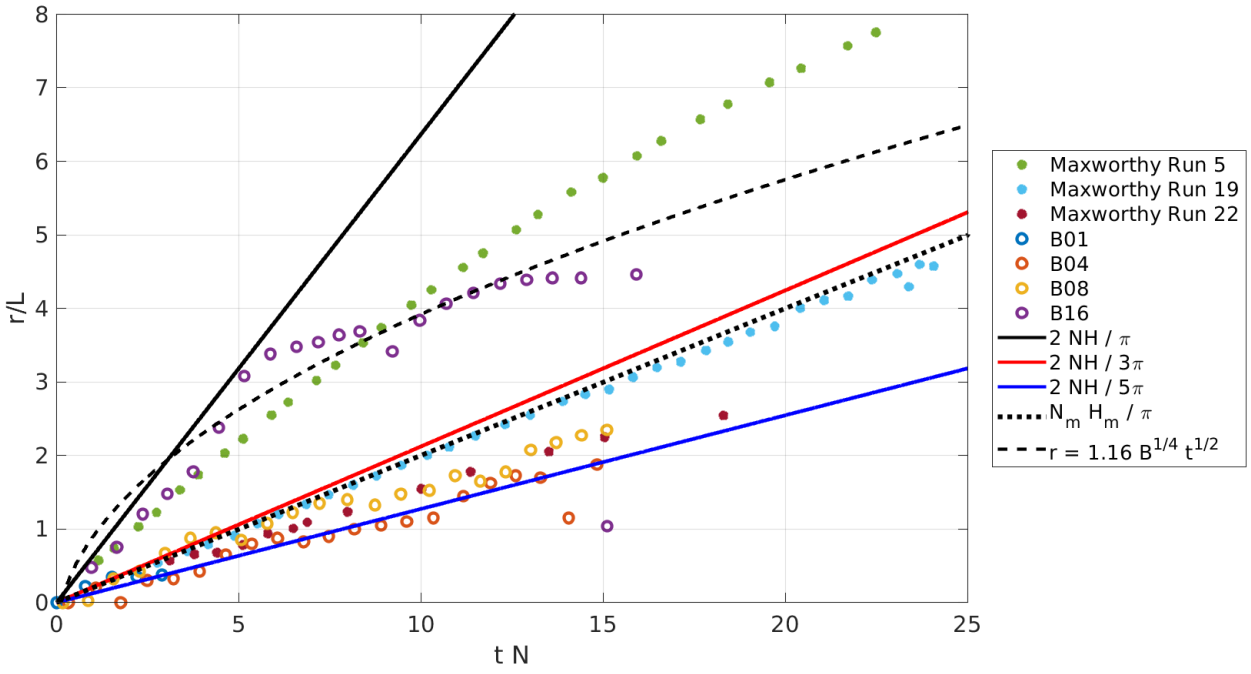


FIGURE 6.16: Radial propagation (m) of B01-B16, scaled by buoyancy frequency $N$ and characteristic length $L$. Lock gate experiments from Maxworthy et al. (2002) are plotted as the filled dots.

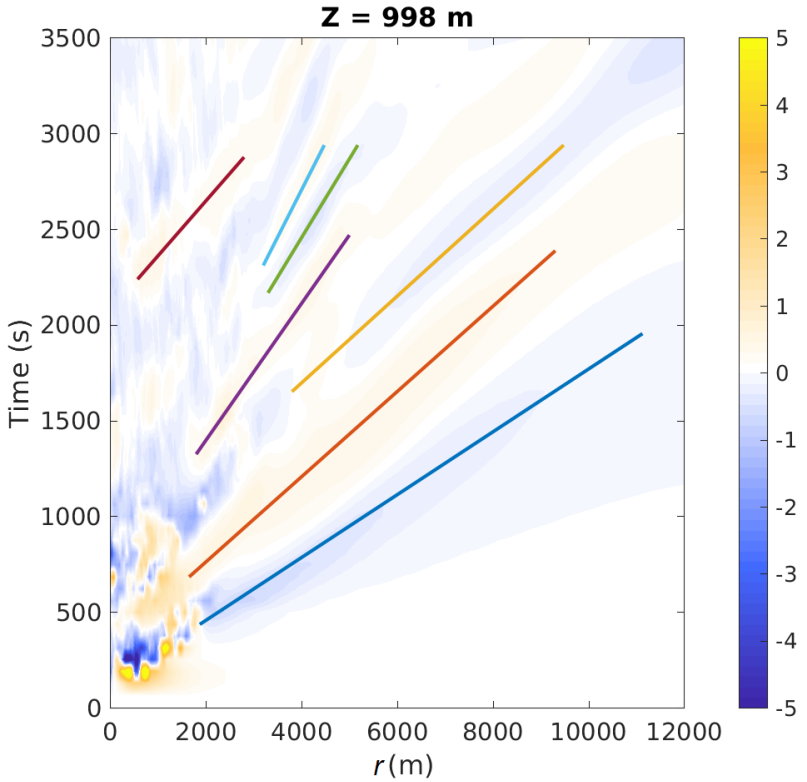


FIGURE 6.17: Methodology of wave speed identification. Horizontal velocity (m s$^{-1}$) ($r-t$) contour plot of B16 at $z$ =998 m. Wave speeds are estimated form the gradients of the coloured lines drawn through the velocity maximum or minimum of wave.

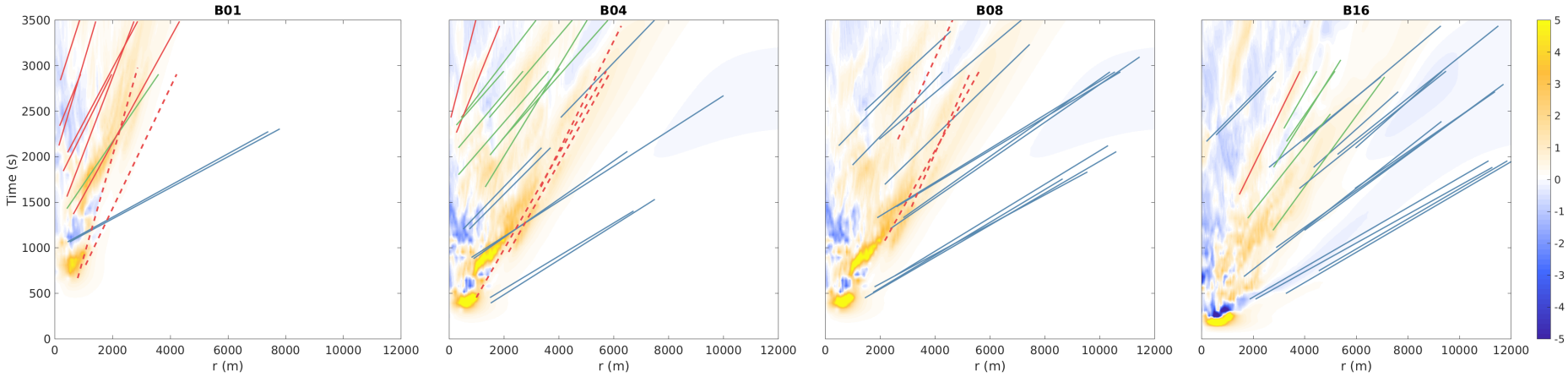


FIGURE 6.18: All of the lines of identified waves for $z = 12, 248, 500, 752$ and 1000m, for all model runs (B01 to B16 from left to right). Horizontal velocity contours for the single height $z = 752$ m are also shown. Identified wave lines are delineated by colour for different gradients. Lines with wave speeds $c > 4$ are plotted in blue, $2<c<4$ are plotted in green, $c < 2$ are plotted in red. Wave structures that the author has identified as being associated with an elevated current are dashed.

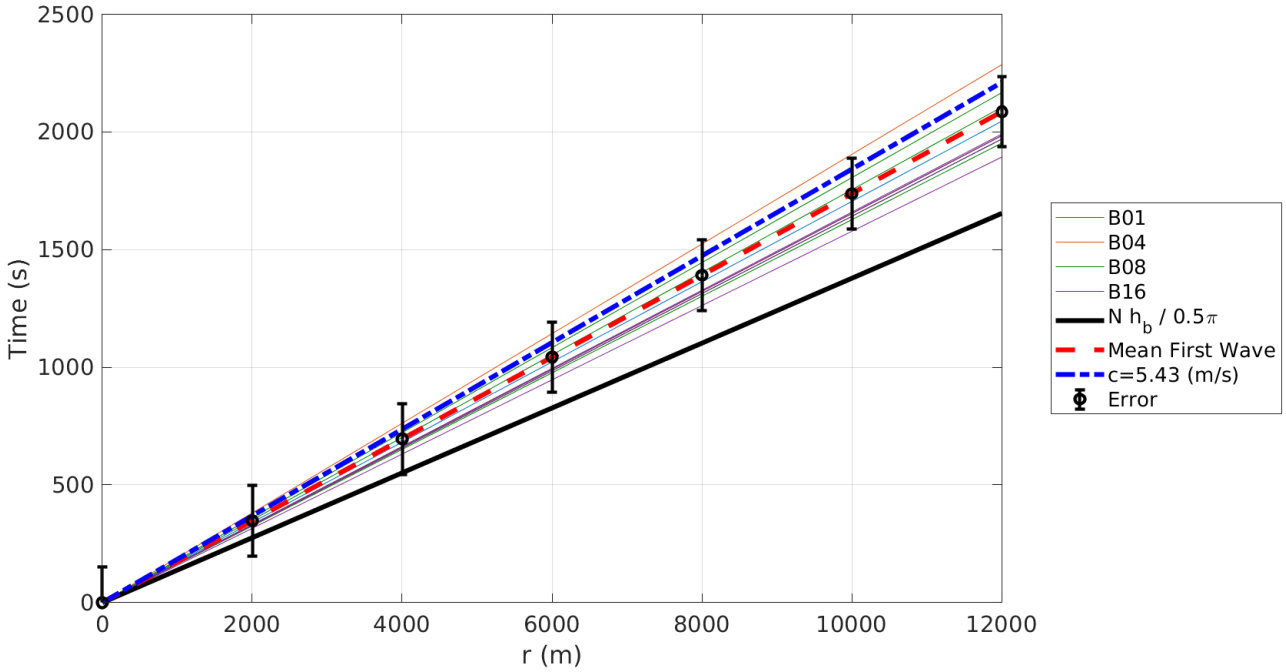


FIGURE 6.19: All of the identified first mode wave speeds (m $s^{-1}$) ($c > 4$) for B01, B04, B08 and B16. The dashed black line is the mean of first mode wave speeds for all model runs. The error bars are $\pm$150s. The black solid line is the long limit theoretical first wave speed. The red dashed line is the mean of all modelled first wave speeds. The blue line is the wave speed for wavenumber $k_w = 2\pi/4L$, determined from Section 6.3, Figure 6.4.

Identified wave lines are delineated by colour for different gradients (and therefore wave speeds). Lines with wave speeds $c > 4$ are plotted in blue, 2<$c$<4 are plotted in green, $c < 2$ are plotted in red. Wave structures that the author has identified as being associated with an elevated current are dashed instead of solid. Figure 6.18 provides a preliminary understanding of the waves generated when a thermal impacts a SBL.

All model runs trigger an initial gravity wave (blue lines). The vertical structure of the horizontal velocity in Figure 6.12 show that this first wave has a velocity maximum at the surface (most clearly seen in B04 and B08), which decreases to 0 around the height of the SBL. This vertical structure of $u$ is consistent with a mode 1 wave, as shown in Figure 6.4. This initial wave mode 1 wave appears to be generated at or shortly after the bubble impact with the SBL and has similar characteristics irrespective of the strength of bubble. Figure 6.19 plots the gradients of all of the waves speeds $c > 4$, translated to a single origin. The higher wave speeds appear to be similar for all model runs and given the uncertainty in the methodology of wave speed measurement, it is likely that all model runs generate an initial wave that is determined by the properties of the SBL and not that of the thermal. The mean of all higher waves speeds is 5.75 $\mathrm{ms}^{-1}$ (plotted in red dashed line), which is slightly lower than the theoretical long-wave first mode wave speed expected in a SBL (plotted as black line),

$$c_1 = \frac{2Nh_b}{\pi}, \tag{6.5.4}$$

where $N$ is the buoyancy frequency and $h_b$ is the height of the boundary layer (see Section 6.3. For this SBL, $c_1 = 7.26$ $\mathrm{ms}^{-1}$. This difference in long-wave speed and measured model first mode wave speed suggests that the long-wave assumption is not applicable. Figure 6.4 plots the expected vertical structure of the mode 1 and mode 2 internal gravity waves for the SBL. Each column in Figure 6.4 corresponds to a different wavenumber $k_w$. The right end column is the approximate long wave limit, where $k_w = 1 \times 10^{-4}$ and wave speed $c \approx Nh_b/((n + 1/2)\pi)$. The other columns from left to right are, $k_w = 2\pi/L, 2\pi/2L$ and $2\pi/4L$, where $L = 2b_0$ is the width of cold bubble ($b_0 = 500$m in all model runs). The third column with

wavenumber $k_w = 2\pi/4L = 0.0016$ m has a vertical structure similar to that in Figure 6.12; a horizontal $u$ maximum at the surface, going to 0 velocity, at around $z = 800$ m instead of $h_b = 1000$ m. The corresponding wave speed for this wavelength is 5.43 $ms^{-1}$ and is plotted as the blue dashed line in Figure 6.19. Qualitatively, this wavenumber appears to describe the wave dynamics for the first mode well.

The corrected wave speed using $k_w = 2\pi/4L = 0.0016$ m is 75% slower than the long wave limit. The radial propagation of the bubbles can now be compared to the revised wave speeds. Figure 6.20 is modified from Figure 6.16. The radial propagation of the numerical runs (estimated from tracking of the positive vorticity) is the same. However, the three plotted wave speed modes are reduced by 75% from the long wave limit. B04 and B08 propagate at a speed consistent with a mode 2 wave. Interestingly, in the early stage ($tN < 5$), B16 appears to be coupled with a mode 1 wave. This finding is contradictory to the assumption that B16 is only surface-current dominated. The radial propagation is still influenced by the wave modes of the SBL.

At longer times, all model runs generate a complex spectrum of different speed waves, all of the subsequently generated waves having lower wave speeds than the initial wave. Typically, the lower speed waves are generated (or only become visible) some time after bubble impact, and their structure is hard to identify or can become superimposed over by highest wave speed, which dominates the development of the flow field (away from actual bubble impact). The contradiction to this behaviour, are the dashed red lines marked on B01, B04 and B08. These structures, are dominant at specific heights ($z = 998$ for B01, $z = 752$ for B04 and B08). In the Flow Visualisation section, it was hypothesised that these features could be elevated currents from the bubble impact. Defining these disturbances as elevated currents is perhaps wrong, since Figure 6.14 showed that the radial propagation of bubble fluid (estimated from vorticity) does not extend beyond 2500 m and Figure 6.9 indicated there was a not a significant net movement of fluid along this disturbance. Instead, this study suggests that the impact of the bubble creates a specific higher mode wave

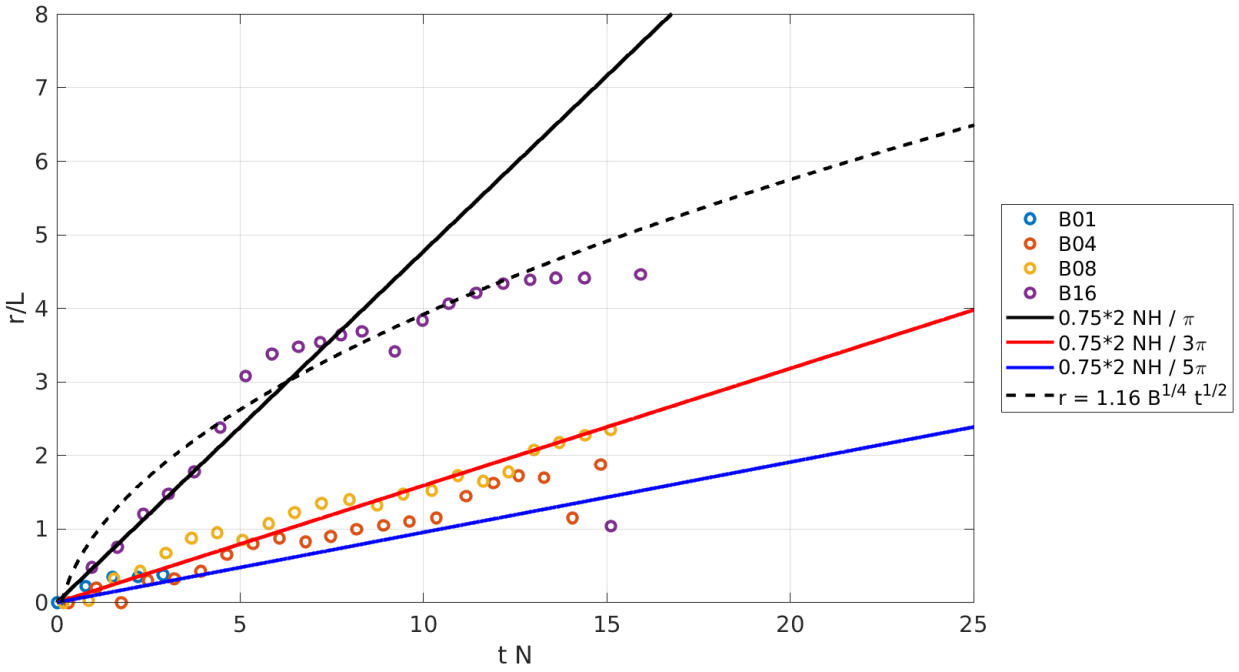


FIGURE 6.20: Radial propagation of B01-B16, scaled by buoyancy frequency $N$ and characteristic length $L$. The dashed line is the estimated radial propagation of B16 without a SBL from (6.5.1). The black, red and blue solid lines are the reduced mode 1, 2 and 3 wave speeds.

(from Figure 6.12 and 6.16, this could be the mode 2 wave) with which the bubble fluid is coupled with. This specific wave is the main mechanism for transporting energy and momentum within the SBL from the bubble. There are three pieces of evidence for this hypothesis; i) the prominent wave created in specific layers of the SBL, at a height dependent on the initial density of bubble. ii) the associated horizontal velocity maximum that is found at this specific height and along this specific wave speed line. iii) B16 features this specific wave, however since the initial bubble was strong enough to become a surface current, and therefore the dominant mechanism for momentum transfer is that surface current.

### 6.5.3 Mixing Scale

Flow visualisation in Section 6.4 showed the turbulent mixing that occurs in the SBL (see Figure 6.5 and 6.11). In addition, Figure 6.7 demonstrated how bubble impacts could actually lead to a surface warming anomaly, instead of the cold signal expected for a cold pool outflow. This anomaly was particularly surprising for

B16, since that was the only bubble that resulted in a surface current but it appears that surface current was still warm relative to its surroundings. This study uses a methodology commonly used in oceanography to assess mixing in the upper layers of the ocean (see Walin (1982) and Nurser, Marsh, and Williams (1999)) to quantitatively describe the mixing due to thermal impact in the SBL. Figure 6.21 plots the volume flux across the whole model domain, where volume is discretized into bins of potential temperature (different coloured lines), relative to the background unperturbed state of the SBL without the cold bubble. For example, for B01 at the first model time dump (60s) relative to a background of SBL without a bubble, the model domain has an additional 1e4 $m^3$ of 0.5K fluid, 2e4 $m^3$ of 1K and -3e4 $m^3$ of 0K, summing to a total domain volume flux of 0 (due to conservation of mass). The B01 bubble initially has a -1K perturbation, as the bubble falls and entrains, the -1K volume flux reduces and is replaced by increases in 0.5K and 0K bins. Impact is at around 600s, coinciding with the sharp drop of the 0.5K bin as the bubble fluid impacts the SBL as is mixed away in less than 500s. The impact of bubble excites mixing in the upper layers of the SBL, with increases to the 1.5K bin and roughly equivalent decreases to the 2K. Remember from Figure 6.13, B01 only penetrated around 250 m into the SBL ($z = 750$m) which is approximately at the -1K level in the SBL. Throughout the entire run, the colder bottom layers of bubble remain relatively unchanged and not affected by the impact of B01. In the long term, B01 creates an increase in the 0K and 1.5K volume bins and a decrease in the 0.5K bins, suggesting that the $\theta$ gradient in the upper SBL has slightly strengthened whilst in lower SBL the $\theta$ gradient remains unchanged. The impact of B04 results in a much greater volume of mixing, over a longer time period (roughly 1500s after bubble impact). Furthermore, B04 impacts to a depth of 250 m which results in perturbation of the colder $\theta$ bins. However, longer term distribution of the volume flux actually readjusts to one similar to B01; a reduction of 0.5K and an increase of 1K and 1.5K. B08 represents a step up in the scale of mixing, bubble impact with the SBL occurs around 300 s and penetrates to the surface (corresponding with the decreases in the largest $\theta$ bins). However, the large scale mixing seems to occur over a faster time period that B04 (up to 1500s). Note that the black $>$ 4K corresponds to all of the bubble fluid that is initially above 4K (B08 has an initial $\theta_p = 8$K). The impact of B16 causes a mixing regime not seen in

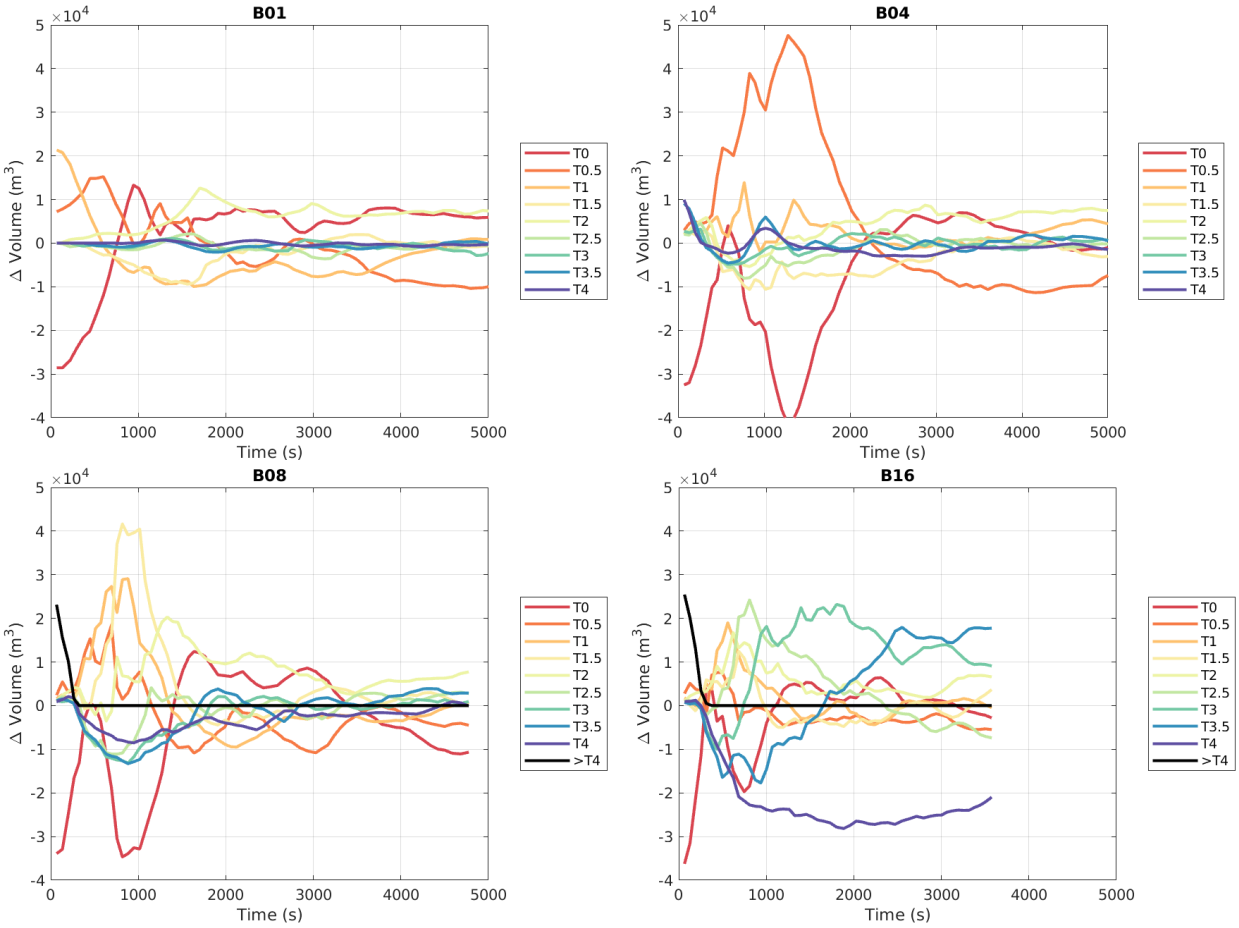


FIGURE 6.21: Volume flux across the whole domain for each model run. Volume is discretized into bins of potential temperature (different coloured lines), relative to the background unperturbed state of the SBL without the cold bubble.

the previous 3 runs, significant mixing occurs across all of the $\theta$ bins, with the coldest -4K seeing a large volume flux decrease (consistent with the surface warming signal associated the SBL) as the 4K bin is mixed away into the 3K and 3.5K bins. On one level, the volume change of SBL after bubble impact is simple to understand; as one intuitively expects, stronger bubbles creates more mixing than weaker bubbles. However, it is the timescale it takes for that SBL to recover to its initial unperturbed state that is of most interest. For example, an hour after the impact of the downburst in B16 and the SBL is still significantly weakened from the turbulent mixing. The $\theta$ gradient from surface to the top of the SBL has been reduced, meaning that the SBL could potentially break down faster than anticipated.

## 6.6 Summary

LES experiments using the MONC were conducted to provide a better understanding of the descent and near-surface evolution of atmospheric downdraughts impacting a stable boundary layer (SBL). The downdraught was represented in the simulations by an instantaneously released bubble of cold fluid, which was allowed to fall freely and then impact the SBL. The SBL was created by imposing a constant potential temperature gradient from surface to the top of the SBL. These experiments were novel, with little previous work available on this subject, therefore the initial part of the study consisted of a thorough flow visualisation exercise to understand how cold bubbles interact with SBLs.

Flow visualisation revealed that:

- Before impacting the SBL, bubbles descend as expected with the same rate of vertical descent observed in Chapter 3 and 5.
- Impact and resulting evolution of bubble within the SBL is determined by the bubble's initial buoyancy. Three flow regimes were observed; i) a weak bubble B01, which only penetrates 250m into the SBL, perturbing only the upper layers of the SBL ii) medium bubbles B04 and B08, which penetrate almost to the surface and to the surface respectively. Causing perturbations throughout the SBL iii) a strong bubble B16, which creates a surface current and significant long-term mixing of the SBL.
- B01, B04 and B08 create either elevated currents or a specific type of wave at a height in the SBL proportional to their initial buoyancy.
- Surprisingly, B04 propagates faster horizontally than the more negatively buoyant bubble B08. This slow down of B08 is attributed to a surface interaction (B04 only reaches $z = 100 - 150$m, whilst B08 impacts the surface).
- Counter-intuitively for a cold bubble event, the impact of B04, B08 and particularly B16 coincided with surface warming signals as warmer air is mixed down from the ambient atmosphere and upper layers of the SBL. This mechanism for surface warming potentially provides explanations for atmospheric

observations in the US and Sahara where suspected downburst events do not coincide with surface cooling (Marsham et al., 2011; Marsham et al., 2013).

- The impact of all bubbles create fast moving waves in the boundary layer.

Equipped with a better understanding of the problem after flow visualisation, some quantitative methods were then applied. Analysis of the vorticity provided estimation of the descent and spread of bubble fluid. In the vertical, horizontal vorticity reached depths in the SBL proportional to the initial buoyancy of bubble. In the radial, the horizontal vorticity of bubbles spread at two different rates when scaled by buoyancy; B16 moved faster and further than the other bubbles at a rate that fitted the radial propagation for a spreading bubble without a SBL (6.5.1). The radial propagation of B01, B04 and B08 also scaled, but at a slower rate. Comparison with analogous laboratory experiments from Maxworthy et al. (2002) and the theoretical long-wave limit modes, showed that this study's numerical runs emulated the two behaviours of i) surface current driven and ii) wave-dominated observed in Maxworthy et al. (2002), depending on the relative density difference between initial bubble (or lock gate release) and SBL, $R$.

Using wave speeds derived from Hovmöller plots of horizontal velocity (Figure 6.8), an assessment of the resulting wave dynamics could be made. It was found that all bubble runs trigger waves in the SBL. The first of these waves appeared consistent for all model runs and had a similar wave speed and was identified as a first mode wave. The assumption of a long-wave limit was shown to overestimate the wave speed. Instead, a wavelength of $k_w = 2\pi/4L$, where $L = 2b_0$ is the width of bubble, was shown to qualitatively represent the wave behaviour well. More complex, higher mode waves were then subsequently generated. Of particular interest were wave-like structures at certain heights for B01, B04 and B08 which were primarily responsible for the transport of momentum. B01, B04 and B08 appear coupled to a mode 2 wave. There is some evidence that B16, despite being identified as a surface current, is still influenced by the mode 1 wave speed. These specific waves are attributed as the main mechanism for momentum transport and the specific waves

properties are determined by the properties of the bubble in addition to the SBL. Finally, examination of the volume flux of different bins of the potential temperature across the whole domain (Figure 6.21) provided insight into magnitudes and time scales of SBL mixing. It was found that stronger downbursts can significantly alter the vertical structure of the SBL, weakening the potential temperature gradient, for sustained time periods.

Numerical simulations of negatively buoyant thermals descending, impacting SBLs and the subsequent evolution of currents and waves have been presented. To the author's best knowledge, this is the first idealised study of this phenomenon. The purpose of this chapter is not to provide comprehensive theoretical scalings or similarity solutions but instead undertake a preliminary study into the different types of flow regimes created by impacting cold bubbles, with the hope that atmospheric scientists will consider this work when searching for explanations for unusual potential temperature signals from downbursts, the unexplained triggering of convection or the early breakdown of a nocturnal stable boundary layer.

# Chapter 7

# Conclusions

The aim of this research was to provide a better understanding of the descent and near-surface evolution of atmospheric downdraughts. Through a combination of theory, analysis of laboratory experiments and numerical simulations, this study: i) evaluates and suggests modifications to existing theory for the descent and spread of buoyant fluid, ii) offers new expressions relating the maximum velocities and kinetic energy of radial spread to the initial conditions at source, iii) compares and contrasts different models of cold pool propagation, and iv) considers the importance of the interaction between downdraughts and stable boundary layers.

Data gathered from saline release experiments conducted as part of an MSc study at the Sorby Laboratory at the University of Leeds, was used as a scale model to analyse an atmospheric fluid dynamics problem. Flow visualisation in Chapter 3 indicated that experimental releases contained all of the salient features of an atmospheric downburst as identified by previous experimental, field and numerical studies (Lundgren, Yao, and Mansour, 1992; Hjelmfelt, 1988; Vermeire, Orf, and Savory, 2011). Specifically, i) as dense fluid is released, a vortex ring formed, ii) the dense fluid propagates vertically downwards, steadily growing in width, iii) upon impact, the vortex ring 'billows' up and begins to propagate radially forming a gravity current.

The properties of the negatively buoyant fluid in the experiments in both the vertical descent and radial propagation stage could be estimated by the initial conditions of experimental set-up by using modified similarity solutions. Experimental releases

were shown to have reasonably reproducible rates of vertical descent. The results were non-dimensionalised by a scaling proposed by Lundgren, Yao, and Mansour (1992), where $R_0$ is pipe outlet and $t_0 = (R_0/g')^{1/2}$. This scaling worked well, propagation rates of experiments with different density releases collapsed onto one line. Vertical descent of experiments was in good agreement with thermal similarity solutions described by Turner (1962) and modified by Rooney (2015) to be,

$$z + z_v = \left(2Fr\, m^{-1/2}\alpha^{-1}B^{1/2}t\right)^{1/2}.$$

The formation of the vortex ring was identified as the determining mechanism for the rate of vertical descent. Experiments with release times greater than their theoretical vortex formation time, had the same rate of vertical descent. Since (7) was developed for quasi-spherical thermals, this study proposed a simple adaptation for vertical descent rate of longer saline releases. Instead of using the total buoyancy $B$, only the buoyancy in the vortex ring $B_v$ is used. This adaptation provided a better, although still imperfect fit to the experimental results.

During the radial propagation, experiments had reproducible propagation rates, particularly when adjusted by the radius of impact. Larger volumetric releases resulted in faster rates of propagation. The similarity solution, developed by Rooney (2015) for the spread of negatively buoyant fluid,

$$r = (2Fr_c)^{1/2}\lambda^{1/4}B^{1/4}(t - t_i)^{1/2} + R_0$$

was validated by the experiments subject to several adaptations. Supporting previous experimental gravity current experiments by Hallworth et al. (1996), $Fr$ and $\lambda$ were changed from 1.4 and 1.0 to 1.19 and $\pi^{-1}$. Experimental releases were not quasi-spherical in origin, therefore $R_0$ was taken as the radius at impact $R_0 = b_0 + \alpha H$, instead of the radius of the quasi-spherical volume of fluid.

In addition to focusing on the bulk fluid properties, attention was given to the instantaneous velocities that occurred in the head of the gravity current, analogous to an

atmospheric gust front. The vertical profile of the horizontal velocity was compared with an empirical profile developed by previous experimental and numerical studies (Wood et al., 2001; Sengupta and Sarkar, 2008), and was found to fit well. This study proposed that the maximum horizontal velocity is simply a function of the gravity current propagation speed $u_{rmax} = f(u_r)$, where the gravity current propagation speed is itself only a function of buoyancy and radius of pipe outlet. A simple relation is suggested,

$$u_{rmax} = ku_r = kFr_c\lambda^{1/2}B^{1/2}r^{-1}, \tag{7.0.1}$$

where from experiments $k = 3$. Figure 3.35 supports this relation for the maximum velocities in the gravity current.

Chapter 3 ended with unanswered questions. Key among those was: are the results from Chapter 3 consistent with a wider parameter regime? Therefore, LES simulations were designed in the new Met Office and NERC Collaboration (MONC) model for a wide parameter regime of cold bubble runs. The challenges of working with an entirely new numerical model (albeit with the physics from the original Met Office Large Eddy Model) were substantial and a significant body of time was spent setting up and then determining a suitable configuration of model runs (Chapter 4).

Chapter 4 outlines a methodology for modelling idealised atmospheric downdraughts. The new Met Office and NERC Collaboration (MONC) model is used to conduct large eddy simulations of idealised downdraughts. The downdraught is represented using a cold bubble which is instantaneously released and allowed to fall freely during the simulation. The methods used for identifying and tracking buoyant fluid are described, and the thresholds needed for those identifications are found. A grid sensitivity test is conducted to determine the necessary grid spacing of model runs. To the authors best knowledge, this study conducts the highest resolution numerical runs for this type of cold bubble experiment. The model configuration described in Chapter 4 was then employed throughout the remainder of thesis.

Chapter 5 used the numerical model of an idealised downdraught to further investigate the descent and near-surface evolution of negatively buoyant fluid. Similarity solutions developed by Rooney (2015) and modified by this study in Chapter 3, were compared against the modelled bubble runs. Analysis of the modelled vertical descent and radial propagation found:

- The vertical descent was evaluated using similarity solutions from Rooney (2015). The proposed adaptation is suggested

$$z + z_v = k_r B^{1/4} t^{1/2}, \tag{7.0.2}$$

  where this study suggests $k_r = 2.63$ due to differences in calculating the Froude number ($Fr = 1.2$) and the entrainment constant ($\alpha = 1.26$).

- The rate of radial propagation for spreading thermal as suggested by Rooney (2015) and modified in Chapter 3, is evaluated.

$$r = (2Fr_c)^{1/2} \lambda^{1/4} B^{1/4} (t - t_i)^{1/2} + r_i. \tag{7.0.3}$$

  The proposed adaptations to Rooney (2015) are: i) that the radius of impingement $r_i$ is included, and ii) the Froude number is taken as $Fr_c = 1.19$ and $\lambda = \pi^{-1}$, which supports the findings in Chapter 3.

- The laboratory experiments in Chapter 3 are compared to the numerical bubble runs using an adapted scaling from Lundgren, Yao, and Mansour (1992), where the length scale is initial radius of bubble (or pipe outlet diameter in the experiments) $b_0$ and the characteristic time is $t_0 = b_0^2 B^{-1/2}$. Figure 5.8 plots the vertical descent of numerical results and laboratory experiments, supporting (7.0.2). Similarly, Figure 5.10 plots the radial propagation of numerical simulations and laboratory experiments in support of (7.0.3).

Section 5.2 presented new expressions for the potential and kinetic energy for the descent and spread of negatively buoyant thermals, derived from Rooney (2015). In the vertical stage, this study suggests the potential energy ($PE_v$) and kinetic energy

($KE_v$) are:

$$PE_v = \rho_0 BH - \rho_0 Bz, \tag{7.0.4}$$

$$KE_v = \frac{1}{2}\rho V Fr_T^2 m^{-1}\alpha^{-2}(k_2+1)Bz^{-2}, \tag{7.0.5}$$

where $k_2 < 1$ is a constant. In the radial stage, this study suggests the kinetic energy ($KE_r$) is:

$$KE_r = \frac{1}{2}\rho\pi H^3\lambda^2 c\alpha^3 Fr_c^2\left(1+\frac{b_0}{\alpha H}\right)^3 Br^{-2}f, \tag{7.0.6}$$

where $f$ is an empirical function proposed as $(r'_{max}/R_0)^{-1.3}$ by Rooney (2015). Numerical simulations support (7.0.4) and (7.0.5), as shown in Figure 5.11 and Figure 5.15. A value of $k_2$ is suggested between 0.25 and 0.5.The numerical simulations support the estimation of $KE_r$ (7.0.6), as shown in Figure 5.15.

Having established expressions for KE and PE, the buoyancy based similarity solutions from Rooney (2015) were then compared to the energy balance similarly solutions from Romps and Jeevanjee (2016) (referred to as RJ). This study demonstrated how RJ could be modified from initial conditions of a collapsing cylinder to that of a thermal at impact, through adaptation of the initial velocity $U_0$ and the radius of thermal at impact, to give the radial propagation $R$:

$$R(t) = R_0 + \frac{1}{\epsilon}\log(1+t\epsilon U_0 M), \tag{7.0.7}$$

where

$$U_{0M} = \sqrt{\frac{2\beta g\kappa\rho'_t(b_0+\alpha H)}{\rho}}. \tag{7.0.8}$$

Comparison of (7.0.3) and (7.0.7) to the numerical simulations showed both theories provided good estimations of the radial propagation of thermal after impact with time. In the near field, (7.0.7) from RJ provides a better estimation of radial propagation to (7.0.3) because of the formulation of the radius of impact. However, Figure 5.20 demonstrated that when the fundamental shape of each theory is compared to the numerical runs, buoyancy based similarity solutions from Rooney (2015) achieve a better $R^2$ value compared to RJ.

Using two different methodologies: laboratory experiments in Chapter 3 and numerical simulations in this chapter, similarity solutions that estimate a thermal's descent and radial spread based only on the initial conditions of source and the time passed, have been shown to provide accurate estimates of the thermals behaviour. Across different mediums (water and air) and different scales, the same equation set can be used to predict the behaviour of negatively buoyant fluid.

Previous field experiments and observations have indicated that downdraughts from elevated convection can impact stable boundary layers (SBLs) and generate gravity current, waves and bores (Browning et al., 2010; Marsham et al., 2010; Marsham et al., 2011; Marsham et al., 2013; Geerts et al., 2017). There has been little previous research into this area and Chapter 6 presents, to the authors best knowledge, the first investigation into idealised downdraughts impacting a SBL. Qualitative analysis of potential temperature and velocity contour plots indicate that the impact and resulting evolution of bubble within the SBL is determined by the bubble's initial buoyancy. Three flow regimes were observed; i) a weak bubble B01, which only penetrates 250m into the SBL, perturbing only the upper layers of the SBL. ii) medium bubbles B04 and B08, which penetrate almost to the surface and to the surface respectively. Causing perturbations throughout the SBL. iii) a strong bubble B16, which creates a surface current and significant long-term mixing of the SBL. The impact of B04, B08 and particularly B16 coincided with surface warming signals as warmer air is mixed down from the ambient atmosphere and upper layers of the SBL. This mechanism for surface warming offers an explanation for atmospheric observations in the USA and Sahara where suspected downburst events do not coincide with surface cooling (Marsham et al., 2011; Marsham et al., 2013).

Analysis of the vorticity provided estimation of the descent and spread of bubble fluid. In the vertical, horizontal vorticity reached depths in the SBL proportional to the initial buoyancy of bubble. In the radial, the horizontal vorticity of bubbles spread at two different rates when scaled by buoyancy; B16 moved faster and further than the other bubbles at a rate that fitted the radial propagation for a spreading

bubble without a SBL (6.5.1). Comparison with analogous laboratory experiments from Maxworthy et al. (2002) and the theoretical long-wave limit modes, showed that this study's numerical runs emulated the two behaviours of i) surface current driven and ii) wave-dominated observed in Maxworthy et al. (2002), depending on the relative density difference between initial bubble (or lock gate release) and SBL, $R$.

Using wave speeds derived from Hovmöller plots of horizontal velocity (Figure 6.8), an assessment of the resulting wave dynamics could be made. It was found that all bubble runs trigger waves in the SBL. The first of these waves appeared consistent for all model runs and had a similar wave speed and was identified as a first mode wave. The assumption of a long-wave limit was shown to overestimate the wave speed. Instead, a wavelength of $k_w = 2\pi/4L$, where $L = 2b_0$ is the width of bubble, was shown to qualitatively represent the wave behaviour well. More complex, higher mode waves were then subsequently generated. Of particular interest were wave-like structures at certain heights for B01, B04 and B08 which were primarily responsible for the transport of momentum. These specific waves are attributed as the main mechanism for momentum transport and the specific waves properties are determined by the properties of the bubble in addition to the SBL. The structure and speed of the waves in the SBL are qualitatively compared to, and found to fit, theory for internal gravity waves moving in a SBL with rigid floor and continuous top boundary.

Finally, examination of the volume flux of different bins of the potential temperature across the whole domain (Figure 6.21) provided insight into magnitudes and time scales of SBL mixing. It was found that stronger downbursts can significantly alter the vertical structure of the SBL, weakening the potential temperature gradient, for sustained time periods.

## 7.1 Conclusions

Drawing together the work within results Chapters 3-6, several overarching conclusions can be made.

- The descent and radial propagations of saline solutions within laboratory experiments and numerical simulations can be well described by similarity solutions that match i) an instantaneous buoyancy release or ii) a constant buoyancy flux with theory for the propagation of gravity currents. However, these similarity solutions are sensitive to the source conditions of outlet or simulation, which ultimately determines the subsequent flow regime.

- Non-dimensional scalings from Lundgren, Yao, and Mansour (1992) and Kaye and Hunt (2007) have been used to compare results from the two different methodologies used in this study, i) laboratory experiments of saline releases and ii) numerical simulations idealised atmospheric downbursts. The good agreement between results from each methodologies suggests that the underpinning fluid dynamics is same across both scales. In particular, MONC is a relatively new numerical model and therefore consistent results with laboratory experiments offers a degree of validation.

- Numerical simulations of negatively buoyant thermals descending, impacting SBLs and the subsequent evolution of currents and waves have been presented. To the author's best knowledge, this is the first idealised study of this phenomenon. SBLs were shown to exhibit different dynamical behaviour (waves or gravity current) depending on the properties of thermal. This study suggests that the complex interactions between the impact of downdraughts and SBLs may offer explanations for unusual potential temperature signals from downbursts, the unexplained triggering of convection or the early breakdown of a nocturnal stable boundary layer.

## 7.2 Future Work and Potential Impact

This work has been a study into idealised downdraughts. There are two paths that future work on this area could take: i) a direct extension of the study into idealised

downdraughts, which continues to explore a widening regime of different flow scenarios. ii) transitioning this work to actual atmospheric downdraughts.

For the continuation of study into idealised downdraughts, suggested areas might include:

- Further scope for experimental studies. The laboratory experiments in Chapter 3 and the subsequent comparison with numerical simulations in Chapter 5 demonstrated the benefits of saline solution experiments to determine the transport of buoyant fluid. However, the laboratory experiments analysed in Chapter 3 covered only a limited parameter regime. Furthermore, on reflection the design of the release mechanism for buoyant fluid (pneumatic valve that opens a header tank) was not ideal. This method was cumbersome and resulted in an undetermined injection of momentum into the saline release. The approach of Lundgren, Yao, and Mansour (1992) who used a needle to pierce a latex film covering a release volume of fluid is suggested as a better alternative.

- Change of source of buoyant fluid. Throughout the numerical simulations, the downdraught is represented as instantaneous releases of a cold bubble. How realistic this representation is in comparison actual atmospheric events is not fully interrogated. Alternatives include using a cooling source (as in Anabor et al. (2011)), which would allow different categories of buoyant release; from instantaneous bubble, to continuous plume. Another option is instead of using spherical bubbles, change the aspect ratio of that bubble (as in Kruger et al. (2017)).

- Change of release height. The height of buoyant fluid release was fixed in both the laboratory experiments and numerical simulations. In the vertical descent stage, experimental and numerical releases were consistent with theory from Morton, Taylor, and Turner (1956) and therefore changing the release height was assumed to simply scale accordingly. However, as was shown in the laboratory experiments, the leading vortex ring has a specific formation time. It is possible that for particularly low release heights (e.g. when cloud base is >2 km), that the similarity solutions for descent and spread are no longer valid.

In these low cases, the problem potentially becomes more similar to the cold collapsing cylinder model from Romps and Jeevanjee (2016).

- Release of multiple bubbles. Observations from Hjelmfelt (1988) show that whilst downbursts can occur in isolation, more commonly they occur in downburst lines comprising of multiple individual downburst. These downburst lines result in much longer-lasting wind shear than exists with isolated downbursts. The author is only aware of one previous study (Orf, Anderson, and Straka, 1996) that considers two colliding microbursts. Questions relating to the superposition of downburst outflow and the additional (if any) increase in wind speed or shear, is worth further investigation.

For transitioning this work for actual atmospheric downdraughts:

- Consideration of microphysics. An assumption used throughout the whole study is that downdraughts can be represented as releases of negative buoyancy or momentum. The complex microphysics are not represented by either experiment or simulation. Proctor (1988) used a microphysics permitting model which generated downbursts from rain and hail. A piece of work started but never completed was running large area idealised simulations, where radiative forcing triggered convective cells. These cells could then be analysed statistically to determine rates of horizontal outflows, maximum 10m wind speeds, and compared to similarity solutions.

- Atmospheric case study. Another piece of work started but not completed was using the German weather service atmospheric model ICON-ART to model an identified downburst event in the Sahara. The rate of horizontal outflow could be compared to that of similarly solutions. In addition, there was interest in a mechanism suggested by Heinold et al. (2013) where a nocturnal low-level jet is triggered by an aged convective cold pool (see Figure 7.1). The idea was to try to reproduce this behaviour in an idealised and realistic numerical simulation.

The work of the impact of downdraughts onto stable boundary layers is the most novel part of the thesis and represents the area with the most scope for future work.

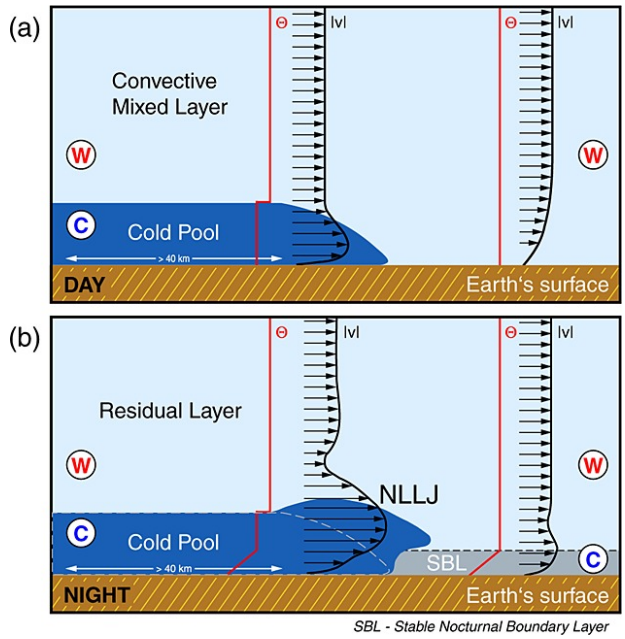


FIGURE 7.1: Schematic diagram illustrating the mechanism of nocturnal LLJ formation triggered by an aged convective cold pool. Shown is the (a) daytime and (b) nighttime boundary layer with typical profiles of mean potential temperature (red line) and wind speed (black line) for the undisturbed case, and the boundary layer disturbed by the cold-pool outflow. The red "W" and blue "C" indicate relatively warm and cold air, respectively. Figure reproduced from Heinold et al. (2013).

Idealised numerical simulations of this interaction resulted in complex and interesting phenomenon; local disturbances at impact, unusual surface temperature signals, mixing of the SBL and generation of gravity waves. Observations indicate that SBL-downdraught interactions do occur, however it will take further research in an atmospheric setting to determine the relative importance of this process on the local environment (Browning et al., 2010; Marsham et al., 2010; Marsham et al., 2011; Marsham et al., 2013). Immediate future work on the idealised case of downdraught-SBL interaction should include:

- Introduction of a bubble tracer. Unfortunately the numerical model used for these simulations (MONC), does not yet the ability to use a tracer (there is a method of using a dummy moisture $q$ variable developed by Anne Barber and Steef Boeing at the University of Leeds). A tracer would have been invaluable for the tracking of bubble fluid.

- Expansion of parameter regime to include different SBLs. Chapter 6 provides analysis for four model runs, all with the same SBL. Only one parameter has

been varied in this study (initial temperature perturbation). The natural extension is to include different buoyancy frequencies, depths of SBL, different SBL profiles, radii of bubble etc.

### 7.2.1 Implications for Atmospheric Science

Scalings and similarity solutions have been proposed for idealised cases of the descent and spread of negatively buoyant fluid. It would naturally be interesting to determine how applicable this body of work is when considering actual atmospheric events. The closest comparison this study can make to actual downbursts is to use measurements from previous studies. Figure 7.2 plots radial propagation scaled by initial radius $b_0$ against buoyancy scaled time, where from Lundgren, Yao, and Mansour (1992), $t_0 = b_0 B^{-1/2}$. The laboratory experiments from Chapter 3 are plotted as black circles, MONC LES runs from Chapter 5 are plotted as solid and dashed coloured lines, LES results from Rooney (2015) are plotted as red circles. The black solid line is this study's modified equation for radial spread (7). The blue triangles are anemometer ground measurements of a real microburst 'DL-191' that caused the crash of Delta Airlines Flight 191 on August 2nd 1985, from Figure 5.9 in Fujita (1986), and extracted from Lundgren, Yao, and Mansour (1992) Figure 3c. Figure 7.2 indicates that by using scalings from Lundgren, Yao, and Mansour (1992), similarity solutions developed in the laboratory and using LES are relevant for atmospheric events.

### 7.2.2 Implications for the Wind Industry

In the late 1970s, research into downbursts was triggered by a series of fatal aviation disasters (Fujita and Byers, 1977), prompting two measurement campaigns: i) the Nothern Illinois Meteorlogical Research On Downburst (NIMROD) and ii) the Joint Airport Weather Studies (JAWS) (McCarthy, Wilson, and Fujita, 1982), which attempted to understand the strong gusts and hazardous wind shear that develop in downbursts, endangering aviation and engineering structures. Now almost 50 years later, their is a new industry building 100 m high structures, in some of the windiest places in the world; the wind industry. Currently, there is a poor understanding

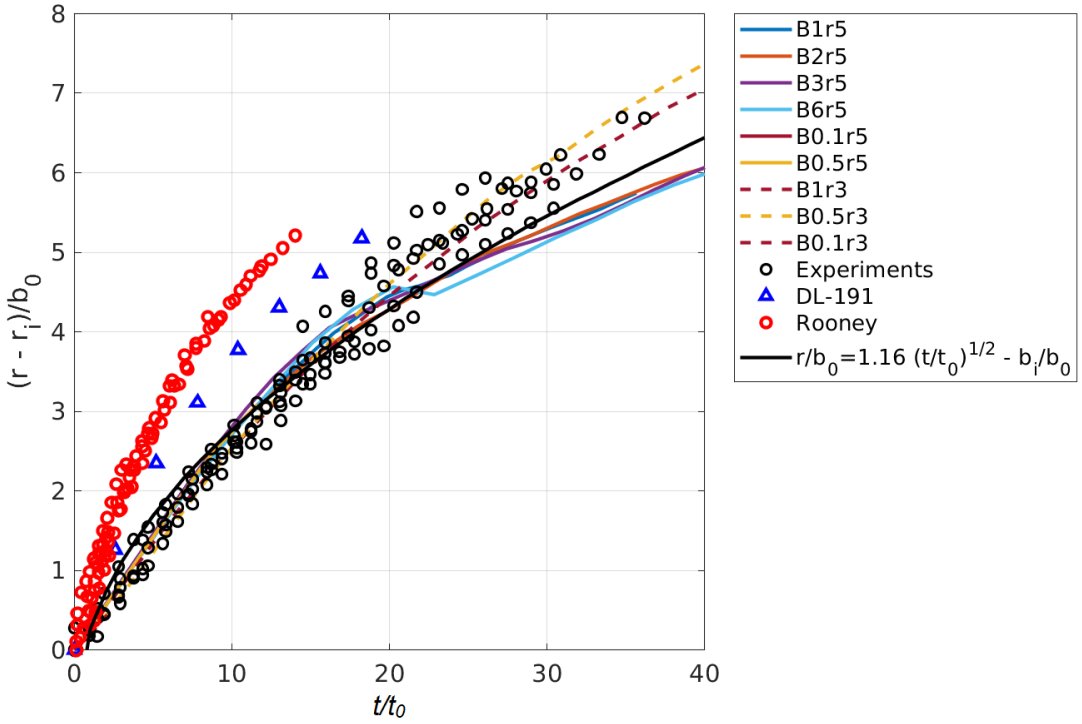


FIGURE 7.2: Scaled radial propagation versus scaled time. Laboratory experiments from Chapter 3 are plotted as black circles, MONC LES runs from Chapter 5 are plotted as solid and dashed coloured lines, LES results from Rooney (2015) are plotted as red circles and anemometer ground measurements of a real microburst is plotted as blue triangles (Fujita, 1986). The black solid line is this study's modified equation for radial spread (7).

of the loading and performance of wind turbines in extreme conditions. Figure 7.3 plots a wind resource map over Denver, Colorado. The original measurement area of the JAWS Project is marked by the dashed black box. In the surrounding area, there are over 25 operational wind farms (marked by the blue turbine symbol). In only 86 days, between the 15th May 1982 to August 9th 1982, the JAWS project identified and recorded 186 downburst events. It is therefore inevitable that the operational wind farms in Figure 7.3 are regularly experiencing downbursts. Whilst the author is not privy to the tools and methodologies in the wind resource and site assessments conducted by the developers of the wind farms in Figure 7.3, it is very unlikely that mesoscale phenomenon such as downbursts are included. Typically when wind resource assessments are conducted, local measurements from a meteorological mast (2+ years) are combined with long term corrections from mesoscale data to provide a representative distribution of the local wind regime (10+ years). The use of long term averaging means that the impact of highly transient phenomenon such as downbursts are neglected in the analysis.

In the International Electrotechnical Commission (IEC) guidelines for wind turbine design (Commission, 2006), extreme wind events are represented by a sinusoidal function for wind speed, applied over a defined gust interval $T$,

$$u(z,t) = \begin{cases} u(z) - 0.37u_{gust}\sin(3\pi t/T)(1-\cos(2\pi t/T)) & (0 \leq t \leq T) \\ u(z) & \text{otherwise} \end{cases} \tag{7.2.1}$$

where $u(z,t)$ is the horizontal wind speed as a function of time and height, $u(z)$ is the power-law wind profile (empirically determined using the site measurements), $u_{gust}$ is the magnitude of gust at hub height. However in Chapter 3 (Section 3.3.7), the vertical profile of the horizontal wind was found to be similar to the empirical profile proposed by Wood et al. (2001) and Sengupta and Sarkar (2008), where

$$\frac{u}{u_m} = C_4\left(\frac{z}{n_1}\right)_1^n\left[1-\text{erf}\left(C_5\frac{z}{b}\right)\right], \tag{7.2.2}$$

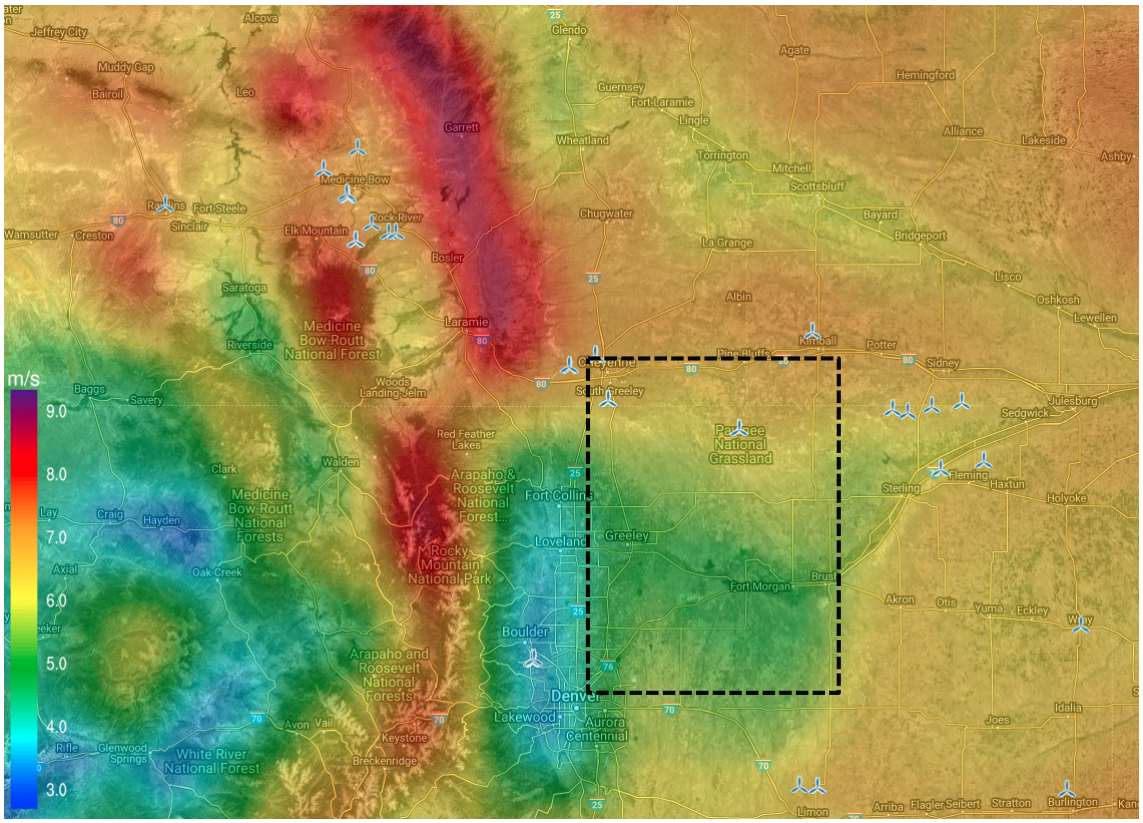


FIGURE 7.3: Wind resource map of Denver, Colorado. Courtesy of Vortex FdC (`https://vortexfdc.com/`). Contours of mean wind speed between 2008-2017, generated by the mesoscale model WRF using ERA5 boundary conditions. The approximate area covered by radar from the 1980 JAWS Project is shown in the dashed black square. Operational wind farms are marked by the blue turbine symbol.

where $C_4$, $C_5$ and $n_1$ are constants, and erf is the error function. Equations (7.2.1) and (7) are significantly different in form to each other, suggests radically different mean wind fields and levels of shear. The consequences of poorly estimating the loading conditions of wind turbines is not be underestimated. In 2011, only 700 miles away from the JAWS measurement site (Figure 7.3), the Buffalo wind farm experienced extreme structural damage as blades from multiple turbines broke off and a tower buckled in the intense winds from downburst outflows (Hawbecker, Basu, and Manuel, 2017).

Whilst some preliminary work has been conducted on this topic (Zhang, Sarkar, and Hu, 2013; Huy Nguyen and Manuel, 2013; Lu et al., 2019), and the author is aware of at least two (both confidential) joint industry project dedicated to better understanding loading from gust events, more research is required. Hopefully, the simplified relations of radial propagation and particularly the estimation of maximum radial velocity based on the initial properties of downburst, suggested in Chapter 3:

$$u_{rmax} = k_u Fr_c \lambda^{1/2} B^{1/2} r^{-1} \tag{7.2.3}$$

where from experiments $k_u = 3$, will provide useful estimations for the wind industry. An obvious next piece of work would be testing (7.0.1) against the numerical runs in Chapter 5, before comparing to actual atmospheric cases.

# Bibliography

Abd-Elaal, El-Sayed, Julie E Mills, and Xing Ma (2013). "A coupled parametric-CFD study for determining ages of downbursts through investigation of different field parameters". In: *Journal of Wind Engineering and Industrial Aerodynamics* 123, pp. 30–42.

Aboshosha, Haitham, Girma Bitsuamlak, and Ashraf El Damatty (2015). "Turbulence characterization of downbursts using LES". In: *Journal of Wind Engineering and Industrial Aerodynamics* 136, pp. 44–61.

Anabor, V et al. (2011). "Large-eddy simulation of a microburst". In: *Atmospheric Chemistry and Physics* 11.17, pp. 9323–9331.

Batchelor, G. K. (1954). "Heat convection and buoyancy effects in fluids". In: *Quarterly Journal of the Royal Meteorological Society* 80.345, pp. 339–358.

Benjamin, T. Brooke (1968). "Gravity currents and related phenomena". In: *Journal of Fluid Mechanics* 31.2, 209–248. DOI: 10.1017/S0022112068000133.

Blyth, Alan M, Sonia G Lasher-Trapp, and William A Cooper (2005). "A study of thermals in cumulus clouds". In: *Quarterly Journal of the Royal Meteorological Society: A journal of the atmospheric sciences, applied meteorology and physical oceanography* 131.607, pp. 1171–1190.

Bond, D and H Johari (2005). "Effects of initial geometry on the development of thermals". In: *Experiments in fluids* 39.3, pp. 591–601.

Bonnecaze, Roger T, Herbert E Huppert, and John R Lister (1993). "Particle-driven gravity currents". In: *Journal of Fluid Mechanics* 250, pp. 339–369.

Britannica, Encyclopaedia (2012). *Microburst*. URL: https://www.britannica.com/science/microburst.

Britter, R (1979). "The spread of a negatively buoyant plume in a calm environment". In: *Atmospheric Environment (1967)* 13.9, pp. 1241–1247.

Brown, Andy R, SH Derbyshire, and Paul J Mason (1994). "Large-eddy simulation of stable atmospheric boundary layers with a revised stochastic subgrid model". In: *Quarterly Journal of the Royal Meteorological Society* 120.520, pp. 1485–1512.

Brown, Nick et al. (2015). "A highly scalable Met Office NERC Cloud model". In: *Proceedings of the 3rd International Conference on Exascale Applications and Software*. University of Edinburgh, pp. 132–137.

Browning, KA et al. (2010). "Observations of dual slantwise circulations above a cool undercurrent in a mesoscale convective system". In: *Quarterly Journal of the Royal Meteorological Society* 136.647, pp. 354–373.

Bryan, George H and J Michael Fritsch (2002). "A benchmark simulation for moist nonhydrostatic numerical models". In: *Monthly Weather Review* 130.12, pp. 2917–2928.

Chay, MT, Faris Albermani, and Richard Wilson (2006). "Numerical and analytical simulation of downburst wind loads". In: *Engineering Structures* 28.2, pp. 240–254.

Chen, JC and CHEN JC (1977). "Spreading of buoyant discharges." In: *ICHMT Seminar on Turbulent Buoyant Convection*, 171–182.

Chen, Jing-Chang (1980). "Studies on gravitational spreading currents". PhD thesis. California Institute of Technology.

Ciriello, F and GR Hunt (2020). "Analytical solutions and virtual origin corrections for forced, pure and lazy turbulent plumes based on a universal entrainment function". In: *Journal of Fluid Mechanics* 893.

Commission, International Electrotechnical et al. (2006). "Wind turbines-part 1: design requirements". In: *IEC 614001 Ed. 3*.

Crook, N Andrew (1988). "Trapping of low-level internal gravity waves". In: *Journal of the Atmospheric Sciences* 45.10, pp. 1533–1541.

Davies-Jones, Robert (2003). "An Expression for Effective Buoyancy in Surroundings with Horizontal Density Gradients". In: *Journal of the Atmospheric Sciences* 60.23, pp. 2922–2925.

Devenish, BJ, GG Rooney, and DJ Thomson (2010). "Large-eddy simulation of a buoyant plume in uniform and stably stratified environments". In: *Journal of Fluid Mechanics* 652, pp. 75–103.

Drysdale, Dougal (2011). *An introduction to fire dynamics*. John Wiley & Sons.

Emanuel, Kerry A (1981). "A similarity theory for unsaturated downdrafts within clouds". In: *Journal of the Atmospheric Sciences* 38.8, pp. 1541–1557.

Fritts, David C (1984). "Gravity wave saturation in the middle atmosphere: A review of theory and observations". In: *Reviews of Geophysics* 22.3, pp. 275–308.

Fujita, T (1985). *The Downburst: Microburst and Macroburst*. Tech. rep. Univ. of Chicago.

Fujita, T Theodore and Horace R Byers (1977). "Spearhead echo and downburst in the crash of an airliner". In: *Monthly Weather Review* 105.2, pp. 129–146.

Fujita, Tetsuya Theodore (1986). "DFW (Dallas-Ft. Worth) microburst on August 2, 1985". In: *NASA Technical Report*.

Geerts, Bart et al. (2017). "The 2015 plains elevated convection at night field project". In: *Bulletin of the American Meteorological Society* 98.4, pp. 767–786.

Gray, MEB et al. (2001a). "Version 2.3 of the Met. Office large eddy model". In: *Met Office (APR) Turbulence and Diffusion Rep* 276.

— (2001b). "Version 2.3 of the Met Office large eddy model: part II. Scientific documentation". In: *Met O (APR) Turbulence and Diffusion note*.

Gregory, D (1997). "The Mass Flux Approach to the Parametrization of Deep Convection". In: *The Physics and Parameterization of Moist Atmospheric Convection*. Springer, pp. 297–319.

Grundy, R and J Rottman (1985). "The approach to self-similarity of the solutions of the shallow-water equations representing gravity-current releases". In: *Journal of Fluid Mechanics* 156, pp. 39–53.

Hallworth, Mark et al. (1996). "Entrainment into two-dimensional and axisymmetric turbulent gravity currents". In: *Journal of Fluid Mechanics* 308, pp. 289–311.

Hawbecker, Patrick, Sukanta Basu, and Lance Manuel (2017). "Realistic simulations of the July 1, 2011 severe wind event over the Buffalo Ridge Wind Farm". In: *Wind Energy* 20.11, pp. 1803–1822.

Heinold, B et al. (2013). "The role of deep convection and nocturnal low-level jets for dust emission in summertime West Africa: Estimates from convection-permitting simulations". In: *Journal of Geophysical Research: Atmospheres* 118.10, pp. 4385–4400.

Hjelmfelt, Mark R (1988). "Structure and life cycle of microburst outflows observed in Colorado". In: *Journal of Applied Meteorology* 27.8, pp. 900–927.

Holmes, JD and SE Oliver (2000). "An empirical model of a downburst". In: *Engineering Structures* 22.9, pp. 1167–1172.

Holyer, Judith Y and Herbert E Huppert (1980). "Gravity currents entering a two-layer fluid". In: *Journal of Fluid Mechanics* 100.4, pp. 739–767.

Hunt, GR and TS Van den Bremer (2011). "Classical plume theory: 1937–2010 and beyond". In: *IMA journal of applied mathematics* 76.3, pp. 424–448.

Hunt, GR and NB Kaye (2005). "Lazy plumes". In: *Journal of Fluid Mechanics* 533, p. 329.

Hunt, GR and NG Kaye (2001). "Virtual origin correction for lazy turbulent plumes". In: *Journal of Fluid Mechanics* 435, p. 377.

Huppert, Herbert E and John E Simpson (1980). "The slumping of gravity currents". In: *Journal of Fluid Mechanics* 99.4, pp. 785–799.

Huy Nguyen, Hieu and Lance Manuel (2013). "Thunderstorm downburst risks to wind farms". In: *Journal of Renewable and Sustainable Energy* 5.1, p. 013120.

Jun-ichi, Yano et al. (2015). *Parameterization Of Atmospheric Convection (In 2 Volumes)*. Vol. 1. World Scientific.

Kaye, N. B. and G. R. Hunt (2007). "Overturning in a filling box". In: *Journal of Fluid Mechanics* 576, 297–323. DOI: 10.1017/S0022112006004435.

Kim, Jongdae and Horia Hangan (2007). "Numerical simulations of impinging jets with application to downbursts". In: *Journal of Wind Engineering and Industrial Aerodynamics* 95.4, pp. 279–298.

Kreczak, H (2015). "An investigation into scaling relations governing the impingment and radial propogation of descending downdraughts". MA thesis. University of Leeds.

Kruger, Emily et al. (2017). "Initial Descent of a Thermal and the Application to Downdraughts". In: *APS*, E33–004.

Lane, Todd P, Michael J Reeder, and Terry L Clark (2001). "Numerical modeling of gravity wave generation by deep tropical convection". In: *Journal of the Atmospheric Sciences* 58.10, pp. 1249–1274.

Lecoanet, Daniel and Nadir Jeevanjee (2019). "Entrainment in resolved, dry thermals". In: *Journal of the Atmospheric Sciences* 76.12, pp. 3785–3801.

Leonard, BP, MK MacVean, and AP Lock (1993). "Positivity-preserving numerical schemes for multidimensional advection". In:

Linden, PF and JE Simpson (1994). "Continuous releases of dense fluid from an elevated point source in a cross-flow". In: *Mixing and transport in the environment*, pp. 401–418.

Lu, Nan-You et al. (2019). "On wind turbine loads during thunderstorm downbursts in contrasting atmospheric stability regimes". In: *Energies* 12.14, p. 2773.

Lundgren, TS, J Yao, and NN Mansour (1992). "Microburst modelling and scaling". In: *Journal of Fluid Mechanics* 239, pp. 461–488.

Mahrt, Larry (1999). "Stratified atmospheric boundary layers". In: *Boundary-Layer Meteorology* 90.3, pp. 375–396.

Manasseh, Richard, Chang-Yun Ching, and Harindra JS Fernando (1998). "The transition from density-driven to wave-dominated isolated flows". In: *Journal of Fluid Mechanics* 361, pp. 253–274.

Marsham, JH et al. (2010). "Multi-sensor observations of a wave beneath an impacting rear-inflow jet in an elevated mesoscale convective system". In: *Quarterly Journal of the Royal Meteorological Society* 136.652, pp. 1788–1812.

Marsham, John H et al. (2011). "Observations of elevated convection initiation leading to a surface-based squall line during 13 June IHOP_2002". In: *Monthly Weather Review* 139.1, pp. 247–271.

Marsham, John H et al. (2013). "Meteorology and dust in the central Sahara: Observations from Fennec supersite-1 during the June 2011 Intensive Observation Period". In: *Journal of Geophysical Research: Atmospheres* 118.10, pp. 4069–4089.

Mason, MS, CW Letchford, and DL James (2005). "Pulsed wall jet simulation of a stationary thunderstorm downburst, Part A: Physical structure and flow field characterization". In: *Journal of Wind Engineering and Industrial Aerodynamics* 93.7, pp. 557–580.

Mason, Paul J (1989). "Large-eddy simulation of the convective atmospheric boundary layer". In: *Journal of the Atmospheric Sciences* 46.11, pp. 1492–1516.

Mason, Paul J and David J Thomson (1992). "Stochastic backscatter in large-eddy simulations of boundary layers". In: *Journal of Fluid Mechanics* 242, pp. 51–78.

Maxworthy, T et al. (2002). "The propagation of a gravity current into a linearly stratified fluid". In: *Journal of Fluid Mechanics* 453, pp. 371–394.

McCarthy, John, James W Wilson, and T Theodore Fujita (1982). "The joint airport weather studies project". In: *Bulletin of the American Meteorological Society* 63.1, pp. 15–22.

Morton, BR and Jason Middleton (1973). "Scale diagrams for forced plumes". In: *Journal of Fluid Mechanics* 58.1, pp. 165–176.

Morton, BR, Geoffrey Taylor, and JS Turner (1956). "Turbulent gravitational convection from maintained and instantaneous sources". In: *Proceedings of the Royal Society of London. Series A. Mathematical and Physical Sciences* 234.1196, pp. 1–23.

Morton, BR 1959 (1959). "Forced plumes". In: *Journal of Fluid mechanics* 5.1, pp. 151–163.

Nappo, Carmen J (2013). *An introduction to atmospheric gravity waves*. Academic Press.

Nurser, AJG, Robert Marsh, and Richard G Williams (1999). "Diagnosing water mass formation from air–sea fluxes and surface mixing". In: *Journal of Physical Oceanography* 29.7, pp. 1468–1487.

Orf, Leigh, Erica Kantor, and Eric Savory (2012). "Simulation of a downburst-producing thunderstorm using a very high-resolution three-dimensional cloud model". In: *Journal of Wind Engineering and Industrial Aerodynamics* 104, pp. 547–557.

Orf, Leigh G, John R Anderson, and Jerry M Straka (1996). "A three-dimensional numerical analysis of colliding microburst outflow dynamics". In: *Journal of the Atmospheric Sciences* 53.17, pp. 2490–2511.

Parker, Matthew D (2008). "Response of simulated squall lines to low-level cooling". In: *Journal of the Atmospheric Sciences* 65.4, pp. 1323–1341.

Piacsek, Steve A and Gareth P Williams (1970). "Conservation properties of convection difference schemes". In: *Journal of Computational Physics* 6.3, pp. 392–405.

Proctor, Fred H (1988). "Numerical simulations of an isolated microburst. Part I: Dynamics and structure". In: *Journal of the Atmospheric Sciences* 45.21, pp. 3137–3160.

Romps, David M and Nadir Jeevanjee (2016). "On the sizes and lifetimes of cold pools". In: *Quarterly Journal of the Royal Meteorological Society* 142.696, pp. 1517–1527.

Rooney, Gabriel G and Paul F Linden (2012). "Radial jet due to plume impingement on a horizontal surface". In: *Proceedings of the ICE-Engineering and Computational Mechanics* 165.4, pp. 223–233.

Rooney, GG (2015). "Descent and spread of negatively buoyant thermals". In: *Journal of Fluid Mechanics* 780, pp. 457–479.

Schmidt, Jerome M and William R Cotton (1990). "Interactions between upper and lower tropospheric gravity waves on squall line structure and maintenance". In: *Journal of the Atmospheric Sciences* 47.10, pp. 1205–1222.

Schmidt, Wilhelm (1941). "Turbulente ausbreitung eines stromes erhitzter luft". In: *ZAMM-Journal of Applied Mathematics and Mechanics/Zeitschrift für Angewandte Mathematik und Mechanik* 21.5, pp. 265–278.

Scorer, Richard (1956). "Experiments with convection bubbles". In: *OSTIV Publications* 4, pp. 153–154.

Scorer, Robert S (1957). "Experiments on convection of isolated masses of buoyant fluid". In: *Journal of Fluid Mechanics* 2.06, pp. 583–594.

Sengupta, Anindya and Partha P Sarkar (2008). "Experimental measurement and numerical simulation of an impinging jet with application to thunderstorm microburst winds". In: *Journal of Wind Engineering and Industrial Aerodynamics* 96.3, pp. 345–365.

Shusser, Michael and Morteza Gharib (2000). "A model for vortex ring formation in a starting buoyant plume". In: *Journal of Fluid Mechanics* 416, pp. 173–185.

Simpson, John E (1999). *Gravity currents: In the environment and the laboratory*. Cambridge University Press.

Slim, Anja C and Herbert E Huppert (2011). "Axisymmetric, constantly supplied gravity currents at high Reynolds number". In: *Journal of fluid mechanics* 675, pp. 540–551.

Stoelinga, Mark T et al. (2003). "Is a cold pool necessary for the maintenance of a squall line produced by a cold front aloft?" In: *Monthly Weather Review* 131.1, pp. 95–115.

Sun, Jielun et al. (2015). "Review of wave-turbulence interactions in the stable atmospheric boundary layer". In: *Reviews of Geophysics* 53.3, pp. 956–993.

Sutherland, Bruce R (2010). *Internal gravity waves*. Cambridge University Press.

Tarshish, Nathaniel, Nadir Jeevanjee, and Daniel Lecoanet (2018). "Buoyant motion of a turbulent thermal". In: *Journal of the Atmospheric Sciences* 75.9, pp. 3233–3244.

Taylor, GI (1946). *Dynamics of a mass of hot gas rising in air*. Vol. 919. Technical Information Division, Oak Ridge Operations.

Turner, JS (1962). "The 'starting plume' in neutral surroundings". In: *Journal of Fluid Mechanics* 13.03, pp. 356–368.

— (1969). "Buoyant plumes and thermals". In: *Annual Review of Fluid Mechanics* 1.1, pp. 29–44.

— (1979). *Buoyancy effects in fluids*. Cambridge University Press.

Vermeire, Brian C, Leigh G Orf, and Eric Savory (2011). "Improved modelling of downburst outflows for wind engineering applications using a cooling source approach". In: *Journal of Wind Engineering and Industrial Aerodynamics* 99.8, pp. 801–814.

Walin, Gösta (1982). "On the relation between sea-surface heat flow and thermal circulation in the ocean". In: *Tellus* 34.2, pp. 187–195.

White, Brian L and Karl R Helfrich (2012). "A general description of a gravity current front propagating in a two-layer stratified fluid". In: *Journal of Fluid Mechanics* 711, pp. 545–575.

Williams, S (2015). "Dynamics of Downdraughts". MA thesis. University of Leeds.

Wood, Graeme S et al. (2001). "Physical and numerical modelling of thunderstorm downbursts". In: *Journal of Wind Engineering and Industrial Aerodynamics* 89.6, pp. 535–552.

Woodward, Betsy (1959). "The motion in and around isolated thermals". In: *Quarterly Journal of the Royal Meteorological Society* 85.364, pp. 144–151.

Zhang, Yan, Partha Sarkar, and Hui Hu (2013). "An Experimental Study of Microburst-Wind Induced Loads on a Wind Turbine Model". In: *31st AIAA Applied Aerodynamics Conference*, p. 3159.

— (2014). "An experimental study on wind loads acting on a high-rise building model induced by microburst-like winds". In: *Journal of Fluids and Structures* 50, pp. 547–564.